ISSN 1984-9648
ISSN 2175-9146 (online)

JOURNAL OF AEROSPACE TECHNOLOGY AND MANAGEMENT

Vol. 8 Nº. 1 – Jan./Mar. 2016

 ISSN 1984-9648 | ISSN 2175-9146 (online)

CONTENTS

doi: 10.5028/jatm.v7i4.549

A Transforming Scenario: the New Space Agenda

Tessaleno Devezas[1]

I believe that most coevals of my generation, the so-called 'baby-boom' generation, living as teenagers in the 1960s, have imagined that at the dawn of the 21st century we were witnessing a very lively space flight era, with manned space stations and human colonies on the Moon and even on Mars. Every teenager at that time, witnessing the 'live transmission' of men walking on the Moon, has certainly dreamed of this possibility, and Kubrik's and Arthur Clarke's *2001 – A Space Odyssey* (produced in 1968) represented the incarnation of this hopeful future. But later, in the 1990s, as mature adults, the idea came to those minds that the Earth seemed to have stood still – at least with regard to space activities. What happened?

What is known today as the 'Space Race' began suddenly in the 1950s and has grown explosively during the following two decades, but decreased steadily after the 1970s. There were many reasons for the twilight of space activities observed after this date, among them we can mention the onset of the worldwide economic crisis triggered by the 'oil crisis' of 1972, diminishing space budgets, the gradual innovation process, technological barriers, the end of the Cold War, and perhaps the most important one – the absence of market forces. An extensive analysis of these causes was recently offered in a paper of mine in collaboration with my co-workers at the Technological Observatory of the IAE - DCTA (Devezas *et al.* 2012). But in the same publication we have demonstrated that, after the 1990s, however, we are witnessing a shy rebirth of space-related activities, with characteristics very different from that imagined by futurists active in the 1960s and 1970s. What means this recovery? Are we witnessing the burgeoning of a new space race?

During the space race that characterized the onset and further development of space exploration, the rules of the game, as stated above, were not dictated by the market. Now things are changing, and with the entry at the stage of several other players, the strong market forces are showing their strength. The exciting news for space enthusiasts is that the space sector is experiencing nowadays important changes with two major characteristics: firstly a transition from an exclusively government-led to a new market-oriented space exploration activity, where private enterprises are increasingly involved, and secondly the participation of several nations struggling for a place in the new space scenario, leaving behind the old fashioned one leaded by incumbent world powers that dominated this field in past decades.

The former constitutes perhaps the most striking aspect of modern aerospace activities, which gave birth near the end of the 1990s to the umbrella term 'NewSpace' (Bizony 2014; Lindsey 2009) which designates the emergent private spaceflight industry, a community of relatively new aerospace companies working to develop low-cost access to space and/or spaceflight technologies, and advocates a new space policy. These two features have given rise to a complex game of interests in the space sector, with the participation of several new players (or agents), nations and private companies, and that still lacks a clear definition of rules that shall better direct the future development of this sector.

The recent dramatic increase in the number of companies engaged in space activities led to the common usage of the phrases 'new space companies' and 'entrepreneurial space', or most commonly 'NewSpace' as stated above, intended to designate a new approach to space development that differ significantly from that taken by NASA and the mainstream aerospace industry. This new group of private enterprises is characterized by seeking the cheaper development of launch systems (Stern 2013) and/or space technologies principally with private funding, with only secondary or no involvement with government spaceflight programs and contractors. Traditional private companies that conduct aeronautical efforts, such as Boeing or Lockheed, are generally not considered part of NewSpace due to their heavy reliance on NASA development funding and military space programs as part of their business model. In some measure, NewSpace companies are still dependent on NASA, often participating in projects such as *Commercial Orbital Transportation*

1.Universidade da Beira Interior – Faculdade de Engenharia – Departamento de Engenharia Eletromecânica – Covilhã – Portugal.

Author for correspondence: Tessaleno Devezas – Universidade da Beira Interior – Faculdade de Engenharia – Departamento de Engenharia Eletromecânica | Calçada Fonte do Lameiro 6201-001 | Covilhã– Portugal | Email: tessalen@ubi.pt

Services, a NASA program established in 2006 to coordinate the delivery of crew and cargo to the International Space Station by private companies. But generally speaking NewSpace companies tend to focus primarily on consumers in the private sector. It is worth pointing out the existence to date of about a hundred of such enterprises, some of them have not yet really started commercial activities. Recent extrapolations of the trend curve point to a probable total of about 200 active private companies around 2030 (Ribeiro 2015).

As mentioned above the other major group of new actors in the new environment of space activities consists of the growing number of nations entering the stage. As spacefaring nations we understand those nations capable of independently building and launching craft into space. The list of spacefaring nations grew from just two in the middle of the last century to about 13 today, namely: Russia, USA, China, UK, France, Canada, Japan, India, Israel, Ukraine, Iran, North Korea, and South Korea. But far more significant is the growing number of nations with satellites (mainly communications, but not only) placed in orbit. This number grew from just 4 in 1962, the year in which UK and Canada entered the club of spacefaring nations, to 82 today. Evidently, this number includes not just those nations that did it with their own launching capabilities, but also those that used launching means of the spacefaring nations.

Returning then to our question: are we witnessing now a new space race? Probably not. This time is different, we do not have now the rush factor, there is not the desperate objective to come first. What we have is simply a redesigned configuration of the space scenario that certainly can be defined as the *New Space Agenda* for the first half of the 21st century.

Undoubtedly, this new agenda appears as an excellent opportunity for companies focused on space activities, and this is even better if the nations that are at their home have technological skills for the deployment of craft in space. I was recently surprised by the news that the next nation to enter the exclusive club of spacefaring nations will be Argentina, which expects to gain space access in 2016 through the development and flight qualification of its launching vehicle project Tronador II.

It follows then the natural question: what is our position (Brazil) on this agenda and in this new scenario? What are our real chances to achieve in the near future the goal set about four decades ago of becoming a spacefaring nation? Obviously it is not my purpose in this editorial to analyze, let alone provide an answer to this disturbing question. But I would like to call the attention of our readers to an article published this year in the pages of *Space Policy*, with the suggestive title: "Brazil's space program: dreaming with its feet on the ground" (Moltz 2015). Indeed, a must read!

The author, a researcher at the well-known Department of National Security Affairs of the Naval Postgraduate School (Monterey, CA), starts his reasoning with the sad (to us) statement that Brazil, placed among the world's top ten economies, is the only country that lacks either a national space launch capability or membership in a space-capable regional body like ESA. Still more vexing is our insignificant (regarding space capability) last place among the BRIC countries. The author also offers an interesting analysis of the factors that have held back Brazil in this field, some of which continue to influence its police today: apart from the obvious 'inadequate funding', but also and importantly, 'conflicting organizations, poorly handled foreign relations, and an unclear vision for Brazil's place in space'. The picture that the author paints about the complex path that Brazil must tread toward becoming an effective member of the restrict club of spacefaring nations constitutes an excellent array of food for thought.

But fortunately not everything we see in the panorama of Brazilian space activities is so negative. I am witness of brilliant initiatives that give us great hope for the future, and wish to highlight the important role that the JATM has played in this context, a journal of high scientific and editorial quality, now indexed in Scopus among other few publications in the aerospace field, and recently upgraded by CAPES as B2 publication. I wish to congratulate the editorial board of JATM for this success, which constitutes an inestimable contribution to enhance Brazilian visibility in the new space agenda.

REFERENCES

Bizony P (2014) New space frontiers: venturing into Earth orbit and beyond. Minneapolis, MN: Zenith Press.

Devezas T, Melo FCL, Gregori ML, Salgado MCV, Ribeiro JR, Devezas CBC (2012) The struggle for space: past and future of the space race. Technol Forecast Soc 79(5):963-985. doi: 10.1016/j.techfore.2011.12.006

Lindsey CS (2009) Defining NewSpace. Hobby Space; [accessed 2015 Sept 10]. http://www.hobbyspace.com/NewSpace/

Moltz JC (2015) Brazil's space program: dreaming with its feet on the ground. Space Policy 32:1-7. doi: 10.1016/j.spacepol.2015.05.001

Ribeiro JR (2015) Construção de cenários futuros para o setor espacial (PhD thesis). São José dos Campos: Instituto Tecnológico de Aeronáutica.

Stern AS (2013) The low-cost ticket to space. Sci Am 308(4):68-73. doi: 10.1038/scientificamerican0413-68

doi: 10.5028/jatm.v8i1.564

A Review on Aerodynamics of Non-Flapping Bird Wings

Mohammed Abdulmalek Aldheeb[1], Waqar Asrar[1], Erwin Sulaeman[1], Ashraf Ali Omar[2]

ABSTRACT: Birds are known for their agility, manoeuvrability, and flexibility during flight. These features allow their ability to fly under a large range of flight conditions. Bio flyers and bio aerodynamic/fluid surfaces have inspired many to perform experiments and simulations as well as to relate their results to engineering applications. Wings specifically have been the most inspirational element. Aerodynamic forces, structure, unsteady flow, fluid-structure interaction, flow control, flow adaptive elements and mechanisms, flow vortices, flapping mechanisms, and hovering flight of birds are examples of research interests. This paper presents an overview of prior analyses and experiments on the aerodynamic performance and mechanical properties of birds in steady non-flapping flight.

KEYWORDS: Flexibility, Porosity, Aerodynamics, Birds, Feather.

INTRODUCTION

Recently, the need for micro air vehicles has resulted in an increase in the attention to bird flight and in the study of their performance as they fly at low Reynolds numbers (Carruthers *et al.* 2010). It is very important to seek the viable aspects in studying natural flyers that can be implemented in practical applications such as wing aerodynamics, structure and control, as noted by Jacob (1998).

Aerodynamics of bird airfoils and wings is classified into three categories. First, the analysis of airfoils/wings of birds as a fixed rigid body; second, birds airfoils/wings in flapping phase; and third, flexible airfoils/wings in non-flapping flight. Bird wing structure is another focus found in some studies in which the feathers bend and twist under aerodynamic forces. Therefore, establishing their mechanical properties leads to an understanding of their influence on aerodynamic performance as studied by Bachmann (2010), Bonser and Purslow (1995), Jacob (1998), Macleod (1980), Purslow and Vincent (1978). Also, movement and vibration of feathers play a role in flight control as mentioned by Brown and Fedde (1993) and Jacob (1998), influencing aerodynamic performance. Adaptive wings improve efficiency, manoeuvrability, control, weight and cost (Jacob 1998).

Natural flyers are difficult to study experimentally due to the complexity in their structural surface, control and agility in manoeuvring (Shyy *et al.* 2008). The wing structure, surface flexibility, flexibility of feathers, vane and surface hair are a huge challenge to mimic. Another challenge is that the fluid motion is unsteady and has many different phases as the birds' flap bend and wings move based on the flight conditions. A challenge is that the scaling of both fluid dynamics and structural dynamics

1.International Islamic University Malaysia – Kulliyyah of Engineering – Department of Mechanical Engineering – Kuala Lumpur – Malaysia. **2.**University of Tripoli – Faculty of Engineering – Department of Aeronautical Engineering – Tripoli – Libya.

Author for correspondence: Waqar Asrar | International Islamic University Malaysia – Kulliyyah of Engineering – Department of Mechanical Engineering | Jalan Gombak, 53100 | Kuala Lumpur – Malaysia | Email: waqar@iium.edu.my

Received: 11/02/2015 | **Accepted:** 01/11/2016

between smaller natural flyer and practical flying hardware/lab experiment (larger dimension) is fundamentally difficult (Shyy *et al.* 2008). A study of wings with flexible and porous surfaces has not been performed yet. Figure 1 shows a dorsal view of a bird wing planform with its nomenclature that highlights the complex geometry of the multilayer planforms with different functionalities for each layer and sublayer components. Figure 2 describes the sublayer component structure that exposes the nature of the non-prismatic, flexible slender beam structure with flexible connections.

MECHANISM/MORPHOLOGY

A feather consists of a shaft and vanes (Fig. 3). The inclination of the barbs makes the vane more resistant to aerodynamic forces from its lower side than upper side (Fig. 4). Vanes of a feather are not equally distributed on the shaft. One vane is larger than the other side of the feather's shaft, which creates moment on a single feather about its shaft. However, multiple feathers overlap resulting in zero moment (a small tilting moment occurs due to the flexibly of the feather) (Muller and Patone 1998).

Mechanical behaviour of wings is affected by differences in morphology and function of feathers. The outer primaries are more resistant to forces than inner primaries, especially at the tip, and the outermost primary acts as a reversible airfoil during take-off (Ennos *et al.* 1995). Tip feathers of a bird's wing reduce the drag by allowing air to pass thorough and use tip reversal upstroke (Crandell and Tobalske 2011).

Mechanoreceptors — alula receptors, convert feather receptors and secondary feathers receptors — (Fig. 1), associated with feathers, function as flow sensors. The discharge frequency of mechanoreceptors is produced by dorsal elevation of coverts, which is related to the elevation of the angle of attack. They detect flow separation point, predict the upcoming flow stall point and measure the airspeed on surface using frequency vibration as noted by Brown and Fedde (1993).

Wing alula makes the underwing coverts deployment closed with wing sweep during pitch-up manoeuver and is protected by passive peeling coming off from its tip (Carruthers *et al.* 2007). The aeroelastic devices were also examined in the Eagle wing using a video camera at a high speed of 500 frames per second placed on the upper wing to analyse the deflection of underwing coverts in outdoor and indoor perching sequences. Carruthers *et al.* (2007) concluded that underwing coverts operate as a high lift device and the alula functions, as strakes.

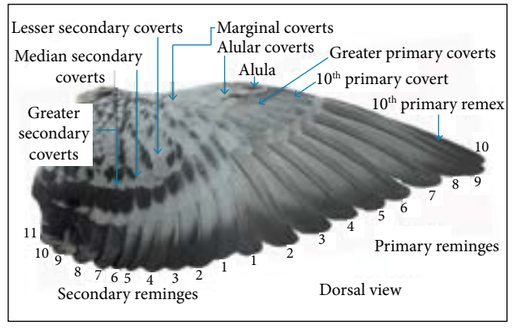

Figure 1. Topography of a Pigeon wing (dorsal view on a separated Pigeon wing; Bachmann, 2010). The numbers represent location of feathers in the wing.

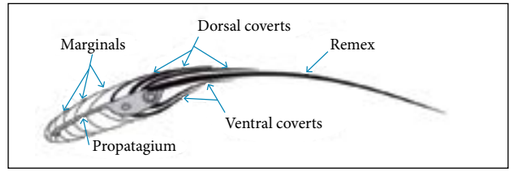

Figure 2. Diagrammatic section of a bird wing at the lower arm level. The shaded area indicates the impervious parts of the extremity (Muller and Patone 1998).

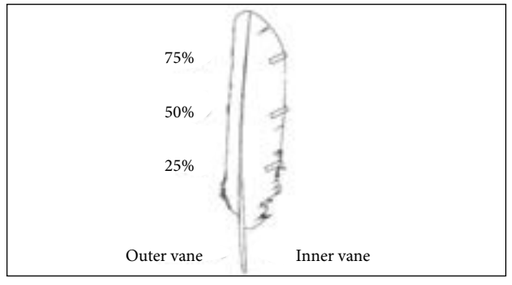

Figure 3. Inner and outer vane of feather (Bachmann 2010).

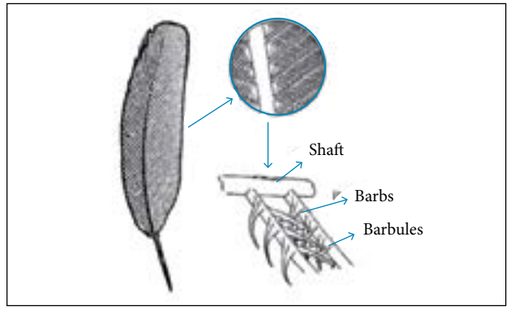

Figure 4. Characteristic of bird feather (Chen *et al.* 2013).

These aeroelastic devices seem to be used for flow control to enhance unsteady manoeuvres. However, these suggestions are based on visualization of a flying bird and were not determined through experiments.

AERODYNAMICS OF BIO WINGS/AIRFOILS

Extensive research on airfoil shape, unsteady flow analysis, structure and control is required for adaptive wing development where such applications are feasible in practical applications such as micro air vehicles (MAVs) (Jacob 1998).

The drag on bird airfoils is almost constant over a range of lift coefficients, as found by Carruthers *et al.* (2010), where the aerodynamic performance of reshaped 2-D airfoil of Eagle wing was analysed at Reynolds number of $1 \times 10^5 < Re < 2 \times 10^5$. However, Withers (1981) found that bird wings have high drag coefficient (0.03 – 0.13), which results in low minimum lift-to-drag (L/D) ratio as experimented on a dried bird wing at $Re = 1 \times 10^5 – 5 \times 10^5$. Bird wings do not perform as good as conventional airfoils and have low efficiency (Carruthers *et al.* 2010; Withers 1981). However, this comparison has been made between high Reynolds number airfoils and low Reynolds number bird wing airfoils, which makes this comparison questionable. On the other hand, bird wings have the advantage of performing at a wide range of angles of attack. (Carruthers *et al.* 2010) used a 2-D airfoil reconstructed from a 3-D scanned wing of a free flying Eagle. However, the 3-D scanning was performed at a single instant of pitching manoeuvre and it represents a single flight phase of the bird. Birds have high lift devices that increase the lift at a high angle of attack (Usherwood 2009), and bird wings with low lift coefficients have low drag coefficient and vice versa (Withers 1981).

Barn Owls and Pigeon wings were experimentally studied by Bachmann (2010) who found that Owls have thicker airfoils than Pigeons, which allows Owls to fly at low speed. On the other hand, Pigeons need to beat their wings faster, which leads to a higher speed, but they are noisier compared to Owls (Bachmann 2010). Owl's feathers absorb the sound that makes them less noisy compared to other birds and they fly almost silently (Chen *et al.* 2012; Geyer *et al.* 2014). Pressure distribution on bird's wing shows that they can be treated using conventional airfoil theory at low Reynolds number as determined by Withers (1981). Thin airfoils with Gottingen-like wing camber are more suitable for MAVs compared to dragon fly wing camber as they produce high L/D ratio, and swept-back leading edge wing increases the performance of MAVs (Lin *et al.* 2007).

Usherwood (2009) estimated lift coefficients of dried and replica Pigeon wing using direct measurement of forces and mapped forces of pressure distribution. The lift coefficient was found to be 1.64 and 1.44 for dried and replica surfaces, respectively (these values do not represent the actual live bird's wing as its shape changes based on aerodynamic forces).

Bechert *et al.* (2000) described techniques of reducing wall shear stress to control boundary layer separation using different surface riblets consisting of biological surfaces such as shark skin replica, plastic model scales, hairy surfaces and surfaces where no-slip condition can be controlled.

Chen *et al.* (2013, 2014) studied the effect of bird wing herringbone riblets on drag and compared them to conventional micro-grooves (riblets). The result shows a drag reduction 16 – 20% higher than in the traditional riblets; moreover, optimal angle between herringbone riblets is about 60°.

The drag on a bird's body is proportional to its mass; as the mass increases, the drag increases as studied by Pennycuick *et al.* (1988) on frozen waterfowl bird. The body drag coefficients were estimated to be 0.25 to 0.39 at Re = 145,000 – 462,000. Lift and drag coefficients decrease with increase in flight velocity in bound flight as experimented by Tobalske *et al.* (2009) on Zebra Finch. The lift and drag coefficients decrease from 1.19 and 0.95 to 0.7 and 0.54 as the velocity increases from 6 to 10 m/s. The lift coefficient decreases significantly as the dihedral angle increases, drag and side forces change significantly by the large dihedral angle that leads to change in the rolling and yawing moments and results in unstable changes of aerodynamics parameters as studied by Sachs and Moelyadi (2010).

POROUS WINGS

Porosity is present in bird wings where the flow can penetrate between/through feathers. Air transmissivity of feathers was studied by Muller and Patone (1998) from the ventral to dorsal direction and vice versa. It was found that both directions have a small difference in air transmissivity that is about 10%. However, significant difference occurs in air transmissivity between inner and outer feather vanes.

Mazellier *et al.* (2012) experimented free-motion flexible-porous flaps mounted on a bluff body and found a reduction in drag by 22%. These flexible flaps move and vibrate through the aerodynamic forces. The displacement and vibration frequency

of the flaps is a function of Reynolds number. However, the properties of flexibility and porosity was not specified, and the study aimed to analyse drag reduction based on changing Reynolds number and the frequency produced by the flap flexibility regardless of its elasticity value. Yang and Spedding (2013) made 180 small cavities using holes of 0.5 mm diameter on the upper surface of an Eppler 387 wing to use acoustic resonance which changed the aerodynamic performance; the lift coefficients increased from 0.7 to 1, and the drag reduced by 10% at Re = 60,000. At a transitional phase, where Re = 40,000 and the angle of attack ranged from 0 to 9, the L/D ratio was higher compared to the same wing without holes. The improvement in lift coefficient occurs due to the flow turbulence inside the hole cavities. However, the study was concerned about resonance effect and not the effect of porosity.

Iosilevskii (2011) analytically studied thin wing membranes segmented into forward solid and aft porous parts. The aerodynamic centre moves non-uniformly to the quarter chord position of the forward section with increase in permeability and leads to a decrease in lift slope. The permeability depends on wing construction and on the flight conditions (it increases with velocity). This analytical model needs to be experimentally verified: an experiment with different permeability values, from low to high, and also at different Reynolds numbers, would prove this analytical model. The seepage flow through the wing reduces the lift slope and creates drag, which can be limited if the aft part width is less than the chord length (Iosilevskii 2013).

Bae *et al.* (2012) used CFD to study the effect of porosity on a trailing edge of a 2-D flat plate at Re = 1,000. They applied numerical penalization method with different porosities and predicted the relationship between pressure drop and flow velocity compared to numerical flow simulation of a non-porous 2-D flat plate. The results showed a reduction in drag and lift due to passive flow suction and blowing on the surface. Porosity has a significant impact on aerodynamic performance if the proper value of permeability is selected. Study on a 3-D model is yet to be performed, and the criteria for the correct selection of surface porosity are unknown.

FLUID-STRUCTURE INTERACTION

Any change in the structure, such as vibration, deformation or movement due to aerodynamic forces, falls under fluid-structure interaction (FSI) analysis. There are two types of FSI: one-way FSI and two-way FSI. One-way FSI changes the fluid's behaviour due to change in structure by controlled deformation, displacement or vibration. Two-way FSI is defined as changes in the structure because of aerodynamic forces and, then, a change in the aerodynamic behaviour due to the changes in the surface structure caused by the flow itself.

Bird wings are flexible, and the airfoil profile changes with aerodynamic forces and flight conditions. Therefore, the study of FSI is significant to understand its impact on flight performance (Gursul *et al.* 2014; Klän *et al.* 2009; Rojratsirikul *et al.* 2009).

PASSIVE CONTROL OF FLOW

Elasticity of feathers, wing coverts, surface velvets and feather mechanoreceptors are passive devices for flow control and aerodynamic force adjustment to the flight conditions as discussed by Brücker and Weidner (2014). The elasticity of the feather shaft helps the flow to stabilize and allows the bird to control the flow during different phases of flight (Bostandzhiyan *et al.* 2008).

Velvet-like surfaces on bird wing force the flow to reattach and delay the stall for a longer period at high angle of attack (Brücker and Weidner 2014; Klän *et al.* 2009; Winzen *et al.* 2013). A significant difference is present in the shear-layer roll up process, where it remains almost normal and locked for a longer period in the case of airfoils with adaptive hairy flaps while there is a rapid increase in the separation region in clean airfoil (Brücker and Weidner 2014).

Flaps and slats of airfoils are other devices used to improve the aerodynamic performance. There are two types of flaps: controlled flaps, used in aircraft, and passive flaps, as in bird wings. Flaps improve the aerodynamic performance and delay the stall at high angle of attack (Schatz *et al.* 2001; Schluter 2010). Numerical study on moveable flaps to control the flow separation shows a reduction in drag by 10% and an increase in lift by 10% at high angle of attack (Schatz *et al.* 2001). However, Schluter (2010) used a water tunnel at Re = 300,000 – 40,000 to analyze the effect of self-activated movable flaps of a 2-D wing mounted on the top surface near the trailing edge. When the flap is of 0.2c length at x/c = 0.6, the lift increased by 50%. When another flap is added at x/c = 0.8c, with length of 0.2c, there is no improvement in the lift. On the other hand, when the flap size length increased to 0.4c at the same location, the lift increased by 15% only. However, number of flaps, size and location still need to be analysed comprehensively in a wide range to arrive carefully at an optimum solution. Wang and Schlüter (2012) performed experiments on a 3-D wing with self-activated flaps using wind tunnel at Re = 4×10^4. The study compared a set of flaps (1 to 4), at different positions along the chord and span. Authors claimed that a single flap performs best. Also, downwash force can be reduced by shortening the span of the flap. It was also determined that self-movable flaps perform best when they cover 80% of the wing span with width of 0.3 of chord and are located at 0.7 of chord measured from the leading edge. More studies have to be undertaken to obtain an optimum solution.

Another device in bird wings is the leading edge slat (Alula) which acts as a spoiler; it increases lift and stall angle of attack as simulated by Ge *et al.* (2013) on a 2-D section of a bird wing. However, the leading edge slat in birds (Alula) does not cover all the leading edge but a portion of it. In the mentioned study, natural flaps were replaced by artificial flaps to represent high lift systems, enhancing the maximum lift by 20%.

Unsteady flow structure and oscillating airfoil were simultaneously measured and compared to a fixed airfoil by Gursul *et al.* (2014) and Rojratsirikul *et al.* (2009). The fluctuation of airfoil was investigated as a function of the angle of attack, and it was found that flow generates rolling vortices on the top surface in case of a vibrating structure that delays the stall at a higher angle of attack (Rojratsirikul *et al.* 2009). The lift coefficients for a flexible wing were found to be higher than the coefficients for a rigid wing at sweep angle of 40 – 55°. If the sweep angle is more than 55°, the lift coefficient for a flexible wing becomes less than the coefficient for a rigid wing (Gursul *et al.* 2014).

The influence of aerodynamic forces on the large flexibility of a wing was examined experimentally in a wind tunnel using an elasto-flexible wing of a pre-stressed membrane by Béguin and Breitsamter (2014), who found that the aerodynamic forces deform the wing surface and adjust camber based on the aerodynamic conditions when experimented in a large flexible wing. However, the question that remains unanswered is the modulus of elasticity selection criteria or the range/criteria of the aeroelastic non-dimensional parameter. Numerical simulations on segmented airfoil show an increase in the lift of up to 39% near the stall angle (Hefeng *et al.* 2015). Three-segmented flexible airfoils produce better results than other segmented configurations. However, further studies on segmented airfoils are needed to find out if equal segments on airfoil surface result in optimal performance or not. Furthermore, experimental data could lead to validated simulation results.

The ability of a flow to vibrate flexible membranes was tested by Genç (2013) on 2-D and 3-D low aspect ratio wings; 2-D membrane wings vibrate more than 3-D wings because of the absence of tip vortex in 2-D wings that allows the shear layer to get closer to the surface. The largest deformation of the flexible membrane occurs near the tip due to the tip vortices.

Flexible surfaces perform aerodynamically better than rigid surfaces; they delay the separation at a high angle of attack and can be used as passive control (Du and Sun 2010; Genç 2013; Gursul *et al.* 2014; Hefeng *et al.* 2015; Rojratsirikul *et al.* 2009).

BIRD WING TIP/WINGLET

Winglets are devices to reduce the induced drag, and, in birds, they are flexible. Wing tip feathers of birds are considered to be winglets and they are flexible with spiral multi-feather elements. Bird wings are considered as non-planar, and a basic theory of non-planar systems is given by Cone Jr (1962) to determine the minimum induced drag and lift that can be expressed regarding aspect ratio and vortices distribution. A spiroid winglet was introduced by Guerrero *et al.* (2012) and was found to increase the lift and its slope by 9% .The L/D ratio improved by approximately 7%. However, it increased the parasite drag due to increase in surface area as well as interference drag. On the other hand, the spiroid winglet used by Guerrero *et al.* (2012) does not represent the bird winglet in terms of shape and flexibility.

Eder *et al.* (2015) estimated the induced drag factor of free-flying White Storks by calculating bird speed *versus* wing loading and aspect ratio. The induced drag factor ranges from 0.7 to 0.96 at lift coefficients of 1.2 – 1.6.

Tucker (1993) compared three types of wingtips: feathers of Harris' Hawk, slotted tip made of balsa wood and shaped as Clark Y airfoils and unslotted Clark Y wingtip mounted on a base wing. Feathers on the tip of bird wings reduce the drag ratio by 105% as the angle of attack increases from 4° to 14°. On the other hand, the L/D ratio of slotted balsa wing tips increased by 49% whereas the L/D ratio of unslotted Clark Y increased by 5% only. As the angle of attack increases from 0° to 15°, the drag increased by 25% in unslotted Clark Y and decreased by 6% in wing with feathers tip. The total drag of wing with feathers decreased by 12% compared to other wings. However, the bird feathers are flexible and bend at airspeed — these affect even the shape of the feather. Flexibility and shape of the wing tip feather under aerodynamic forces cause difference in L/D ratio and drag reduction.

Tucker (1995) investigated the effects of Harris' Hawk wing tip feathers (Fig. 5) on induced drag factor and compared

J. Aerosp. Technol. Manag., São José dos Campos, Vol.8, Nº 1, pp.7-17, Jan.-Mar., 2016

them to the same wing tip but with clipping of the feather tip. The tests were performed in a wind tunnel for a free gliding Hawk at speeds from 7.3 to 15 m/s. The induced drag factor of unclipped feathers is about 0.56 and increased to 1.1 in clipped feathers. Thus, it has been verified that bird wing tip feathers cause a reduction in drag.

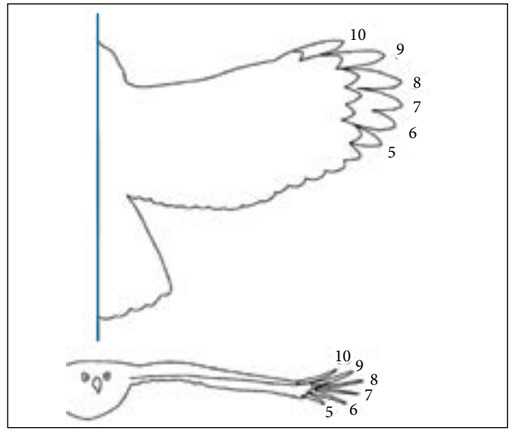

Figure 5. Tip of Harris' Hawk in flight (Tucker 1995).

ACTIVE CONTROL

Changes in wing/airfoil shape affect the flow behaviour. Pinkerton and Moses (1997) evaluated the capabilities of a piezoelectric actuator called THUNDER to vary the upper surface geometry of subscale airfoil, improving the performance. Venkataraman *et al.* (2014) derived a model for a poroelastic actuator on the upper surface to study FSI and its effect on the wake. They confirmed that the flow region behind an airfoil depends on the flexibility characteristics of the upper surface. Bilgen *et al.* (2010) used an actuator of microfiber composite to morph an airfoil (NACA 009 and NACA 0013). The airfoil with a chord of 127 mm was tested in wind tunnel at Re = 127,000, and the voltage ranged from 100 to 1,700 V. The results show an increase in lift by 1.67 with maximum actuation, and a maximum L/D ratio of 26.7 can be achieved. Further analytical studies for variable twist and variable camber using the same airfoil and actuators have been presented by Bilgen *et al.* (2011) to study the response of a morphing structure to achieve optimal lift and L/D ratio. A panel method software XFOIL has been used. The maximum lift achieved is 1.67 at a certain shape, and the maximum L/D ratio obtained was 40.3 at another specific morphed shape. However, even if this study was done using active control, it shows the effect of surface shape on aerodynamic performance, which is similar to the case of birds, since their wing surfaces are flexible and can be morphed to accommodate the varying flight conditions during different flight phases, producing maximum aerodynamic performance.

AERODYNAMICS OF GLIDING FLIGHT

Gliding is flying without flapping the wings, and birds use gliding mode to save energy (Videler and Groenewold 1991). Birds adjust their wing span in gliding to have enough lift and fly at a certain glide angle to keep them aloft (Tucker and Parrott 1970; Zahedi and Khan 2007). Gliding is described as the relationship between bird wing speed and airspeed. There are two types of gliding: static, in which birds depend on the upward wind velocity, and dynamic, where the birds use the changing axial airspeed to stay aloft (Tucker and Parrott 1970). Zahedi and Khan (2007) studied theoretically the wing taper factors for birds. The model was developed from three birds (Jackdaw, Harris' Hawk and Laggar Falcon) to estimate the taper factor of their wings which are 1.8, 1.5 and 1.8, respectively. Also, an equation was derived to estimate the minimum wing span ratio during glide flight. Tucker (1987) analytically studied the effect of variable wing span on gliding and defined the gliding maximum performance curve as the minimum sinking speed at each air speed.

Experiments on bird glide show that L/D ratio of Pigeon in gliding is 10, and the maximum vertical diving speed of Laggar Falcon is 100 m/s. Tucker and Parrott (1970) used a trained Pigeon in a wind tunnel to glide at different speeds, investigating the gliding performance in a more accurate sense. However, the L/D ratio of Kestrel gliding is 10.9 at a speed of 14.9 m/s, and the angle of attack is 5.5° (Videler and Groenewold 1991). Extended wings are great for both gliding and turning. Swept wings are better for fast glide but less active in generating lift while turning at high speeds, sink speed and turning rate are hugely affected by selecting the right sweep (Lentink *et al.* 2007).

Field experiments by Videler and Groenewold (1991) suggest that birds use three methods to adjust lift and drag in gliding: wing span variation, pitching angle of bird's longitudinal axis (which is independent from wind speed) and spreading the tail to adjust the lift and drag. Bird tail has effect on L/D ratio; if the tail is trimmed, it reduces the L/D ratio and, if extended, it increases the L/D ratio (Tobalske *et al.* 2009). However, in wind tunnel, the birds only use wing span to control lift and drag (Tucker 1987). Glide angle increases with the increase in dihedral angle of bird wing (Sachs and Moelyadi 2010).

STRUCTURE

An understanding of the mechanical properties of feathers is essential as they directly affect the aerodynamic properties due to their elasticity. A general review of feather on bird's feather biomechanics and structure was done by Zahedi and Khan (2007). The structure and shape of rachis allow them to withstand high forces and prevent them from cracking. Studies on feather microstructure show that the fiber matrix of keratin is arranged in such a way that it provides stiffness and strength; at the same time, it is flexible and elastic.

Bonser and Purslow (1995) examined the properties of feather keratin to find the Young's modulus (E) through tensile tests for eight different bird feathers. Modulus of elasticity for feathers was E = 2.5 GPa for all birds except for Grey Heron — E = 1.78 GPa. However, Purslow and Vincent (1978) found an E for the feather shaft of Pigeon equal to 7.8 ± 2% GPa. Bachmann *et al.* (2012) found the Young's modulus values of Pigeon and Barn Owl feathers between 4.14 and 6.93 GPa. On the other hand, Macleod (1980) examined the Young's modulus of contour feather for Brown Chicken, Turkey, Pheasant and Herring Gull in tension and bending tests and for distal and proximal regions. The results from the tension tests show that E ranges from 0.045 to 0.181 GPa and from 0.21 to 0.682 GPa for proximal and distal regions, respectively. In bending tests, E ranges from 0.005 to 0.024 GPa and from 0.457 to 1.85 GPa for proximal and distal regions, respectively. There is a difference in range of magnitude for the stiffness values due to different methods or tests used (Bonser and Purslow 1995). Rachis cross-section geometry controls the flexural stiffness rather than keratin material properties according to Bachmann *et al.* (2012), Bonser and Purslow (1995) as well as Purslow and Vincent (1978). The geometry and the second moment of area of the feather shaft increase as the body weight increases and vice versa. Second moment of area gradually decreases along the shaft from feather base to its tip, which results in higher rigidity in feather shaft at its root and greater elasticity at the tip (Bostandzhiyan *et al.* 2008; Macleod 1980; Purslow and Vincent 1978).

Bird wings can withstand higher forces than the forces they are normally exposed to. Normal stress applied on birds feather is 8.3 up to 15.7 MPa while the ultimate stress point at the bending is 137 MPa, which gives a safety factor between 6 and 12 (Corning and Biewener 1998). This feature of safety allows them to fly under extreme conditions. Flexural stiffness is more critical than strength in feather shaft.

However, all the studies mentioned above focused on the feather structure properties, especially feather shaft properties, which gives strength for the bird wing to withstand the forces. Investigation of the elasticity modulus of the coverts (hairs) is still required. The coverts pop-up when birds fly at a high angle of attack. To make a flexible surface similar to a bird's surface or to study the effect of coverts on aerodynamic performance, the properties of the coverts need to be known.

EXPERIMENTS/SIMULATION METHODS

In Aerodynamics, there are three ways of predicting or calculating the aerodynamic performance of wings/airfoil, which are: analytical/mathematical model, numerical simulation and experimental test. Analytical/mathematical model is used to represent a specific problem, but in general it is derived for simple geometries/airfoils. Numerical simulation is widely used to solve complicated problems as it reduces the cost of experiments, although it is costly in terms of time. Experimental test is considered the most robust method if done correctly, because it gives more realistic results. It is also used to verify the results of simulations.

One of the experimental methods is the particle image velocimetry (PIV), which has been used to measure the influence of hairy surfaces on aerodynamic performance and separation control by Brücker and Weidner (2014), Klän *et al.* (2009) and Winzen *et al.* (2013). Pressure distribution measurements and oil pattern method were used by Klän *et al.* (2009) to verify the results obtained from PIV, and the results show agreement among the three methods. In their experiments, the airfoil profile used was obtained form an average reconstructed artificial wing obtained by scanning an Owl's wing. Rojratsirikul *et al.* (2009) used high speed PIV to study the fluid structure interaction of a 2-D airfoil at a Reynolds number range of 53,100 – 106,000. The measurements were taken for the unsteady flow and structural changes simultaneously, and the oscillation in structure behaviour was investigated as a function of angle of attack and velocity.

Tobalske *et al.* (2009) studied Zebra finch wing aerodynamics in intermittent bound phases using PIV and force transducer.

The measurements were performed at different speeds from 2 to 12 m/s and different angles of attack ranging from –5° to 50°. A uniform structure of the wake was observed, and the forces derived from both measurements of PIV and force transducer have a close agreement.

The dual-plane PIV has been used by Waldman and Breuer (2012) to increase the dynamic range of PIV measurements on a fixed wing and has been compared to PIV. Both measurements indicate the same position of vortex downstream but dual-plane PIV covers a more dynamic range by an order of magnitude. Dual-plane PIV captures the velocity of outer flow more accurately, which leads to more accurate results. It is also able to capture the strength of the wake downstream qualitatively and quantitatively.

Another development of PIV, called digital PIV (DPIV), has been used by Spedding *et al.* (2003) in low-turbulence wind tunnel to study the free-flying bird wake. DPIV measurement uses two cameras and allows a moving object to wake so that it can be measured more accurately and with more reliability. The shortcoming of the method is the difficulty in matching the optical axis of the two cameras. However, mismatches can be removed to quite high accuracy, by careful mapping of the apparent displacements of stationary control objects imaged by both cameras. It removes the disturbances of lens/camera and examines only the effect of moving object disturbances. Spedding *et al.* (2009) confirmed the ability of DPIV to measure the background structure of small turbulences in a low turbulence wind tunnel, which can be used to measure the aerodynamics of small flyers. Genç (2013) also used DPIV in a closed loop open-jet wind tunnel to calculate the average and instantaneous velocity field on a membrane wing at Re = 48,700. They also used digital image correlation system to measure membrane deformation and load cell, calculating forces on the wing. Waldman and Breuer (2012) used a fixed model with load cell direct measurement of aerodynamic forces to explore the challenges of selecting appropriate experimental parameters to have more accurate dynamic measurements. Isaac *et al.* (2006) used hydrogen bubbles and dyes as traces to visualize the flow over a moving and pitching flat blade.

Visualization of flow on flying birds is another method for examining the flight mechanism or flow separations. Carruthers *et al.* (2007) used a high-speed camera carried by an Eagle to examine the function of coverts in perching modes. Eder *et al.* (2015) performed field measurements using infrared laser tracking to estimate the induced drag of souring and gliding flight of White Storks. The test was carried for 100 adult White Storks and it was found that the speed ranges of these birds at soaring, gliding and fast speed are 7.5 – 10, 10 – 14 and 14 – 19 m/s, respectively. The wrist angle (angle between the frontal edge of the cascade and the propatagium sinew — see Fig. 6) ranges of soaring, gliding and fast flight are 15° – 19°, 20° – 24° and 25° – 50°, respectively.

Chen *et al.* (2013, 2014) used SEM and CFD to investigate the effects of herringbone-type riblets on drag reduction using a microstructure of secondary feathers of Pigeon and then used a 3-D plane with herringbone riblets to compare them to traditional riblets.

Sachs and Moelyadi (2010) used CFD to study the effect of large dihedral angle of Pigeon-like wings on aerodynamic performance. A CAD model for Pigeon wing at different dihedral angles was used. The airfoil section is the same for all dihedral angles. However, the shape of airfoil in real birds changes during each flight phase; thus, this simulation is simplified to a minimum complexity of bird wing geometry.

On the other hand, analytical aerodynamic analysis of flexible and bird-like wing/airfoils was attempted by Iosilevskii (2013), who derived a closed-form mathematical model for the lift and pitching-moment coefficients of a thin wing membrane by sectioning the surface into two parts: a solid forward part that is impermeable and the aft part, which is porous. Another closed-form solution is obtained to study the seepage drag for the same model using Darcy's law. Venkataraman *et al.* (2014) developed a linear mathematical model by combining vortex-shedding minimal-order model with oscillator mode to study FSI and its effects on the flow region. Both minimal model proelastic coating and FSI coupling are assumed to be linear.

Biomimetics of a bird wing is defined as the replication and development of a wing/airfoil similar to those of the birds regarding

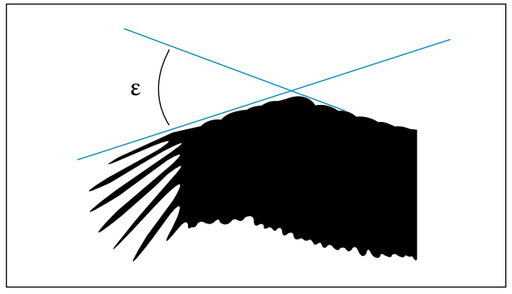

Figure 6. The wrist angle (ε) between the frontal edge of the cascade and the propatagium sinew (Eder *et al.* 2015).

shape and properties in mathematical, simulation or experimental form. Mazellier *et al.* (2012) implemented a biomimetic approach and used a squared cylinder geometry with free-rotating elastic self-deformable (made of a rigid material coated with plastic skeleton) porous (fabric) flaps to replicate the feather vane to study its effects on aerodynamic performance. Lin *et al.* (2007) developed aluminum plates with Gottingen wing — a wing span of 15 cm, thickness to chord ratio of 1.3 and camber of 6% — and compared their aerodynamic performance to other airfoils that have a half-forward part similar to a dragonfly wing. Corning and Biewener (1998) used a metal foil strain gauge to evaluate the safety factor in feather shaft of a free-flying Pigeon. Strain was recorded at both compression (down stroke) and tension (up stroke). Photogrammetric reconstruction technique was used by Carruthers *et al.* (2010) to reconstruct the wing section of a free-flying Eagle. A mathematical model was used to reshape 2-D airfoil, analyzing the aerodynamic performance. Klän *et al.* (2009) also used Owl airfoil extracted from a 3-D scanned wing and experimented it in a wind tunnel at Re = 2,000 – 4,000 with and without velvet to study the effect of velvet on delaying stall angle. However, the 3-D shape was smoothed and the twist was removed. The effect of smoothing Owl wing and removing the twist might have significant impact on aerodynamic performances.

The aerodynamic performance of real birds was studied by Pennycuick *et al.* (1988), who used a frozen waterfowl in a wind tunnel to estimate the drag coefficient at Reynolds number of 145,000 - 462,000, and Usherwood (2009), who used a dried Pigeon wing and a replica flat plate to measure and compare aerodynamic forces on both revolving surfaces at a Reynolds number of 108,000 using a propeller rig. The direct measurement of forces was taken, and the mapped forces of pressure distribution were calculated. Withers (1981) also used dried wings of different types of birds and experimented them at Re = $1 - 5 \times 10^5$. Dried wings, however, differ from live bird wings, which might affect the aerodynamic performance.

MAVs, wind turbines, tidal wave turbines and other devices perform at low Reynolds numbers similar to birds. Thus, lessons learnt from aerodynamics of bird wings in steady flight could be implemented in such applications to enhance their performance.

CONCLUSION

This paper focuses on the past research carried out on fixed bird wings (non-flapping wing), in terms of analysis, simulation and experiments which have been performed by researches for a wide range of bird wing aerodynamics. However, some areas in bird aerodynamics can be studied more thoroughly as the bird wings consist of highly complex representation of flexible (not flapping) and porous surfaces. Many of these problems are mentioned throughout this article.

REFERENCES

Bachmann T (2010) Anatomical, morphometrical and biomechanical studies of barn owls' and pigeons' wings (Master's thesis). Aachen: RWTH Aachen University.

Bachmann T, Emmerlich J, Baumgartner W, Schneider JM, Wagner H (2012) Flexural stiffness of feather shafts: geometry rules over material properties. J Exp Biol 215(Pt 3):405-415. doi: 10.1242/jeb.059451

Bae Y, Jeong YE, Moon YJ (2012) Computation of flow past a flat plate with porous trailing edge using a penalization method. Comput Fluid 66:39-51. doi: 10.1016/j.compfluid.2012.06.002

Bechert D, Bruse M, Hage W, Meyer R (2000) Fluid mechanics of biological surfaces and their technological application. Naturwissenschaften 87(4):157-171.

Béguin B, Breitsamter C (2014) Effects of membrane pre-stress on the aerodynamic characteristics of an elasto-flexible morphing wing. Aero Sci Tech 37:138-150. doi: 10.1016/j.ast.2014.05.005

Bilgen O, Friswell MI, Kochersberger KB, Inman DJ (2011) Surface actuated variable-camber and variable-twist morphing wings using piezocomposites. Proceedings of the 52nd AIAA/ASME/ASCE/AHS/ASC Structures, Structural Dynamics, and Materials 4(7):2011-2072. doi: 10.2514/6.2011-2072

Bilgen O, Kochersberger KB, Inman DJ, Ohanian OJ (2010) Novel, bidirectional, variable-camber airfoil via macro-fiber composite actuators. J Aircraft 47(1):303-314.

Bonser R, Purslow P (1995) The Young's modulus of feather keratin. J Exp Biol 198(4):1029-1033.

Bostandzhiyan S, Bokov A, Shteinberg A (2008) Flexural characteristics and aerodynamic aspects of the design of the bird feather shaft. Doklady Physics 53(9):476-479. doi: 10.1134/S1028335808090036

Brown RE, Fedde MR (1993) Airflow sensors in the avian wing. J Exp Biol 179(1):13-30.

Brücker C, Weidner C (2014) Influence of self-adaptive hairy flaps on the stall delay of an airfoil in ramp-up motion. J Fluid Struct 47:31-40. doi: 10.1016/j.jfluidstructs.2014.02.014

Carruthers A, Thomas AL, Taylor GK (2007) Automatic aeroelastic devices in the wings of a steppe Eagle Aquila nipalensis. J Exp Biol 210(Pt 23):4136-4149.

Carruthers A, Walker S, Thomas A, Taylor G (2010) Aerodynamics of aerofoil sections measured on a free-flying bird. Proc IME G J Aero Eng 224(8):855-864. doi: 10.1243/09544100JAERO737

Chen H, Rao F, Shang X, Zhang D, Hagiwara I (2013) Biomimetic drag reduction study on herringbone riblets of bird feather. J Bionic Eng 10(3):341-349. doi: 10.1016/S1672-6529(13)60229-2

Chen H, Rao F, Shang X, Zhang D, Hagiwara I (2014) Flow over bio-inspired 3D herringbone wall riblets. Exp Fluids 55:1698. doi: 10.1007/s00348-014-1698-4

Chen K, Liu Q, Liao G, Yang Y, Ren L, Yang H, Chen X (2012) The sound suppression characteristics of wing feather of owl (*Bubo bubo*). J Bionic Eng 9(2):192-199. doi: 10.1016/S1672-6529(11)60109-1

Cone Jr CD (1962) The theory of induced lift and minimum induced drag of nonplanar lifting systems. NASA TR R-139.

Corning WR, Biewener AA (1998) *In vivo* strains in Pigeon flight feather shafts: implications for structural design. J Exp Biol 201(Pt 22):3057-3065.

Crandell KE, Tobalske BW (2011) Aerodynamics of tip-reversal upstroke in a revolving Pigeon wing. J Exp Biol 214(11):1867-1873. doi: 10.1242/jeb.051342

Du G, Sun M (2010) Effects of wing deformation on aerodynamic forces in hovering hoverflies. J Exp Biol 213(Pt 13):2273-2283. doi: 10.1242/jeb.040295

Eder H, Fiedler W, Neuhäuser M (2015) Evaluation of aerodynamic parameters from infrared laser tracking of free-gliding white storks. Journal of Ornithology 156(3):1-11. doi: 10.1007/s10336-015-1176-7

Ennos A, Hickson J, Roberts A (1995) Functional morphology of the vanes of the flight feathers of the Pigeon Columba livia. J Exp Biol 198(5):1219-1228.

Ge C, Ren L, Liang P, Zhang C, Zhang Z (2013) High-lift effect of bionic slat based on owl wing. J Bionic Eng 10(4):456-463. doi: 10.1016/S1672-6529(13)60243-7

Genç MS (2013) Unsteady aerodynamics and flow-induced vibrations of a low aspect ratio rectangular membrane wing with excess length. Exp Therm Fluid Sci 44:749-759. doi: 10.1016/j.expthermflusci.2012.09.018

Geyer T, Sarradj E, Fritzsche C (2014) Measuring owl flight noise. Proceedings of the Inter-Noise Congress and Conference; Melbourne, Australia.

Guerrero JE, Maestro D, Bottaro A (2012) Biomimetic spiroid winglets for lift and drag control. C R Mec 340(1-2):67-80. doi: 10.1016/j.crme.2011.11.007

Gursul I, Cleaver D, Wang Z (2014) Control of low Reynolds number flows by means of fluid-structure interactions. Progr Aero Sci 64:17-55. doi: 10.1016/j.paerosci.2013.07.004

Hefeng D, Chenxi W, Shaobin L, Zhen SX (2015) Numerical research on segmented flexible airfoils considering fluid-structure interaction. Procedia Eng 99:57-66. doi: 10.1016/j.proeng.2014.12.508

Iosilevskii G (2011) Aerodynamics of permeable membrane wings. Eur J Mech B Fluids 30(5):534-542. doi: 10.1016/j.euromechflu.2011.05.003

Iosilevskii G (2013) Aerodynamics of permeable membrane wings. Part 2: Seepage drag. Eur J Mech B Fluids 39:32-41. doi: 10.1016/j.euromechflu.2012.11.004

Isaac KM, Rolwes J, Colozza A (2006) Unsteady flow features of a flapping and pitching wing at low Reynolds number. AIAA Paper3145.

Jacob J (1998) On the fluid dynamics of adaptive airfoils. American Society of Mechanical Engineers, Aerospace Division 57:167-176.

Klän S, Bachmann T, Klaas M, Wagner H, Schröder W (2009) Experimental analysis of the flow field over a novel owl based airfoil. Exp Fluids 46(5):975-989. doi: 10.1007/s00348-008-0600-7

Lentink D, Müller U, Stamhuis E, De Kat R, Van Gestel W, Veldhuis L, Henningsson P, Hedenström A, Videler JJ, Van Leeuwen JL (2007) How swifts control their glide performance with morphing wings. Nature 446(7139):1082-1085. doi: 10.1038/nature05733

Lin J, Wei C, Lin C (2007) Aerodynamic performance of thin wings at low Reynolds numbers. Aircr Eng Aerosp Tech 79(3):245-253. doi: 10.1108/00022660710743840

Macleod GD (1980) Mechanical properties of contour feathers. J Exp Biol 87(1):65-71.

Mazellier N, Feuvrier A, Kourta A (2012) Biomimetic bluff body drag reduction by self-adaptive porous flaps. C R Mec 340(1-2):81-94. doi: 10.1016/j.crme.2011.11.006

Muller W, Patone G (1998) Air transmissivity of feathers. J Exp Biol 201(Pt 18):2591-2599.

Pennycuick C, Obrecht HH, Fuller MR (1988) Empirical estimates of body drag of large waterfowl and raptors. J Exp Biol 135(1):253-264.

Pinkerton JL, Moses RW (1997) A feasibility study to control airfoil shape using THUNDER. NASA technical memorandum; 4767. Washington: National Aeronautics and Space Administration.

Purslow P, Vincent J (1978) Mechanical properties of primary feathers from the Pigeon. J Exp Biol 72(1):251-260.

Rojratsirikul P, Wang Z, Gursul I (2009) Unsteady fluid-structure interactions of membrane airfoils at low Reynolds numbers. Exp Fluids 46:859. doi: 10.1007/s00348-009-0623-8

Sachs G, Moelyadi MA (2010) CFD based determination of aerodynamic effects on birds with extremely large dihedral. J Bionic Eng 7(1):95-101. doi: 10.1016/S1672-6529(09)60191-8

Schatz M, Bunge U, Lübcke H, Thiele F (2001) Numerical study of separation control by movable flaps. In: Thiede P, editor. Aerodynamic Drag Reduction Technologies. Berlin: Springer. p. 385-390.

Schluter JU (2010) Lift enhancement at low Reynolds numbers using self-activated movable flaps. J Aircraft 47(1):348-351. doi: 10.2514/1.46425

Shyy W, Lian Y, Tang J, Liu H, Trizila P, Stanford B, Bernal L, Cesnik C, Friedmann P, Ifju P (2008) Computational aerodynamics of low Reynolds number plunging, pitching and flexible wings for MAV applications. Acta Mechanica Sinica 24(4):351-373. doi: 10.1007/s10409-008-0164-z

Spedding G, Hedenström A, Johansson L (2009) A note on wind-tunnel turbulence measurements with DPIV. Exp Fluids 46(3):527-537. doi: 10.1007/s00348-008-0578-1

Spedding G, Hedenström A, Rosén M (2003) Quantitative studies of the wakes of freely flying birds in a low-turbulence wind tunnel. Exp Fluids 34(2):291-303. doi: 10.1007/s00348-002-0559-8

Tobalske BW, Hearn JWD, Warrick DR (2009) Aerodynamics of intermittent bounds in flying birds. Exp Fluids 46(5):963-973. doi: 10.1007/s00348-009-0614-9

Tucker VA (1987) Gliding birds: the effect of variable wing span. J Exp Biol 133(1):33-58.

Tucker VA (1993) Gliding birds: reduction of induced drag by wing tip slots between the primary feathers. J Exp Biol 180(1):285-310.

Tucker VA (1995) Drag reduction by wing tip slots in a gliding Harris' Hawk, Parabuteo unicinctus. J Exp Biol 198(Pt 3):775-781.

Tucker VA, Parrott GC (1970) Aerodynamics of gliding flight in a Falcon and other birds.J Exp Biol 52(2):345-367.

Usherwood JR (2009) The aerodynamic forces and pressure distribution of a revolving Pigeon wing. Exp Fluids 46(5):991-1003. doi: 10.1007/s00348-008-0596-z

Venkataraman D, Bottaro A, Govindarajan R (2014) A minimal model for flow control on an aerofoil using a poro-elastic coating. J Fluid Struct 47:150-164. doi: 10.1016/j.jfluidstructs.2014.02.012

Videler J, Groenewold A (1991) Field measurements of hanging flight aerodynamics in the kestrel Falco tinnunculus. J Exp Biol 155(1):519-530.

Waldman RM, Breuer KS (2012) Accurate measurement of streamwise vortices using dual-plane PIV. Exp Fluids 53(5):1487-1500. doi: 10.1007/s00348-012-1368-3

Wang CJ, Schlüter J (2012) Stall control with feathers: Self-activated flaps on finite wings at low Reynolds numbers. C R Mec 340(1-2):57-66. doi: 10.1016/j.crme.2011.11.001

Winzen A, Klaas M, Schröder W (2013) High-speed PIV measurements of the near-wall flow field over hairy surfaces. Exp Fluids 54:1472. doi: 10.1007/s00348-013-1472-z

Withers PC (1981) An aerodynamic analysis of bird wings as fixed aerofoils. J Exp Biol 90(1):143-162.

Yang S, Spedding G (2013) Passive separation control by acoustic resonance. Exp Fluids 54:1603. doi: 10.1007/s00348-013-1603-6

Zahedi MS, Khan MYA (2007) A mechanical model of wing and theoretical estimate of taper factor for three gliding birds. J Biosci 32(2):351-361. doi: 10.1007/s12038-007-0034-z

doi: 10.5028/jatm.v8i1.576

Methodologies for Characterization of Aerospace Polymers/Energetic Materials – a Short Review

Shirley Motta Pedreira[1], Juliano Ribeiro Aguiar Pinto[1,2], Eunice Aparecida Campos[1,2], Elizabeth da Costa Mattos[1,2], Mauro Santos de Oliveira Junior[3], José Irineu Sampaio de Oliveira[1], Rita de Cássia Lazzarini Dutra[1]

ABSTRACT: Fourier transform infrared spectroscopy techniques, associated or not to others, are a well-studied subject used for characterizing polymers/energetic materials that have been employed mainly in aerospace industries. However, the infrared analyses are usually qualitative and performed using the mid-infrared. This paper discusses the Fourier transform infrared spectroscopy qualitative and quantitative methodologies, coupled or not with thin layer chromatography and thermogravimetric analysis, for characterization of aerospace polymer systems, in some cases, using mid-infrared, near-infrared and far-infrared regions, by traditional accessories and the latest generation spectra mode, universal attenuated total reflection. This short review was made based on methodologies developed during the last two decades and published by many scientific and industrial research groups, emphasizing studies usually carried out in the last five years. A critical assessment and future trends were included.

KEYWORDS: Aerospace polymer, Energetic material, FT-IR, Methodologies.

INTRODUCTION

STUDIES ABOUT BINDERS OF PROPELLANTS

As well-known, hydroxyl-terminated polybutadiene (HTPB) reacts with isocyanate (curing agent) to obtain polyurethane (PU) formation and it is the usual binder used in solid propellant grain of the rocket motors. Thus, the determination of its hydroxyl (-OH) and isocyanate (-NCO) groups by instrumental techniques is an important parameter for predicting properties of these composites.

Hydroxyl and isocyanate numbers could be faster determined by Fourier transform infrared spectroscopy (FT-IR) methodologies than wet chemical method, and the functionality distribution of HTPB binder, by specific methodology, is a good example and we can include these determinations among the several studies, developed in our laboratories (Takahashi *et al.* 1996; Lourenço *et al.* 2006).

Takahashi *et al.* (1996) applied FT-IR analysis for determining contents of hydroxyl groups (IOH) in HTPB resins and free NCO groups in diisocyanates and NCO-terminated prepolymers. FT-IR methodology provided accurate results equivalent (IOH) or higher (% NCO) than classic wet methods and within the FT-IR instrument accuracy limit, ≤ 2%. The FT-IR methodology has the additional advantages of being fast, inexpensive and requiring small amount of sample and solvent, e.g. CS_2 (IOH) and CCl_4 (% NCO). These methods have some advantages that may be useful in industries and research centers, especially to those who work with polyurethanes, for characterization of

1.Departamento de Ciência e Tecnologia Aeroespacial – Instituto Tecnológico de Aeronáutica – Divisão de Ciências Fundamentais – São José dos Campos/SP – Brazil. **2.**Departamento de Ciência e Tecnologia Aeroespacial – Instituto de Aeronáutica e Espaço – Divisão de Química – São José dos Campos/SP – Brazil. **3.**Universidade Federal de São Paulo – Instituto de Ciência e Tecnologia – São José dos Campos/SP – Brazil.

Author for correspondence: Rita de Cássia Lazzarini Dutra | Departamento de Ciência e Tecnologia Aeroespacial – Instituto Tecnológico de Aeronáutica – Divisão de Ciências Fundamentais | Praça Mal. Eduardo Gomes, 50 – Vila das Acácias | CEP: 12.228-901 – São José dos Campos/SP – Brazil | Email: ritacld@ita.br

Received: 11/23/2015 | **Accepted:** 12/18/2015

raw materials (resins and isocyanates) and product control (NCO-terminated prepolymers).

This methodology for determining hydroxyl groups is important, but it is necessary to know how these groups were distributed in the molecular chain. Lourenço *et al.* (2006) developed a size exclusion chromatography (SEC) methodology, with double detection, to determine the functionality distribution of HTPB polymer. This method showed to be sensitive to small differences in the functionality distribution of the HTPB, affecting the tensile tests performed with HTPB polyurethane.

Recent study about HTPB was developed by Clemente *et al.* (2014). Polyurethane polymer matrix was synthesized using polyols as a raw material to obtain a binder such as (HTPB) prepolymer in energetic material formulation. They concluded that the soybean-based polyol was the best starting raw material for producing binder. Characterization of the binder was carried out by employing FT-IR analysis to the mid-infrared (MIR) region and thermal techniques, such as differential scanning calorimetry (DSC) and thermogravimetric analysis (TG). Glass transition (Tg) (−39 °C) of the polyol derived from soybean oil was determined by employing DSC technique. It was considered a good value because the Tg of the HTPB-based polymer matrix is around −50 °C. By TG, it was possible to evaluate the thermal degradation process of polymer obtained and to determine the activation energy (Ea) (122.4 kJ·mol^{-1}), whose value is very close to the HTPB-based polymer matrix. Thus, the application of synthesized material as solid fuel has shown promising results for tests in rocket engines. They showed good results by using soybean-based polyol as a raw material to obtain a binder, such as HTPB prepolymer in energetic material formulation, but the IR region used for the qualitative characterization was just the usual MIR.

The energetic binders are usually low-molecular-weight hydroxyl-terminated polyethers, with nitro or azido groups, capable of holding together fuel and oxidizer compounds from the propellant. These chemical groups give a significant contribution to the propellant impulse characteristics. The energetic binders can produce propellants systems in which metal fuels, such as aluminum, can be reduced. Glicidyl azide polymer (GAP) (Kawamoto *et al.* 2008; Sciamareli *et al.* 2009a, 2009b), GAP/BAMO (Kawamoto *et al.* 2010), poly[3,3-bis(azidomethyl)oxetane] (poly-BAMO) and 3-azidomethyl-3-methyl oxetane polymer (poly-AMMO) (Oliveira *et al.* 2006, 2007; Kawamoto *et al.* 2009) have been studied by AQI group from Instituto de Aeronáutica e Espaço in the last decade.

In relation to FT-IR characterization methodologies of energetic materials used in propellants, it is possible to include the characterization of poly-AMMO and poly-BAMO and their precursors as energetic binders in the near-infrared (NIR), MIR and far-infrared (FIR) regions by Oliveira *et al* (2006). Their study was focused on the characterization of polymers containing energetic groups that have been synthesized at ICT (Fraunhofer Institute for Chemical Technology) group, an important Germany Research Center of propellants. This characterization identified analytical bands and allowed quantitative and/or kinetic studies of these compounds, using the whole spectral ranges of NIR/MIR/FIR. Basically, it was possible to visualize differences between chemical structures of these compounds and also to identify spectrometric changes (formation or disappearance of functional groups) that can occur during the polymerization process. It is also possible to use the absorptions around 4200, 2100 and 550 cm^{-1} as analytical bands to study these compounds containing azide groups for quantitative determinations. Bands found in the region of 1250 and 660 cm^{-1} can be used in similar studies of Br-substituted binders. Bands near 980 cm^{-1} can be used to study the ring opening polymerization reaction of compounds containing azide and/or bromine.

Oliveira *et al.* (2007) analyzed azide polymers samples by FT-MIR in order to develop a quantitative methodology to determine the C, H and N content in energetic polymers used in propellants. The elemental analysis data were used as reference. The FT-MIR results showed a good agreement with CHN analysis, and a good linear relationship was obtained, suggesting that the developed methodology can be useful for quality control of these energetic polymers.

In another study about energetic material (Ribeiro *et al.* 2012), GAP was synthesized and characterized by FT-IR, ultraviolet spectroscopy (UV), nuclear magnetic resonance spectroscopy (NMR), DSC, elemental analysis (CHN), TG and SEC. Through these conventional techniques, it was possible to identify the material content and some of its properties related to its use as an energy plasticizer in propellants. This new method with dimetylformamide (DMF) solvent was effective in obtaining high molecular weight, high yield and better conversion of azide.

Oliveira *et al.* (2014) evaluated the interaction between two energetic polymer/oxidizer systems, GAP and ADN (ammonium dinitramide, a chlorine-free oxidizer) as well as GAP and AP (ammonium perchlorate) by FT-IR spectroscopy, in the NIR and MIR regions. Major spectrometric changes were observed for the GAP/ADN system, with a broadening of the bands in

the region between 3100 – 3500 cm^{-1}, pointing to interactions between OH groups from GAP and NH_4^+ groups from ADN or AP. A decrease in band intensity was observed for the N_3 group in GAP as well as an increase of nitronium (NO_2^+) of ADN, suggesting interaction between these groups in the GAP/ADN system.

POLYMERS USED IN COATING PROCESS OF ENERGETIC MATERIALS

FT-IR surface techniques have been used for characterization and/or quantification of different polymers applied in coating process of energetic material (Mattos *et al.* 2004a, 2004b, 2008; 2009).

Mattos *et al.* (2008) made a surface characterization of RDX/fluoroelastomer (Viton®) system by FT-IR techniques such as transmission, photoacoustic (PAS) and attenuated total reflectance (ATR). The transmission spectrum of the cast film showed some evidence of the presence of fluoroelastomer, which covers the energetic material. ATR showed excellent results to analyze HMX/Viton® system for characterization of Viton® bands.

Mattos *et al.* (2009) developed a new FT-IR methodology to characterize quantitatively the polymer content in PBX (HMX/Viton®) using the TG as reference technique. ATR was used as surface technique and showed excellent results, being faster than the usual methodologies, as high performance liquid chromatography (HPLC).

According to Tourné (2013), in the field of explosives and other energetic materials, detection and characterization brought new challenges. Detection schemes at the molecular level provide a wide variety of analytical technique, such as Raman, Infrared (IR) and Mass Spectroscopy, among others. However, studies cited in the IR part of her paper are only about the characterization of explosives without reference to polymer/explosive (PBX); probably, the main objective was only to identify some micromolecules. Thus, qualitative characterization and quantification of polymer that can be found on the surface of this system can be contributive for the area of energetic materials.

THERMAL INSULATION STUDIES

RUBBERS

Main methodologies developed by AQI group on rubbers, such as natural rubber (NR), ethylene propylene diene monomer (EPDM) and butadiene and acrylonitrile copolymer (NBR) used in the aerospace industry, are discussed below and related to other publications (Lanxess Rubber 2012; ASTM D3900 – 05a 2010; Chitta 2014). The topics are organized by methodologies, including also the IR or FT-IR techniques couplings with thin layer chromatography (TLC/IR) (Dutra 1996; Damazio 2015; Damazio *et al.* 2014, 2015) and thermogravimetric analysis (TG/FT-IR) (Sanches 2015; Sanches *et al.* 2014, 2015).

TLC and IR Methods for the Characterization of Rubbers and Their Additives

Analysis of vulcanized elastomer composition is often an important quality control requirement and suitable for determining rubber formulation. Dutra (1996) developed a methodology for separating and identifying additives in rubber, by TLC/IR coupling techniques. This study was carried out by two methods: one that uses potassium bromide (KBr) pyramids and another, more simple, without the use of pyramids, to reduce costs.

According to the first method, the material obtained by solvent extraction is applied in an appropriate silica plate, in which it is developed in a closed vessel chromatography, using a mobile phase. The plate is dried and reveals deposits with suitable developer. Deposits are scraped and placed in a tube containing KBr pyramids. Small amount of solvent used in the extraction is added to bring the sample to the top of the pyramid. After solvent evaporation, this top is removed, crushed and compressed in the form of KBr disc for transmission infrared analysis. Basically, in the second method, the deposits are scraped and treated with the solvent used in the extraction, filtered to remove silica, dried, mixed with KBr (200 mg) in order to obtain pellets and analyzed by transmission.

It was concluded that the TLC/IR coupling, for both methods, is particularly useful for polymer research centers to expand knowledge on identification and characterization of the main constituents of rubbers, such as antioxidants and plasticizers in previously known formulations. The choice of a suitable analysis condition allows the evaluation of other components.

The development of quantitative methods which detect low content of components of elastomeric system, especially in compounds, is still a challenge. Damazio *et al.* (2014) developed a methodology by FT-IR (UATR and transmission techniques) for determining the ethylene (ET) and propylene (P) content on rubber samples (neat, raw and vulcanized elastomer) EPDM (ethylene propylene diene monomer), used in aerospace industry. Both techniques showed good accuracy, being

UATR analysis the most appropriate for neat elastomer. Transmission/pyrolysis was suitable for analyzing all types of EPDM (neat, raw and vulcanized elastomer), suggesting to be useful for similar formulations.

Damazio *et al.* (2015) developed a method using FT-IR transmission for determining the content of 5-ethylidene-2-norbornene (ENB) on rubber samples (neat elastomer) burned in controlled pyrolysis and Bunsen burner. The determination was done by observing the variation of relative band and relative concentration, and they were also suitable for estimating ET and P contents of the same rubber.

TLC/IR using UATR accessory was applied for characterization of additives, in order to evaluate the applicability of these techniques together. Two formulations were used in this elastomer – a type of eluent system and the Gibbs reagent, the developer. Basically, all organic components were detected by this methodology that showed to be promising for detecting additives of similar chemical structures, though small quantities of some components presented in the formulation (Damazio *et al.* 2016).

Lanxess Rubber (2012) developed on an industrial laboratory a methodology for determining the ET, ENB and 2-vinyl norbornene (VNB) content in EPDM, but only applied to EPDM rubber which does not have a plasticizer. For extended rubber, oil extraction must be made in advance, because plasticizer interferes with proper execution of the analysis. It may take more time for the process to be finished.

Another method (ASTM D3900 – 05a 2010) for the determination in question uses EPDM samples with ET content (35 – 85%) established by nuclear magnetic resonance of carbon 13 (^{13}C NMR) and analyzed by FT-IR transmission. Samples were prepared as films without plasticizer. Four methods have been established as well as the analytical bands (cm^{-1}) of P and ET used, being on the relative band (P/ET): 1156/722; 1379/722; 1379/1460; 1156/4255 (by using band in NIR region for ET, which, although, did not found the assignment in the text, being a combination of bands at the same region). Some interference in determining proper baseline was cited due the presence of additive bands around 1156 cm^{-1} of P, recommending the use of other bands. Lanxess Rubber (2012) obtained spectra by transmission mode, but details of sample preparation, number of replications and error methodology are not mentioned.

The methodology was fairly detailed on ASTM standard (ASTM D3900 – 05a 2010), but some points should be highlighted: (a) pressed samples are not suitable for vulcanized materials; (b) the presence of additives in one of the methods interferes in the choice of baseline, implying the use of other bands; (c) the use of a non-selective band of ethylene (1460 cm^{-1}), which is attributed to the CH_2 and CH_3 angular deformation, indicating that the best analytical bands would be found at 1379 cm^{-1} to P and 722 cm^{-1} to ET.

Recent study (Chitta 2014) applied HPLC to separate EPDM terpolymers based on diene content. It was found that the nature of diene contributes with the retention. According to the author, the difference between the elution volume obtained experimentally from an EPDM sample and the expected elution volume of an EP sample, with identical ethylene content, contributes to calculate the diene content of EPDM. HPLC analysis of polymers is a prerequisite to determine solubility of macromolecules in the corresponding sample solvent or mobile phase, at a specific temperature. Complete dissolution of polymer molecules is important for liquid adsorption chromatographic separation and also to avoid any blockage in the chromatographic system during analysis. Damazio (2015) developed a quantitative analysis. As HPLC analysis conditions are more complex than other techniques, TLC/IR can be used for separation and identification of additives.

TG and IR Methods for Characterization of Rubbers and Their Additives

The main methodologies that have been developed for additives analysis generally involve solvent extraction step, increasing analysis time. Sanches (2015) investigated unvulcanized and vulcanized EPDM and their additives by FT-IR analysis of gaseous pyrolysates (PIR-G/FT-IR) (Sanches *et al.* 2014) and by thermogravimetric analysis coupled with FT-IR (TG/FT-IR) (Sanches *et al.* 2015), both without solvent extraction step. A comparison between these two methodologies was also carried out. The results showed that functional groups of additives can be detected from unvulcanized and vulcanized rubbers, without prior extraction. The sulfur additives, monossulfide of tetrametil tiuram (TMTM) and 2-mercaptobenzothiazole (MBT), at levels as low as 0.7 phr (0.63 wt %), were detected by both methods. However, other additives such as paraffin oil, stearic acid and 2,2,4-trimethyl-1,2-dihydroquinoline (TMQ) can not be identified by these methodologies. Individually, all analyzed additives presented distinct FT-IR spectra and were also identified from each other by coupled PIR-G/FT-IR and TG/FT-IR methodologies.

Sanches *et al.* (2006) used PIR-G/FT-IR technique for investigating gaseous products of other rubbers. The developed methodology was suitable to identify different elastomers

and elastomer blends, including rubbers that present similar IR spectra of pyrolyzed liquid products, such as halogenated forms of copolymer of isobutylene and isoprene rubber (CIIR and BIIR), natural and copolymer of butadiene and styrene rubber (NR/SBR) as well as EPDM/SBR, SBR and butadiene rubber (SBR/BR) and SBR.

Arockiasamy *et al.* (2012) studied the decomposition behaviour of SBR using a system equipped with TG, DSC, FT-IR and mass spectroscopy (MS). Thermal decomposition and oxidation of SBR rubber was examined with focus on the composition of evolved gases during the process. FT-IR detected the presence of the following functional groups: OH, C–H and C=C, C=O and O–C–O. The interaction of these techniques proved to be useful for this kind of characterization.

Sanches *et al.* (2015) developed a methodology of TG/IR in order to evaluate additives in EPDM rubber composition. Unvulcanized and vulcanized EPDM rubbers and their additives were investigated by TG/FT-IR without solvent extraction and in a wide temperature range. TG/FT-IR detected absorptions due to the additives tetramethylthiuram monosulfide and 2-mercaptobenzothiazole present in the EPDM formulation at concentrations of 0.7 phr (0.63 wt %). Paraffin oil, stearic acid and 2,2,4-trimethyl-1,2-dihydroquinoline functional groups were not observed in either the unvulcanized or vulcanized EPDM. Nevertheless, in addition to the ability of this method to detect sulfur-containing groups, the lack of a pre-extraction reduces the time and effort required for additive analysis in rubbers. Therefore, the TG/FT-IR technique can be employed for analyzing additives separately, neat rubber (raw), vulcanized and unvulcanized compounds. Additives degradation can also be investigated by TG/FT-IR, because of the temperature selectivity.

FT-IR Surface Analysis of EPDM Rubber

Elastomers of the ethylene-propylene, such as EPDM, are apolar and present low adhesion properties, in most cases, requiring surface treatment. Plasma surface treatments have been an alternative to improve these characteristics, besides being harmless to the environment.

Most of mentioned studies and reviewed literature have shown the contribution of FT-IR to characterize chemical species formed on surface as a consequence of the treatment. Some studies in which plasmas were used to treat EPDM rubbers also showed a good response and sensitivity by using some FT-IR techniques to analyze their surfaces (Moraes *et al.* 2007; Grythe and Hansen 2006; Awaja *et al.* 2009). Spectra of EPDM and polyolefin treated by plasmas were obtained with ATR, but UATR, the new generation of the FT-IR technique, has not been used to study polymer surfaces.

Santos (2013) modified the surface of vulcanized EPDM, Nordel IP 3430 and Nordel IP 4520 with plasma excited by microwaves in Ar, N_2, Ar/O_2, N_2/O_2, N_2/H_2 and $N_2/H_2/Ar$, aiming the improvement of their adhesive properties. The characterization was made by FT-IR techniques of reflection: UATR, MIC with ATR objective and PAS (Santos *et al.* 2012b, 2013, 2014). They were used to evaluate the degrees of different sampling depth for the characterization of rubbers after plasma treatments, mainly by the different permeability of gases (oxygen and nitrogen) chosen to form gaseous mixtures. UATR technique was the most suitable for this purpose, because it showed less interference with the components of the rubber formulation, detecting spectrometric changes arising from the formation of polar groups promoted by the plasma treatment. In order to validate the results obtained by FT-IR, X-ray photoelectron spectroscopy (XPS) analysis was performed before and after treatment, and it was observed an increase in the percentage of atomic oxygenated and nitrogenated groups on the surface after treatments by Ar/O_2 plasma and N_2/H_2, confirming the results found by FT-IR. It was observed a reduction in the values of the contact angle, high values of work of adhesion and peel strength test of adhesive gasket (EPDM/Adhesive PU/PVC). These results were attributed to the improvement in adhesive properties of treated surface. After Ar/O_2, N_2/H_2 and $N_2/H_2/Ar$ plasma treatments, Nordel IP 4520 rubber showed fairly aging stability, evaluated by measuring contact angle. Nordel IP 3430 achieved its best result just with Ar/O_2 plasma. Samples submitted to mechanical tests were characterized by FT-IR/UATR, and bond failures were confirmed between the interface of the adhesive film of PU and EPDM (Nordel IP 3430) rubber, noticing the contribution of this technique for studying interfaces.

A recent study (Pistor and Zattera 2014) about reclaiming of elastomer residues has used instrumental techniques for characterization of devulcanization caused by microwaves exposure. The efficiency of devulcanization of EPDM was determined by subjecting the elastomer samples to 2, 3 and 4 min of microwaves exposure. Scanning electron microscopy (SEM) and TG using different heating rates were used to determine the kinetic degradation parameters according to the Flynn-Wall-Ozawa method. It was observed that, up to 4 min of devulcanization exposure period, the degradation temperature of EPDM was not exceeded. Microwaves exposure delivered a maximum devulcanization temperature range that is consistent with the degradation temperatures observed by TG. The morphology of the samples was altered by the microwave treatment. The devulcanization process favored particle size reduction, while additionally increasing the particles surface roughness after the devulcanization process. Activation energy values were also reduced as a result of the change in morphology, probably due to the diminished concentration in polysulfide links characteristic of the vulcanized EPDM-r 3-D network.

FT-IR ANALYSIS OF COMPOSITE SYSTEMS

Epoxy systems (ES) are very important due their versatility and potential of use, including the aerospace area. Depending on the physical and chemical properties of the curing agents (CA) and the process conditions, it is possible to vary significantly the properties of the final material, such as mechanical strength, thermal and chemical resistance etc. Therefore, the mechanism of cure must be known in order to establish the relationship between structure and properties of the material, optimizing how it will be used, i.e. adhesive, coating or matrix composites. Thus, it is evident the importance of characterization and identification of curing agents in ES.

Romão (2003) studied ES based on diglycidyl ether of bisphenol A (DGEBA) cured with nine CA. The characterization of these ES and CA was done by DSC, FT-IR, TG and coupling TG/FT-IR. The curing conditions of ES were determined by DSC. Chemical changes that occurred during the curing reaction of certain systems were evaluated by MIR and NIR spectroscopy. The ES decomposition temperature determined by TG was used for identifying the respective CA by controlled pyrolysis FT-IR (CONTROLPIR/FT-IR).

A recent study (Ahamad and Alshehri 2014), including epoxy resin and coupled methodologies for its characterization, was found. A polymeric blend has been prepared using urea formaldehyde (UF) and epoxy resin (DGEBA) in 1:1 mass ratio. TG coupled with FT-IR and spectrometric mass (MS) technique were used to study the thermal degradation of UF/epoxy resin blend (UFE). The TG results showed the pyrolysis process divided into three stages: drying process, fast thermal decomposition and cracking of the sample. There were no solid products except ash content for UFE during ignition at high temperature. Volatile products, such as CO_2, CO, H_2O, HCN, HNCO, and NH_3, were identified during thermal degradation of UFE. These two techniques could be complementary since they were refined to identify more precisely evolved gases.

FUTURE TRENDS

There are new studies being carried out in different areas, such as polymers systems for hybrid propulsion (Santos *et al.* 2012a), FT-IR characterization of polymers used in microencapsulation of oxidizer for propellants (Oliveira 2014) and substitution of asbestos in polymers thermal insulation compositions.

In recent publications found in literature about these subjects, we can cite the "Review on the fundamentals of polymer combustion and flammability characteristics for hybrid propulsion" (Chen and Gao 2014), which emphasizes properties of potential polymeric fuels and their modification.

Novozhilov et al. (2011), in a review, cites that hybrid propulsion is an attractive alternative to conventional liquid and solid rocket motors, which has been an active area of research and technological developments. Fundamental flammability characteristics of polymeric fuels have been discussed. Success of polymer fuel applications to hybrid propulsion depends on further improvement of their combustion characteristics, by the enhancement of regression rates. Estimates suggest that the regression rate needs to be increased dramatically, but chemical fuel modification is a promising route to overcome this bottleneck.

Santhosh (2010) discussed about the use of ethyl cellulose (EC) and poly(methyl methacrylate) (PMMA) as coating materials of spherical grains of ADN. A comparison of the moisture absorption profiles of ADN coated with EC and PMMA was made. Preliminary coating studies on spherical ADN grains were carried out using EC and PMMA at relative humidity of 62 and 74%. ADN coated with PMMA showed better properties than EC. The moisture pickup was reduced over 50% for the ADN grains coated with either EC or PMMA.

Virta (2005) noticed a considerable decline consumption of asbestos in the United States, part of Europe and some other countries. In fact, many asbestos substitutes have been successful used for a long time, being an integral part of the product. Asbestos still have been used in some places; however, it is observed a considerable expansion in sales of substitutes or alternative materials.

In this context, Maxim *et al.* (2014) show in a review the perlite toxicology and epidemiology, being used as

asbestos substitute. They concluded that the available data are not reliable to use for risk calculations of perlite-exposed populations and warn that perlite is regulated as a nuisance dust in some countries.

According to future trends, characterization of these polymer/energetic materials, based on FT-IR and other complementary techniques, could be suitable mainly for aerospace technology.

CONCLUSIONS

This review focused on the recent developments of aerospace polymers/energetic materials. The characterization of aerospace polymers/energetic materials can be considered a dynamic process presenting new challenges for the future. Many developments have been made in recent years towards this goal. Characterization schemes help to provide researchers with a wide variety of analytical techniques. It was realized that there is a small number of FT-IR studies on the NIR region, coupling techniques application, measurement and surface analysis by UATR of aerospace polymers. Thus, studies that have been developed in this area can contribute for the increase in technical and scientific research of these materials.

ACKNOWLEDGEMENTS

This study was supported in part by the National Senior Visiting Professor Program (PVNS) from the Coordination for the Improvement of Higher Education Personnel (CAPES) and the São Paulo Research Foundation (FAPESP) (grant #2014/00560-9).

REFERENCES

Ahamad T, Alshehri SM (2014) Thermal degradation and evolved gas analysis: a polymeric blend of urea formaldehyde (UF) and epoxy (DGEBA) resin. Arabian J Chem 7:1140-1147. doi: 10.1016/j.arabjc.2013.04.013

American Society for Testing and Materials (ASTM) D3900 – 05a (2010) Determination of Ethylene Units in Ethylene-Propylene Copolymers (EPM) and in Ethylene-Propylene-Diene Terpolymers (EPDM) by Infrared Spectrometry, Annual Book of ASTM Standards, Philadelphia.

Arockiasamy A, Toghiani H, Oglesby D, Horstemeyer MF, Bouvard JL, King RL (2012) TG-DSC-FTIR-MS study of gaseous compounds evolved during thermal decomposition of styrene-butadiene rubber. J Therm Anal Colorim 111(1):535-542. doi: 10.1007/s 10973-012-2559-0

Awaja F, Gilbert M, Kelly G (2009) Adhesion of polymers. Prog Polym Sci 34(9):948-968.

Chen J, Gao X (2014) Review on the fundamentals of polymer combustion and flammability characteristics for hybrid propulsion. Journal of Polymer and Biopolymer Physics Chemistry 2(4):78-83. doi: 10.12691/jpbpc-2-4-4

Chitta R (2014) Development of high temperature liquid chromatography for chemical composition separation of polyolefins (PhD thesis). Darmstadt: Technischen Universität Darmstadt.

Clemente M, Rocha RJ, Iha K, Rocco JAFF (2014) Desenvolvimento de tecnologia de pré-polímeros na síntese de poliuretanos empregados em combustíveis sólidos. Quím Nova 37(6):982-988. doi: 10.5935/0100-4042.20140154

Damazio DB (2015) Caracterização por FT-IR e TLC de EPDM (master's thesis). São Paulo: Instituto Tecnológico de Aeronáutica. In portuguese.

Damazio DB, Campos EA, Diniz MFD, Mattos EC, Dutra RCL (2016) TLC/IR (UATR) off-line coupling for the characterization of additives in EPDM rubber compositions. Polímeros. In press.

Damazio DB, Diniz MF, Mattos EC, Dutra RCL (2014) Determinação por FT-IR de transmissão e reflexão (UATR) de etileno e propileno em EPDM. Polímeros 24(6):703-710. doi: 10.1590/0104-1428.1536

Damazio DB, Santos RP, Diniz MF, Mattos, EC, Dutra RCL (2015) Determinação do teor de ENB em EPDM (elastômero puro) por FT-IR de transmissão, por meio de banda relativa. Polímeros 25(2):181-185. doi: 10.1590/0104-1428.1777

Dutra RCL (1996) Aplicação de técnica TLC-IR em estudos de separação, identificação e quantificação de aditivos em borrachas. Polímeros 6(2):26-31.

Grythe KF, Hansen FK (2006) Surface modification of EPDM rubber by plasma treatment. Langmuir 22(14):6109-6124. doi: 10.1021/la053471d

Kawamoto AM, Barbieri U, Keicher, T, Krause H, Holanda JAS, Kaiser M, Polacco G (2008) Synthesis and characterization of glycidyl azide-r-(3,3-bis(azidomethyl) oxetane) copolymers. Propellants Explos Pyrotech 33(5):365-372. doi: 10.1002/prep.200700221

Kawamoto AM, Diniz MF, Lourenço VL, Takahashi MFK, Keicher T, Krause H, Menke K, Kempa PB (2010) Synthesis and characterization of GAP/BAMO copolymers applied at high energetic composite propellants. J Aerosp Technol Manag 2(3):307-322. doi: 10.5028/jatm.2010.02037910

Kawamoto AM, Oliveira JIS, Dutra RCL, Rezende LC, Keicher T, Krause H (2009) Synthesis and characterization of energetic thermoplastic elastomers for propellant formulations. J Aerosp Technol Manag 1(1):35-42. doi: 10.5028/jatm.2009.01013542

Lanxess Rubber (2012) Catalogo técnico – determinação do conteúdo de eteno, ENB e VNB no EP(D)M.

Lourenço VL, Kawamoto AM, Sciamareli J, Rezende LC, Pires DC, Takahashi MFK, Berdugo AV, Cruz SM, Dutra RCL, Soares BG (2006) Determinação da distribuição de funcionalidade de HTPB e verificação de sua influência no comportamento mecânico de poliuretano utilizado em motor-foguete. Polímeros 16(1):66-70.

Mattos EC, Diniz MF, Dutra RCL, Iha K (2004a). Avaliação do uso de técnicas FT-IR para caracterização de cobertura polimérica de material energético. Polímeros 14(2):63-68. doi: 10.1590/S0104-14282004000200007

Mattos EC, Diniz MF, Nakamura NM, Dutra RCL (2009) Determination of polymer content in energetic materials by FT-IR. J Aerosp Technol Manag 1(2):167-175. doi: 10.5028/jatm.2009.0102167175

Mattos EC, Diniz MF, Viganó I, Iha K, Dutra RCL (2004b) Application of FT-IR techniques for identification of different polymers used in the coating process of energetic materials. Proceedings of the International Annual Conference of the Fraunhofer ICT, 147; Karlsruhe, Germany

Mattos EC, Moreira ED, Diniz MF, Dutra RCL, Silva G, Iha K, Teipel U (2008) Characterization of polymer-coated RDX and HMX particles. Propellants Explos Pyrotech 33(1): 44-50. doi: 10.1002/prep.200800207

Maxim LD, Ron Niebo R, McConnell EE (2014) Perlite toxicology and epidemiology – a review. Inhal Toxicol 26(5):259-270. doi: 10.3109/08958378.2014.881940

Moraes JH, da Silva Sobrinho AS, Maciel HS, Dutra JCN, Massi M, Mello SAC, Schreiner WH (2007) Surface improvement of EPDM rubber by plasma treatment. J Phys D Appl Phys 40(24):7747-7748. doi: 10.1088/0022-3727/40/24/022

Novozhilov V, Joseph P, Ishiko K, Shimada T, Wang H, Liu J (2011) Polymer combustion as a basis for hybrid propulsion: a comprehensive review and new numerical approaches. Energies 4(10):1779-1839. doi: 10.3390/en4101779

Oliveira JIS (2014). Síntese e caracterização do oxidante ADN (dinitramida de amônio), usado em propelentes para aplicação aeroespacial (PhD thesis). São Paulo: Instituto Tecnológico de Aeronáutica. In portuguese.

Oliveira JIS, Diniz MF, Kawamoto AM, Dutra RCL, Keicher T (2006) MIR/NIR/FIR characterization of poly-AMMO and poly-BAMO and their precursors as energetic binders to be used in solid propellants. Propellants Explos Pyrotech 31(5):395-400. doi: 10.1002/prep.200600054

Oliveira JIS, Dutra RCL, Diniz MF, Kawamoto AM, Keicher T (2007) Determination of CHN content in energetic binder by MIR analysis. Polímeros 17(1):43-47. doi: 10.1590/S0104-14282007000100011

Oliveira JIS, Sciamareli J, Diniz MF, Dutra RCL (2014) Avaliação por FT-IR de interações entre polímero energético e oxidante: GAP/ADN e GAP/AP. Polímeros 24(5):620-627. doi: 10.1590/0104-1428.154

Pistor V, Zattera AJ (2014) Degradation kinetics of ethylene propylene diene terpolymer residues devulcanized by microwaves. J Elastomers Plast 46(1):69-83. doi: 10.1177/0095244312462159

Ribeiro SP, Santiago DG, Vianna Jr AS (2012) Poli (Metil Azoteto de Glicidila) – GAP. I. Síntese e caracterização. Polímeros 22(5):407-413. doi: 10.1590/S0104-14282012005000045

Romão BMV (2003) Caracterização e avaliação de sistemas epoxídicos utilizados na indústria aeroespacial (master's thesis). São Paulo: Instituto Tecnológico de Aeronáutica. In portuguese.

Sanches NB (2015) Caracterização de proteções térmicas de EPDM por PIR-G/FT-IR e TG/FT-IR (PhD thesis). São Paulo: Instituto Tecnológico de Aeronáutica. In portuguese.

Sanches NB, Cassu SN, Diniz MF, Dutra RCL (2014) Characterization of additives typically employed in EPDM formulations by using FT-IR of gaseous pyrolyzates. Polímeros 24(3):269-275. doi: 10.4322/polimeros.2014.066

Sanches NB, Cassu SN, Dutra RCL (2015) TG/FT-IR characterization of additives typically employed in EPDM formulations. Polímeros 25(3):247-255. doi: 10.1590/0104-1428.1819

Sanches NB, Diniz MF, Reis TB, Cassu SN, Dutra RCL (2006) Avaliação do uso de técnicas PIR-G/FT-IR para caracterização de elastômeros. Polímeros 16(3):211-216. doi: 10.1590/S0104-14282006000300010

Santhosh G (2010) Coating and burn-rate studies of ammonium dinitramide (ADN). Chapter 7; p. 228-239. Prepared by Beehive Digital Concepts Cochin for Mahatma Gandhi University Kottayam.

Santos GP, Pedreira SM, Lacava PT (2012a) Physical property and carbon black distribution impact on propulsion efficiency of paraffin-based fuel. Proceedings of the ASME International Mechanical Engineering Congress and Exposition, volume 1; Houston, USA.

Santos RP (2013) Estudo por meio de técnicas FT-IR e de propriedades adesivas da borracha de EPDM vulcanizada e modificada por plasma (master's thesis). São Paulo: Instituto Tecnológico de Aeronáutica. In portuguese.

Santos RP, Oliveira Junior MS, Mattos EM, Diniz MF, Dutra RCL (2012b) Caracterização por FT-IR da superfície de borracha EPDM tratada via plasma por micro-ondas. Polímeros 22(5):440-446. doi: 10.1590/S0104-14282012005000065

Santos RP, Oliveira Junior MS, Mattos EC, Diniz MF, Dutra RCL (2013) Study by FT-IR technique and adhesive properties of vulcanized EPDM modified with plasma. J Aerosp Technol Manag 5(1):65-74. doi: 10.5028/jatm.v5i1.163

Santos RP, Oliveira Junior MS, Mattos EC, Diniz MF, Dutra RCL (2014). Técnicas FT-IR (PAS, UATR e objetiva ATR) aplicadas à caracterização de EPDM modificada com plasma. Polímeros 24(3):411-416. doi: 10.4322/polimeros.2014.015

Sciamareli J, Costa JR, Takahashi MFK, Diniz MF, Lourenço VL, David LH, Iha K, Miyano MH, Ferreira C (2009a) Síntese e caracterização do polímero energético metil azoteto de glicidila (GAP) via análises instrumentais. Polímeros 19(2):1-4. doi: 10.1590/S0104-14282009000200008

Sciamareli J, Costa JR, Takahashi MFK, Iha K, Berdugo AAV, Diniz MF, Miyano MH, Ferreira C (2009b) Otimização do processo de obtenção do pré-polímero metil azoteto de glicidila. J Aerosp Technol Manag 1(1):29-34. doi: 10.5028/jatm.2009.01012934

Takahashi MFK, Dutra RCL, Diniz MF, Polito WL (1996) Determinação de índices de hidroxila em polibutadienos hidroxilados e de grupos NCO em diisocianatos e pré-polímeros por espectroscopia no infravermelho com transformada de Fourier. Polímeros 6(4):45-52.

Tourné M (2013) Developments in explosives characterization and detection. J Forensic Res S12:1-10. doi: 10.4172/2157-7145.S12-002

Virta RL (2005) Asbestos substitutes; [accessed 2016 Jan 06]. http://www.segemar.gov.ar/bibliotecaintemin/LIBROSDIGITALES/Industrialminerals&rocks7ed/pdffiles/papers/090

J. Aerosp. Technol. Manag., São José dos Campos, Vol.8, Nº 1, pp.18-25, Jan.-Mar., 2016

doi: 10.5028/jatm.v8i1.537

Applicability of FT-IR Techniques and Goniometry on Characterization of Carbon Fiber Surfaces

Mauro Santos de Oliveira Junior[1,2], Milton Faria Diniz[3], Rita de Cássia Lazzarini Dutra[3,4], Marcos Massi[1,2], Choyu Otani[2]

ABSTRACT: Carbon fibers have been widely used as structural reinforcement in aeronautical composites, because of their exceptional mechanical properties. However, carbon fibers present few polar groups on their surfaces inducing a weak interaction with some thermosetting and thermoplastic matrices. Surface treatments, such as thermal and electrochemical oxidation, are generally followed by sizing in order to improve interfacial adhesion between carbon fibers and some matrices. The precise surface characterization, by means of its chemical groups and radical identification, has been pointed out as an effective tool of carbon fibers finishing assessment process. Goniometry and Fourier transform-infrared spectroscopy are widely used to characterize some materials applied in industry, but not for carbon fibers, mainly because of their filamentary shape and the high concentration of carbon even in their near surface. In this paper, unsized and sized Torayca T300 carbon fibers were characterized by goniometry tests to evaluate hydrophilic or hydrophobic character. Qualitatively, it was noticed the effect of sizing on carbon fibers by their hydrophilic behavior, which has not been observed in unsized samples. Chemical analysis was performed by Fourier transform-infrared spectroscopy using different setups: photoacoustic, attenuated total reflectance and universal attenuated total reflectance. The Fourier transform-infrared spectroscopy/attenuated total reflectance/Germanium was shown to be the most promising technique to analyze carbon fibers surface, despite the low level of relative intensities of some bands. By this technique, it was possible to observe differences between unsized and sized carbon fibers spectra.

KEYWORDS: Carbon fiber, Infrared spectroscopy, Wettability, Characterization, Surface properties.

INTRODUCTION

In the last decades, carbon fibers (CF) have become a requisite and worthy material used in strategic applications. They have been widely used in structural reinforcement in composites, mainly in aeronautics, aerospace and automotive industries because of their excellent mechanical, thermal and electrical properties. Furthermore, their low volumetric expansion coefficient and low density turned them more attractive for these industries. CF used in structural applications are normally obtained at temperatures above 1500 °C. They present special characteristics, such as ordered graphitic structure disposed preferentially in parallel to the fiber axis and their high concentration of carbon is at least 92% (Chung 1994). The crystallinity of CF is strongly influenced by the carbonization process parameters (Chung 1994; Morgan 2005). However, the concentration of elements like nitrogen and oxygen is poor in CF, even on their surface. Thus, the low content of polar groups in the CF surface can compromise their adhesion to some polymeric matrices (Chan *et al.* 1996; Montes-Morán *et al.* 2001; Xu *et al.* 2008).

A surface treatment is necessarily employed at the end of the process to obtain CF, in order to reduce the electrostatic charge on their surface and to handle them. It is important to improve the interfacial adhesion between CF and the composite matrix. Basically, these treatments can be divided into two groups: wet and dry processes. In dry processes, plasmas have been widely used for this purpose (Donnet *et al.* 1986, 1987; Chan *et al.* 1996; Montes-Morán *et al.* 2001; Park *et al.* 2010; Oliveira Jr *et al.* 2011). On the other hand, the wet processes based on electrochemical reactions, such as oxidation, fluorination, and oxyfluorination, have been employed to modify the CF surface (Basova *et al.* 1999; Ho *et al.* 2008; Seo and Park 2009). Generally, following these processes, a coating of polymeric sizing, also denoted as finishing, can be applied to protect the CF surface.

These treatments generally increase the surface energy and wettability of some materials. Goniometry has been a simple technique that can be applied to analyze these thermodynamic properties. The hydrophobic or hydrophilic features of any material can be quickly assessed just by measuring the contact angle of a liquid dropped over its flat surface, in order to determine its adhesive potential. Fowkes (1964) showed the contribution of some molecular interactions to the total surface energy. For polymers, dispersive and polar forces are usually the main components that make up the total surface energy. These parameters are generally calculated by measuring contact angles of two different liquids. Owens and Wendt (1969) and Kaelble and Uy (1970) developed a method called geometric mean that is applied to calculate the surface energy of polymers using polar and apolar liquids in the goniometry setup. Wu (1971) described a method called harmonic mean that can be suitable when goniometry measurements are made with high surface tension liquids. However, the contact angle of samples with high surface energy can not be measured reliably, mainly for polymers, because the liquid usually spread irregularly over the surface, but the wettability can be analyzed in a qualitative way.

In order to infer from mechanical and chemical changes occurred on CF by a specific treatment, the characterization of their surface is important to evaluate how efficient this treatment is. For chemical analysis, the spectroscopy techniques are widely used to characterize polymers. The use of light-based spectroscopy, like Fourier transform-infrared spectroscopy (FT-IR), is a challenge in the analysis of CF, because they intensively absorb electromagnetic radiation and the scattering can make it difficult to obtain good spectra from them. Thus, few authors have worked intensively with various FT-IR techniques to characterize CF (Morita *et al.* 1986; Graf *et al.* 1987; Ishida 1987; Ohwaki 1993; Boehm 1994; Ohwaki and Ishida 1995; Yang and Simms 1995).

Ohwaki (1993) characterized CF by some FT-IR techniques and X-ray photoelectron spectroscopy (XPS). It was possible to identify some chemical bonds on the CF surface with good sensibility by FT-IR analysis, and the results are in agreement with those obtained by XPS analysis. By varying some parameters from FT-IR/attenuated total reflectance (ATR), such as the light polarization states, the crystal type and the beam incident angle, Ohwaki also verified an improvement of the signal/noise (S/N) ratio spectra. The improvement in the S/N ratio was better for small incident angles in non-polarized light, but it aims a deeper layer from the bulk sample (Ohwaki and Ishida 1995).

Jiang *et al.* (2015) have recently studied CF surface modified by electrophoretic deposition using FT-IR and other techniques. Despite of FT-IR spectra have indicated formation of C=O and C–O groups on CF surface, they used the transmission mode that is inappropriate to analyze surfaces. Samples prepared with KBr pellet are inadequate, because of its hygroscopic character that can introduce bands related to OH groups from humidity around 3300 and 1650 cm^{-1}, interfering in spectrum interpretation. Therefore, it can be supposed that the analysis of CF surface through specific techniques could be promising.

Thus, this study was focused on the investigation of chemical contents on unsized and sized CF surfaces by FT-IR and goniometry. These techniques are useful and applied to some materials, being cheaper than XPS. By comparing already-known photoacoustic (PAS), ATR and the new technique universal attenuated total reflectance (UATR), it was possible to verify that each technique has an appropriate sensibility to identify some differences between these two types of fibers. Goniometry analysis was also employed to evaluate qualitatively the hydrophilic or hydrophobic characteristics of these CF.

EXPERIMENTAL

RAW MATERIAL

Tows with 3,000 filaments of unsized and sized Torayca T300 CF have been used in this paper. The polymeric sizing coating of these CF is based on epoxy resin and it represents 1 wt%.

GONIOMETRY

Unsized and sized CF were analyzed by goniometry using a 500-00 Goniometer Drop Image Advanced-2004 from Hamé-Hart. The contact angle measurements of the samples were performed just after placing a drop of deionized water with 13 ± 1 μL on the surface at room temperature and controlled relative humidity (40%). Samples were prepared in accordance with the illustrated scheme as shown in Fig. 1. This procedure was employed in order to make the surface as flat as possible to obtain enough reproducibility and achieve good qualitative results. Goniometry is widely used to analyze flat and continuous

1.Universidade Federal de São Paulo – Instituto de Ciência e Tecnologia – Departamento de Ciência e Tecnologia – São José dos Campos/SP – Brazil. **2.**Departamento de Ciência e Tecnologia Aeroespacial – Instituto Tecnológico de Aeronáutica – Divisão de Ciências Fundamentais – São José dos Campos/SP – Brazil. **3.**Departamento de Ciência e Tecnologia Aeroespacial – Instituto de Aeronáutica e Espaço – Divisão de Química – São José dos Campos/SP – Brazil. **4.**Departamento de Ciência e Tecnologia Aeroespacial – Instituto Tecnológico de Aeronáutica – Divisão de Engenharia Mecânica – São José dos Campos/SP – Brazil.

Author for correspondence: Mauro Santos de Oliveira Junior | Universidade Federal de São Paulo – Instituto de Ciência e Tecnologia – Departamento de Ciência e Tecnologia | Rua Talim, 330 – Vila Nair | CEP: 12.231-280 – São José dos Campos/SP – Brazil | Email: msozero@gmail.com

Received: 09/01/2015 | **Accepted:** 12/03/2015

J. Aerosp. Technol. Manag., São José dos Campos, Vol.8, Nº1, pp.26-32, Jan.-Mar., 2016

surfaces. However, CF tows (3,000 filaments) have a non-planar and discontinuous surface, and it is difficult to make a quantitative analysis by this technique.

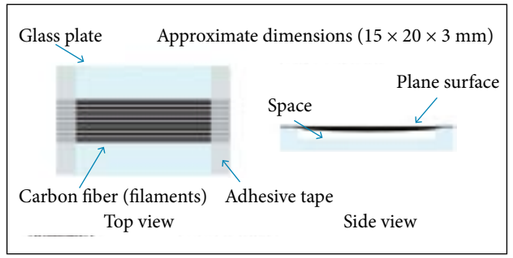

Figure 1. Sample of CF prepared for goniometry analysis.

FT-IR ANALYSIS

The chemical analysis of the CF surface was made using the PAS accessory coupled to a FT-IR Spectrometer Spectrum 2000 – PerkinElmer as well as ATR and UATR accessories coupled in a Spectrum One FT-IR Spectrometer – PerkinElmer. For FT-IR/PAS analysis two distinct speed conditions were set up under nitrogen. The fast scan was made with a speed of 0.2 cm/s, 32 scans, 8 cm^{-1} of resolution and spectral range from 4000 to 400 cm^{-1}. The slow analysis has the same parameters, but a speed of 0.05 cm/s. FT-IR/UATR analysis was made using a ZnSe crystal in the region between 4000 and 550 cm^{-1} and 40 scans. A pressure of 100 N over the sample was set up to improve the surface contact with the crystal. The FT-IR/ATR analysis was made using Ge crystals. Each of these two techniques operates with the following parameters: 40 scans, light beam incident angle of 45° and, in this case, the samples were spread over both faces of the crystal. For FT-IR/ATR/Germanium (Ge), the range of operation was from 4000 to 700 cm^{-1}. The environmental condition of all spectroscopy analysis was 25 ± 2 °C and 45 ± 3% of humidity.

RESULTS AND DISCUSSION

GONIOMETRY CHARACTERIZATION

Drops of deionized water were deposited on the CF surface. The drop profile was taken for analysis in the parallel and transverse CF axis direction, in order to infer from the influence of the roughness of the whole sample (multiple filaments), as shown in Fig. 2. In the parallel direction, roughness tends to be smoother than in a transverse direction, because transversal filaments hold the drop by mechanical anchorage.

The geometric form of the drop, oval, is similar to the form visualized at the middle of the drop shown in Fig. 2a. These results are qualitative, because the measurement of the contact angle is compromised by the difficulty to obtain the baseline that is necessary to define the interface between the drop and the surface which allows measuring correctly the angle. The contact angle seems to be near to 90° in the parallel profile. On the other hand, the angle seems to be higher in the transversal profile, as shown in Fig. 2b. When unsized CF were compared with sized ones, the latter proved to be more hydrophilic, because the drop of water spread out the whole sample, as shown in Fig. 3.

These results obtained by goniometry technique are important in order to show that the sized CF have a surface energy higher than that of the unsized ones, despite having a low percentage in weight of polymeric sizing over the CF surface. With these results, the FT-IR techniques were applied in order to compare both fibers and identify some chemical bonds.

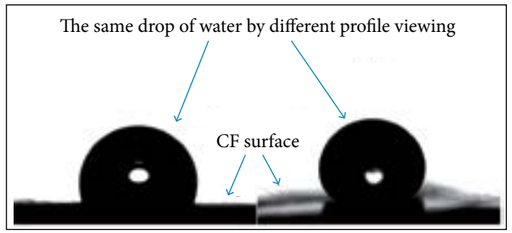

Figure 2. Profile of deionized water on the CF surface. (a) Parallel to the CF axis; (b) Transverse to the CF axis.

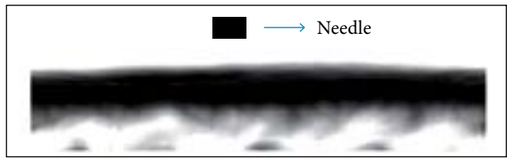

Figure 3. Drop of water deposited on sized CF surface.

FT-IR ANALYSIS

The spectroscopic analysis of CF was carried out by three different FT-IR techniques starting by those considered near-surface, such as FT-IR/PAS. Other techniques, FT-IR/UATR and FT-IR/ATR/Ge, were also used in order to obtain good spectra from unsized and sized CF Toray T-300.

PHOTOACOUSTIC DETECTION

It is possible to obtain spectra in different degrees of depth with FT-IR/PAS. The control of the depth degree of IR beam

is reached basically by choosing the adequate scan speed. This technique proved to be effective in the analysis of opaque materials, such as the CF and most of its composites (Graf 1987). The first analyses of unsized (A) and sized (B) CF were performed at speed scan of 0.2 cm/s. This condition is considered the fastest and prior to detect chemical groups near to the surface. In this case, as can be seen in Fig. 4, the relatively low S/N ratio spectrum was obtained due to the absence of strong absorption bands, leading to a difficult assessment among spectra band with specific chemical species.

The results obtained by the speed scan of 0.2 cm/s led to the decision of carrying out the analysis with the slow speed scan of 0.05 cm/s. This choice was based on previous study performed in other researches, in which a better S/N ratio was obtained in the spectra produced by using a slower scan speed (Nogueira *et al.* 2007). Slow scan keeps the incident beam at the same region for a considerable time, contributing to the spectra accumulation, which becomes favorable to enrich the main spectrum (Stegge and Urban 2001).

The FT-IR/PAS (0.05 cm/s) spectra of unsized (A) and sized (B) CF are presented in Fig. 5. It was noted an attenuation of the noise, but the profile of the spectra presented the same appearance of those in the fast speed scan. It was not possible to clearly identify any chemical bonds on CF bulk or on their surfaces.

In our case, the procedure of obtaining FT-IR/PAS of CF was limited. The results were not satisfactory, mainly because the spectra had a low S/N ratio and did not show any difference between them. This result could be related to the fact that the PAS technique investigates more properly near-surface specimens, and the chemical content of CF can be placed in a depth between 1 – 4 µm. Therefore, FT-IR/UATR was chosen to be the next step to analyze the surface of both CF (Abidi and Hequet 2005; Sanches *et al.* 2008).

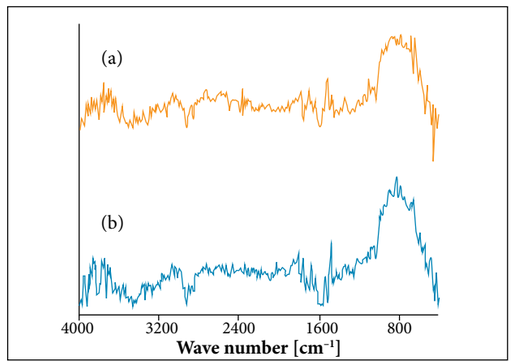

Figure 4. FT-IR/PAS spectra (0.2 cm/s). (a) Unsized CF; (b) Sized CF.

UNIVERSAL ATTENUATED TOTAL REFLECTANCE

The FT-IR/UATR method does not need a considerable amount of samples, because the exposed surface area of the crystal is positioned to make the contact with the sample which has a diameter of 2 mm (Sanches *et al.* 2008). The FT-IR/UATR spectra of unsized (A) and sized (B) CF showed an anomalous spectrum in the region between 1220 and 3600 cm^{-1}. Inverted bands with high intensities in the region between 1900 and 2200 cm^{-1} were given, producing spectra in which the main baseline was easily lost, making it difficult a good analysis of the spectra, as shown in Fig. 6. These results lead to the conclusion that it was not possible to explore this technique, at least by the method of the direct analysis of CF. Thus, the FT-IR/ATR/Ge technique was employed to analyze CF in order to verify the chemical

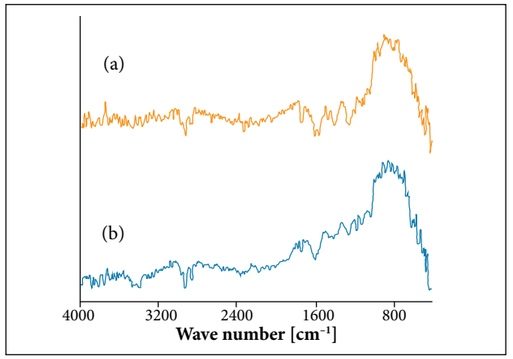

Figure 5. FT-IR/PAS spectra (0.05 cm/s). (a) Unsized CF; (b) Sized CF.

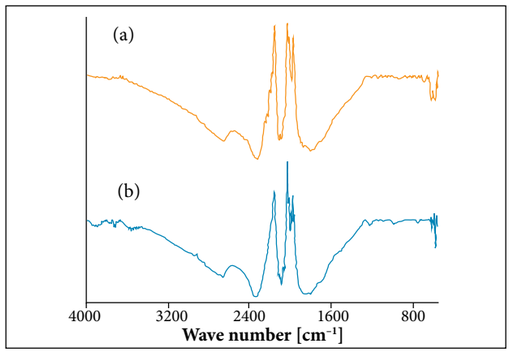

Figure 6. FT-IR/UATR spectra. (a) Unsized CF; (b) Sized CF.

changes in the surface not observed by other techniques (Ohwaki 1993; Ohwaki and Ishida 1995).

The use of Germanium crystal as fiber samples holder was introduced in this part of the study aiming at the analysis of carbon layers close to the sample surface, due to its better efficiency presented against the use of the Thallium Bromo-Iodine crystal (KRS-5) (Urbaniak-Domagala 2012; Barbeş *et al.* 2014; Technical Note, 2004).

ATTENUATED TOTAL REFLECTANCE

FT-IR/ATR/Ge was also employed to make a comparative analysis between unsized and sized CF. The advantage of this technique over FT-IR/UATR consists of a larger contact area of the crystal used in the present method (20 × 50 mm) in relation to the crystal size used in the UATR method, which uses a small crystal of 2 mm in the diameter. The refractive index of Ge crystal is 4.0, consequently, it allows to access near-depth surface up to 0.67 μm, which can be useful for thin-films, composites and fibers (Urbaniak-Domagala 2012). This means that the FT-IR/ATR/Ge method permits a near-surface analysis in a large amount of points of the sample, enriching the spectrum. The FT-IR/ATR/Ge spectra of unsized (A) and sized (B) Torayca T-300 CF showed well-defined absorption band profiles and baselines, as shown in Fig. 7.

However, it is known the Torayca T-300 is not graphitized CF and some elements of the precursor can be presented in its structure. These CF could also have been undergone a surface treatment, even being sold as an unsized CF. This was evidenced by the observation of some bands, mainly in the region near 1200 cm^{-1} of FT-IR/ATR/Ge spectrum (A), as shown in Fig. 7. Sized CF were characterized with the same technique and their FT-IR/ATR/Ge spectrum (B) was a little richer than that of the unsized CF. A pasty residual substance was extracted from sized CF (B) by immersion in acetone at room temperature. In this case, a little amount of sample was obtained because the quantity of sizing in the CF surface is near 1 wt%. However, this residue was enough to be characterized by UATR, as can be observed by the FT-IR/UATR spectrum (C) in Fig. 7. The region between 700 and 1800 cm^{-1} is rich in absorption bands and some of them have their correspondent on sized CF.

The partial spectra from this region are presented in Fig. 8, in which there is a variation of approximately 5% in intensities of some bands from unsized (A) and sized (B) CF, mainly in the region between 700 and 1300 cm^{-1}. The intensity of FT-IR/ATR/Ge bands is somewhat 10 times higher than FT-IR/UATR spectrum bands, at the same region.

It can be observed some intense bands in the UATR spectrum of the residue (C) and some of them can also be observed in sized CF (B), as shown in Fig. 8. The appearance of bands in the regions 1070 – 1150 cm^{-1} and 1230 cm^{-1} are probably related to the stretching of C–O bond, corroborating the presence of epoxy resin in CF, because this bond is presented in the basic structure of this resin. The band at 1500 cm^{-1} can be attributed to the stretching of C–C bond, which is a characteristic of aromatic molecules and it can compose complementary structures of some resins, such as C=O bond, observed at 1710 cm^{-1}, commonly present in modified epoxy resins and/or esters (Smith 1979; Ohwaki 1993; Boehm 1994; Dutra *et al.* 1995; Ohwaki and Ishida 1995; Pamula and Rouxhet 2003).

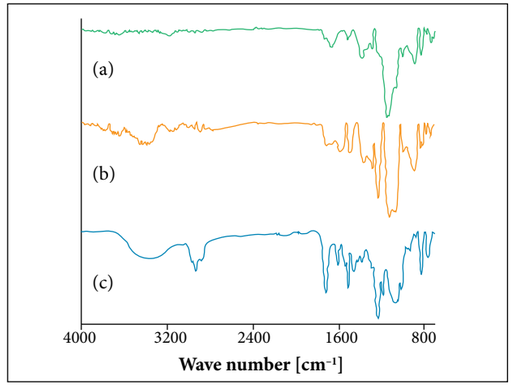

Figure 7. FT-IR/ATR/Ge spectra. (a) Unsized CF; (b) Sized CF; (c) FT-IR/UATR spectrum of residual substance removed from sized CF.

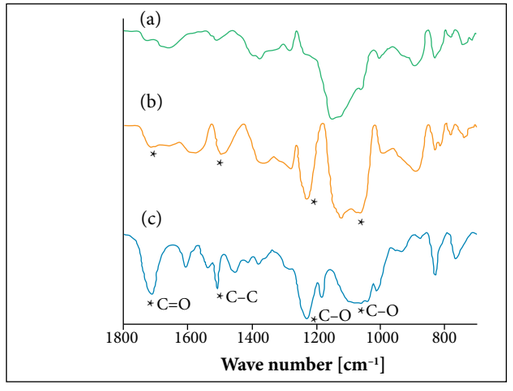

Figure 8. FT-IR/ATR/Ge partial spectra. (a) Unsized CF; (b) Sized CF; (c) FT-IR/UATR partial spectrum of residual substance removed from sized CF.

CONCLUSIONS

In this study, it was clearly observed in a qualitative way that unsized and sized CF showed hydrophobic and hydrophilic behavior, respectively, indicating goniometry as a quick and cheap technique for CF surface assessment. It was possible to verify the limitations and advantages of PAS, ATR and UATR techniques to analyze near-surface chemical groups of CF. The FT-IR/PAS is one of the most efficient techniques to do near-surface analysis. However, its response was not satisfactory to characterize CF, mainly due to difficulties in preparing samples and the depth of chemical content. As CF are filamentary, it is difficult to keep them in rest and consequently the signal detection of PAS is compromised. A low S/N ratio was obtained, independently of the speed scan used. The characterization of CF by FT-IR/UATR was also compromised, in function of the appearance of a negative absorption in a large area in the middle of the spectra for both fibers. The reason why this phenomenon occurred must be deeply studied and other ways must be explored. The FT-IR/ATR/Ge was shown to be the most promising technique to analyze CF, despite the low level of relative intensities of some bands presented by CF. However, it was possible to verify that unsized CF (as received) had already been submitted to a surface treatment through comparative analysis. It was also possible to identify some chemical bonds present in both sized CF as in the residue removed from them. These results showed that FT-IR/ATR/Ge can be useful to the characterization of carbon fiber surface, mainly after the surface treatment made at the end of carbonization processes.

REFERENCES

Abidi N, Hequet E (2005) Fourier transform infrared analysis of trehalulose and sticky cotton yarn defects using ZnSe-diamond universal attenuated total reflectance. Text Res J 75(9):645-652. doi: 10.1177/0040517505057527

Barbeş L, Rădulescu C, Stihi C (2014) ATR-FTIR spectrometry characterisation of polymeric materials. Rom Rep Phys 66(3): 765-777.

Basova YV, Hatori H, Yamada Y, Miyashita K (1999) Effect of oxidation-reduction surface treatment on the electrochemical behavior of PAN-based carbon fibers. Electrochem Commun 1(11):540-544. doi: 10.1016/S1388-2481(99)00112-5

Boehm HP (1994) Some aspects of the surface chemistry of carbon blacks and other carbons. Carbon 32(5):759-769. doi: 10.1016/0008-6223(94)90031-0

Chan CM, Ko TM, Hiraoka H (1996) Polymer surface modification by plasmas and photons. Surf Sci Rep 24(1-2):1-54. doi: 10.1016/0167-5729(96)80003-3

Chung DDL (1994) Carbon fiber composites. Washington: Butterworth-Heinemann.

Donnet JB, Brendle M, Dhami TL, Bahl OP (1986) Plasma treatment effect on the surface energy of carbon and carbon fibers. Carbon 24(6):757-770. doi: 10.1016/0008-6223(86)90186-7

Donnet JB, Dhami TL, Dong S, Brendle M (1987) Microwave plasma treatment effect on the surface energy of carbon fibres. J Phys D: Appl Phys 20(3):269-275. doi: 10.1088/0022-3727/20/3/005

Dutra RCL, Takahashi MFK, Diniz MF (1995) Importância da preparação de amostras em espectroscopia no infravermelho com transformada de Fourier (FTIR) na investigação de constituintes em materiais compostos. Polimeros 5(1):41-47.

Fowkes FM (1964) Attractive forces at interfaces. Ind Eng Chem 56(12):40-52. doi: 10.1021/ie50660a008

Graf RT, Koenig JL, Ishida H (1987) Introduction to optics and infrared spectroscopic techniques. In: Fourier transform infrared characterization of polymers. vol. 36. New York: Springer. p. 1-32.

Ho KKC, Lee AF, Lamoriniere S, Bismarck A (2008) Continuous atmospheric plasma fluorination of carbon fibres. Compos Appl Sci Manuf 39(2):364-373. doi: 10.1016/j.compositesa.2007.10.008

Ishida H (1987) Quantitative surface FT-IR spectroscopic analysis of polymers. Rubber Chem Technol 60(3):497-554. doi: 10.5254/1.3536139

Jiang JJ, Liu F, Deng C, Fang LC, Li DJ (2015) Influence of deposited CNTs on the surface of carbon fiber by ultrasonically assisted electrophoretic deposition. IOP Conf Ser Mater Sci Eng 87(1):1-4. doi: 10.1088/1757-899X/87/1/012103

Kaelble DH, Uy KC (1970) A reinterpretation of organic liquid-polytetrafluoroethylene surface interactions. J Adhes 2(1):50-60. doi: 10.1080/0021846708544579

Montes-Morán MA, Martínez-Alonso A, Tascón JMD, Paiva MC, Bernardo CA (2001) Effects of plasma oxidation on the surface and interfacial properties of carbon fibres/polycarbonate composites. Carbon 39(7):1057-1068. doi: 10.1016/S0008-6223(00)00220-7

Morgan P (2005) Carbon fiber and their composites. Boca Raton: CRC Press.

Morita K, Murata Y, Ishitani A, Murayama K, Ono T, Nakajima A (1986) Characterization of commercially available PAN (polyacrylonitrile)-based carbon fibers. Pure Appl Chem 58(3):455-468. doi: 10.1351/pac198658030455

Nogueira LM, Dutra RCL, Diniz MF, Pires M, Evangelista M, Santana FA, Tomasi L, Santos P, Nonemacher R (2007) Avaliação da aplicabilidade de técnicas MIC/FT-IR/DSC para a caracterização de filmes multicamadas. Polímeros 17(2):158-165. doi: 10.1590/S0104-14282007000200015

Ohwaki T (1993) Surface characterization of carbon fiber by infrared spectroscopy (PhD thesis). Cleveland: Case Western Reserve University.

Ohwaki T, Ishida H (1995) Optimization of the surface characterization of carbon fiber by FT-IR internal reflection spectroscopy. Appl Spectrosc 49(3):341-348. doi: 10.1366/0003702953963634

Oliveira Jr MS, Santos LV, Sagas JC, Pereira FP, Machado JPB, Otani C, Massi M, Sobrinho ASS (2011) Surface treatment of pan-based carbon-fibre with microwave excited plasmas. Paper presented at: V Brazilian Carbon Conference; Rio de Janeiro, Brazil.

Owens DK, Wendt RC (1969) Estimation of the surface free energy of polymers. J Appl Polym Sci 13(8):1741-1747. doi: 10.1002/app.1969.070130815

Pamula E, Rouxhet PG (2003) Bulk and surface functionalities of type III PAN-based carbon fibres. Carbon 41(10):1905-1915. doi: 10.1016/S0008-6223(03)00177-5

Park SJ, Chang YH, Moon CH, Suh DH, Im SS, Kim YC (2010) A study of atmospheric plasma treatment on surface energetics of carbon fibers. Bull Korean Chem Soc 31(2):335-338. doi: 10.5012/bkcs.2010.31.02.335

Sanches NB, Diniz MF, Alves LC, Dutra JCN, Cassu SN, Azevedo MFP, Dutra RCL (2008) Avaliação da aplicabilidade de técnicas FT-IR de reflexão (UATR) e de transmissão para a determinação do teor de acrilonitrila (AN) em NBR. Polímeros 18(3):249-255. doi: 10.1590/S0104-14282008000300011

Seo MK, Park SJ (2009) Surface characteristics of carbon fibers modified by direct oxyfluorination. J Colloid Interface Sci 330(1):237-242. doi: 10.1016/j.jcis.2008.10.005

Smith AL (1979) Applied infrared spectroscopy. New York: John Wiley & Sons.

Stegge JM, Urban MW (2001) Stratification processes in thermoplastic olefins monitored by step-scan photoacoustic FT-IR spectroscopy. Polymer 42(12):5479-5484. doi: 10.1016/S0032-3861(00)00852-1

Technical Note - FT-IR spectroscopy, attenuated total reflectance (ATR). 2004. Shelton (CT): PerkinElmer; [accessed 2015 Aug 21]. http://shop.perkinelmer.com/Content/technicalinfo/tch_atraccessories.pdf

Urbaniak-Domagala W (2012) The use of the spectrometric technique FTIR-ATR to examine the polymers surface. In: Farrukh MA, editor. Advanced aspects of spectroscopy. Rijeka: InTech. p. 85-104. doi: 10.5772/48143

Wu S (1971) Calculation of interfacial tension in polymer systems. J Polym Sci Part C Polym Symp 34(1):19-30. doi: 10.1002/polc.5070340105

Xu Z, Chen L, Huang Y, Li J, Wu X, Li X, Jiao Y (2008) Wettability of carbon fibers modified by acrylic acid and interface properties of carbon fiber/epoxy. Eur Polym J 44(2):494-503. doi: 10.1016/j.eurpolymj.2007.11.021

Yang CQ, Simms JR (1995) Comparison of photoacoustic, diffuse reflectance and transmission infrared spectroscopy for the study of carbon fibres. Fuel 74(4):543-548. doi: 10.1016/0016-2361(95)98357-K

doi: 10.5028/jatm.v8i1.559

Finite Element Analysis of Pilot's Helmet Design Using Composite Materials for Military Aircraft

Puran Singh[1], Debashis Pramanik[2], Ran Vijay Singh[2]

ABSTRACT: The objective of this research was to design pilot helmets and to perform analysis of designed ballistic helmet against impact strength of bullet in Solidworks and Laminator software. The material used for construction of the helmet is fiber reinforced polymer matrix composite in which polymer matrix is made of nylon, a thermoset resin, and the fibers are aramid, an aromatic polymide resin developed by E.I. duPont de Nemours and Company and sold under the trademarks "Kevlar®" and "Nomex®". The design of the helmet is done by deciding the stacking sequence of various laminae which are oriented with main material directions at different angles to the global laminate axes in order to produce a structural element in the form of a shell. The simulation of the helmet in Solidworks and Laminator is done with an 8-g AK 47 bullet, hitting it with a velocity of 710 m/s. The model is validated against published data and a good correlation is observed. The result of this project is that a 1.30 kg helmet with shell thickness of 7 mm is obtained, which is economical, light weight and is able to give high-performance protection against ballistic shrapnel and bullets.

KEYWORDS: Finite element analysis, Pilot helmets, Thermoplastic aramid, Composite materials.

INTRODUCTION

The sizing, fit, and comfort have been the most frequent concern of the aviators in each of the different types of aircraft squadrons. Pilot helmet has been used as protective equipment in order to shield human head against serious injuries from shrapnel and bullets. Most modern ballistic helmets are made from a plurality of plies of ballistic material which are laid up in a mold and shaped to the configuration of the helmet. Pilot helmet made of composite materials has become a better equipment compared to traditional steel helmet in terms of the reduction in weight and the improvement in ballistic resistance. Therefore, finite element analysis can be used as a method to characterize the response of composite pilot helmet and to obtain valuable information on parameters affecting impact phenomena (Othman 2009). The first dimension of the helmet is decided according to the average size of human head (Figure 1).

In general, there are two ballistic test standards that are used to determine the quality of protection of the helmet: (1) NIJ-STD-0106.01 Type II and (2) MIL-H-44099A. Nevertheless, different helmet manufacturers may have different ballistic test methods.

Helmet improvement around the head and over the eyes during air combat maneuvers (ACM) or sharp turns in flight involves positive "G" forces in excess of 2 "G". This is attributable to the poor profile of the helmet and its misplaced center of gravity (CG).

The main focus of this research is to study the response of pilot helmet made of composite materials when impacted

1.Amity School of Engineering & Technology – Mechanical & Automation Engineering Department – FEM Laboratory – New Delhi/Delhi – India. **2.**Manav Rachna International University – Faculty of Engineering Technology – Mechanical Engineering Department – Faridabad/Haryana – India.

Author for correspondence: Puran Singh | Amity School of Engineering & Technology – Mechanical & Automation Engineering Department – FEM Laboratory | 580, Najafgarh Kapashera Rd, Dalmia Vihar, Bijwasan | 110061 – New Delhi/Delhi – India | Email: puran.singh910@gmail.com

Received: 10/01/2015 | **Accepted:** 12/07/2015

at high velocity for different sequences of lamina or plies by using finite element analysis. The objectives of this research are:

- To design a pilot helmet that provides high performance protection against ballistic shrapnel and bullets.
- To design a light-weight and economical pilot helmet.
- To analyze deformation as well as stress distribution of the helmet when struck by a bullet at a velocity of 710 m/s.
- To evaluate the failure mechanism occurred on pilot helmet after the impact.

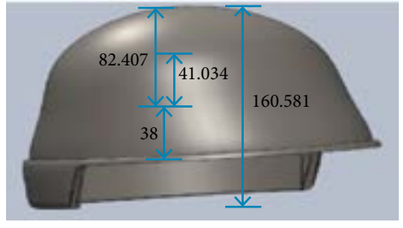

Figure 1. Front view showing dimensions of the helmet.

HELMET DESIGN AND MATERIAL CONSIDERATIONS

Helmet materials and designs have evolved primarily in light of prevailing threats and the invention of new and improved ballistic materials. Figure 2 is a basic summary of U.S. helmet designs and materials since World War I (WWI). For example, the helmet design in WWI was significantly different than in World War II (WWII). WWI was characterized by an unprecedented amount of trench warfare, and the hot and sharp debris falling from relatively high angles were typical. This gave rise to the fairly wide "brim" that gave the WWI helmet its distinctive look.

The combined shells provided higher protection levels over a greater coverage area than the previous M1917 copy of the British Mk I "Brodie" helmet of WWI. The one-size M1 helmet weighed 1.55 kg, had 0.12 m^2 of surface coverage, and protected against the 0.45 caliber round at 244 m/s with a 50% ballistic limit of 396 m/s against the standard North Atlantic Treaty Organization (NATO) 1.1-gram fragment simulator. Thermoplastic aramid matrix systems, one of the most commom materials used, have excellent, mass-efficient ballistic properties. However, the thermoplastic matrix is typically 30 to 60% less rigid than even the toughened thermoset (e.g. phenolic) matrix. This has significant implications for the overall static structural stability and resilience of the thermoplastic aramid shell, as well as the dynamic deflections associated with a ballistic event. To illustrate this phenomenon, consider Fig. 3. A Phantom v.7 high-speed digital camera was used to capture the effects of a simulated ballistic fragment impact on the back side of a flat thermoplastic aramid panel.

This panel had an areal density that was nearly 50% of that recommended for producing a helmet shell. As can be seen in

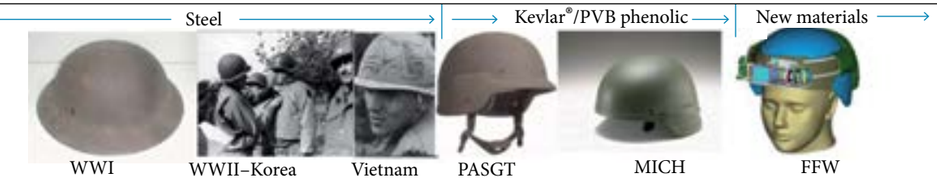

Figure 2. Historical perspective of U.S. Army helmet design and materials (Walsh et al. 2005).

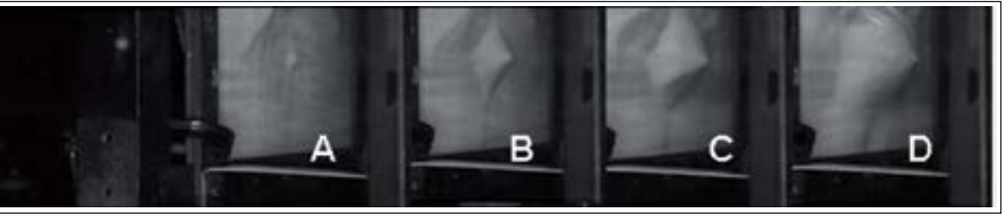

Figure 3. Still photographs from high-speed digital imaging of thermoplastic aramid panel (Walsh et al. 2005).

the sequence of images, the fragment is effectively contained and stopped but not before it induced significant deformation to the overall panel.

A thermoplastic Kevlar® shell at this low areal density may be well-suited for certain applications, but given that the deformation is well over 1 in, it could cause severe skull fracture (and possibly death).

The primary goal of the helmet shell is to protect the pilot from a variety of threats. First, the requirement is to limit the perforation by fragments or bullets through the helmet. Even if the fragment is stopped, the deflection of the shell can engage the skull and cause injury. The current PASGT uses an effective air gap of approximately 13 mm between the inner shell wall and the soldier's head to accommodate any deflection during projectile arrest.

Transient deformation is a direct result of the kinetic energy being dissipated within the ballistic material. Fabrics, although extremely ballistically resilient at real densities around 0.975 g per cm^2, tend to deform significantly. The fragment or bullet could conceivably be arrested by the fabric, but the resulting deformation could still result in a fatal injury by adversely engaging the skull. By contrast, thermoset composites, such as polyvinylbutyral (PVB) phenolic aramid systems, reduce the transient deformation, even though their ballistic performance may be less than that of a pure fabric system. Thermoplastic composite materials offer a compromise of fabric and thermoset composite performance. That is, the thermoplastic tends to deform but not as much as pure fabric, and it tends to have better ballistic resistance than a thermoset-based composite material (Campbell and Cramer 2008).

Practical durability is a necessary trait for any article used in combat. Helmets must also pass static structural tests as well. "Ear-to-ear" loads of 2,000 to 3,500 kPa must be withstood by the helmet for several cycles without any permanent deformation in its structure. Thermoset composites tend to do well, given the higher matrix modulus (as compared to a thermoplastic matrix).

Fully realizing the material and performance benefits of thermoplastic aramids and hybridized solutions will require the rethinking of the manufacturing processes currently in use by most of the U.S. helmet manufacturers. Current processes are configured for mass production of thermoset-based, monolithic Kevlar® helmets. These manufacturing systems typically use expensive, matched steel tools to consolidate the materials. Cold helmet pre-forms are placed in a hot mold and held under pressure until fully cured. Figure 4 is a conceptual schema of such a process.

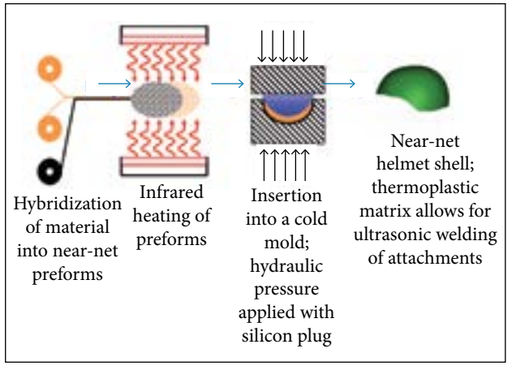

Figure 4. Conceptual schema of the production process of thermoset-based, monolithic Kevlar® helmets (Walsh et al. 2005).

The composite consists of two or more constituents. One is called matrix and the other, reinforcement. The main functions of matrix are:

- It binds the fibers (reinforcement) together and transfers the load to fibers. It provides rigidity and shape to the structure.
- It isolates the fibers so that an individual fiber can act separately. This helps to stop propagation of cracks.
- It provides good surface finish quality and protection to reinforcement fibers against chemical attack and mechanical damage (wear).
- Failure mode of composite is strongly affected by the type of matrix material,and performance characteristics, such as ductility, impact strength etc., are also influenced.

Reinforcement is an important constituent of composite materials. Fiber reinforcement is a thin rod-like structure (Fig. 5). The main functions of fiber reinforcement are:

- It carries the load. In structural composites, 70 to 90% of the load is carried by fiber reinforcements.
- It provides stiffness, strength and thermal stability to the composite.
- It provides electrical conductivity or insulation, depending on the fiber used in the composite.

The general properties of composite materials are light weight, low thermal expansion, high stiffness, high strength and high fatigue resistance.

The matrix in a reinforced plastic may be either thermoset or thermoplastic. In the early days nearly all the thermoset moulding materials were composites in that they contained fillers such as wood flour, mica, cellulose etc. to increase

their strength. However, these were not generally regarded as reinforced materials in the sense that they did not contain fibers. Nowadays the major thermoset resins, used in conjunction with glass fiber reinforcement, are unsaturated polyester resins and, to a lesser extent, epoxy resins (Piggott 1980). The most important advantages which these materials can offer are: (i) they do not liberate volatiles during cross-linking and (ii) they can be moulded using low pressures at room temperature.

A wide variety of thermoplastics have been used as the base for reinforced plastics. These include polypropylene, nylon, styrene-based materials, thermoplastic polyesters, acetyl, polycarbonate, polysulfone etc. The choice of a reinforced thermoplastic depends on a wide range of factors which include the nature of the application, the service environment and costs. In many cases conventional thermoplastic processing techniques can be used to produce moulded articles.

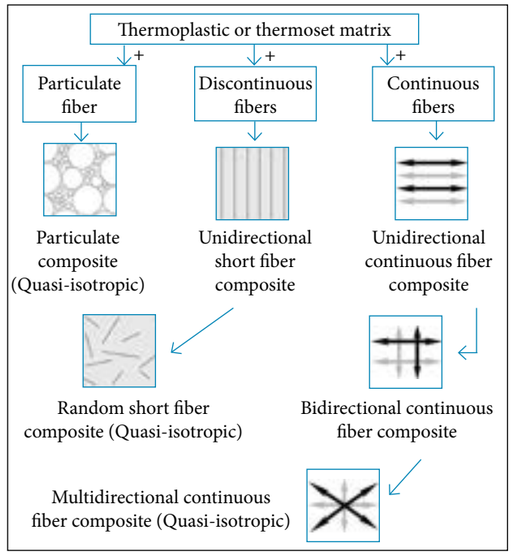

Figure 5. Types of reinforcement.

DESIGN CALCULATIONS AND ANALYSIS

The following assumptions have been taken while designing and analyzing this project:

- It is assumed that the velocity at which the bullet hits the helmet surface is the same as the muzzle velocity.
- It is assumed that the impact time of the bullet on the helmet is 1.5 ms, i.e. the bullet comes to rest 1.5 ms after hitting the surface of the helmet.
- The impact of the bullet on the helmet is assumed to be uniaxial (along *x*-axis).
- For applying the boundary conditions of the helmet during analysis, the bottom part of the helmet is fixed.
- The shape of the bullet is not taken into account while calculating the force of the bullet on the helmet.

The dimensions of the helmet are: width — 180.00 mm, height — 160.58 mm and length — 180.00 mm (Fig. 6).

The composite material chosen is Kevlar® 149/epoxy (fiber/matrix) whose material properties are mentioned in Table 1. Various laminae are prepared out of this composite material,

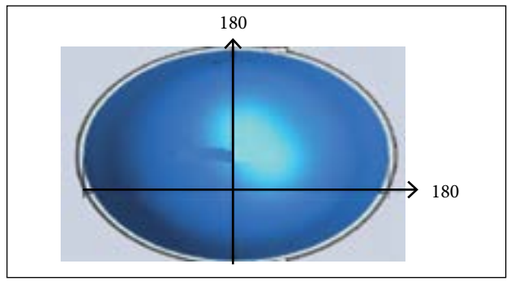

Figure 6. Top view showing the dimensions of the helmet.

Table 1. Properties of Kevlar® 149/epoxy.

Property	Value	Units	Value type
Elastic modulus	1.26e+007	Psi	Constant
Elastic modulus	8e+005	Psi	Constant
Poisson's ratio	0.34	NA	Constant
Shear modulus	3.1e+005	Psi	Constant
Mass density	0.05299	lb/in^3	Constant
Tensile strength	1.85e+005	Psi	Constant
Compressive strength	49,000	Psi	Constant
Yield strength	1.8e+005	Psi	Constant
Thermal expansion coefficient	1.1e–006	F	Constant
Thermal expansion coefficient	3.3e–005	F	Constant
Tensile strength	4,200	Psi	Constant
Compressive strength	22,900	Psi	Constant
Shear strength	7,100	Psi	Constant

and the stacking of various laminae is done, which is oriented with principal material directions at different angles to the global laminate axes producing a structural element in the form of a shell. The strength of this shell is analyzed when a bullet, at a certain velocity, hits it (Silva *et al*. 2005).

The specification of the bullet is as follows: AK 47; caliber: 7.62; mass: 8 g; muzzle velocity: 710 m/s. The force exerted on the helmet is: $m \times a = 8 \times 10^{-3} \times (710/0.0015) = 3{,}786.667$ N. The force with which the bullet hits the helmet is approximately taken as 4,000 N along the *x*-axis.

Here a software called Laminator is used, which takes the abovementioned material properties, load applied (4,000 N) and different angles of each lamina as the input. It calculates the [*A*], [*B*] and [*D*] matrices and the inverse of these matrices, as well as laminate stiffness properties. Each stacking sequence has 24 laminae. The material of each ply is the same and their thickness is taken as 0.21 mm. This process is repeated for several combinations.

STACKING SEQUENCE 1

After applying the load and defining the boundary conditions to the helmet with the given stacking sequence, a simulation was made to run. The following plots in the form of results were obtained and studied to find the optimum configuration.

Stacking sequence 1: [(45)4, (0)4, (90)4] s with each lamina thickness of 0.21 mm. [*A*], [*B*] and [*D*] matrices are:

$$[A] = \begin{bmatrix} 2.910e{+}007 & 6.300e{+}006 & 4.993e{+}006 \\ 6.300e{+}006 & 2.910e{+}007 & 4.993e{+}006 \\ 4.993e{+}006 & 4.993e{+}006 & 6.481e{+}006 \end{bmatrix}$$

$$[B] = \begin{bmatrix} -4.889e{-}009 & -2.328e{-}010 & -2.328e{-}010 \\ -2.328e{-}010 & -9.546e{-}009 & -4.657e{-}010 \\ -2.328e{-}010 & -4.657e{-}010 & -6.985e{-}010 \end{bmatrix}$$

$$[D] = \begin{bmatrix} 6.412e{+}007 & 2.490e{+}007 & 2.231e{+}007 \\ 2.490e{+}007 & 3.594e{+}007 & 2.231e{+}007 \\ 2.231e{+}007 & 2.231e{+}007 & 2.529e{+}007 \end{bmatrix}$$

The inverse of these matrices is:

$$[A]^{-1} = \begin{bmatrix} 3.998e{-}008 & -3.884e{-}009 & -2.780e{-}008 \\ -3.884e{-}009 & 3.998e{-}008 & -2.780e{-}008 \\ -2.780e{-}008 & -2.780e{-}008 & 1.971e{-}007 \end{bmatrix}$$

$$[B]^{-1} = \begin{bmatrix} 4.872e{-}024 & -3.116e{-}024 & -2.562e{-}024 \\ -3.423e{-}024 & 2.372e{-}023 & -1.668e{-}023 \\ -1.750e{-}024 & -1.825e{-}023 & 2.165e{-}023 \end{bmatrix}$$

$$[D]^{-1} = \begin{bmatrix} 2.339e{-}008 & -7.510e{-}009 & -1.401e{-}008 \\ -7.510e{-}009 & 6.394e{-}008 & -4.979e{-}008 \\ -1.401e{-}008 & -4.979e{-}008 & 9.583e{-}008 \end{bmatrix}$$

The laminate stiffness properties are:

Ex: 4.963e+006

Ey: 4.963e+006

Gxy: 1.006e+006

Vxy: 0.097

We have similar stacking sequence for 2, 3, 4, 5, and 6. After applying the load and defining the boundary conditions to the helmet with the given stacking sequence, a simulation was made to run. The following plots in the form of results were obtained and studied to find the optimum configuration.

Firstly, taking the dimensions for the ballistic helmet, three circular sketches were made. By using those circular sketches as a guiding profile and carefully adjusting various parameters, a shell was formed with the help of surface loft feature (Fig. 7a).

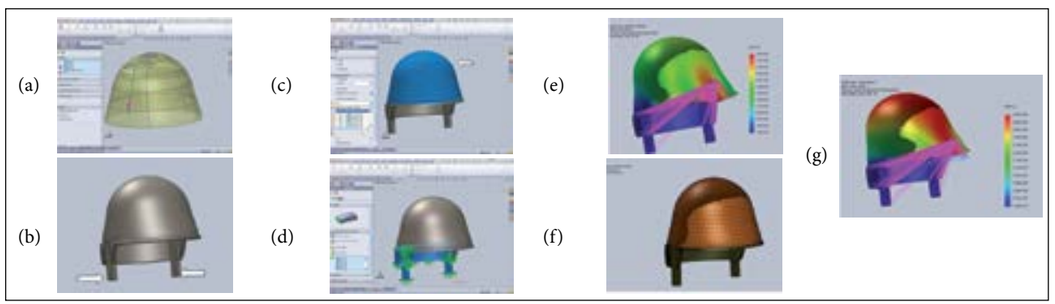

Figure 7. Helmet configuration. (a) Shell forming; (b) Helmet with the support structure; (c) Defining composite layers; (d) Fixed support at the bottom; (e) Application of force; (f) Meshing; (g) Displacement distribution.

For analysis purposes, a support structure was designed to provide the fixture support at the sides of pilot helmet (Fig. 7b). This support works similarly to the straps provided for the support of the helmet in real time.

Linear elastic orthotropic material Kevlar® 149 is defined for all the layers (Fig. 7c). The bottom part of the helmet along with the designed vertical fixtures are fixed and used as boundary conditions for analysis purposes (Fig. 7d). Now, after defining the boundary conditions, the calculated force is applied (Fig. 7e) at the target point taken (where the bullet will hit the helmet). A fine high-quality mesh (with approximate element size equal to 7.9 mm) is generated having parabolic triangular elements with 10,354 nodes and total number of elements equal to 5,058 (Fig. 7f). Results in the form of stress distribution, strain distribution, displacement distribution and factor of safety distribution are obtained and analyzed (Fig. 7g).

ANALYSIS RESULTS

Displacements are measured in meters from the position where the bullet hits the helmet surface before any deformation occurs (Fig. 8a).

Distributions of von Mises stresses are shown in the stress plot obtained after running the simulation (in N/m^2). In this case, a material is said to start yielding when its von Mises stress reaches a critical value known as yield strength. The von Mises stress is used to predict yielding of materials under any loading condition from results of simple uniaxial tensile tests (Fig. 8b).

The plot in Fig. 8c shows the distribution of strain in the top part of pilot helmet when the bullet hits the surface. The plot in Fig. 8d shows the factor of safety at every node. Factor of safety (FoS) is a term describing the structural capacity of a system beyond the applied or actual loads. Tsai-Hill failure criterion is used to evaluate the FoS at the top part of pilot helmet (composite shell). This criterion considers the distortion energy portion of the total strain energy that is stored due to loading. The reaction forces are shown in Table 2. It has proposed that

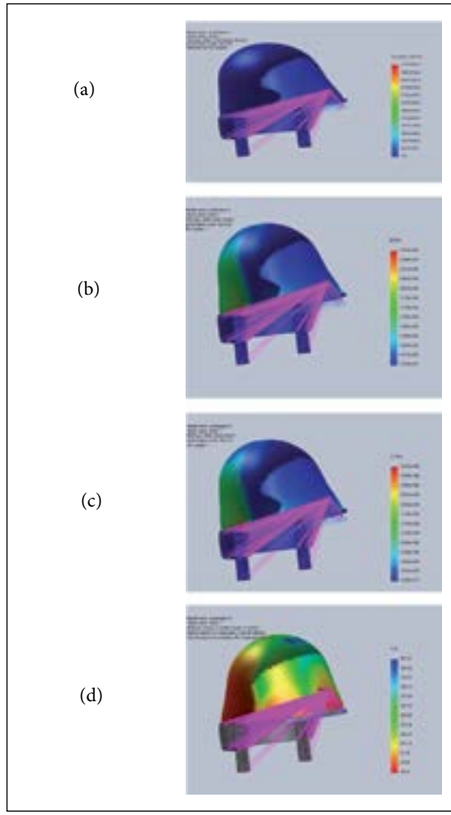

Figure 8. Analysis results. (a) Displacement plot for [(90)4, (0)4, (90)4] s; (b) Stress plot for [(90)4, (0)4, (90)4] s; (c) Strain plot for [(90)4, (0)4, (90)4] s; (d) Factor of safety plot for [(90)4, (0)4, (90)4] s.

Table 2. Reaction forces.

Selection set	Unit	Sum of X	Sum of Y	Sum of Z	Resultant
Entire body	N	−2,403.53	0.100185	−0.00871483	2,403.53
Entire body	N	−2,403.56	−0.0747453	−0.00140771	2,403.56
Entire body	N	−2,403.56	−0.0443136	−0.00578333	2,403.56
Entire body	N	−2,403.49	0.140461	0.0142988	2,403.49
Entire body	N	−2,403.57	−0.00499602	0.000274185	2,403.57
Entire body	N	−2,403.53	0.0195969	−0.00771621	2,403.53

Table 3. Configuration by analysing the results of both Laminator and Solidworks simulations.

Serial number	Sequence	Ex	Ey	Gxy	Vxy	FoS
1	[(45)4, (0)4, (90)4] s	4.963e+006	4.963e+006	1.006e+006	0.097	21
2	[(0)4, (90)2, (0)2, (45)2, (0)2] s	8.857e+006	2.959e+006	7.074e+005	0.152	14
3	[(90)2, (0)2, (45)2, (0)2, (90)2, (0)2] s	6.903e+006	4.934e+006	7.263e+005	0.092	17
4	[(90)2, (0)2, (45)2, (0)2, (90)2, (0)2] s	4.821e+006	1.033e+006	8.338e+005	0.454	6.8
5	[(90)4, (0)4, (90)4] s	4.760e+006	8.715e+006	3.100e+005	0.031	17
6	[(0)2, (45)2, (90)2, (0)2, (45)2, (90)2] s	4.963e+006	4.963e+006	0.097	0.097	20

there should be four helmets to suit flight requirements. After the careful study and comparison of different composite layer combinations in Solidworks and Laminator, the most optimum configuration is shown by stacking sequence 1 — [(45)4, (0)4, (90)4] s, as can be seen in Table 3.

CONCLUSIONS

It has been concluded that the pilot helmet with 24 layers (each layer with 0.21 mm) with total thickness equal to 5.04 mm provides the optimum configuration with the best combination of laminate stiffness properties and FoS (Chawla 1998) under the specified testing conditions (8 g bullet travelling with 710 m/s velocity). The weight of the helmet shell comes out to be 300 g but, in order to give stability and comfort, certain features like foam padding, straps etc. are provided, which increases the weight of the helmet to approximately 1 kg.

The stacking sequence 1 [(45)4, (0)4, (90)4] s, is found as the optimum configuration by analysing the results of both Laminator and Solidworks simulation.

REFERENCES

Othman RB (2009) Finite element analysis of composite ballist helmet subjected to high velocity impact (Master's thesis). Penang: Universiti Sains Malaysia.

Chawla KK (1998) Composite materials: science and engineering. New York: Spinger-Verlag.

Silva MAG, Cismaşiu C, Chiorean CG (2005) Numerical simulation of ballistic impact on composite laminates. Int J Impact Eng 31(3):289-306. doi: 10.1016/j.ijimpeng.2004.01.011

Piggott MR (1980) Load bearing fibre composites. Oxford: Pergamon Press.

Campbell DT, Cramer DR (2008) Hybrid thermoplastic composite ballistic helmet fabrication study. Glenwood Springs: Fiberforge Corporation.

Walsh SM, Scott BR,Spagnoulo DM (2005) The Development of a Hybrid Thermoplastic Ballistic Material With Application to Helmets [accessed 2016 jan 21]. http://www.dtic.mil/dtic/tr/fulltext/u2/a441165.pdf

doi: 10.5028/jatm.v8i1.514

Integration Analysis of Conceptual Design and Stealth-Aerodynamic Characteristics of Combat Aircraft

Cheng Liangliang[1,3], Yue Kuizhi[1,2], Guo Weigang[2], Yu Dazhao[2]

ABSTRACT: In order to study stealth strike-fighter, an analysis on stealth-aerodynamic integration and conceptual design is conducted. A conceptual 3-D digital model with internal antiship missiles and air-to-air missiles is designed in CATIA software. Based on the physical optics and equivalent electromagnetic current methods, using the self-programmed RCSAnsys software, the Radar Cross Section (RCS) characteristics and characteristics of scattering intensity distribution of the model are numerically simulated. Based on the turbulence theory of standard *k-ε* equations, using Fluent software, the pressure, velocity and lift-to-drag characteristics of the conceptual aircraft are numerically simulated. The simulation results show that the stealth and aerodynamic characteristics of the conceptual aircraft can be designed through integration analysis process, which can provide technical support to the design of the advanced operational aircrafts.

KEYWORDS: Conceptual design, Stealth, Strike-fighter, Computational fluid dynamics, Simulation.

INTRODUCTION

Stealth operational aircraft is one of the trends of the development of modern military aircrafts. Depending on the stealth characteristics of the aircraft, the radar detection probability is reduced, aircraft survivability is enhanced and then the operational function is improved. For that reason, stealth operational aircrafts are under vigorous research and development, such as B-2 (Scott 2006), F-22 (Anonymous 2009), F-35 (Starosta 2013), X-45 (Wise and Lavretsky 2011) and X-47 (Zhang *et al.* 2009) of the USA, stealth T-50 of Russia etc.

Stealth aircraft has been studied throughly by researchers at home and abroad in several respects. Many academic results have been achieved in aircraft conceptual design, the Radar Cross Section (RCS) algorithm and stealth-aerodynamic analysis etc. In Deng and Yu (2013), the conceptual configuration parameters of all-wing aircrafts are discussed. In Yue *et al.* (2014a), the influence of symmetrical incline of double-vertical fins on RCS characteristics is studied based on the physical optics method. In Yue *et al.* (2014b), the RCS characteristics of the aircraft are numerically simulated based on the physical optics and equivalent electromagnetic current methods, and the RCS characteristics of the aircraft are analyzed comparatively between when it is armed with external weapons and with internal weapons. In Saha and Majumdar (2012), the aerodynamic characteristics of delta wing are theoretically simulated at 65° leading edge sweepback angle and a subsonic velocity. Kazuhiro (2013) discusses the application of unstructured mesh in Computer Fluid Dynamics (CFD) aviation. In Vallespin *et al.* (2012), the flight dynamic performances of jet trainers and Unmanned Combat Air Vehicle (UCAV) are estimated using CFD method. In Peng and Jinglong (2012), the intercoupling theory of CFD and computational structural dynamics (CSD) is applied to discuss wing flutter problem and analyze the aerodynamic and structural properties of the wings with winglets of cargo planes. He *et al.* (2009) studied the numerical simulation of stealth-aerodynamic integration of flying-wing. Although several respects in the domain have been over-studied by researchers at home and abroad, certain problems still need to studied. No public academic reports on stealth strike-fighters have been obtained, and there is a lack of deep research in stealth-aerodynamic integration of conceptual aircrafts.

Aiming at the issue mentioned above, this article conceptually designs the operational aircraft and analyzes the stealth-aerodynamic characteristics of the aircraft. It is expected that the results of the research will provide reference basis and technical support to the conceptual and stealth design of the aircraft.

1.Beijing University of Aeronautics and Astronautics – School of Aeronautic Science and Engineering – Department of Airborne Vehicle – Beijing – China. **2.**Naval Aeronautical and Astronautical University – Department of Airborne Vehicle Engineering – Laboratory of Aircraft – Yantai – China. **3.**Naval Aviation Institute – Department of Carrier-based Engineering – Laboratory of Aviation Maintenance – Huludao – China.

Author for correspondence: Yue Kuizhi | Beijing University of Aeronautics and Astronautics – School of Aeronautic Science and Engineering – Department of Airborne Vehicle | Beijing 100191 – China | Email: yuekuizhi_2000@sohu.com

Received: 07/10/2015 | **Accepted:** 02/15/2016

CONCEPTUAL DESIGN

The strike-fighter conceptually designed in the article is a kind of operational aircraft with a single seat, double vector engines and normal configuration (Table 1). The layout of the conceptual strike-fighter is as follows: a pair of flaperons, a pair of fore flaps, a pair of moveable strake wings, canted double-vertical stabilators, a pair of differential tailplanes, blended wing body configuration, tricycle landing gears, a internal weapon bay, and four hardpoints under the main wings. The 3-D digital prototype of the conceptual strike-fighter is designed with CATIA software, including digital prototype, a sketch map of the weapon mounting scheme and basic parameters (Fig. 1).

Table 1. Basic parameters of the conceptual strike-fighter.

Parameter	Size
Length	22 m
Height	6.05 m
Span	14.2 m
Leading edge sweepback angle	45°
Trailing edge sweep forward angle	16°
Wingtip chord	1.865 m
Root chord	11.085 m
Canted fin angle	28°
Engine number	2
Airfoil main wing profile	NACA64a204
Airfoil horizontal wing profile	NACA64a202
Airfoil fin profile	NACA64a003

The weapon mounting scheme is shown in Fig. 2 as follows: (a) Scheme 1, the aircraft carries an internal long-range supersonic antiship missile and executes antiship missions; (b) Scheme 2, the aircraft carries 2 × 5 internal mid-range air-to-air missiles and executes air battle missions; (c) Scheme 3, the aircraft carries a mid-range supersonic antiship missile and five mid-range air-to-air missiles as well as executes antiship and air battle missions.

After the conceptual design, the RCS characteristics and aerodynamic characteristics are numerically simulated so that the stealth-aerodynamic performance can be analyzed.

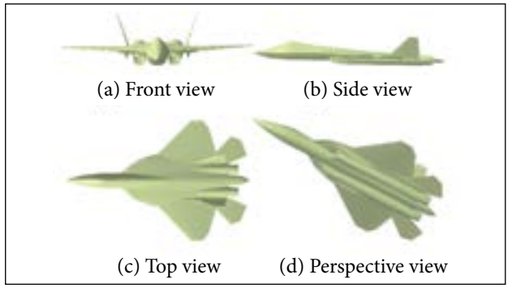

Figure 1. 3-D digital prototype.

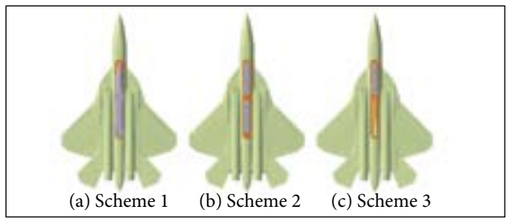

Figure 2. Diagram of the aircraft with missiles.

THEORETICAL BASIS

The theoretical basis of stealth and aerodynamics of combat aircraft includes three parts: the testing algorithm of RCS, the theoretical basis of CFD, and the process of analysis of the stealth-aerodynamic integration.

TESTING ALGORITHM OF RCS

Two respects are usually considered in stealth performance: radar stealth and infrared stealth. The article only analyzes the

RCS characteristics of the aircraft for it is the main characteristic in the stealth domain.

Regardless camouflage paint, when looking at the geometric profile of an aircraft, the testing algorithms for the numerical simulation of RCS characteristics are the physical optics and equivalent electromagnetic current methods. The surface element scattering is calculated by the former method, and the edge diffraction is calculated by the latter (Baussard *et al.* 2011; Rochdi *et al.* 2010).

The equation of the physical optics method is:

$$\sqrt{\sigma_{po}} = -j\frac{k}{\sqrt{\pi}}\int_s \vec{n}\cdot(\vec{e}_r \times \vec{h}_i)\exp[jk\vec{r}\cdot(\vec{i}-\vec{s})]\mathrm{d}S \quad (1)$$

where: $\sqrt{\sigma_{po}}$ (in m²) is the RCS of a single surface element; j is the imaginary unit and $j^2 = -1$; $k = 2\pi/\lambda$ is the free space wave beam, where λ (in m) is the length of incoming radar wave; s is the surface exposed to radar; $\vec{n}$ is the unit normal vector of object surface; $\vec{e}_r$ is the unit vector at the electromagnetic direction of receiving antenna; $\vec{h}_i$ is the unit vector of the direction of the incoming wave field; · is the dot product; × is the cross product; $\vec{r}$ is the vector from local origin to surface unit dS; $\vec{i}$ is the unit vector of the incoming direction; $\vec{s}$ is the unit vector of scattering direction.

The equation of equivalent current method is:

$$\sqrt{\sigma_{ecm}} = \frac{1}{\sqrt{\pi}\sin\theta}\left|(\vec{E}_o^i\cdot\vec{t})f\vec{s}\times(\vec{s}\times\vec{t}) - \right.$$
$$\left. - Z_0(\vec{H}_0^i\cdot\vec{t})g\vec{s}\times\vec{t}\right]\cdot e^{-j2k\vec{r}_t\cdot\vec{s}}\frac{\sin(k\vec{l}\cdot\vec{s})}{k\vec{l}\cdot\vec{s}} \quad (2)$$

where: $\sqrt{\sigma_{ecm}}$ (in m²) is the RCS of a single edge; $\vec{t}$ is the tangential unit vector of the edge; q is the angle between incoming waves $\vec{i}$ and $\vec{t}$; $\vec{E}_o^i$ (in V/m) is the intensity of incoming electric field; f and g are Ufimtsev diffraction coefficients; Z_0 (in Ω) is the impedance of vacuum wave; $\vec{H}_o^i$ (in A/m) is the incoming magnetic field intensity; $\vec{r}_t$ is the middle-position vector of the edge; $\vec{l}$ is the edge vector.

The RCS of the strike-fighter is the total of the RCS of n surface units and m edges. The superposition equation is:

$$\sigma = \left|\sum_{i=1}^{n}(\sqrt{\sigma_{po}})_i + \sum_{j=1}^{m}(\sqrt{\sigma_{ecm}})_j\right|^2 \quad (3)$$

The arithmetic mean value of RCS of the fighter is:

$$\bar{\sigma} = \frac{1}{N}\sum_{i=1}^{N}\sigma_i \quad (4)$$

The RCS unit conversion of the fighter is:

$$\sigma_{dBsm} = 10\lg_{10}\sigma \quad (5)$$

where: σ (in m²) is the RCS of the fighter; $\bar{\sigma}$ is the RCS arithmetic mean; σ_{dBsm} (in dBsm) is the RCS of the fighter.

THEORETICAL BASIS OF CFD

The turbulence numerical simulation theory of the conceptual strike-fighter adopts the standard k-ε equations, which are:

$$\frac{\partial(\rho k)}{\partial t} + \frac{\partial(\rho k u_i)}{\partial x_i} = \frac{\partial}{\partial x_j}\left[(\mu + \frac{\mu_t}{\sigma_k})\frac{\partial k}{\partial x_j}\right] + G_k + G_b - \rho\varepsilon - Y_M + S_k \quad (6)$$

$$\frac{\partial(\rho\varepsilon)}{\partial t} + \frac{\partial(\rho\varepsilon u_i)}{\partial x_i} = \frac{\partial}{\partial x_j}\left[(\mu + \frac{\mu_t}{\sigma_\varepsilon})\frac{\partial\varepsilon}{\partial x_j}\right] + C_{1\varepsilon}\frac{\varepsilon}{k}(G_k + C_{3\varepsilon}G_k) - C_{2\varepsilon}\rho\frac{\varepsilon^2}{k} + S_\varepsilon \quad (7)$$

where: ρ is fluid density; k is the turbulent kinetic energy; t is the time; u_i is the speed per time; μ is the viscosity of fluid power; μ_t is the turbulent viscosity; σ_k is the Prandtl number corresponding to the turbulent kinetic energy k; G_k is the production of turbulent kinetic energy caused by the average velocity gradient; G_b is the production caused by the buoyancy of the turbulent kinetic energy; $\boldsymbol{\varepsilon}$ is the turbulent dissipation rate; Y_M is the contribution to the expansion of pulsation in the turbulence; S_k is the source term defined by users; σ_ε means the Prandtl number corresponding to dissipation rate; $C_{1\varepsilon}$, $C_{2\varepsilon}$ and $C_{3\varepsilon}$ are the empirical constants; S_k is the source term defined by users.

The RANS method is applied to solve the turbulent flow problem.

The standard k-$\boldsymbol{\varepsilon}$ model is applied to turbulence model with high Reynolds number (Re) values while the wall-function method is adopted to solve the model with low Re values.

The wall-function method which contains a set of semi-empirical formulae is used to refine the near-wall region.

$u^+ = 1/k\ln(Ey^+)$ and $y^+ = \Delta y_p(C_\mu^{1/4}k_p^{1/2})/\mu$ are derived, where $y^+ > 11.63$ on the control node near the wall.

$u^+ = y^+$ and $y^+ = \Delta y/\nu\sqrt{\tau_w/\rho}$ are derived, where $y^+ < 11.63$ on the control node near the wall.

where: y^+ is a non-dimensional parameter and $y^+ = \Delta y\rho u_\tau/\mu$; Δy is the distance to the wall; $u_\tau = (\tau_w/p)^{1/2}$ is the wall friction velocity and τ_w is the wall shear stress; u^+ is a non-dimensional parameter and $u^+ = u/u_\tau$; u is the mean velocity of the fluid; E is the energy of the fluid; Δy_p is the distance from node p to the wall; C_μ is an empirical constant and k_p is the kinetic energy of node p.

THE ANALYSIS PROCESS OF THE STEALTH-AERODYNAMIC INTEGRATION

The main steps for analysis of the stealth-aerodynamic integration are as follows. A 3-D model of the aircraft is built in CATIA software; (2) with the self-compiled software named RCSAnsys, the RCS of the model is numerically simulated based on physical optics and equivalent electromagnetic current methods; (3) the CFD numerical simulation of the model is conducted with Fluent software; (4) the performances of stealth-aerodynamic integration of the model will be analyzed comprehensively. The model of the aircraft should be improved or rebuilt until the results meet the demands.

After the theoretical basis is obtained, the analysis and simulation are conducted as follows.

RESULTS AND DISCUSSION

There are two parts in this section: the results and discussion of RCS and the results and discussion of CFD.

RCS

Based on the physical optics and equivalent electromagnetic current methods, it was used the self-programmed RCSAnsys software to make numerical simulation on the RCS characteristics of the 3-D digital prototype.

The RCS numerical simulation method applied in the paper is an approximate method for cavity calculation, and the exact solution for the inlets and nozzles cannot be obtained. The engines that have not been exposed to radar wave directly for the inlets are closed with inclined protective screening. The inlets of the model are also sealed with inclined planes for the calculation of RCS. The nozzles of the model are closed with cones and annuluses for calculation.

The conditions for the simulation in this paper are: two ways of polarization: H-H and V-V polarization; three pitch angles of incoming radar waves: −5°, 0° and +5°; four frequency bands: L, S, C and X. With Eqs. 1 to 5, the RCS of the plane is numerically simulated and the RCS characteristic curves of 24 planes and 8,640 pictures of RCS scattering feature are obtained.

Under H-H polarization and 0° pitch angle, RCS characteristic curves of frequencies equal to 1.5, 3, 6 and 10 Hz are numerically simulated, as shown in Fig. 3. The RCS mean characteristics are simulated and shown in Tables 2–4. The RCS scattering characteristics of various parts of the plane are obtained, as shown in Fig. 4.

On the one hand, the RCS value of the model in specific direction can be as low as −40 dBsm, which is a very low value shown in Fig. 3 and Tables 2–4; on the other hand, the relatively higher RCS value can be obtained in certain forward angle range of the model. The mean RCS value in a range of ± 30° of the forward direction is −5.625 dBsm when exposed to 10-GHz radar wave. In general, it is the same or even exceeds the stealth level of modern fighters in the world.

The distribution of RCS scattering characteristics of the conceptual strike-fighter is shown in Fig. 4: (a) in the

Table 2. Pitch angle of −5 ° and azimuth range of ± 30° — RCS mean value (in dBsm).

Frequency (GHz)	Polarization type	Front	Side	Back
1.5	HH	−4.040	15.220	−1.834
	VV	−3.971	15.214	−1.839
3	HH	−4.657	18.598	−1.679
	VV	−3.971	15.214	−1.839
6	HH	−2.585	16.492	−0.580
	VV	−2.583	16.484	−0.585
10	HH	−4.943	14.611	−0.927
	VV	−4.952	14.604	−0.927

forward direction, RCS intensity distribution is fairly high on the engine in the air inlet, so there should be measures taken in the entrance of the inlet to reduce the intensity on the engine; (b) in both sides, the RCS intensity in the nose, the body, the air inlet and the tail cone is high; (c) in the backward side, the intensity of the engine is high; (d) under 0° pitch angle of the incoming radar wave and 10° azimuth, the intensity in the front edge of the strake wings and canopies is relatively high; (e) under −5° pitch angle of the incoming radar wave and 170° azimuth, the RCS intensity in the jet nozzle of the engine and in the tail is high; (f) under 10° pitch angle of incoming radar wave and 75° azimuth, the intensity in nose, middle body, tail cone, the air inlet and vertical tailsis high and measures should be taken to reduce the intensity.

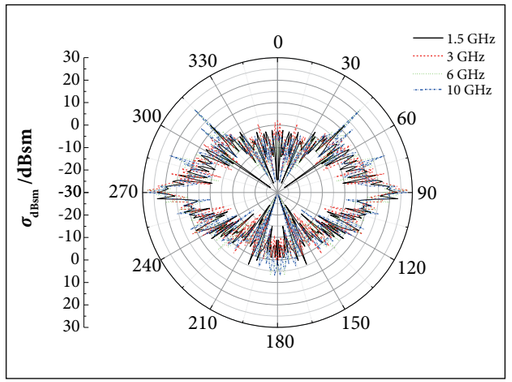

Figure 3. RCS characteristic curves (H-H polarization, pitch angle = 0°).

The numerical simulation of RCS characteristics can be used to calculate the RCS of each component of a plane and understand the RCS scattering characteristics there. It is significant for the further improvement of the forms and structures of the plane and reduction of its RCS intensity.

Next, there is the analysis on the aerodynamic characteristics after the stealth characteristics.

Table 3. Pitch angle of 0° and azimuth range of ± 30° — RCS mean value (in dBsm).

Frequency (GHz)	Polarization type	Front	Side	Back
1.5	HH	−6.056	13.070	−1.374
	VV	−6.197	13.102	−1.496
3	HH	−4.596	15.010	−1.735
	VV	−4.615	15.010	−1.796
6	HH	−7.991	15.248	−0.224
	VV	−8.021	15.238	−0.196
10	HH	−7.982	14.737	−0.140
	VV	−8.003	14.737	−0.133

Table 4. Pitch angle of 5° and azimuth range of ± 30° — RCS mean value (in dBsm).

Frequency (GHz)	Polarization type	Front	Side	Back
1.5	HH	−3.520	8.991	−0.449
	VV	−3.687	8.961	−1.058
3	HH	−5.589	13.885	−0.571
	VV	−5.663	13.859	−0.695
6	HH	−4.922	13.077	0.423
	VV	−4.963	13.098	0.444
10	HH	−5.625	13.542	0.970
	VV	−5.708	13.562	0.951

CFD

It was used ANSYS14.5 software and the Fluent module in the Workbench software so that a CFD analysis was carried out on the conceptual strike-fighter, which mainly includes the following several parts: mesh generation, CFD numerical simulation and lift-drag characteristics analysis.

Mesh Generation

An analysis of the fluid mechanics of the strike-fighter is done. First, the 3-D digital prototype of the plane space is closed. Then we import the Workbench module in the Fluent software. In the Geometry, submodule generates geometric form of the strike-fighter. Then the geometric form is placed on the flow field; then, in the Mesh module, the mesh is generated. The region near the wall is refined with unstructured tetrahedron grid.

The specific processing of the wall function is as follows: the velocity values present a linear distribution along the normal direction of the wall where $y^+ < 11.63$ for the corresponding layer is the viscous sublayer. In this case, $u^+ = y^+$.

The log-law distribution of velocity is observed on normal direction of the wall where $11.63 < y^+ < 300$ for the flow is in log-law layer and $u^+ = 1/\kappa \ln y^+ + B = 1/\kappa \ln(Ey^+)$, where κ is Karman constant, B and E are constants connected with surface roughness and $\kappa = 0.4$, $B = 5.5$ and $E = 9.8$ for smooth surface.

A non-structural mesh of the plane is generated in Mesh module, shown in Fig. 5. The number of grids of the plane in the flow field is 39,686,281.

CFD Numerical Simulation and Lift-Drag Characteristics Analysis

In this section, using Fluent module in Workbench software, the aerodynamic characteristics of the conceptual strike-fighter are numerically simulated. Turbulence numerical simulation theory of the plane uses the standard k-ε equation. As the velocity is 270 m/s and air flow has significant compressibility, the density-based solver is adopted.

Using Fluent software, setting the pressure of the incoming flow at 101,325 Pa, when the coming flow angle is 0°, CFD numerical simulation obtains: pressure distribution on the conceptual strike-fighter surface, as shown in Fig. 6; velocity distribution of flow field of the conceptual strike-fighter, as shown in Fig. 7.

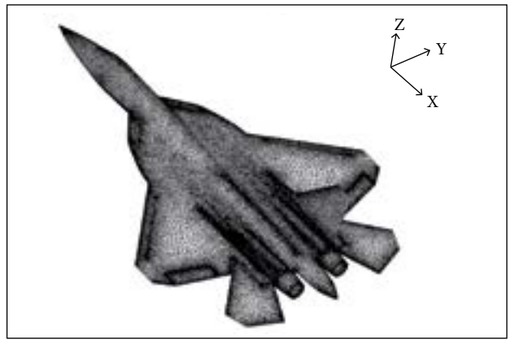

Figure 5. Grids of the conceptual strike-fighter.

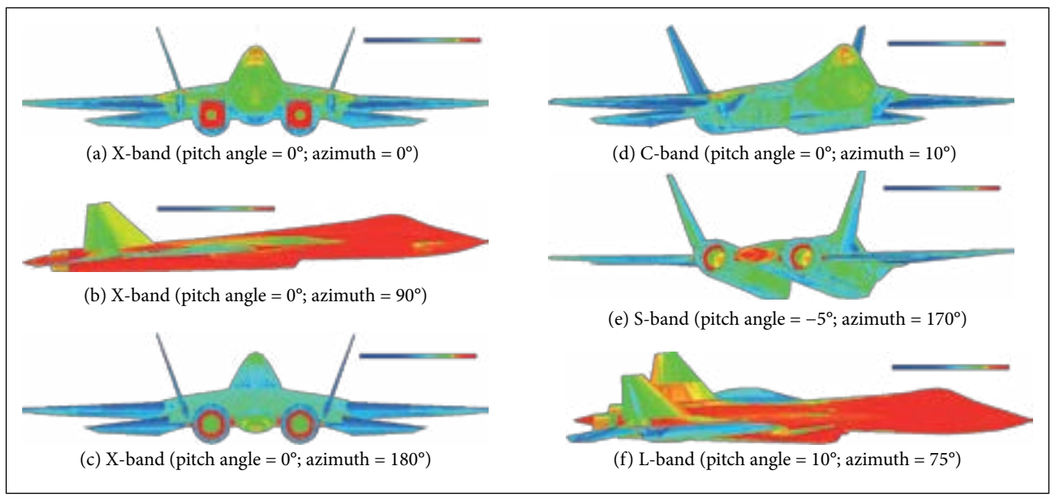

(a) X-band (pitch angle = 0°; azimuth = 0°)

(b) X-band (pitch angle = 0°; azimuth = 90°)

(c) X-band (pitch angle = 0°; azimuth = 180°)

(d) C-band (pitch angle = 0°; azimuth = 10°)

(e) S-band (pitch angle = −5°; azimuth = 170°)

(f) L-band (pitch angle = 10°; azimuth = 75°)

Figure 4. RCS scattering properties of aircraft components.

Figure 6 shows the distribution of pressure on the upper and bottom surfaces of the plane. Figure 6a shows that: the pressure on the upper plane surface is small; the plane nose pressure is strong and radome frontal pressure is greater than 1.2×10^5 Pa; pressure on the aircraft canopy and on the wing leading edge is smaller, and the minimum is 8.679×10^4 Pa; the greatest pressure is on the horizontal tail wing surface, near the 9.714×10^4 Pa; the tail cone rear pressure is strong, where the maximum pressure is about 1.2×10^5 Pa.

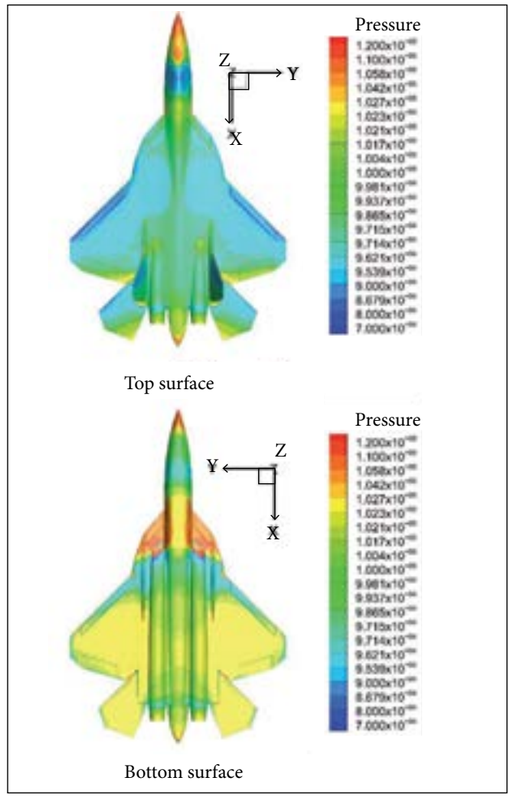

Figure 6. Pressure distribution of the conceptual strike-fighter.

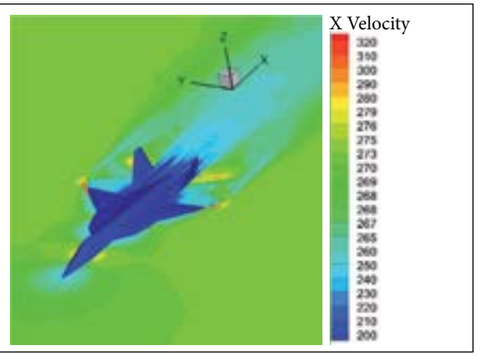

Figure 7. Flow field velocity distribution of the conceptual strike-fighter.

It is known from Fig. 6b that: the bottom surface of the plane is under higher pressure; the pressure on the bottom surface is higher than that on the top surface of the forward part of the plane body, the effect of which provides a lift for the plane; on the fuselage, bottom surface and the top surface have similar pressure. The bottom surface of the middle part contributes with a small part to the lift force; on the backward fuselage, the bottom surface is under stronger pressure than on the top surface, about 1.021×10^5 Pa, and the bottom surface of backward body has a contribution to the lift; the wings, flat tail and moving strake wings are under stronger pressure on the bottom surface than on the top surface pressure, and the lower pressure is about 1.027×10^5 Pa. The wings, flat tail and movable strake wings all contribute to the lift force.

Under the coming flow velocity of 270 m/s and the pitch angle of 0°, in x-y plane, the aircraft and its surrounding air flow field velocity distribution is shown in Fig. 7: in x-y plane, the incoming wave velocity is axisymmetric along x axis; the front of the nose, movable strake wings and main wings have a small flow speed, the minimum of which is less than 200 m/s; air flow is slow behind the rear fuselage and the back of wings, and flow separation phenomenon is observed. Low speed air flow area is longer than the others; on both sides of the nose cockpit and airplane wing tips, the air velocity is larger, and in some parts it is more than 290 m/s.

The distribution of pressure and velocity of the case as well as the lift-drag characteristics of the aircraft are obtained through CFD numerical simulation in Fluent software under the following conditions: the pressure of incoming flow from the distant flow field is 101,325 Pa, the incoming flow velocity is 270 m/s and the pitch angle is in a range of −6° to +15°. The simulation results are shown in Table 5.

A total of eight simulations are conducted in Fluent software with angles of attack at −6°, −3°, 0°, 3°, 6°, 9°, 12° and 15°, respectively, to obtain the lift and drag coefficients and lift-drag ratios. The CFD simulation converges after about 6,000 steps of calculation; then the convergence property of the simulations is verified and the results at different angles of attack are also obtained.

Table 5. Lift-drag characteristics.

Angle of attack (°)	Lift-drag characteristics		
	Lift coefficient	Drag coefficient	Lift-drag ratio
−6	−0.1313	0.0373	−3.5201
−3	0.0239	0.0349	0.6848
0	0.1732	0.0389	4.4524
3	0.3277	0.0485	6.7567
6	0.4976	0.0801	6.2122
9	0.6837	0.1535	4.4540
12	0.8568	0.1969	4.3514
15	1.0866	0.3159	3.4396

A CFD numerical simulation of the aerodynamic characteristics of the plane cannot obtain the distribution of pressure and velocity of the plane as well as analyze the lift-drag characteristics so as to evaluate aerodynamic designs of the conceptual aircraft.

The integrated design and analysis of stealth and aerodynamics are embodied in the process of parametric variation study. The parameters are changing until they meet the design requirements. The satisfied parameters are obtained through iterating in integrated analysis and the process of analysis on stealth-aerodynamic integration is presented in this paper.

CONCLUSION

In the present research, the advanced combat aircraft is conceptually designed, and its stealth-aerodynamic characteristics are analyzed, reaching the following conclusions:

- The design and analysis of the stealth-aerodynamic characteristics of the conceptual aircraft can be based on the analysis process of the integration of stealth aircraft conceptual design and aerodynamic analysis.
- Under V-V polarization, the mean RCS of forward ± 30° part of the plane is $\overline{\sigma}_{dBs}m = -6.1497$ dBsm (frequency band in 1 to 4 GHZ), 8.021 dBsm (4 to 8 GHZ) and 8.003 dBsm (8 to 12 GHZ).
- Pressure and velocity distribution of the strike-fighter in flow field is in good condition. When the pitch angle is 3°, lift coefficient is 0.3277, drag coefficient is 0.0485 and lift-drag ratio is 6.7567.

The analysis method of conceptual design and stealth-aerodynamic characteristics of the combat aircraft can provide theoretical basis and technical support to the conceptual and stealth design of the aircraft.

ACKNOWLEDGEMENTS

This study was supported by the Natural Science Foundation of China (51375490).

REFERENCES

Anonymous (2009) Obama pledges F-22 veto as Senate gears up for aircraft fights. Defense Dail 243(9):57-62.

Baussard A, Rochdi M, Khenchaf A (2011) PO/MEC-based bistatic scattering model for complex objects over a sea surface. Eletromagnetic Waves/Progress In Electromagnetics Research (PIER) 111:229-251.

Deng H, Yu X (2013) Configuration optimization of subsonic blended wing body UAV conceptual design. Acta Aeronautica et Astronautica Sinica. 35(5): 1200 – 1208

He K, Qian W, Chen J (2009) Integrated aircraft design of aerodynamic and stealthy performance with numerically solving fluid dynamics and electro-magnetics equations. Acta Aerodynamica Sinica 27(2):180-185.

Kazuhiro N (2013) Aeronautical CFD in the age of Petaflops-scale computing: from unstructured to Cartesian meshes. Eur J Mech B Fluid 40:75-86. doi: 10.1016/j.euromechflu.2013.02.005

Peng C, Jinglong H (2012) Prediction of flutter characteristics for a transport wing with wingtip devices. Aero Sci Tech 23(1):461-468. doi: 10.1016/j.ast.2011.10.005

Rochdi M, Baussard A, Khenchaf A (2010) PO/MEC-based bistatic scattering model for complex objects over a sea surface. Proceedings of the 2010 IEEE Radar Conference; Washington, USA.

Saha S, Majumdar B (2012) Flow visualization and CFD simulation on 65° delta wing at subsonic condition. Procedia Eng 38:3086-3096. doi: 10.1016/j.proeng.2012.06.359

Scott WB (2006) B-2 program lore. Aviation Week and Space Technology 164(13):60-61.

Starosta G (2013) The F-35 readies for takeoff. Air Force Mag 96(4):38-42.

Vallespin D, Badcock KJ, Da Ronch A, White MD, Perfect P, Ghoreyshi M (2012) Computational fluid dynamics framework for aerodynamic model assessment. Progr Aero Sci 52:2-18.

Wise KA, Lavretsky E (2011) Robust and adaptive control of X-45A J-UCAS: a design trade study. Proceedings of the 18th IFAC World Congress; Milano (Italy).

Yue K, Sun C, Ji J (2014a) Numerical simulation on the stealth characteristics of twin-vertical-tails for fighter. Journal of Beijing University of Aeronautics and Astronautics 40(2):160-165.

Yue K, Sun C, Liu H (2014b) Numerical simulation on the RCS of combat aircraft for mounted missile. J Syst Eng Electron 36(1): 62-67.

Zhang H, Tan H, Li X (2009) Flow structure and performance characteristics of X-47-like slot-shaped inlet. Acta Aeronautica et Astronautica Sinica 30(12):2243-2249.

doi: 10.5028/jatm.v8i1.575

Reinforced Transparencies for Aerospace Application – Case Description

Melis De Bruyn Neto[1], Rita de Cássia Mendonça Sales[1,2], Koshun Iha[1], José Atílio Fritz Fidel Rocco[1]

ABSTRACT: This paper describes the polycarbonate acrylic laminated development that can be applied in aeronautics and aerospace transparencies. The case studied is a laminated double-curved transparency (bubble form) used in an observation side window of a military aircraft. Side windows need strength and specific characteristics, similar to windshields, allowing the perfect visualization and image capture. Laminated transparencies composed by different materials have better qualities than the monolithic ones. This kind of transparency can offer high mechanical and chemical resistance, high transparency, no fragmentation and easy maintenance or recovery. A significant amount of information about materials and processes was jointed in order to build the reinforced transparency and validate this study. The final results were analyzed based on two points of view: mechanic resistance and, especially, optical quality.

KEYWORDS: Transparency, Laminated polycarbonate, Acrylic, Window.

INTRODUCTION

Whenever it is necessary to see or capture images through a protective barrier, it arises the need to define it and build it as effectively and efficiently as possible. The problem that comes from this observation is to measure all the variables that can influence the requirements and, mostly important, to define the materials that can be used, as well as the methods and processes that will lead to the manufacture of a quality product. The materials chosen, suitable for the construction of reinforced transparencies for aerospace industry, as windshields, must to be taken into account, as well as all loads they are subjected to, including structural terms, mechanical and thermal loads (Fam and Rizkalla 2006). In addition, superior optical characteristics are also essential (Fixler 1977).

The modern engineering and architecture "design" requires glazing materials that offer high levels of safety and high-performance mechanical properties. These properties include: ballistic resistance; wind loads; explosion; and physical attacks resistance. In some applications, noise level reduction, solar radiation resistance, and thermal barrier behavior are also desirable. The laminated glazing is the union of multiple layers of various materials such as glass, polymeric films, resins, and flexible sheets of transparent polymers (polycarbonate and/or acrylic), usually applied to obtain complex geometric shapes (Fixler 1977; Smith *et al.* 1996).

It is necessary a prior knowledge of the physicochemical properties of the engineering materials to make the right choice for each application. To the right choice, it is necessary to know the load or the effort to which the transparency must resist and the kind of effort that will be neutralized by the transparent barrier. However, it should be clear that there will always be an effort

1.Departamento de Ciência e Tecnologia Aeroespacial – Instituto Tecnológico de Aeronáutica – Divisão de Ciências Fundamentais – São José dos Campos/SP – Brazil.
2.Centro Estadual de Educação Tecnológica Paula Souza – Faculdade de Tecnologia de São José dos Campos - Prof. Jessen Vidal – São José dos Campos/SP – Brazil.
Author for correspondence: Rita de Cássia Mendonça Sales | Centro Estadual de Educação Tecnológica Paula Souza – Faculdade de Tecnologia de São José dos Campos - Prof. Jessen Vidal | Avenida Cesare Mansueto Giulio Lattes, 1.350 – Eugênio de Melo | CEP: 12.247-014 – São José dos Campos/SP – Brazil | Email: rita.sales@fatec.sp.gov.br
Received: 11/19/2015 | **Accepted:** 02/04/2016

that can overcome the barrier, because there is no definitive mechanical barrier. Thus, the barrier will be "strengthened" until reaching the desired resistance and including a safety factor.

Besides the mechanical strength, transparent barriers must have optical quality, being able to see or capture images by means of high light transmission level, with a minimum deviation or absorption, until the images reach the observer's eye or the image capture device.

Reinforced transparencies are not only intended to prevent a mechanical failure, but to perform with maximum efficiency and preferably not releasing fragments that reach whom or what will be protected by the transparent barrier. The objective of this study was to describe the information needed to design and to construct a reinforced transparency for aerospace application made with polymeric materials, which is part of the "observation window" of a military patrol aircraft.

MATERIALS AND METHODS

MATERIALS CHOICE

The materials chosen for the observation window were based on MIL-PRF-5425E (1998) and MIL-P-46144C (1986). The chosen structural materials, in sheet form, were: acrylic or polymethylmethacrylate – PMMA (ASTM D4802-02) (Modified "cast" acrylic ACRYLITE® 249, CYRO Ind, USA); polycarbonate – PC (Fox and Christopher 1962; LeGrant and Bendler 2000) (LEXAN® 9034, GE-Plastics, USA); and, for bonding, in film form, polyurethane – PU (KRYSTALFLEX®PE399, Huntsman, USA), which is the material that allows a good adhesion between acrylic and polycarbonate.

The following sequence was used to prepare the specimens: two outer layers with 3.18 mm thickness of acrylic (PMMA); a central PC layer with 6.35 mm thickness; and between acrylic and PC layers, two aliphatic PU layers with 1.27 mm thickness were inserted. In other words, the final composition was: PMMA + PU + PC + PU + PMMA (Fig. 1).

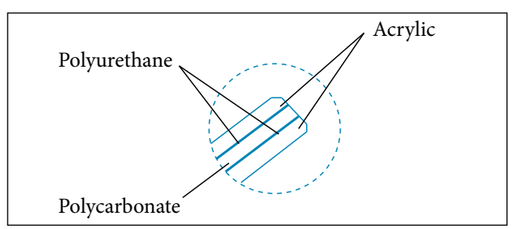

Figure 1. Materials sequence in specimens section.

TEMPERATURE RESISTANCE TEST

Two samples with nominal size (20 × 10 cm) were prepared and laminated in the same way of the shearing test samples. The samples were submitted to 100 °C for 50 min, using a circulating air oven (Kamp).

SPECIMENS PREPARATION

All the raw material plates were cut into dimensions much larger than the finished parts, using a circular saw. After this process, the plates were dehumidified at 100 °C, during 6 h in an air circulating oven.

The dehumidified materials were laminated in the sequence previously defined. A vacuum bag was prepared around the laminated (all the bagging materials are from Airtech®, USA; vacuum film and sealant tape). The set, formed by the laminate and the vacuum bag, was placed in an autoclave (FERLEX®, Brazil) to be bonded. To ensure the bonding material, the set formed by the laminate and the vacuum bag was heat-treated to 120 °C for 2 h at a 2 °C/min heating rate and pressured at 0.7 MPa inside the autoclave. The temperature and pressure were maintained during 3 h; then, it was cooled until the ambient temperature was reached. At the end, the pressure was released and the cycle, finished.

THERMOFORMING PROCESS

After autoclave process, the set was placed on a tool designed for the observation window manufacture. The tooling (Fig. 2) was heated to 180 °C at a 6 °C/min heating rate. After the laminate reached the melting point, it was blown at a pressure of 0.14 MPa to achieve its definitive new shape. The specimen was then cooled at 2 °C/min.

The part trimming was performed in a conventional manner using bandsaw and sander. The polishing was done using fine finishing hand tools and then through sandpapers and finer abrasives, until it reached the desired polishing. The specimen, properly polished, was placed against a reticule grid to check possible optical distortions.

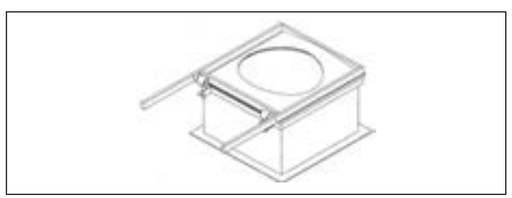

Figure 2. Thermoforming tool.

SHEARING TESTS IN PLANE

Six samples with nominal size (4.0 × 5.0 cm; section area: 20 cm²) were prepared using the following materials: an acrylic sheet, with 3.18 mm thickness, adhered to a PC sheet, with 6.35 mm thickness. For the sheets adhesion, it was used an aliphatic PU crystal adhesive film with 1.27 mm thickness.

The samples were laminated in the same way of the observation window. They were tested after 48 h of stabilization. The shearing test was performed in plane (Fig. 3) using MIL-P-25690B (1995) as general references. It was used an electromechanical testing machine for tension and compression Tinus Olsen brand, model H100KS, with maximum capacity of 100 kN. The test speeds were 3 and 5 mm/min.

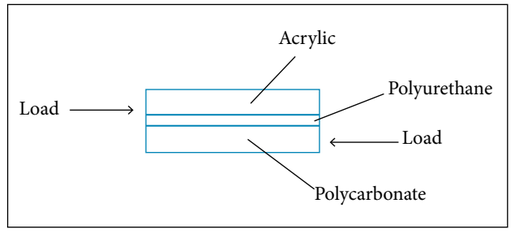

Figure 3. Schematic diagram of load applied in samples during the shearing tests in plane.

Table 1. Acrylic and polycarbonate mechanical properties.

Material	Modified "Cast" Acrylic	Polycarbonate
Standard	MIL-PRF-5425E 1998	MIL-P-46144C 1986
Commercial type	ACRYLITE® 249	LEXAN® 9034
Provider	CYRO Ind, USA	GE-Plastics, USA
Poisson's ratio	0.35	0.37
Tensile strength	80.3 MPa	65.5 MPa
Maximum elongation	4.4 %	110.0 %
Tensile Modulus	2.76 GPa	2.39 GPa
Compressive strength	124.1 MPa	86.18 MPa
Flexural strength	113.76 MPa	93.08 MPa
Shear strength (ultimate)	62.05 MPa	68.95 MPa
Izod impact (notched)	21.35	640.5 – 854

RESULTS AND DISCUSSION

MATERIALS CHOICE

Nowadays, most of civil and military aircraft windows are made with acrylic (PMMA) due to its transparency, availability, strength and ease maintenance, fulfilling all the aviation requirements and standards (Blass 1985; LaPluma and Bridenbaugh 1988). This material also meets the requirements for external surfaces of reinforced transparency. However, in case of violent impact, it can shatter, causing sudden aircraft depressurization. To satisfy the high impact strength requirement, the best polymer is PC, already used in military fighter aircraft canopies (Wiser 1971). Both materials have high light transmission levels and they are thermoformable. To connect these two materials, the aliphatic PU films (Plepis 1991; Vilar 1991) can be used, providing the adhesion between layers. Table 1 shows the properties of the chosen materials for the manufacture of aircraft observation window.

After materials selection, it was carried out a temperature resistance test to verify the laminate behavior at 100 °C. There was no appearance of undesirable bubbles, yellowing, delamination or any other conduct that could compromise the functions of the laminate or its general appearance. It was also verified that the temperature would not compromise the good light transmission without distortion or deformation.

SHAPE DETERMINATION

The final shape of the transparency is better defined by the obtaining process than by a geometry defined through engineering software (Fig. 4). The method used to obtain the transparency form was the thermoforming by blowing compressed air (Blass 1985), since it allows the material to expand freely until the desired format is obtained.

The expansion process by free blowing determines the shape and cooperates with the optical quality, avoiding deformities, and it does not cause undesirable distortions in contact with the tool — they are visible only at the edges of transparency. The result by thermoforming is an elliptical paraboloid shape (Fig. 5), caused by laminated thinning (more in the center than in the edges), because of area increasing and thickness loss.

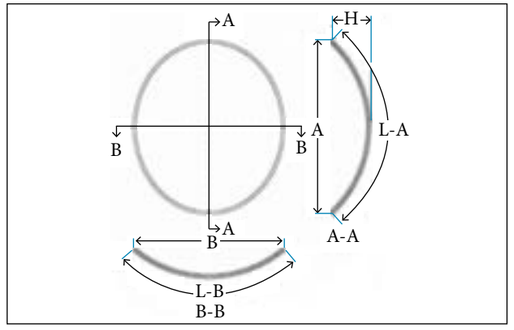

Figure 4. Orthogonal views and transparency section. A-A: Height; B-B: Width; L-A: Vertical vision angle; L-B: Horizontal vision angle; H: Depth.

Figure 5. Laminated after thermoforming made with an appropriate tool.

OPTICAL DISTORTIONS

Samples submitted for verification did not have relevant distortions, detected by the human eye, which could compromise the good appearance of the grid images captured through the transparence (Fig. 6). However, it was detected the presence of a slight optical power due to thickness variation at the center of the part, resulting from thinning, occurred during the thermoforming process, which creates a kind of diverging lenses. The contact with the thermoforming tool produces contact marks that are manifested in the form of distortion of the edge part; however, these distortions do not affect the results, when transparency is in use, since it does not become apparent because this region is covered by the transparency frame.

The optical distortions verification (Fixler 1977) is an important parameter in reinforced transparencies (Pardini and Peres 1996). The reinforced transparency, besides being considered a barrier to prevent an effort to continue, should allow observing or capturing images through it with the best possible quality, not adding deviations image distortions, retain the light wavelength or filter visible spectrum.

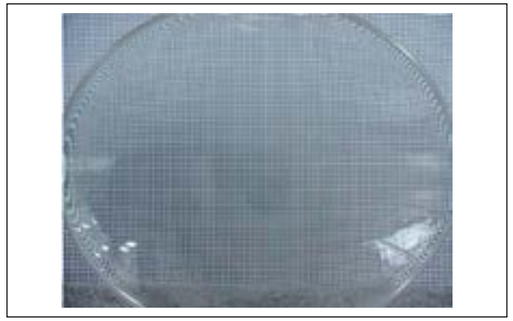

Figure 6. Transparency view without distortions in the central area.

All the images captured during the transparencies flight test had an excellent clarity and no visible distortions, which confirmed the prior results obtained with the grid.

SHEARING RESULTS IN PLANE

Aircraft side windows have a significant temperature differential between inner and outer layer, as much higher as the aircraft flying altitude. The internal temperature is usually around 20 °C, and the outer temperature can be less than −54 °C, so the dimensional variation between layers produces high big shear forces that must be compensated by the polyurethane layer elasticity. In this case, the PU adhesion between acrylic and/or polycarbonate must be verified. The shear test indicates the degree of adhesion acquired by the laminated.

Each trial lasted until a little over 2 min, since the total displacement was around 6 mm. Tables 2 and 3 contain the results obtained in the shear test.

The test speed of 3 mm/min was appropriate, according to the behavior observed, which does not present a premature rupture and produces a clear "load × deflection" curve. The standard deviation in general demonstrates a short range of values, or more reliability in the results obtained. The test speed of 5 mm/min does not produce results with small variation, since the values obtained were two or three times higher than the values obtained with test speed of 3 mm/min.

The maximum shear stress average demonstrates a satisfactory adhesion degree between layers in both speed tests and was greater than the expected.

A more detailed analysis of the displacement data between the sheets of acrylic and polycarbonate may provide an order of magnitude for the lengthening ability of the polyurethane adhesive, but the PU manufacturer (Huntsman, USA) indicates

Table 2. Results obtained in the shear test at the speed of 3 mm/min.

Sample	Maximum load (kgf)	Breaking load (kgf)	Displacement (mm)	Shear stress (kgf/cm²)
S1	1,010.2	982.7	6.2	49.1
S3	1,034.3	967.7	6.4	48.4
S5	972.8	896.7	6.3	44.8
Average	1,005.8	949.0	6.3	47.5
Standard deviation	31.0	45.9	0.1	2.3

Table 3. Results obtained in the shear test at the speed of 5 mm/min.

Sample	Maximum load (kgf)	Breaking load (kgf)	Displacement (mm)	Shear stress (kgf/cm²)
S2	1,059.2	1,027.5	6.2	51.4
S4	881.4	793.3	5.8	39.7
S6	951.1	913.7	5.7	45.7
Average	963.9	911.5	5.9	45.6
Standard deviation	89.6	117.1	0.3	5.9

500% of elongation at the KRYSTALFLEX® PE399 datasheet (Huntsman 2015).

All samples tested were broken or showed detachment from plastic layers. The S2 had supported the major load, and S4, the minor one. Figure 7 shows a typical curve of "load × deflection" generated by S2 test.

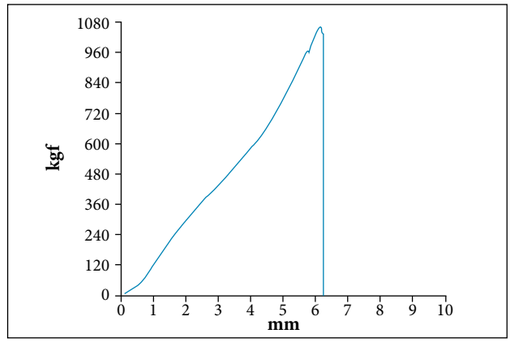

Figure 7. Curve "load × deflection" of the S2.

CONCLUSIONS

The objective was achieved by implementing the proposed road map, which was to organize some of the information needed to design and to construct a reinforced transparency for an aerospace application, which is part of the "observation window" of a military patrol aircraft, as well as to validate such information through the construction of the transparency and analysis of the results.

The combination of the techniques used and the layers union in an appropriate and sequential manner was essential for the construction of transparency, which was successfully completed. Any failure would not allow the following step.

The optical results allow to state that the material choices were appropriate, especially on the composition and position of them. The acrylic usage on the internal and external faces of transparency had ensured the necessary optical quality. The fabrication process chosen, by the free expanding thermoforming, guaranteed a regular format of the visible area because there were no contacts with any tool.

All samples presented a satisfactory adhesion degree between layers during the shearing tests in plane. The parameters of speed test were greater than the expected, but this did not affect the results; the samples showed mechanical resistance parameters required by the aeronautical industry. Therefore, it was possible to demonstrate the technological knowledge necessary for the development and manufacture of reinforced aerospace transparencies for this type of application.

REFERENCES

Blass A (1985) Processamento de polímeros. Florianópolis: UFSC.

Fam A, Rizkalla S (2006) Structural performance of laminated and unlaminated tempered glass under monotonic transverse loading. Construct Build Mater 20(9):761-768. doi: 10.1016/j.conbuildmat.2005.01.051

Fixler SZ (1977) Thermsstructural and material considerations in the design of the F-14 Aircraft Transparencies. J Aircraft, 14(3):257-264.

Fox DW, Christopher WF (1962) Polycarbonates. New York: Reinhold Publishing Corporation.

Huntsman (2015) KRYSTALFLEX® PE399 data sheet on line. [accessed 2015 Oct 15]. http://www.huntsman.com/polyurethanes

LaPluma PT, Bridenbaugh JC (1988) Specifications and measurement procedures for aircraft transparencies. Wright-Patterson AFB, OH: Armstrong Aerospace Medical Research Laboratory.

LeGrant DG, Bendler JT (2000) Handbook of polycarbonate science and technology. New York: Marcel Dekker.

Pardini LC, Peres RJC (1996) Tecnologia de fabricação de pré-impregnados para compósitos estruturais utilizados na indústria aeronáutica. Polímeros 6(2):32-42.

Plepis AMD (1991) Caracterização térmica e viscoelástica de resinas poliuretanas derivadas do óleo de mamona (Master's thesis). São Paulo: Universidade de São Paulo.

Smith FC, Moloney LD, Matthews FL, Hodges J (1996) Fabrication of woven carbon fibre/polycarbonate repair patches. Compos Appl Sci Manuf 27(11):1089-1095. doi: 10.1016/1359-835X(96)00070-X

Vilar WD (1991) Química e tecnologia dos poliuretanos. 2nd ed. Rio de Janeiro: Vilar Consultoria Técnica Ltda.

Wiser GL (1971) Transparency applications of polycarbonates. Aircraft Eng 43(8):18-20. doi: 10.1108/eb034797

doi: 10.5028/jatm.v8i1.529

Functional Characteristics Improvement of Metal Transformable-Volume Structures for Space Applications

Leonid M. Lobanov[1], Valentin S. Volkov[1], Alexander V. Yakimkin[1], Viktor V. Savitsky[1]

ABSTRACT: Under conditions of the influence of space environment factors, the thin-walled load-carrying transformable-volume structures are subjected to volumetric deformation and long-time exposure to external loads, close to maximum permissible design values. The required functional properties of transformable-volume structures are ensured on the basis of applying surface engineering methods, whose effectiveness is difficult to confirm as there is no possibility to reproduce the space environment factors complex under the terrestrial conditions. The method for verification of applied technologies regarding the modification of surface properties was described. It was based on the comparison of finite-element and experimental-computational models of displacements in equivalent fragments of the transformable-volume structures surface. Qualitative and quantitative evaluation of methods is given, allowing changing the rigidity-strength characteristics of transformable-volume structures for space applications without alteration of their mass and compactness.

KEYWORDS: Transformable-volume structures, Surface engineering, Non-destructive testing, Electron shearography, Load-carrying shells, Foldable shells.

INTRODUCTION

Deployable structures refer to the actively developing field of space technologies, which allow simplifying the delivery of useful freight to the near-Earth orbit. In the majority of cases the deployable or inflatable space structures represent shells made of elastic soft materials, capable of withstanding multiple non-fracturing bends. Therefore, the main attention of developers of these types of structures is focused on the provision of shell rigidity and its stability after deployment by using different methods of strengthening, which have limited effectiveness (Pellegrino 2015; Underwood *et al.* 2015; Schenk *et al.* 2014).

A separate class of deployable structures are transformable-volume structures (TVS) with a metal shell (Fig. 1c), in which the use of geometric regularities of surface bending allows realizing the volumetric deforming, comparable with the bends of soft materials (Paton *et al.* 2015). One of the applications of such structures is their use as a sliding bearing rod rigidly fixed at one of its ends on the outer surface of the base spacecraft (e.g. the International Space Station — ISS). In the working state after unfolding the metal TVS has higher spatial rigidity compared with the initial metal shell before its transformation to a compact state. In creation of similar structures the main objects for research are the methods of surface engineering, whose application allows providing the required functional properties of the transformable shell with minimum weight and maximum compactness under condition of aggressive space environment factors (SEF) action. Finally, it is necessary to solve the problem of correctness of calculated evaluations at the stage of laboratory and check tests. This problem is predetermined by

1.National Academy of Sciences of Ukraine – The E. O. Paton Electric Welding Institute – Kiev – Ukraine.

Author for correspondence: Valentin S. Volkov | National Academy of Sciences of Ukraine – The E. O. Paton Electric Welding Institute | 11, Bozhenko str. | 03680 – Kiev – Ukraine | Email: valentinvolkov@ukr.net

Received: 08/08/2015 | **Accepted:** 11/26/2015

the impossibility of reproduction of all SEF spectrums, under the Earth conditions, and also by complexity and high cost of experiments for their simulation.

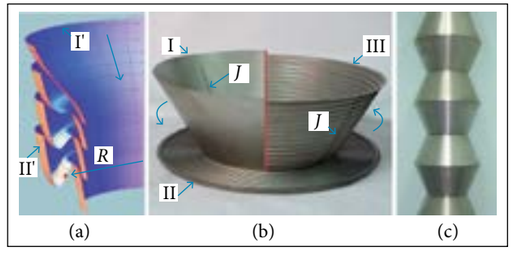

Figure 1. Graphic representation of the mathematical model for: (a) Fragment transformation of the initial conical shell (I') into a single corrugation (II'); (b) The transformation stages of the metal TVS shell; (c) Design solution for multi-conical TVS. J represents the welded joints of the shells.

METHODOLOGY

The strength and spatial rigidities are referred to the main functional characteristics of TVS, subjected to improvement. They guarantee the mechanical integrity of the transformable shell, its minimum deformability and absence of a local buckling at any combinations of external and operational loads, as well as stability, speed of unfolding and its sequence. The mentioned characteristics depend not only on a general geometric configuration of TVS, properties and thickness of the structural material, type of joining stiffening elements between separate sections, but also on local features of surface geometry (type of surface folding) and on others, first of all, thermal optical properties of the surface.

Selection of design parameters and the task of improvement in the functional characteristics of TVS are reduced to the search for the best combination of strength and rigidity characteristics of the shell and its compactness at minimum possible weight. The thin metal shell of TVS should preserve the mechanical integrity and functional properties under the effect of mechanical loading factors, acting in the process of orbital injection (impact-pulsed loading and acoustic noise) and in the process of operation under space environment conditions. In particular, in case of rigid fixation at the external surface of the ISS, the structure can be subjected to the action of sinusoidal (harmonic) vibration in the range of frequencies from 5 up to 20 Hz and wide-band random vibration in the range of frequencies from 20 up to 2,000 Hz, linear and angular inertial loads. It is also subjected to cyclic temperature influence in solar terminator transition with a maximum admissible temperature difference from –150 up to +125 °C. The decrease in a given range provides the decrease in temperature gradients in the shell structure at cyclic heating and, consequently, leads to the decrease in deformations, in which the maximum values are almost always regulated for definite conditions of service and application of TVS. In addition, the working temperatures of optical surfaces also predetermine other parameters, whose range is limited by the requirements of structures for space applications — for example, the rate of precipitation of volatile condensing substances and duration of a possible contact of an operator in a space suit during the work beyond the ISS (for conical TVS it is more than 5s at temperatures from –43 up to +63 °C). The combination of the above-mentioned requirements allows selecting in most cases stainless steel as the optimum material for a TVS shell, providing also the lower deformability of structure under service conditions due to the value of Young's modulus, which is 1.5/2.0 times higher than that of titanium and aluminium.

The use of a complex approach to the surface engineering allows providing the optimum combination of factors which, to a larger extent, determine the strength and stability of the structure under the SEF effect at the best mass-dimensional characteristics. The design configuration of multisectional conical TVS, which is given by the authors as a main example, is defined by their definite functional application and can vary by changing the geometric sizes of separate sections and thickness of their structural material. On the other hand, the compactness, or coefficient of transformation K_T, is related to geometric parameters of conical sections of given thin-walled TVS with a stainless steel shell by the dependence:

$$K_T = 2 \times n = \frac{S \times \sin\alpha}{14 \times \delta} \qquad (1)$$

where: n is the number of folds (circumferential corrugations) in the shell transformed into a flat disc (Fig. 1b, II); S is the slant height of initial cone (Fig. 1b, I); α is the angle of conicity of initial cone; δ is the thickness of structural material of the TVS shell.

The tendency to maximum values of K_T, attainable at δ → min, at unchanged preset design configuration of TVS, requires the correction of flat disks manufacture technology and, finally, the decrease in radius of bending in apexes of

circumferential corrugations. The volume deforming of the initial steel shell with the formation of surface folds allows changing its space rigidity after deployment (Fig. 1b, III) at δ = constant and at different variants of meridian profile (Fig. 1a). In our case, not only the operation of shape formation is achieved by plastic deformations of the steel shell, but also the required complex of properties of the structural material is attained.

Further, the application of surface engineering methods applied to metal TVS is of current importance for changing their thermal optical properties. The temperature of TVS surface (T_S), whose material has a high coefficient of thermal expansion, defines mainly its deformation mode. The value T_S under other equal conditions is determined only by the A_S/ε ratio, where A_S is the coefficient of solar radiation absorption and **ε** is the emissivity coefficient of TVS optical surface. The possibility to influence this ratio allows changing within wide ranges the structure deformability under conditions of the orbital flight.

Figure 2 illustrates the dependence of minimum (T_{Smin}) and maximum (T_{Smax}) calculated values of temperatures on the TVS surface of a conical type (material: steel AISI 321) on the A_S/ε ratio in service of the structure in random working point of the ISS's external surface. The selected zone (T_{Sopt}) limits the selected optimum range of temperatures (–43 to +63 °C), corresponding to the ratio A_S/ε = 0.26/0.54.

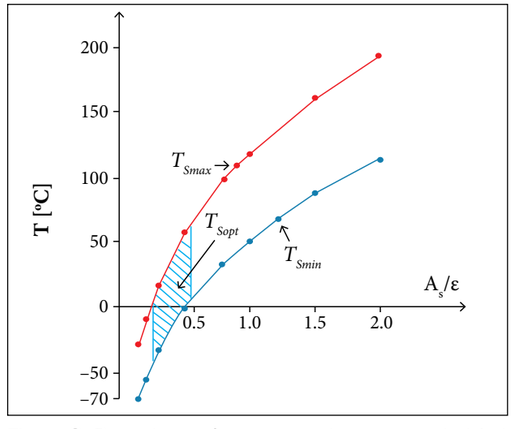

Figure 2. Dependence of minimum and maximum calculated temperature values on the surface of conical-type TVS on the A_S/ε ratio.

The precise selection of temperature range and the determination of required thermal optical characteristics of the surface can be made after the solution to the problem of stability and strength analysis of a definite structure and the estimation of optimum combination of methods for strengthening and for optical surfaces treatment, which allows deformability reduction. At this stage it is necessary to implement the effective methods of monitoring, which could confirm the correctness of calculations by using numerical methods and reduce as much as possible the cycle of complex and expensive on-land stand tests of the structure at the stage of manufacture. In creating a TVS (Fig. 1c) the verification of a finite-element computational model of the structure has been implemented by the method of electronic shearography. At the same time, the effectiveness of the discussed methods below for surface property modification was confirmed in the modelling of radiation heating under vacuum conditions on separate segments of the conical structure. For these segments the boundary conditions on the circular mating contours corresponding to a multi-sectional shell have been reproduced.

RESULTS AND DISCUSSION

ALTERATION IN SPATIAL RIGIDITY OF A TVS SHELL

The transformation of a circumferential fragment of the conical shell surface into a fold corrugation with width **AB** (Fig. 1a) should be maximally approached to the equality condition of cone fragment meridian length before and after the transformation that allows producing the shell folding in a compact shape without tension and compression of the material. It is evident that this condition can be fulfilled at different flatnesses of the fold meridian's profile. The formation of fold meridian can be described, in particular, by the deformation of the function $f(x) = (x - R)^3$:

$$y = t \times (x - R)^3 + k \times (x - R) \times (1 - t) \qquad (2)$$

where: $t \in [0; 1 + \gamma]$, $\gamma \geq 0$, $k = \text{tg}\alpha$; R is the equivalent radius of a fold (Fig. 1a).

So, the shape of the meridian profile, present in the process of volumetric deformation of the shell, greatly influences the space rigidity of the structure and the parameters of its stability under the SEF conditions. The residual plastic deformations in the apexes of the folds lead to the formation of circular corrugations (Fig. 1b, III), which fulfil the function of stiffeners in a TVS shell after deployment. To determine the critical values of external loads of single shells, for example, under the influence of the axial compressive force, there are known

analytic solutions. Nevertheless, such solutions are absent for the stability problems of conical shells with a complex shape of generatrix in the configuration of the folding multi-layered systems at a random direction of the loads application. In modern studies, considering the problems of non-linear mechanics of multilayered structures, the numerical methods of calculation, based on the principle of minimum potential energy of the system, are applied for the solution to stability problems (determination of bifurcation points, critical loads and forms of stability losses, accompanied by snap-through behaviour (Ario and Watson 2009, 2010). In particular, in the study of Ario and Watson (2009), the equilibrium equation, as applied to the bar system, is written by using the mentioned principle:

$$F_i(\ldots,v_i,\ldots)=\frac{\partial \Pi}{\partial v_i}=\frac{\partial \Pi}{\partial v_i}\frac{\partial \overline{v}_i}{\partial v_i}=0, \quad for \quad i=1,\ldots,n \tag{3}$$

where: F_i is the critical force; $\overline{v}_i$ and v_i are the angular and linear displacement; Π is the total potential energy of model; n is the number of bars in the model.

It is assumed that a stability criterion of the system is the non-equality to zero of a determinant of rigidity matrix R (Jacobian for $J \in R^{n\times n}$), which is presented in the form:

$$J=\left(J_{ij}\right)=\left(\frac{\partial^2 \Pi}{\partial v_i \partial v_j}\right)=\left(\frac{\partial^2 \Pi}{\partial \overline{v}_i \partial \overline{v}_j}\frac{\partial \overline{v}_i \partial \overline{v}_j}{\partial v_i \partial v_j}\right)= \\ =\left(\frac{\partial F_i}{\partial \overline{v}_j}\frac{\partial \overline{v}_j}{\partial v_j}\right), \quad for \quad i,j=1,\ldots,n \tag{4}$$

Similarly to Ario and Watson (2009), at the first stage, the neutral surface of the multifolding TVS is approximated by a set of discrete elements, where, for each of them, an expression of potential energy Π_e is formed taking into account the rigid characteristics and mutual links. The general view of this expression can be written in the form:

$$\Pi_e = 1/2\ [D]^T\ [K][D] - [D]^T\ [R] \tag{5}$$

where: $[D]$ is the matrix of nodal displacements; $[D]^T$ is the transposed matrix D; $[K]$ is the stiffness matrix; $[R]$ is the matrix of external load.

By summing up the expression Π_e for all n elements of the model, we shall obtain the expression of the potential energy for all the calculated regions:

$$\Pi=\sum_{i}^{n}\Pi_{ei}, \quad for\ i=1\ldots n \tag{6}$$

The equilibrium of the system is determined by the principle of minimum total potential energy:

$$\delta\Pi=\frac{\partial \Pi}{\partial u_i}\delta u_i+\frac{\partial \Pi}{\partial v_i}\delta v_i+\frac{\partial \Pi}{\partial w_i}\delta w_i+\ldots\frac{\partial \Pi}{\partial \beta_i}\delta\beta_i+ \\ +\frac{\partial \Pi}{\partial \vartheta_i}\delta\vartheta_i+\frac{\partial \Pi}{\partial \theta_i}\delta\theta_i=0, \ for \ \ i=1,\ldots,m \\ or\ \frac{\partial \Pi}{\partial [D]}=0 \tag{7}$$

where: u, v and w are linear displacements; β, ∂ and θ are angular displacements; m is the number of nodes in the model.

The equilibrium stability of TVS is determined similarly to Eq. 4 by double differentiation of Eq. 6: $J = \partial^2\Pi/\partial[D]^2$. Under the condition $J > 0$, the structure is at the stable equilibrium and, at $J = 0$, it is at a non-stable one. In the second case, the critical load leads to the appearance of the bifurcation point, i.e. to the probability of formation of several stability losses forms.

At the equivalency of approach to the solution, the calculation of TVS is more complicated than that of the bar systems. This is caused by the degree of approximating polynoms, determining the number of nodes in a finite element and by a number of degrees of freedom (angular and linear displacements) in its nodes. In addition, the segments of multifolding TVS are characterized by a more complicated three-dimensional work, while the structural elements of bar hinged systems experience single-axis loading.

The modelling of the TVS unfolding process with different initial shapes of the meridian profile by applying the dynamic finite-element model (FEM) (Mayes *et al.* 2009; Silver and Warren 2010), carried out by using standard finite-element analysis, allows determining the final shapes of profile, taking into account the physical and mechanical properties of the real structural material. Figure 3 presents the shells in unfolded state with two maximum different shapes of initial profile of the meridian: at $\gamma = 1.5$(a) and at y = 0.5 (b) (see Eq. 2).

In the computational model of the structure variant, the thickness of shell structural material (stainless steel AISI 321, proof stress $R_{p0.2}$ = 205 MPa) is taken as δ = 0.15 mm. The number of truncated conical elements with diameters of bottoms D = 400 mm, d = 250 mm and height h = 160 mm is equal to 11. Figure 3 illustrates the calculated maximum values of equivalent stresses in the joining zone of structure's support

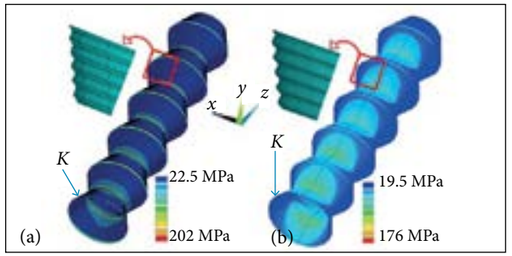

Figure 3. Equivalent stresses σ_e in TVS with a piecewise smooth (a) and sinusoidal (b) profiles of the shell meridian subjected to the effect of maximum SEF values.

conical sections, rigidly fixed on the circular base K, under the effect of typical combination of mechanical loads. They include linear (a_X = +12 m/s², a_Y = +12 m/s², a_Z = +9 m/s²) and angular (ε_X = +1.4 rad/s², ε_Y = +1.4 rad/s², ε_Z = +0.4 rad/s²) accelerations of the structure's centre of mass in combination with admissible values of temperature effects (from −150 up to +125 °C). As a main criterion of structure strength, the following condition is taken:

$$R_{p0.2} > \sigma_e \tag{8}$$

where: σ_e are the equivalent stresses in the TVS shell, determined in accordance with the von Mises-Hencky theory given as:

$$\sigma_e = \{[(\sigma_1 - \sigma_2)^2 + (\sigma_2 - \sigma_3)^2 + (\sigma_1 - \sigma_3)^2]/2\}^{1/2} \tag{9}$$

where: σ_1, σ_2 and σ_3 are the principal stresses.

At equivalent combinations of maximum external effects, the values of maximum equivalent stresses in a supporting part of the structure with a sinusoidal profile (Fig. 3b) are 1.15 times lower than in the structure with a profile of corrugations close to the piecewise smooth one (Fig. 3a). TVS with a piecewise smooth profile are characterized by the formation of clearly expressed stress raisers at the broken regions of corrugations and, as a consequence, by less uniform distribution of stresses over the surface; the maximum values of stresses σ_{eMAX} = 202 MPa practically correspond to the $R_{p0.2}$ value.

Figure 4 shows an experiment on TVS unfolding consisting of 11 sections (according to Fig. 3) with a different fold profile of structural elements (Fig. 4a) and the result of dynamic FEM of the unfolding process of the equivalent structure (Fig. 4b). In the isofields scales, the equivalent stresses σ_e(MPa) in the neutral surface of the structure shell are shown; *a* and *b* are conical sections with the shape of a meridian profile, corresponding to Fig. 3a and 3b. It can be seen that the integration into a multisectional TVS of structural elements with a different shape of a meridian profile also allows the process of the controlled unfolding, where the transformation of structural elements can start, for example, on the side of a free edge, and finish with an element, rigidly fixed on the support contour. This approach gives an opportunity to greatly decrease the deformability of TVS in the unfolding process, caused by non-uniform heating of its surface with the flux of solar radiation, and also to reduce the values of stresses in the zone of a supporting conical section fixation and in the zones of conical sections joining.

It should be noted that the flatter profile of a corrugation greatly complicates the technology of the volumetric deformation of the shell and, as shown above, it has no decisive effect on the structure stability during its service after unfolding. Hence, the tendency to simplify the technology of TVS manufacture and its improvement causes the need for changing the thermal optical properties of the shell surface.

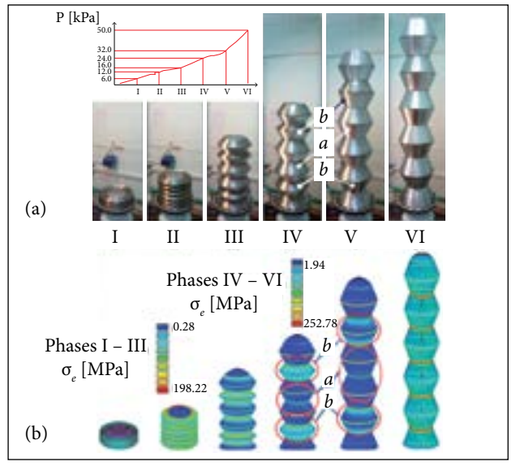

Figure 4. (a) The experiment on TVS unfolding and the growth curve of the excessive unfolding pressure (*P*) in the inner cavity of the shell; (b) The result of dynamic FEM of the process.

THE MODIFICATION OF TVS SURFACE PROPERTIES

The surface of the metal shell, absorbing the solar radiation mainly in the visible part of the spectrum, should possess a low absorbing capacity A_S and a high radiating capacity ε under conditions of heating and, respectively, high A_S in the spectrum's

infrared part. In the definite range the change of the mentioned value is attainable with mechanical and chemical treatment of the surface. Thus, the increase in roughness leads to the simultaneous reduction of A_S and ε and does not allow reducing greatly the maximum temperatures on the TVS surface neither under conditions of heating by the solar radiation flux, nor during the heat emission by radiation in the shade side of the orbit. For this reason, during the TVS development, the object of investigation was the A_S/ε ratio correction of definite shell material by deposition of different combinations of materials and their compounds on TVS surface, which performed functions of selective-coatings. The option of the necessary coating was determined not only by its thermal optical properties, but also by adhesion to the surface of the metal shell taking into account the large deformations of its surface during unfolding, as well as by different rates of sublimation of materials under vacuum space conditions.

Unique functional characteristics of the transformable shells, capable of changing one of their dimensions by 40 and more times, do not allow applying the known materials with preset thermal optical properties for their passive heat protection, for example, enamels, screen-vacuum heat insulation etc. The preparation of TVS optical surfaces after roughness correction was carried out by using electron beam spraying of thin coatings of metals and their compounds with required A_S/ε ratios. At the same time, it is evident that the result of this modification in the shell, expressed in values of displacement of random parts of its surface at different temperature values, requires a valid experimental confirmation even at the intermediate stages of large-sized transformable structures manufacture.

At the stage of laboratory testing, the efficiency of coatings with different values of ε and A_S was determined on the transformed conical section parts, which were fixed on the rigid frame and, within equal time, were subjected to a vacuum test while heating with an imitation of the spectrum and intensity of the radiation flux close to sunlight. Caused by plates heating, the surface deformation was recorded by a non-contact method of electronic shearography (Lobanov and Pivtorak 2014).

Since the experiments were conducted under the same mechanics and thermal optical conditions, the data on the maximum observed number of fringes N were used to simplify circuit calculations and comparative assessment.

The number of fringes N, which is recorded by the method of electron shearography using the shearographic system during the object deformation, is connected with values $\partial V/\partial X$ by the following expression (Lobanov and Pivtorak 2014):

$$\frac{\partial V}{\partial X} = \frac{N\lambda}{2\Delta x} \quad \text{(light interference fringes)} \qquad (10)$$

where: λ is the wave length of the laser radiation source; Δx is the value of a shear (shift) in the direction of OX axis in the optical scheme of the interferometer; V is the component of displacement vector, directed normally to the surface. The higher deformations of the surface at thermal loading of the object correspond to the larger number of fringes, observed in the shearographic pattern.

Figure 5 shows the results of the experiment on the determination of the fringes of order N in the TVS shell part with different thermal optical coatings at radiation heating, simulating the conditions of heating at the near-Earth orbit. The temperature drop during heating is $\Delta T = 2$ °C. At the stage of heating three surfaces were examined: (1) the TVS surface of stainless steel AISI 321 without coatings after chemical etching (Fig. 5, I); (2) the same surface after the deposition by the method of electron beam spraying of aluminium coating of 480 nm thickness (Fig. 5, III); (3) the antecedent surface with spraying of Al_2O_3 of 45 nm thickness on the aluminium layer, simulating the formation of the oxide film, greatly increasing the absorption coefficient A_S (Fig. 5, II). It should be noted that, at applied thicknesses of coatings, the surface's thermal and optical properties depend also on the properties of the coated metal, and small thicknesses of the coated layer were used for the accuracy evaluation of the experimental part of the procedure. The dependence of N values (see Eq. 10) for different variants of surfaces on the heating time t is given in Fig. 5.

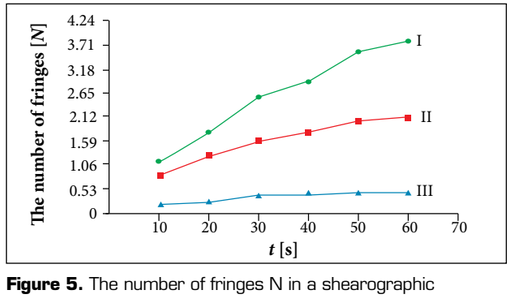

Figure 5. The number of fringes N in a shearographic interferogram depending on the time of radiation heating t in a TVS shell part.

As the coatings, sprayed on the object's surface, have a small thickness and cannot significantly change the thermo-mechanical properties of plates, the deformation $\partial V/\partial X$ and, consequently, the number of observed fringes N in the shearographic interferogram are proportional to the temperature attained on the surface due to the radiation heating. Thus, as to the data of the diagram in Fig. 5, it is possible to obtain the quantitative evaluation of effectiveness of sprayed layer reflecting properties.

In TVS development the experimental-computational method was used, which consists in the verification of a FEM of temperature deformations in a random part of the structure shell. The method was performed by applying standard finite-element analysis. The FEM is compared with a three-dimensional surface of function $\partial V/\partial X$ of the examined part of the metal shell with different surface's thermal and optical properties.

At radiation heating of the shell under the conditions, simulating with a maximum validity the regular service conditions in space vacuum, the interference patterns (shearographic interferograms) were formed (Fig. 6a, II). These patterns were obtained by comparison of two speckle-patterns corresponding to different stages of heating (Fig. 6a, I) at the reflection of the dissipated laser radiation from TVS surface part (Fig. 6a). The further processing of interference patterns using a special software allows plotting a three-dimensional pattern of deformations at thermal loading in the part being examined (Fig. 6a, III).

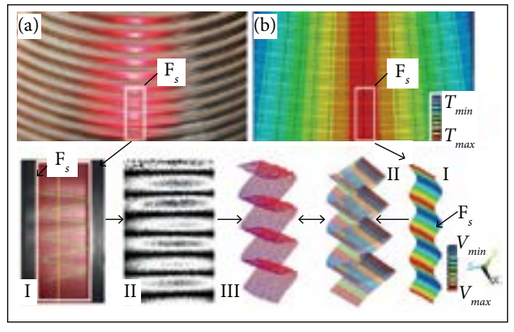

Figure 6. The use of the method of electronic shearography (a) for verification of the FEM (b) of temperature deformations of the random TVS shell fragment F_S

The obtained three-dimensional pattern (Fig. 6a, III) is compared with three-dimensional distribution of values of the $\partial V/\partial X$ function (Fig. 6b, II), obtained by differentiation of the displacement field V in the direction OX of the FEM of the examined part (Fig. 6b, I). For the examined part, the temperature experimental values of the structure's optical surfaces are taken, which are determined in the experiment process on the radiation heating of TVS surface. Thus, the sufficient coincidence degree of two models (Fig. 6a and b) can confirm both the effectiveness of surface engineering methods and the validity of the accepted computational model (correctness of calculation of structure using numerical methods) without applying full-scale stand tests. The advantage of the experimental calculation method is the possibility to obtain the interference patterns during vacuum tests with simulation of a solar spectrum and density of radiation flux applied to a TVS part. It can be a single conical segment of the multisectional structure, subjected to proportional deformations at orientation of solar radiation flux, normal to the TVS symmetry axis or to the pair of adjacent segments at any other orientation of the flux.

Thus, Fig. 5 illustrates the effectiveness of the applied method of surface modifying. To verify the calculated results of its application, expressed in the deformation pattern, the described experimental-calculation method (Fig. 6), also including differentiation of displacement field V in the directions OY ($\partial V/\partial Y$) and OZ ($\partial V/\partial Z$), can be used.

With respect to the structure in Fig. 3b, as a result of its calculation using standard finite-element analysis, it was determined that taking into account both the effect of maximum values of temperature loads (−150 to +125 °C) and accelerations on optical surfaces without protective coating leads to 2.32 times increase in maximum displacements in the TVS shell and 1.23 times growth of equivalent stresses. Further, the change in shape of a corrugation profile (Fig. 3) allows reducing the maximum values of stresses in the structure by 15% (from 202 to 176 MPa). The application of coatings, decreasing the temperature load to the range of −43 to +63 °C, leads to the deformability decrease of the multisectional shell by 1.45 times and to the reduction of maximum values of equivalent stresses by 1.17 times (from 175 to 150 MPa). Thus, the surface modification in combination with a profile shape variation of shell folds can reduce the deformability and increase the stability of the studied TVS type to values which require the increase in the structure mass by more than 30% at simultaneous reduction of its compactness using standard design approaches (in particular, 2 times increase in material thickness of four conical sections at the attachment side). The results of calculations and their experimental verification demonstrate the possibility to use these types of thin metal shells as the load-bearing elements under SEF conditions. It should be added that the examined example of the conical TVS can be described as the most complicated structural and technological embodiment of this type, which has a small ratio of the diameter of the supporting contour to the overall

length and is subjected to direct radiation heating influence on the vacuum of space environment. The determination of optimum ratio of the used surface engineering methods, as well as qualitative and quantitative evaluation of the effectiveness examined in this paper, depends, in each case, on a number of factors — primarily, on the specific functionality of the TVS and the duration of its exposure under SEF.

CONCLUSIONS

The development of new shell structures, with unique functional characteristics and their adaptation to extreme service conditions, predetermines the need to verify the results of superposition modelling of complex stress-strain states, subjected to significant changes in the long-time exposure process. The integrated approach, suggested by the authors, allows evaluating the equivalency of fields of TVS surface displacements, obtained in contactless diagnostics and in the databasis of numerical modelling. It also determines the optimum relation of methods used for modification of its rigidity-strength characteristics. It is shown the possibility of improving the functional characteristics of the examined structure by means of profile adjustment of circular folds of its separate shell elements and spraying on them thin coatings with required thermal and optical properties. The result of this study demonstrates the possibility of effectiveness evaluation of the applied surface engineering methods under the terrestrial conditions, excluding the valid experimental confirmation of computational model results.

REFERENCES

Ario I, Watson A (2009) Structural stability of multi-folding structures with contact problem. J Sound Vib 324(1-2):263-282. doi: 10.1016/j.jsv.2009.01.057

Ario I, Watson A (2010) Non-linear dynamic behaviour of multi-folding microstructure systems based on origami skill. Int J Nonlinear Mech 45(4):337-347. doi: 10.1016/j.ijnonlinmec.2009.11.010

Lobanov LM, Pivtorak VA (2014) Diagnostics of structures by the methods of electron shearography and speckle-interferometry. Mater Sci 49(4):442-448. doi: 10.1007/s11003-014-9635-5

Mayes RL, Miller AK, Holzmann WA, Tipton DG, Adams CR (2009) A structural dynamics model validation example with actual hardware. Proceedings of the IMAC-XXVII Conference on Structural Dynamics; Orlando, USA.

Paton BE, Lobanov LM, Volkov VS (2015) Metal transformable-volume structures for space engineering. Acta Astronaut 110:50-57. doi: 10.1016/j.actaastro.2015.01.005

Pellegrino S (2015) Folding and deployment of thin shell structures. In: Bigoni D, editor. Extremely deformable structures. vol. 562. Springer: CISM International Centre for Mechanical Sciences. p. 179-267.

Schenk M, Viquerat AD, Seffen KA, Guest SD (2014) Review of inflatable booms for deployable space structures: packing and rigidization. J Spacecraft Rockets 51(3):762-778. doi: 10.2514/1.A32598

Silver MJ, Warren P (2010) Dynamic modeling of the folding of multi-shell flexible composites. Proceedings of the 51st AIAA/ASME/ASCE/AHS/ASC Structures, Structural Dynamics, and Materials Conference; Orlando, USA.

Underwood C, Pellegrino S, Lappas VJ, Bridges CP, Baker J (2015) Using CubeSat/micro-satellite technology to demonstrate the Autonomous Assembly of a Reconfigurable Space Telescope (AAReST). Acta Astronaut 114:112-122. doi: 10.1016/j.actaastro.2015.04.008

doi: 10.5028/jatm.v8i1.542

A Comparative Study of Four Feedback Linearization Schemes for Motion Planning of Fixed-Wing Unmanned Aerial Vehicles

Hossein Bonyan Khamseh[1]

ABSTRACT: In this paper, different feedback linearization schemes are studied to address the motion planning problem of fixed-wing unmanned aerial vehicles. For a unmanned aerial vehicle model with second-order dynamics, several schemes are studied to make the vehicle (i) fly over and (ii) make a loitering around the objective position. For each scheme, comparisons are made to illustrate the advantages and disadvantages. Lyapunov stability analysis is used to prove the stability of the proposed schemes, and simulation results for some case studies are included to show their feasibility.

KEYWORDS: Feedback linearization, Unmanned aerial vehicle, Motion planning.

INTRODUCTION

In recent years, unmanned aerial vehicles (UAVs) have gained increasing attention for various missions such as remote sensing of agricultural products (Costa *et al.* 2012), forest fire monitoring (Casbeer *et al.* 2006), search and rescue (Almurib *et al.* 2011), transmission line inspection (Li *et al.* 2013) and border monitoring (Beard *et al.* 2006). To this date, various approaches have been employed to address the motion planning of UAVs to reach, fly over or loiter around an objective position. As an example, in Frew *et al.* (2008) and Lawrence *et al.* (2008), vector fields with a stable limit cycle centered on the target position were constructed. In the mentioned studies, the authors employed a Lyapunov vector field guidance (LVFG) law to bring the UAV to an observation "orbit" around the target. Also, in Gonçalves *et al.* (2011), a vector field approach was used to bring several non-holonomic UAVs to a static curve embedded in the 3-D space. In Gonçalves *et al.* (2010), vector fields were determined such that a robot converged to a time-varying curve in n-dimensions and circulated it. In Hsieh *et al.* (2008), decentralized controllers were proposed to bring a number of robotic agents to generate desired simple planar curves, while avoiding inter-agent collision. In Hsieh *et al.* (2007), the controllers were modified such that the robots converged to a star-shaped pattern and, once on the objective curve, circulated it. In Bonyan Khamseh *et al.* (2014), based on the concept of flight corridor, a decentralized coordination strategy was proposed to bring a team of fixed-wing UAVs to a circular orbit, while avoiding inter-UAV collision. In Hafez *et al.* (2013), model predictive control was used to create a

1.Universidade Federal de Minas Gerais – Escola de Engenharia Elétrica – Departamento de Engenharia Elétrica – Belo Horizonte/MG – Brazil.

Author for correspondence: Hossein Bonyan Khamseh | Universidade Federal de Minas Gerais - Escola de Engenharia Elétrica - Departamento de Engenharia Elétrica Av. Pres. Antônio Carlos, 6627 – CEP: 31 270-901 – Pampulha - Belo Horizonte/MG – Brazil | Email: h.bonyan@gmail.com

Received: 08/25/2015 | **Accepted:** 12/04/2015

dynamic circular formation around a given target. By means of simulations, it was shown that the system was stable, but formal stability analysis was not provided. In Marasco *et al.* (2012), the same approach was improved to address encirclement of multiple targets, without stability analysis.

It is also possible to employ feedback linearization to simplify the equations of motion in motion planning problems (Lawton *et al.* 2003; Fan and Zhiyong 2009; Kanchanavally *et al.* 2006). As an example, in Lawton *et al.* (2003), feedback linearization was employed to study the formation control of the end-effector position of a team of non-holonomic robots. Having obtained simpler double-integrator equations, control laws were designed and formation control was achieved. Stability of the system was proven by means of Lyapunov stability theory. In Fan and Zhiyong (2009), for a multi-agent system, the authors proposed a dynamic feedback linearization scheme to describe the equations of motion of each agent by third-order integrators. Then, a formation control law with inter-agent damping was developed, and asymptotic stability of the system was verified using Lyapunov stability analysis. In Kanchanavally *et al.* (2006), the specific problem of 3-D motion planning of UAVs via feedback linearization was studied. In that study, a non-holonomic UAV equipped with a fixed-angle camera was considered. The footprint of the camera was defined as the system output, and it was shown that it converged to an objective position. Similar to the previous papers (Lawton *et al.* 2003; Fan and Zhiyong 2009), the stability of the system was studied by means of Lyapunov stability theory. Yet, an important drawback of Kanchanavally *et al.* (2006) is that it did not include the constraints of minimum and maximum forward velocity of fixed-wing UAVs. Therefore, the UAVs came to rest, i.e. zero forward velocity, once the camera footprint converged to the target position.

In this paper, several feedback linearization schemes are studied to address the problem of motion planning of fixed-wing UAVs flying with constant forward velocity. The objective here is that the UAV (i) flies over or (ii) loiter around a static objective position, without coming to rest.

FEEDBACK LINEARIZATION SCHEMES

In the following subsections, a UAV with an on-board camera will be considered. For a fixed-angle forward-looking camera, the results were presented in Kanchanavally *et al.* (2006), where the UAV finally came to rest. Due to minimum forward velocity constraint, that method is not applicable to fixed-wing UAVs. Here, we define several schemes such that the footprint of the on-board camera converges to an objective position while the UAV either flies over or loiters around the objective position with constant forward velocity.

UAV WITH FORWARD-LOOKING CAMERA, SCHEME #1

In the first scheme a fixed-wing UAV with variable-angle forward-looking camera is considered. In the control affine form, considering a simplified rigid-body model, the dynamic equations of motion of the system are given by:

$$\begin{bmatrix} \dot{x}_1 \\ \dot{x}_2 \\ \dot{x}_3 \\ \dot{x}_4 \\ \dot{x}_5 \\ \dot{x}_6 \\ \dot{x}_7 \\ \dot{x}_8 \end{bmatrix} = \begin{bmatrix} \dot{r}_x \\ \dot{r}_y \\ \dot{\theta} \\ \dot{\omega} \\ \dot{r}_z \\ \dot{v}_z \\ \dot{\phi} \\ \dot{v}_\phi \end{bmatrix} = \begin{bmatrix} v\cos x_3 \\ v\sin x_3 \\ x_4 \\ 0 \\ x_6 \\ 0 \\ x_8 \\ 0 \end{bmatrix} + \begin{bmatrix} 0 & 0 & 0 \\ 0 & 0 & 0 \\ 0 & 0 & 0 \\ \frac{1}{I} & 0 & 0 \\ 0 & 0 & 0 \\ 0 & \frac{1}{m} & 0 \\ 0 & 0 & 0 \\ 0 & 0 & \frac{1}{J} \end{bmatrix} \begin{bmatrix} u_1 \\ u_2 \\ u_3 \end{bmatrix} = \boldsymbol{f} + g\boldsymbol{u} \quad (1)$$

where: r_x, r_y and r_z represent x, y, and z positions of the UAV; v and v_z represent the constant velocity v in the $x - y$ horizontal plane and the velocity v_z in the z-direction; θ and ω represent the heading angle and angular velocity of the UAV; ϕ and v_ϕ represent the angle and angular speed of the camera, respectively. The UAV constants are given by m (UAV mass), I (UAV moment of inertia about z-axis) and J (camera moment of inertia about its rotation axis). The input vector is $\boldsymbol{u} = [u_1\ u_2\ u_3]^T$.

In the model given by Eq. 1, it has been assumed that the forward velocity in the $x - y$ plane, i.e. v, is constant. With this simplification, if one initially chooses the forward velocity to satisfy $v_{min} \le v \le v_{max}$, one can conclude that the minimum and maximum forward velocity constraints will be automatically satisfied throughout the mission. Also, since the camera is not mounted with a fixed angle, one can come up with scenarios in which the UAV does not come to rest when the camera footprint converges to the objective position. As it can be seen from Eq. 1, the camera dynamics has been assumed to be second-order and completely decoupled from the UAV dynamics. For a forward-looking camera, one can consider the following output for the system (Kanchanavally *et al.* 2006):

$$\boldsymbol{\Gamma} = \begin{bmatrix} x_1 + L\cos x_3 \\ x_2 + L\sin x_3 \\ x_5 \end{bmatrix}, \quad (2)$$

where: $L = r_z \cot\phi$.

As schematically shown in Fig. 1, the first two elements of Γ represent x and y positions of the footprint of the forward-looking camera. Also, the third element represents the altitude of the UAV. An important advantage of this scheme, compared to Kanchanavally *et al.* (2006), is that ϕ is not constant here and is considered one of the system state variables.

Assuming relative degree of r_i for the i-th elements of Γ, after r_i times differentiation, one finds:

$$\begin{bmatrix} \Gamma_1^{(r_1)} \\ \Gamma_2^{(r_2)} \\ \Gamma_3^{(r_3)} \end{bmatrix} = \begin{bmatrix} L_f^{r_1}\Gamma_1 + \sum_{i=1}^{3} L_{g_i}\left(L_f^{r_1-1}\Gamma_1\right)u_i \\ L_f^{r_2}\Gamma_2 + \sum_{i=1}^{3} L_{g_i}\left(L_f^{r_2-1}\Gamma_2\right)u_i \\ L_f^{r_3}\Gamma_3 + \sum_{i=1}^{3} L_{g_i}\left(L_f^{r_3-1}\Gamma_3\right)u_i \end{bmatrix} = \boldsymbol{A} + B\boldsymbol{u} \quad (3)$$

where: $L_f\Gamma_i$ is the Lie derivative, i.e. $L_f\Gamma_i = \partial\Gamma_i/\partial x$ and g_i is the i-th column of the matrix g. Also, $\boldsymbol{A} \in \boldsymbol{R}^{3\times1}$ and $\boldsymbol{B} \in \boldsymbol{R}^{3\times3}$, where the elements of $\boldsymbol{A}$ are given below. For the system given by Eq. 1 and with output given by Eq. 2, one can obtain the vector of relative degree as $[r_1\ r_2\ r_3] = [2\ 2\ 2]$.

$$A_1 = -vx_4\sin x_3 - 2x_6x_8\frac{1}{\sin^2 x_7}\cos x_3 + \\ + 2x_5(x_8)^2\frac{\cos x_7}{\sin^3 x_7}\cos x_3 - 2x_6\cot x_7\, x_4\sin x_3 + \\ + 2x_5x_8\frac{1}{\sin^2 x_7}x_4\sin x_3 - L(x_4)^2\cos x_3$$

$$A_2 = vx_4\cos x_3 - 2x_6x_8\frac{1}{\sin^2 x_7}\sin x_3 + \\ + 2x_5(x_8)^2\frac{\cos x_7}{\sin^3 x_7}\sin x_3 + 2x_6\cot x_7\, x_4\cos x_3 - \\ - 2x_5x_8\frac{1}{\sin^2 x_7}x_4\cos x_3 - L(x_4)^2\sin x_3$$

and $A_3 = 0$.

Also:

$$B = \begin{bmatrix} \frac{-L}{I}\sin x_3 & \frac{1}{m}\cot x_7\cos x_3 & -\frac{1}{J}\frac{x_5}{\sin^2 x_7}\cos x_3 \\ \frac{L}{I}\cos x_3 & \frac{1}{m}\cot x_7\sin x_3 & -\frac{1}{J}\frac{x_5}{\sin^2 x_7}\sin x_3 \\ 0 & \frac{1}{m} & 0 \end{bmatrix}$$

One can verify that $\det(B) = -(x_5)^2\cos x_7/m{\cdot}I{\cdot}J\sin^3 x_7$. This determinant can be zero if $x_5 = 0$ or $\cos x_7 = 0$. In order to show that $x_5 \neq 0$, we define the error as:

$$\boldsymbol{E} = (\boldsymbol{\Gamma} - \boldsymbol{R}) + \left(\dot{\boldsymbol{\Gamma}} - \dot{\boldsymbol{R}}\right) \quad (4)$$

where: $\boldsymbol{R}$ is the reference signal and, for a stationary reference signal, one will have $\dot{\boldsymbol{R}} = 0$. Assuming $E_3(0) > -R_3$, one can rewrite the third row of Eq. 4 as:

$$\dot{\Gamma}_3 = -\Gamma_3 + \underbrace{(E_3 + R_3)}_{u'} \quad (5)$$

Therefore:

$$\Gamma_3(t) = e^{-t}\Gamma_3(0) + \int_0^t e^{-(t-\tau)}u'(\tau)d\tau \quad (6)$$

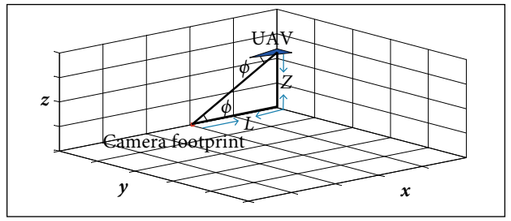

Figure 1. The UAV and its camera footprint in scheme #1.

In the following paragraphs it will be shown that the absolute value of E_3 monotonically decreases and converges to zero. Therefore, noting that $R_3 > 0$, it will be easy to see that $u'(t)$ is always positive. With $\Gamma_3(0) > 0$, from Eq. 6, one can conclude that $\Gamma_3(t) > 0$ and therefore $x_5 \neq 0$, i.e. the altitude cannot be zero. Also, for $\cos x_7 = 0$, one must have $x_7 = k\pi + \pi/2$. It means that the objective position is exactly underneath the UAV actual position. This is an important drawback which can lead to the failure of this scheme. Yet, due to discretization, control errors and other real-world phenomena, this is not a concern in practical situations. In our simulations, no problem was encountered due to this drawback. Also, $\det(B) \to \infty$ if $x_7 \to k\pi$. Yet, $x_7 \to k\pi$ means that $L \to \infty$. In practice, it is not a legitimate concern because $\Gamma_3(0) > 0$ and also the UAV cannot be infinitely far from its target ($x_7 \neq k\pi$). Therefore it is concluded that $\det(B) = -(x_5)^2\cos x_7/m{\cdot}I{\cdot}J\sin^3 x_7 \neq 0$ for practical applications.

In order to study the error dynamics, we differentiate Eq. 4 to obtain:

$$\dot{E} = \dot{\Gamma} + \ddot{\Gamma} = \dot{\Gamma} + A + Bu \tag{7}$$

Similar to Kanchanavally *et al.* (2006), if we define $u = B^{-1}(-A - \dot{\Gamma} + v)$ and , it is easy to see that:

$$\dot{E} = KE \tag{8}$$

where: $K \in R^{3\times3}$ and eigenvalues of K have negative real parts.

In order to study the error dynamics given by Eq. 8, one may consider the following Lyapunov function:

$$V = \frac{1}{2}E^T E \tag{9}$$

The time derivative of the above positive definite V is given by:

$$\dot{V} = \dot{E}^T E = E^T K^T E < 0 \tag{10}$$

Therefore the error converges to zero. Regarding the internal dynamics with a vector of relative degree of [2 2 2], one needs to propose two more transformations to complete the diffeomorphism. The internal dynamics is given by Eq. 11:

$$\begin{cases} \eta_7 = x_3 \rightarrow \dot{\eta}_7 = x_4 \\ \eta_8 = x_4 \rightarrow \dot{\eta}_8 = \frac{1}{J}u_1 \end{cases} \tag{11}$$

For a UAV with a forward-looking camera, the only possible motion where the error goes to zero is when the UAV flies on a straight line over the objective position. Therefore, as $t \rightarrow \infty$, $x_4 \rightarrow 0$. With $x_4 \rightarrow 0$, it is easy to conclude that x_3 will be bounded and therefore it is not going to cause undesirable effects. Simulation results verifying the feasibility of this approach will be given in "Simulations" section.

UAV WITH SIDE-LOOKING CAMERA, SCHEME #2

In this subsection, a UAV with variable-angle side-looking camera is considered. The equations of motion of this configuration are identical to those given in Eq. 1 and therefore are not repeated here. For a side-looking camera, the output is given by:

$$\Gamma = \begin{bmatrix} x_1 + L\sin x_3 \\ x_2 - L\cos x_3 \\ x_5 \end{bmatrix} \tag{12}$$

where the first two elements of Γ represent x and y positions of the footprint of the camera (see Fig. 2).

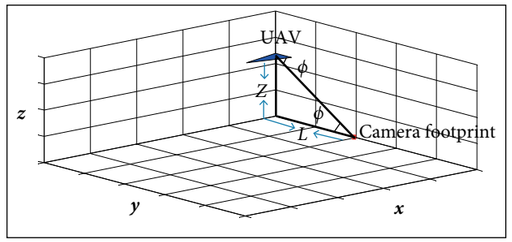

Figure 2. The UAV and its camera footprint in scheme #2.

For the given output, one can verify that $[r_1\ r_2\ r_3] = [2\ 2\ 2]$. Therefore, an equation identical to that given in Eq. 3 is obtained, in which:

$$A_1 = -vx_4\sin x_3 - 2x_6x_8\frac{1}{\sin^2 x_7}\sin x_3 + \\ + 2x_5(x_8)^2\frac{\cos x_7}{\sin^3 x_7}\sin x_3 + 2x_6\cot x_7\, x_4\cos x_3 - \\ - 2x_5x_8\frac{1}{\sin^2 x_7}x_4\cos x_3 - L(x_4)^2\sin x_3$$

$$A_2 = vx_4\cos x_3 + 2x_6x_8\frac{1}{\sin^2 x_7}\cos x_3 - \\ - 2x_5(x_8)^2\frac{\cos x_7}{\sin^3 x_7}\cos x_3 + 2x_6\cot x_7\, x_4\sin x_3 - \\ - 2x_5x_8\frac{1}{\sin^2 x_7}x_4\sin x_3 + L(x_4)^2\cos x_3$$

$$A_3 = 0$$

$$B = \begin{bmatrix} \frac{1}{J}\cos x_3 & \frac{1}{m}\cot x_7\sin x_3 & -\frac{1}{J}\frac{x_5}{\sin^2 x_7}\sin x_3 \\ \frac{1}{J}\sin x_3 & -\frac{1}{m}\cot x_7\cos x_3 & \frac{1}{J}\frac{x_5}{\sin^2 x_7}\cos x_3 \\ 0 & \frac{1}{m} & 0 \end{bmatrix}$$

One can verify that $\det(B) = -(x_5)^2\cos x_7/m{\cdot}I{\cdot}J\sin^3 x_7$. This determinant can be zero if $x_5 = 0$ or $\cos x_7 = 0$. With the reasoning given in the previous subsection (see Eqs. 4 – 6), one can conclude that $x_5 \neq 0$, i.e. the altitude cannot be zero. For a UAV with constant forward velocity and a side-looking camera, the only possible motion where the error goes to zero is when the UAV loiters around the objective position, with a fixed loitering radius. Therefore, with a non-zero loitering radius, it is easy to conclude that $\cos x_7 \neq 0$. Also, $\det(B) \rightarrow \infty$ if $x_7 \rightarrow k\pi$. Yet, $x_7 \rightarrow k\pi$ means that $L \rightarrow \infty$, which is not common in practical scenarios. Therefore, it is concluded that $\det(B) = -(x_5)^2\cos x_7/m{\cdot}I{\cdot}J\sin^3 x_7 \neq 0$ for practical applications, and thus the system given by Eq. 1 with output given by Eq. 12 is input-output linearizable.

For this scheme, the Lyapunov stability analysis is identical to that given by Eqs. 7 – 10. Therefore, it can be concluded that the error dynamics asymptotically converges to zero. Regarding the internal dynamics with a vector of relative degree of [2 2 2], one needs to propose two more transformations to complete the diffeomorphism. The internal dynamics is given by and in Eq. 13:

$$\begin{cases} \eta_7 = x_3 \rightarrow \dot{\eta}_7 = x_4 \\ \eta_8 = x_4 \rightarrow \dot{\eta}_8 = \frac{1}{J}u_1 \end{cases} \tag{13}$$

For a UAV loitering around a given objective position with constant (finite) forward velocity, x_4 will be bounded and cannot go to infinity. Also, in a loitering motion, x_3, i.e. the heading angle, can be shown by $2k\pi + \theta$' where θ' is a finite value and therefore the internal dynamics will not cause undesirable effects in our approach. Simulation results regarding this scheme will be given in "Simulations" section.

An important drawback of this method is that one cannot explicitly control the final loitering radius of the UAV. Therefore, in the next scheme, we try to explicitly define the loitering radius as one of the system outputs.

UAV WITH SIDE-LOOKING CAMERA, SCHEME #3

In this section, we modify the equations of motion given in Eq. 1 in a manner that a new useful scheme is obtained. In the control affine form, the new dynamic equations of motion are given by Eq. 14:

$$\begin{bmatrix} \dot{x}_1 \\ \dot{x}_2 \\ \dot{x}_3 \\ \dot{x}_4 \\ \dot{x}_5 \\ \dot{x}_6 \\ \dot{x}_7 \\ \dot{x}_8 \end{bmatrix} = \begin{bmatrix} \dot{r}_x \\ \dot{r}_y \\ \dot{\theta} \\ \dot{\omega} \\ \dot{r}_z \\ \dot{v}_z \\ \dot{L} \\ \ddot{L} \end{bmatrix} = \begin{bmatrix} v\cos x_3 \\ v\sin x_3 \\ x_4 \\ 0 \\ x_6 \\ 0 \\ x_8 \\ 0 \end{bmatrix} + \begin{bmatrix} 0 & 0 & 0 \\ 0 & 0 & 0 \\ 0 & 0 & 0 \\ \frac{1}{J} & 0 & 0 \\ 0 & 0 & 0 \\ 0 & \frac{1}{m} & 0 \\ 0 & 0 & 0 \\ 0 & 0 & 1 \end{bmatrix}\begin{bmatrix} u_1 \\ u_2 \\ u_3 \end{bmatrix} = f + gu \tag{14}$$

Here, the main difference is that L and $\dot{L}$ are explicitly considered to be state variables. One may define the system output as:

$$\Gamma = \begin{bmatrix} x_1^2 + x_2^2 \\ x_5 \\ x_7 \end{bmatrix} \tag{15}$$

where the first element of Γ is the square of the distance of the UAV from the origin of the coordinate system, i.e. the stationary objective position.

It can be readily seen that $[r_1\ r_2\ r_3] = [3\ 2\ 2]$. Therefore, in a compact form, one can write:

$$\begin{bmatrix} \ddot{\Gamma}_1 \\ \ddot{\Gamma}_2 \\ \ddot{\Gamma}_3 \end{bmatrix} = A + Bu \tag{16}$$

where:

$$A = \begin{bmatrix} -2vx_4^2(x_1\cos x_3 + x_2\sin x_3) \\ 0 \\ 0 \end{bmatrix},$$

$$B = \begin{bmatrix} \frac{-2v}{J}(x_1\sin x_3 - x_2\cos x_3) & 0 & 0 \\ 0 & \frac{1}{m} & 0 \\ 0 & 0 & 1 \end{bmatrix}$$

One can verify that $\det(B) = -2v_c/m{\cdot}I\,(x_1\sin x_3 - x_2\cos x_3)$. An important disadvantage is that this determinant can be zero if $x_1\sin x_3 - x_2\cos x_3 = 0$, i.e. when the UAV is either flying radially inward or radially outward. Yet, if the heading of the UAV does not fall within this region, the UAV can converge to a loitering motion around the origin of the coordinate system. On the other hand, the advantage of this scheme is that, depending on the value of R_1, i.e. the first element of the reference signal, one can come up with scenarios in which the UAV converges to a loitering radius either smaller or greater than the initial one. Also, a second advantage is that one can explicitly control L, as R_3. Therefore, for $R_3 < 2\sqrt{R_1}$, $R_3 = 22\sqrt{R_1}$ and $R_3 > 2\sqrt{R_1}$, one can define scenarios in which the UAV loiters around the origin while the camera footprint sweeps a circle with the radius smaller than, equal to or greater than $\sqrt{R_1}$. This is schematically shown in Figs. 3a to 3c.

Regarding the stability of the system, if we define the error as:

$$\begin{bmatrix} E_1 \\ E_2 \\ E_3 \end{bmatrix} = \left(\begin{bmatrix} \Gamma_1 \\ \Gamma_2 \\ \Gamma_3 \end{bmatrix} - \begin{bmatrix} R_1 \\ R_2 \\ R_3 \end{bmatrix}\right) + \left(\begin{bmatrix} \dot{\Gamma}_1 \\ \dot{\Gamma}_2 \\ \dot{\Gamma}_3 \end{bmatrix} - \begin{bmatrix} \dot{R}_1 \\ \dot{R}_2 \\ \dot{R}_3 \end{bmatrix}\right) \tag{17}$$

for a stationary reference signal, one will have $\dot{R} = \ddot{R} = 0$.

Differentiating Eq. 17, one has:

$$\begin{bmatrix}\dot{E}_1\\ \dot{E}_2\\ \dot{E}_3\end{bmatrix}=\begin{bmatrix}\dot{I}_1\\ \dot{I}_2\\ \dot{I}_3\end{bmatrix}+\begin{bmatrix}\ddot{I}_1\\ \ddot{I}_2\\ \ddot{I}_3\end{bmatrix} \quad (18)$$

Now, if we define $\boldsymbol{u} = B^{-1}(-\boldsymbol{A} - \dot{I} + v)$ and $v = K\boldsymbol{E}$, it is easy to see that:

$$\dot{\boldsymbol{E}} = K\boldsymbol{E} \quad (19)$$

where: K is a matrix with eigenvalues which have negative real parts.

In order to study the error dynamics given by Eq. 19, one may consider the following Lyapunov function:

$$V = \frac{1}{2}\boldsymbol{E}^T\boldsymbol{E} \quad (20)$$

The time derivative of the above positive definite V is given by:

$$\dot{V} = \dot{\boldsymbol{E}}^T\boldsymbol{E} = \boldsymbol{E}^T\boldsymbol{K}^T\boldsymbol{E} < 0 \quad (21)$$

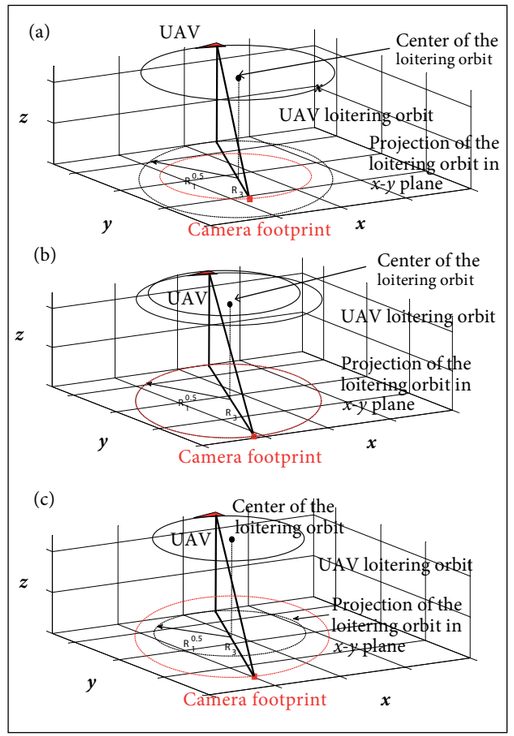

Figure 3. Three different scenarios in scheme #3.

Therefore the error dynamics is asymptotically stable. Regarding the internal dynamics with a vector of relative degree of [3 2 2], one needs to propose one more transformation to complete the diffeomorphism. The internal dynamics is given by $\dot{\eta}_8$ in Eq. 22:

$$\eta_8 = x_4 \rightarrow \dot{\eta}_8 = \frac{1}{j}u_1 \quad (22)$$

For a UAV loitering around a given objective position with constant (finite) forward velocity, x_4 will be bounded and cannot go to infinity. Therefore, the internal dynamics will not cause undesirable effects in our approach. Simulation results regarding this scheme will be given in "Simulations" section.

UAV WITH SIDE-LOOKING CAMERA AND ONE VIRTUAL FORWARD-LOOKING CAMERA, SCHEME #4

In this subsection, we modify the previous scheme in the sense that the UAV can loiter around the origin with a desirable radius while avoiding the singularity problem of scheme #3. Convergence to a loitering radius (i) smaller or (ii) greater than the initial radius is studied separately.

Convergence to a Loitering Radius Smaller than the Initial One

In this scenario, it is initially assumed that the UAV is equipped with a virtual forward-looking camera. From geometry, one can find two tangent lines (and their corresponding tangency points) between the initial position of the UAV and the circle with the reference radius. In the first phase, the UAV can choose one of the tangency points as its virtual objective position and fly over it, according to scheme #1, discussed earlier. Assuming that the UAV flies over the tangent line, its heading will be perpendicular to the radius of the objective circle as it reaches the virtual objective position. As the UAV reaches the tangency point, it switches to scheme #3. The advantage here is that, in the second phase, it is ensured that the heading of the UAV is far from inward-outward direction and therefore scheme #3 can bring the UAV to loiter around the objective position, with desirable radius. This is schematically shown in Fig. 4.

The details of feedback linearization, control laws and stability analysis of scheme #1 and scheme #3 were discussed in the previous subsections and are not repeated here. Simulation results of this scheme will be given in "Simulations" section.

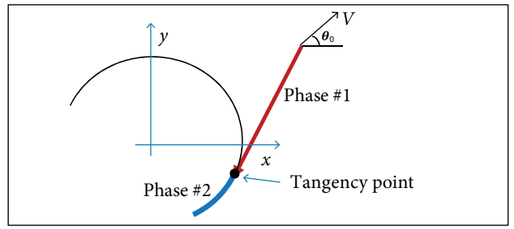

Figure 4. Scheme #3, convergence to a loitering radius smaller than the initial one.

Convergence to a Loitering Radius Greater than the Initial One

Similar to the previous subsection, we assume that the UAV is equipped with a virtual forward-looking camera and a side-looking camera. The scenario proposed here consists of three phases, as shown in Fig. 5.

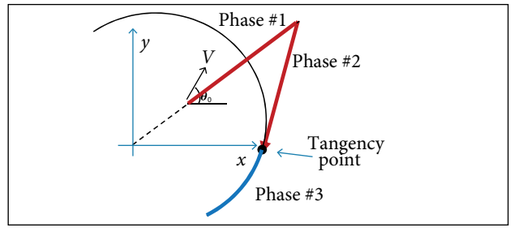

Figure 5. Scheme #3, convergence to a loitering radius greater than the initial one.

In the first phase, based on scheme #1, the UAV flies to a virtual objective position which is on the extension of the line connecting the origin to the initial position of the UAV. Let's denote the UAV distance from the origin by d and the desired loitering radius by R^*. At the end of the first phase, when d is relatively greater than R^*, the UAV finds the tangent lines from its current position to the circle with the radius R^*. With d relatively greater than R^*, one can assume that, in the second phase, based on scheme #1, the UAV flies on the tangent line to reach the tangency point (second virtual objective position). Once at this point, the UAV has reached the reference radius and switches to scheme #3. In the third phase, based on scheme #3, the UAV loiters around the origin with $R_1 = R^*$. The details of feedback linearization, control laws and stability analysis of scheme #1 and scheme #3 were discussed in the previous subsections and are not repeated here. Simulation results of this scheme will be given in "Simulations" section.

SIMULATIONS

In this section, some case studies are developed to verify the feasibility of the proposed schemes. A light fixed-wing UAV is considered, with its characteristics given in Table 1. In the simulations, where applicable, the initial condition of the UAV is assumed to be $[-1{,}800\text{ m}\ \ 2{,}500\text{ m}\ \ 240\text{ deg}\ \ 1\text{ deg/s}\ \ 300\text{ m}\ \ 10\text{ m/s}\ \ 10\text{ deg}\ \ 1\text{ deg/s}]^T$. For the first scheme, the reference signal is assumed to be $[100\text{ m}\ \ -20\text{ m}\ \ 500\text{ m}]^T$. For the described case study, simulations were carried out and the results are shown in Fig. 6.

As it can be readily seen from Fig. 6, after the initial transition, the UAV has aligned its motion such that it flies almost over the objective position on a straight line. Once on this line, the objective position is monitored by merely controlling the angle of the camera (see Fig. 7).

As it was expected, in this scheme, the camera angle will approach zero as the UAV flies toward the objective position. As the UAV flies away from the objective position, the camera angle will approach π, as $t \rightarrow \infty$.

Table 1. Characteristics of the light fixed-wing UAV.

Mass (kg)	Moment of inertia — z-axis (kg·m²)	Moment of inertia of the camera (kg·m²)	Forward velocity (m/s)
1	0.01	0.001	10

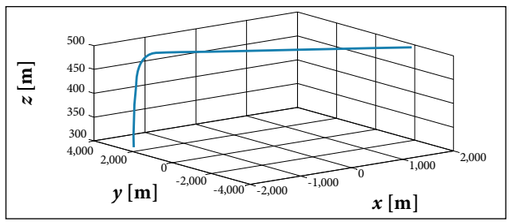

Figure 6. UAV trajectory obtained from scheme #1.

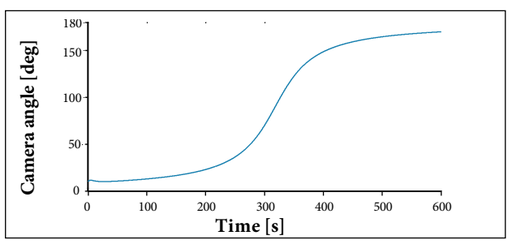

Figure 7. Forward-looking camera angle obtained from scheme #1.

For the second scheme, the reference signal is assumed to be $[-50\ \text{m}\ -50\ \text{m}\ 500\ \text{m}]^{\text{T}}$. For the described case study, simulations were carried out and the results are shown in Fig. 8.

As it can be seen from Fig. 8, the UAV has successfully converged to a loitering motion around the objective position. Also, as expected, the camera angle converges to a fixed value in the loitering motion (see Fig. 9).

The initial conditions of the third scheme are assumed to be identical to those of the first scheme. Here, the reference signal is assumed to be $[R_0\ 500\ \text{m}\ 30\ \text{deg}]^{\text{T}}$, where R_0 is the square distance of the UAV from the origin, at the initial time. Similar to the previous scenarios, simulations were carried out and the results are shown in Fig. 10.

Also, in this scheme, it is possible for the UAV to converge to a loitering circle with radius smaller/greater than the initial one. For the loitering radius of 1,500 and 4,500 m, simulations were carried out and the results are shown in Figs. 11 and 12, respectively. It can be seen from Figs. 11 and12 that the UAV has successfully converged to a loitering motion around the origin in both scenarios. Yet, it must be reminded that scheme #3 can fail if the UAV flies in the radial direction. Thus, it is recommended that one employs scheme #4 if a loitering motion is desirable.

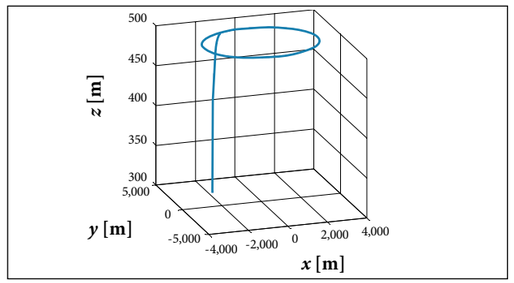

Figure 8. UAV trajectory obtained from scheme #2.

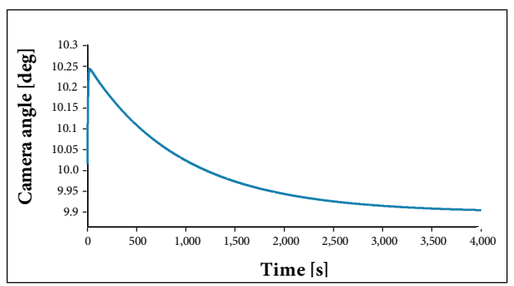

Figure 9. Side-looking camera angle obtained from scheme #2.

It is important to note that scheme #4 includes scenarios where the loitering radius can be smaller/greater than the initial distance of the UAV from the origin.

To verify the feasibility of scheme #4, a case study is developed in which the UAV is at the same initial condition as before. In the first example, let's assume that the UAV is desired to loiter around the origin with a radius of 1,500 m, a value smaller than its initial distance to the origin. For this case study, simulation results are shown in Fig. 13.

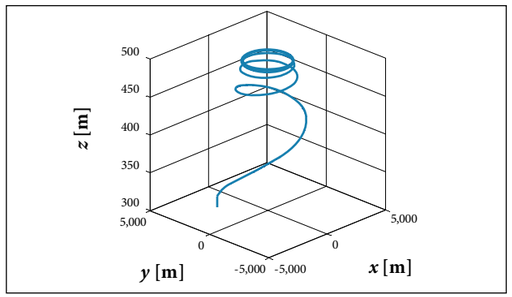

Figure 10. UAV trajectory obtained from scheme #3 — first example.

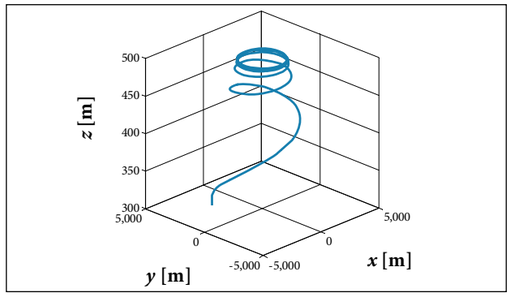

Figure 11. UAV trajectory obtained from scheme #3 — second example.

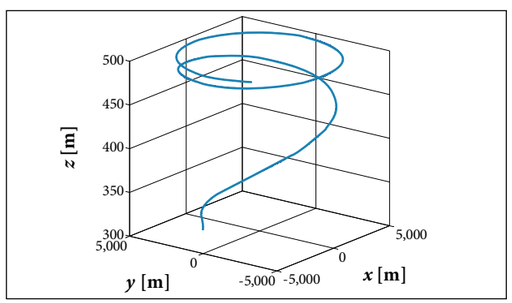

Figure 12. UAV trajectory obtained from scheme #3 — third example.

In Fig. 13, the first and the second phases of the path are shown in red and blue, respectively (see Fig. 4). As it can be seen from the figure, the UAV has successfully converged to the desired reference signal. In the second case study, assume that the UAV is desired to loiter around the origin with a radius of 4,000 m, a value greater than its initial distance to the origin. For this case study, simulation results are shown in Fig. 14, where the first and the second phases of the path are shown in red and the last phase is shown in blue (see Fig. 5). As it can be seen from Fig. 14, the UAV has successfully converged to a loitering motion around the origin with the desired loitering radius.

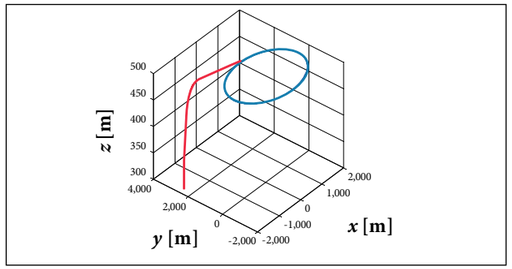

Figure 13. UAV trajectory obtained from scheme #4 — first case study.

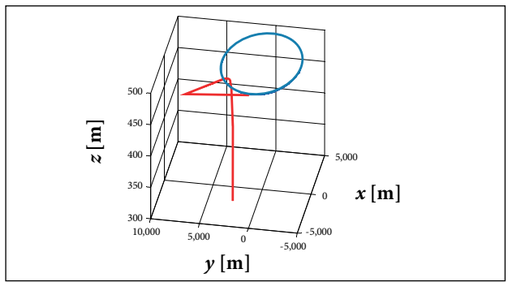

Figure 14. UAV trajectory obtained from scheme #4 — second case study.

CONCLUSION

In this paper, several feedback linearization schemes were studied to make a fixed-wing UAV, with constant forward velocity, (i) fly over or (ii) loiter around a stationary objective position. Throughout the paper, advantages and disadvantages of each scheme were discussed. A main drawback of the proposed schemes is that they do not take account of the maximum angular velocity constraint of fixed-wing UAVs. In scheme #1, the proposed method failed if the UAV was exactly above the objective position. Scheme #2 was disadvantageous in the sense that the loitering radius cannot be explicitly controlled. This was improved in scheme #3. Yet, the method in scheme #3 failed when the UAV had to fly radially inward or radially outward. However, if the heading of the UAV did not fall within this region, the UAV converged to a loitering motion around the origin. In scheme #4, the UAV had to be far enough from the objective circle. In this manner, one could assume that the UAV reaches the tangency point with its heading far from inward-outward direction, and therefore scheme #3 could bring the UAV to loiter around the objective position, with desirable radius. It is important to note that, in scheme #3 and scheme #4, the switching from a control strategy to another was given as an equality-type condition. Therefore, for real-world implementation, thresholds must be defined, and the equalities must be replaced by appropriate inequalities.

ACKNOWLEDGEMENTS

The authors gratefully acknowledge the financial support of Conselho Nacional de Desenvolvimento Científico e Tecnológico (CNPq), Financiadora de Estudos e Projetos (FINEP), Fundação de Amparo à Pesquisa do Estado de Minas Gerais (FAPEMIG) and Coordenação de Aperfeiçoamento de Pessoal de Nível Superior (CAPES), Brazil.

REFERENCES

Almurib HAF, Nathan PT, Kumar TN (2011) Control and path planning of quadrotor aerial vehicles for search and rescue. Proceedings of the IEEE SICE Annual Conference; Tokyo, Japan.

Beard RW, McLain TW, Nelson DB, Kingston D, Johanson D (2006) Decentralized cooperative aerial surveillance using fixed-wing miniature UAVs. Proc IEEE 94(7):1306-1324. doi: 10.1109/JPROC.2006.876930

Bonyan Khamseh H, Pimenta LCA, Tôrres LAB (2014) Decentralized coordination of constrained fixed-wing unmanned aerial vehicles: circular orbits. Proceedings of the IFAC World Congress; Cape Town, South Africa.

Casbeer DW, Kingston DB, Beard RW, McLain TW, Li SM, Mehra R (2006) Cooperative forest fire surveillance using a team of small unmanned air vehicles. Int J Syst Sci 37(6)351-360. doi: 10.1080/00207720500438480

Costa FG, Ueyama J, Braun T, Pessin G, Osório FS, Vargas PA (2012) The use of unmanned aerial vehicles and wireless sensor network in agricultural applications. Proceedings of the IEEE International Geoscience and Remote Sensing Symposium; Munich, Germany.

Fan W, Zhiyong G (2009) An approach to formation maneuvers of multiple nonholonomic agents using passivity techniques. Proceedings of the Chinese Control and Decision Conference; Guilin, China.

Frew E, Lawrence D, Morris S (2008) Coordinated standoff tracking of moving targets using Lyapunov guidance vector fields. J Guid Contr Dynam 31(2):290-306. doi: 10.2514/1.30507

Gonçalves MM, Pimenta LCA, Pereira GAS (2011) Coverage of curves in 3D with swarms of nonholonomic aerial robots. Proceedings of the IFAC World Congress; Milano, Italy.

Gonçalves VM, Pimenta LCA, Maia CA, Dutra BCO, Pereira GAS (2010) Vector fields for robot navigation along time-varying curves in n-dimensions. IEEE Trans Robot26(4):647-659. doi: 10.1109/TRO.2010.2053077

Hafez AT, Marasco AJ, Givigi AN, Beaulieu A, Rabbath CA (2013) Encirclement of multiple targets using model predictive control. Proceedings of the American Control Conference; Washington, USA.

Hsieh MA, Kumar V, Chaimowicz L (2008) Decentralized controllers for shape generation with robotic systems. Robotica 26(5):691-701. doi: 10.1017/S0263574708004323

Hsieh MA, Loizou S, Kumar RV (2007) Stabilization of multiple robots on stable orbits via local sensing. Proceedings of the IEEE International Conference on Robotics and Automation; Rome, Italy.

Kanchanavally S, Ordonez R, Schumacher CJ (2006) Path planning in three dimensional environment using feedback linearization. Proceedings of the American Control Conference; Minneapolis, USA.

Li H, Wang B, Liu L, Tian G, Zheng T, Zhang J (2013) The design and application of SmartCopter: an unmanned helicopter based robot for transmission line inspection. Proceedings of the Chinese Automation Congress; Changsha, China.

Marasco AJ, Givigi SN, Rabbath CA (2012) Model predictive control for the dynamic encirclement of a target. Proceedings of the American Control Conference; Montreal, Canada.

doi: 10.5028/jatm.v8i1.555

Structure Synthesis and Optimization of Feed Support Mechanisms for a Deployable Parabolic Antenna

Xiaoke Song[1], Hongwei Guo[1], Rongqiang Liu[1], Zongquan Deng[1]

ABSTRACT: In this paper, a systematic method to synthesize parallel mechanisms for feed support mechanisms based on screw theory is proposed. First, the motion requirement of the feed support mechanism is studied. Then, a class of parallel mechanisms having a translational motion with different degrees of freedom is synthesized based on the constraint-synthesis method. Then, these parallel mechanisms are modified based on the specificities of deployable mechanisms, and two kinds of mechanisms are selected as the unit for the feed support mechanism. Finally, the deployment ratio of two kinds of mechanisms is optimized. The configurations obtained in this paper can enrich the types of feed support mechanisms.

KEYWORDS: Feed support mechanism, Deployable mechanism, Structure synthesis, Deployment ratio, Parallel mechanism, Screw theory.

INTRODUCTION

Large deployable parabolic antennas are widely used on the aerospace equipment with the development of satellite communication technology (Sauder and Thomson 2014; Cherniavsky *et al.* 2004; Yurduseven *et al.* 2012). They are composed of parabolic reflector, feed, feed support mechanism, and so on. There are positive and offset feed for the position of the feed in the parabolic antenna. The position accuracy concerns the properties of the antennas (Tayebi *et al.* 2013; Pour *et al.* 2014; Silver 1949). Thus, for the feed support mechanism, it should present high precision, high stiffness, large deployment ratio, simple structure etc. At present, there are several types of feed support mechanisms, such as robot arm, static truss and so on (Sauder and Thomson 2014).

This paper studies the feed support mechanism of an inflatable deployable parabolic antenna. As the support of the feed, the mechanism takes it to a predetermined position, so the mechanism only needs to carry out the translation motion in one dimension. Based on the requirements on the feed support mechanisms and the advantages of parallel mechanisms, such as high precision and high rigidity (Merlet 2006; Tsai 1999), we select the one dimensional parallel mechanisms as the research object and take structure synthesis and optimization for it. Regarding the structure synthesis of the parallel mechanism, lots of achievements have been obtained. Fang and Tsai (2002), Huang and Li (2002) and Xu *et al.* (2012) have used the screw theory to synthesize lots of parallel mechanisms. Li *et al.* (2004) synthesized the 3R2T 5DOF parallel mechanisms by Lie group. Gao *et al.* (2011) synthesized the parallel mechanisms with two

1.Harbin Institute of Technology – State Key Laboratory of Robotics and System – Harbin/Heilongjiang – China.
Author for correspondence: Hongwei Guo | Yikuang Street 2, Nangang District | Harbin/Heilongjiang – China | Email: ghwhit@163.com
Received: 09/17/2015 | **Accepted:** 11/23/2015

dimensional rotations. In this study, we have chosen screw theory to synthesize the parallel mechanisms.

The rest of this paper is organized as follows. Firstly, the inflatable deployable parabolic antenna is introduced, and the requirement of the feed support mechanism is given. Following, the constraint-synthesis method based on screw theory is briefly introduced. Then, the structure synthesis of the mechanism is carried out. The resulted structures are modified and one suitable type is selected. The deployment ratio of the selected structure is optimized next. At last, a conclusion is given.

MOTION REQUIREMENT FOR THE FEED SUPPORT MECHANISM

Figure 1 shows the studied inflatable deployable parabolic antenna. The antenna has two forms: folded and deployed. Regarding the feed support mechanism, it is composed of several deployable units serially connected. The unit should output a translation along the z-axis. It can also have motions in other directions. As parallel mechanisms have the advantages of high stiffness and high precision, we selected parallel mechanisms as the unit. Based on the experience of practical engineering, we focused on the synthesis of parallel mechanisms with the degree of freedom (DOF) of $1T^z$, $1T^z1R^z$, and $1T^z2R^{xy}$ (the numbers before T and R denote the number of DOF; T and R denote the translational and rotational freedom separately; the right superscripts denote the direction of the motion). Because of the difficulties in driving and locking prismatic joints, we only used revolute joints in the structure synthesis. Therefore, we considered the structure synthesis for parallel mechanisms with the DOF of $1T^z$, $1T^z1R^z$, and $1T^z2R^{xy}$, which have only revolute joints.

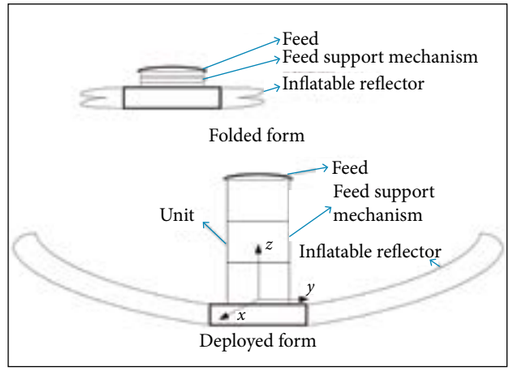

Figure 1. The inflatable deployable parabolic antenna.

BASIC CONCEPTS AND THE CONSTRAINT-SYNTHESIS METHOD

In screw theory, a unit screw is defined as below:

$$\$ = (s; s_0) = (s; \boldsymbol{r} \times \boldsymbol{s} + h\boldsymbol{s}) \tag{1}$$

where: $\boldsymbol{s}$ is a unit vector and denotes the direction of the screw axis; $\boldsymbol{r}$ is the position vector of any point on the screw axis; h is the pitch of the screw.

For a screw, $\$^r = (\boldsymbol{s}_r; \boldsymbol{s}_{0r})$, and a set of screws, $\$_1, \$_2, \ldots, \$_n$, they are said to be reciprocal if they satisfy the condition:

$$\$_j \circ \$^r = \boldsymbol{s}_j \cdot \boldsymbol{s}_{0r} + \boldsymbol{s}_r \cdot \boldsymbol{s}_{0j} = 0 \ (j = 1, 2, \ldots, n) \tag{2}$$

where: o represents the reciprocal product; $\$_j$ represents the j-th screw.

We call the screw a twist if it represents an instantaneous motion of a rigid body. We call the screw a wrench if it represents a force and a coaxial couple acting on a rigid body. A force or a rotation can be given by $(\boldsymbol{s}; \boldsymbol{r} \times \boldsymbol{s})$, and a couple or a translation can be given by $(0; \boldsymbol{s})$. In the synthesis process, the prismatic joint (P) outputs a translation, and the revolute joint (R) outputs a rotation. Other types of joints can be expressed as the combination of the two basic joints. For example, the spherical joint (S) can be expressed as three R joints intersecting at a point, but they are not coplanar; the universal joint (U) can be expressed as two intersecting R joints; the cylindrical joint (C) can be expressed as a P joint and a R joint which are concentric.

For the parallel mechanisms, if a set of screws represent the twists of one limb, then its reciprocal screws, $\$^r_1, \$^r_2, \ldots, \$^r_n$ ($n < 6$) represent the constraint wrenches the limb exerted on the moving platform. Thus the combination of these reciprocal screws of all limbs determines the constraints of the moving platform, and the motion twists of the moving platform are reciprocal to the combination of the constraint wrenches. This is the mathematical basis for the constraint-synthesis method.

The process of the structure synthesis by constraint-synthesis method is shown as follows. First, the motion twists are obtained based on the motion requirement of the mechanism, then we get the constraint wrenches of the moving platform, which are reciprocal to the motion twists. Next, we distribute the constraint wrenches to each limb. Thus we get the motion twists of each limb based on the constraint wrenches of the limb, as they are reciprocal, then construct the limb kinematic chain based on the motion twists. Finally, we assemble the limbs in proper configuration to guarantee that the combination of the limb constraint wrenches of each limb is equal to the constraint wrenches of moving platform.

STRUCTURE SYNTHESIS OF PARALLEL MECHANISMS FOR FEED SUPPORT MECHANISMS

The feed support mechanism is used to support the feed of antennas; it would suffer the interference from every direction, so the mechanism should have roughly the same load capacity on every direction. According to the experience on practical engineering and the load of feed support mechanisms, the mechanism should have three or four limbs, as more limbs make the manufacturing complicated and less limbs cannot get the uniform load capacity. So the objective in this study is to synthesize parallel mechanisms with three or four limbs composed of only revolute joints.

For the parallel mechanisms with one DOF of $1T^z$, the twist system of the moving platform is represented as:

$$\$_1 = (1\ \ 0\ \ 0;\ \ 0\ \ 0\ \ 0)$$
$$\$_2 = (0\ \ 1\ \ 0;\ \ 0\ \ 0\ \ 0) \tag{3}$$
$$\$_3 = (0\ \ 0\ \ 0;\ \ 0\ \ 0\ \ 1)$$

From Eq. 2, the constraint wrench system which is reciprocal to the twist system is obtained as:

$$\$^r_1 = (1\ \ 0\ \ 0;\ \ 0\ \ 0\ \ 0)$$
$$\$^r_2 = (0\ \ 1\ \ 0;\ \ 0\ \ 0\ \ 0)$$
$$\$^r_3 = (0\ \ 0\ \ 0;\ \ 1\ \ 0\ \ 0) \tag{4}$$
$$\$^r_4 = (0\ \ 0\ \ 0;\ \ 0\ \ 1\ \ 0)$$
$$\$^r_5 = (0\ \ 0\ \ 0;\ \ 0\ \ 0\ \ 1)$$

which represents two constraint forces whose direction is parallel to the x-axis and y-axis separately and three constraint couples whose direction is parallel to the x-axis, y-axis, and z-axis separately.

Then we get the constraint wrench system of mechanisms with DOF of $1T^z1R^z$ and $1T^z2R^{xy}$ in the same way, just as Eqs. 5 and 6.

$$\$^r_1 = (1\ \ 0\ \ 0;\ \ 0\ \ 0\ \ 0)$$
$$\$^r_2 = (0\ \ 1\ \ 0;\ \ 0\ \ 0\ \ 0) \tag{5}$$
$$\$^r_3 = (0\ \ 0\ \ 0;\ \ 1\ \ 0\ \ 0)$$
$$\$^r_4 = (0\ \ 0\ \ 0;\ \ 0\ \ 1\ \ 0)$$

$$\$^r_1 = (1\ \ 0\ \ 0;\ \ 0\ \ 0\ \ 0)$$
$$\$^r_2 = (0\ \ 1\ \ 0;\ \ 0\ \ 0\ \ 0) \tag{6}$$
$$\$^r_3 = (0\ \ 0\ \ 0;\ \ 0\ \ 0\ \ 1)$$

Based on the reciprocal condition of screws, we then analyze the relation between a revolute joint and its constraint wrenches (Fang and Tsai 2002).

We define three unit screws, $\$_r = (\boldsymbol{w}; \boldsymbol{r}_1 \times \boldsymbol{w})$, $\$_F = (\boldsymbol{f}; \boldsymbol{r}_2 \times \boldsymbol{f})$, $\$_C = (0\ 0\ 0; \boldsymbol{c})$, to indicate the revolute joint, constraint force and constraint couple, respectively, where $\boldsymbol{w}$ indicates the direction of the revolute joint; $\boldsymbol{r}_1$ indicates a point on the joint; $\boldsymbol{f}$ indicates the direction of the constraint force; $\boldsymbol{r}_2$ indicates a point on the force; $\boldsymbol{c}$ indicates the direction of constraint couple. As the reciprocal product of revolute joint and constraint force is zero, as well as the reciprocal product of revolute joint and constraint couple, we have Eqs. 7 and 8.

$$\begin{aligned}\$_r \circ \$_F &= \boldsymbol{w} \cdot (\boldsymbol{r}_2 \times \boldsymbol{f}) + \boldsymbol{f} \cdot (\boldsymbol{r}_1 \times \boldsymbol{w}) \\ &= \boldsymbol{r}_2 \cdot (\boldsymbol{f} \times \boldsymbol{w}) + \boldsymbol{r}_1 \cdot (\boldsymbol{w} \times \boldsymbol{f}) \\ &= (\boldsymbol{r}_2 - \boldsymbol{r}_1) \cdot (\boldsymbol{f} \times \boldsymbol{w}) \\ &= 0\end{aligned} \tag{7}$$

From Eq. 7, we conclude that $\boldsymbol{r}_2 - \boldsymbol{r}_1 = 0$ or $\boldsymbol{f} \times \boldsymbol{w} = 0$, so $\boldsymbol{r}_2 = \boldsymbol{r}_1$ or $\boldsymbol{f} /\!/ \boldsymbol{w}$, that is to say, the axis of a revolute joint is parallel or intersects the constraint force.

$$\$_r \circ \$_C = \boldsymbol{w} \cdot \boldsymbol{c} = 0 \tag{8}$$

From Eq. 8, we conclude that $\boldsymbol{w} \perp \boldsymbol{c}$, that is to say, the axis of a revolute joint is perpendicular to the constraint couple.

For a kinematic chain with only revolute joints, the geometric condition of the revolute joints would change after motion, then the relation between revolute joints and constraints would change. So the mobility of the parallel mechanism composed of these kinematic chains would change. Only the revolute joints which are parallel or intersect at one point, or the chains composed of these two kinds of revolute joints, would keep their geometric conditions steady and their constraints would keep steady. These kinematic chains are shown in Fig. 2, where $\boldsymbol{F}$ indicates the constraint force and $\boldsymbol{C}$ indicates the constraint couple.

In these kinematic chains, there exist two kinds of revolute joints: the type-1 joints intersect at a common point and are not coplanar; the type-2 joints are parallel. According to the relation between revolute joint and its constraints, the geometric

condition and constraint wrenches of the kinematic chains are shown in Table 1.

In Table 1, the subscript numbers represent the type of revolute joints, and the superscript letters represent the axis to which the joints are parallel.

Using the kinematic chains shown above, we carry out the synthesis of the three kinds of mechanisms.

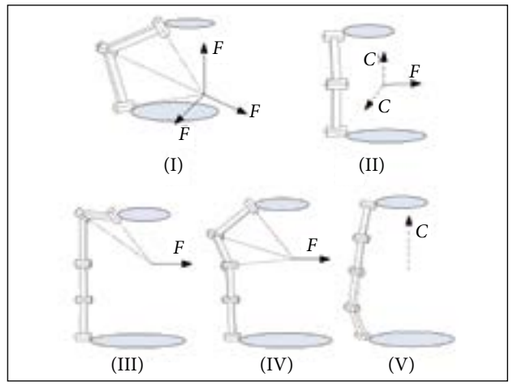

Figure 2. The kinematic chains with constant geometric conditions.

Table 1. The limbs with constant geometrical condition.

Limb type	Constraint wrenches	Denotation
I	Three forces passing through the central point which are not coplanar	$R_1R_1R_1$
II	One force parallel to the R joints; two couples perpendicular to the R joints which are not parallel	$R_2R_2R_2$
III	One force passing through the central point and parallel to the R joints	$R_1R_1R_2R_2R_2$
IV	One force passing through the central point and parallel to the R joints	$R_1R_1R_1R_2R_2$
V	One couple perpendicular to all the R joints	$R^A{}_2R^A{}_2R^A{}_2R^B{}_2R^B{}_2$

1 T^z PARALLEL MECHANISMS

From the constraint-synthesis method, we know that the moving platform constraint system is the combination of all the limb constraint systems, so they can be derived from Eq. 4 and the relationship of constraint forces, couples, and constraint motion, just as shown in Table 2.

The mechanisms constructed in the mentioned ways are shown as follows.

In Fig. 3, the numbers i (i = 1, 2, …) indicate the number of the limb; $\boldsymbol{F}_i$ (i = 1, 2, …) indicate the constraint force which the limb i exerts on the mobile platform; $\boldsymbol{C}_i$ (i = 1, 2, …) indicate the constraint couple exerted by the limb i; $\boldsymbol{C}_{ij}$ (i = 1, 2, …; j = 1, 2, …) indicate the constraint couple j which the limb i exerts on the mobile platform.

For the mechanism in Fig. 3a, $\boldsymbol{F}_1$ and $\boldsymbol{F}_2$ constrain the translations along the x-y-axes; $\boldsymbol{C}_{11}$ and $\boldsymbol{C}_{21}$ constrain the rotations around the x-y-axes; $\boldsymbol{C}_{12}$ and $\boldsymbol{C}_{22}$ are parallel and constrain the rotation around the z-axis, then the mechanism retains only one DOF of the translation along the z-axis.

For the mechanism in Fig. 3b, $\boldsymbol{F}_1$ and $\boldsymbol{F}_2$ are coplanar and intersect at the common point A, so they constrain two translations in the plane. As the plane is parallel to the base platform, the translations along the x-y-axes are constrained.

Table 2. The limbs of the 1 T^z parallel mechanism.

Limb type	Limb number	Limb constraint	Geometric conditions
II	2	1 force and 2 couples	The type-2 revolute joints in two limbs are not parallel
III or IV	2	1 force	The central points of the type-1 revolute joints of the two limbs are coincident, and the type-2 revolute joints are parallel to the fixed base and not parallel between two limbs
V	3	1 couple	The three constraint couples C are not coplanar

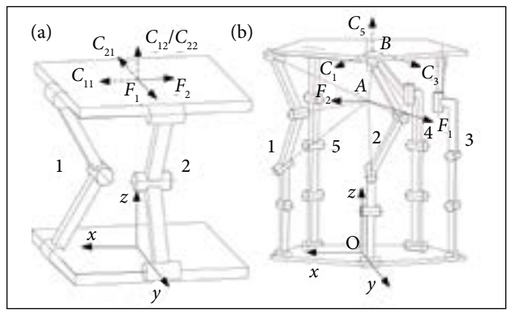

Figure 3. The parallel mechanisms with the DOF of 1 T^z.

$\boldsymbol{C}_3$, $\boldsymbol{C}_4$, and $\boldsymbol{C}_5$ are not coplanar and constrain three rotations in space. So the mechanism has only the DOF of translation along the z-axis.

The first mechanism is the Sarrus mechanism. It is widely used as deployable mechanisms with three or four limbs, such as the HIMAT. The other mechanism is too complicated to use as a deployable unit for the feed support mechanisms.

1 T^z1 R^z PARALLEL MECHANISMS

For the parallel mechanisms with the DOF of 1 T^z1 R^z, the moving platform is constrained with two forces and two couples. The constraint could be exerted by four limbs, two limbs of type III or IV and two limbs of type V, with each limb exerting a force or a couple. The limbs of the structures are shown in Table 3.

The mechanism constructed by the mentioned way is shown as follows.

For the mechanism in Fig. 4, as well as the analysis in the structure synthesis of 1 $\boldsymbol{T^z}$ parallel mechanisms, $\boldsymbol{F}_1$ and $\boldsymbol{F}_2$ intersect at the common point A, so they constrain two translations along the x-y-axes. $\boldsymbol{C}_3$ and $\boldsymbol{C}_4$ are coplanar and constrain the rotations around the x-y-axes. So the mechanism has the DOF of 1 T^z1 R^z.

Table 3. The limbs of the 1 T^z1 R^z parallel mechanism.

Limb type	Limb number	Limb constraint	Geometric conditions
III or IV	2	1 force	The central points of the type-1 revolute joints of the two limbs are coincident. The type-2 revolute joints are parallel to the fixed base and not parallel between two limbs
V	2	1 couple	The constraint couples are parallel to the fixed base, but not parallel to each other.

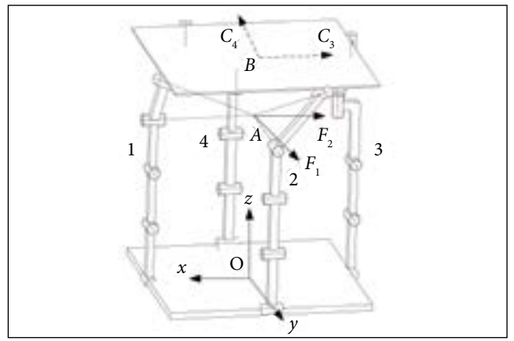

Figure 4. The parallel mechanisms with the DOF of 1 T^z1 R^z.

1 T^z2 R^{xy} PARALLEL MECHANISMS

For the parallel mechanisms with DOF of 1 T^z2 R^{xy}, the constraint wrenches are composed of two forces along the x-axis and y-axis, respectively, and a couple around the z-axis. The constraints could be exerted by three kinematic limbs of type III or IV, where the three constraint forces are parallel to the fixed base and coplanar but do not intersect at a point. Or the constraints are exerted by two chains of type III or IV and one chain of type V, where the two constraint forces are parallel to the fixed base, intersect at a point, and the constraint couple is perpendicular to the fixed base. The constraint could also be exerted by four limbs, type III or IV, where the couple is exerted by two parallel forces. The detailed configuration is given in Table 4.

The mechanisms constructed in the mentioned way are shown in Fig. 5 as follows.

Table 4. The limbs of the 1 T^z1 R^{xy} parallel mechanism.

Limb type	Limb number	Limb constraint	Geometric conditions
III or IV	2	1 force	The central points of the two limbs are coincident. The type-2 revolute joints are parallel to the fixed base and not parallel between two limbs
V	1	1 couple	The constraint couples are perpendicular to the fixed base
III or IV	3	1 force	The central points of the three limbs are coplanar. The type-2 revolute joints of each group are parallel to the fixed base, but they are not parallel between different groups
III or IV	4	1 force	The four limbs are divided into two groups, each one with two limbs. The central points of the four limbs are coplanar. The type-2 revolute joints of each group are parallel, but they are not parallel between two groups

In Fig. 5, $\boldsymbol{C}_{i-j}$ ($i = 1, 2, \ldots; j = 1, 2, \ldots$) indicate the constraint couple exerted by two parallel constraint forces, $\boldsymbol{F}_i$ and $\boldsymbol{F}_j$; $\boldsymbol{C}_{i-j-k}$ ($i = 1, 2, \ldots; j = 1, 2, \ldots; k = 1, 2, \ldots$) indicate the constraint couple exerted by three coplanar constraint forces, $\boldsymbol{F}_i$, $\boldsymbol{F}_j$ and $\boldsymbol{F}_k$.

For the mechanism in Fig. 5a, as well as the analysis in the structure synthesis of $1\boldsymbol{T}^z$ and $1\boldsymbol{T}^z\boldsymbol{R}^{xy}$ parallel mechanisms, the constraint forces $\boldsymbol{F}_1$ and $\boldsymbol{F}_2$ intersect at the point A and they are parallel to the base platform, so they constrain the translations along x-y-axes. The constraint couple $\boldsymbol{C}_3$ constrains the rotation around z-axis. So this mechanism has the DOF of $1T^z2R^{xy}$.

For the mechanism in Fig. 5b, $\boldsymbol{F}_1$, $\boldsymbol{F}_2$, and $\boldsymbol{F}_3$ are coplanar and not parallel; besides, they do not intersect at a common point, so they exert a couple $\boldsymbol{C}_{1-2-3}$ to the mobile platform. The two translations in the plane and one rotation around the normal of the plane are constrained. As plane ABC is parallel to the base platform, the mechanism meets our requirements.

For the mechanism in Fig. 5c, $\boldsymbol{F}_1$ and $\boldsymbol{F}_3$ are parallel; $\boldsymbol{F}_2$ and $\boldsymbol{F}_4$ are parallel; $\boldsymbol{F}_1$, $\boldsymbol{F}_2$, $\boldsymbol{F}_3$, and $\boldsymbol{F}_4$ are coplanar, so two couples, $\boldsymbol{C}_{1-3}$ and $\boldsymbol{C}_{2-4}$, are exerted to the mobile platform and then the translations along x-y-axes and rotation around z-axis are constrained.

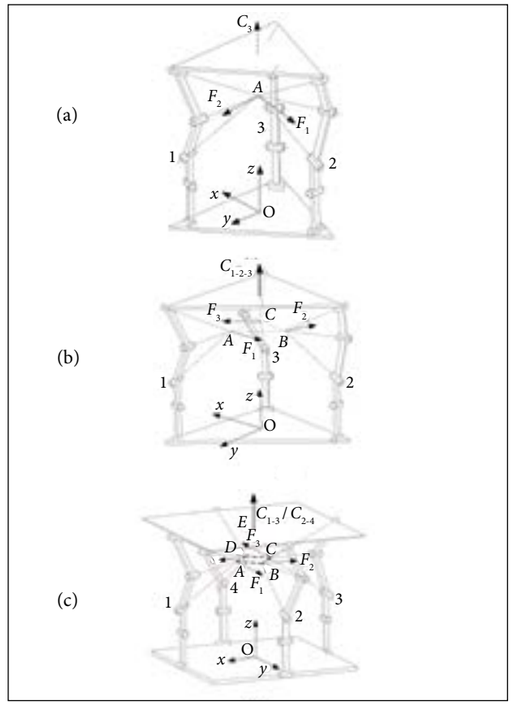

Figure 5. The parallel mechanisms with the DOF of $1T^z1R^{xy}$.

THE MODIFICATION OF THE PARALLEL MECHANISMS AND THE SELECTION OF THE DEPLOYABLE UNIT

For the feed support mechanism, the linkage in the limb of the mechanism should be as few as possible, in order to actuate and lock the mechanism easily. Based on the content of the basic concepts, two intersecting revolute joints compose a U joint, and three revolute joints which are intersecting but not coplanar compose a S joint. So we can use the U and S joints to substitute the revolute joints in special configuration to reduce the linkages. The result is shown in Table 5. Three mechanisms with the typical configurations, 3 - $R_1U_{12}R_2R_2$, 3 - R_2R_2S, and 4 - R_2R_2S, are shown in Fig. 6.

Table 5. The mechanisms containing universal and spherical joints.

Mobility	Limb composed only of *R* joints	Limb composed of U and S joints
$1T^z$	2 - $R_2R_2R_2$	None
	$2-R_1R_1R_2R_2R_2-3-R^A_2R^A_2R^A_2R^B_2R^B_2$	$2-R_1U_{12}R_2R_2-3-R^A_2R^A_2U^{AB}_2R^B_2$
	$2-R_1R_1R_1R_2R_2-3-R^A_2R^A_2R^A_2R^B_2R^B_2$	$2-R_1R_1U_{12}R_2-3-R^A_2R^A_2U^{AB}_2R^B_2$
$1T^z1R^z$	$2-R_1R_1R_2R_2R_2-2-R^A_2R^A_2R^A_2R^B_2R^B_2$	$2-R_1U_{12}R_2R_2-2-R^A_2R^A_2U^{AB}_2R^B_2$
	$2-R_1R_1R_2R_2R_2-2-R^A_2R^A_2R^A_2R^B_2R^B_2$	$2-R_1R_1U_{12}R_2-2-R^A_2R^A_2U^{AB}_2R^B_2$
$1T^z2R^{xy}$	$2-R_1R_1R_2R_2R_2-1-R^A_2R^A_2R^A_2R^B_2R^B_2$	$2-R_1U_{12}R_2R_2-1-R^A_2R^A_2U^{AB}_2R^B_2$
	$2-R_1R_1R_2R_2R_2-1-R^A_2R^A_2R^A_2R^B_2R^B_2$	$2-R_1R_1U_{12}R_2-1-R^A_2R^A_2U^{AB}_2R^B_2$
	3 - $R_1R_1R_2R_2R_2$	3 - $R_1U_{12}R_2R_2$, 3 - R_2R_2S
	3 - $R_1R_1R_1R_2R_2$	3 - $R_1R_1U_{12}R_2$
	4- $R_1R_1R_2R_2R_2$	4 - $R_1U_{12}R_2R_2$
	4 - $R_1R_1R_1R_2R_2$	4 - $R_1R_1U_{12}R_2$, 4 - R_2R_2S

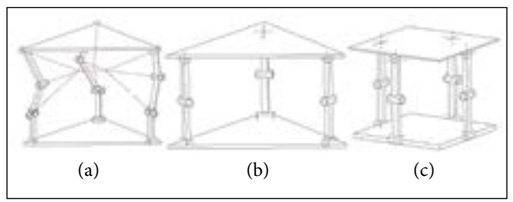

Figure 6. The 3-D model of parallel mechanisms 3 - $R_1U_{12}R_2R_2$, 3 - R_2R_2S, and 4 - R_2R_2S.

As the limb of 2 - $R_2R_2R_2$, 4 - R_2R_2S, and 3 - R_2R_2S mechanisms consists of only two linkages, we select the three mechanisms as the alternative unit. The aerospace mechanism requires high reliability and robustness. The overconstraint mechanism would get stuck because of the interference between the limbs, and the light weight drive cannot provide enough power to overcome the deformation in the mechanism, so it is not the good candidate. Denote M as the number of DOF of the mechanism, n as the number of constraints of the limb, $\boldsymbol{F}_O$ as the number of overconstraints of the mechanism, then for the three kinds of mechanisms, the overconstraint is calculated as follows.

For the mechanism with the limb of $R_2R_2R_2$, it should consist of three limbs in order to have identical load capacity in all directions. Then we have:

$$F_O = 3n-(6-M) = 3\times3-(6-1) = 4 \tag{9}$$

For the mechanism with the configuration of 4 - R_2R_2S, we have:

$$F_O = 4n-(6-M) = 4\times1-(6-2) = 0 \tag{10}$$

For the mechanism with the configuration of 3 - R_2R_2S, we have:

$$F_O = 3n-(6-M) = 3\times1-(6-3) = 0 \tag{11}$$

From the result, we conclude that the 3 - $R_2R_2R_2$ mechanism has four overconstraints, and the other two mechanisms are not overconstrainable. Then we select the mechanisms 3 - R_2R_2S and 4 - R_2R_2S as the unit.

THE OPTIMIZATION OF DEPLOYMENT RATIO

The deployment ratio is the ratio between the length in deployed form and the length in folded form of the feed support mechanism. As the feed support mechanism is composed of the serially connected units, the deployment ratio of the feed support mechanism equals to the ratio between the length in the deployed form and the length in the folded form of the unit, as shown in Fig. 7.

$$\lambda = \frac{l_d}{l_f} \tag{10}$$

where: λ defines the deployment ratio; l_d defines the length in deployed form; l_f defines the length in folded form.

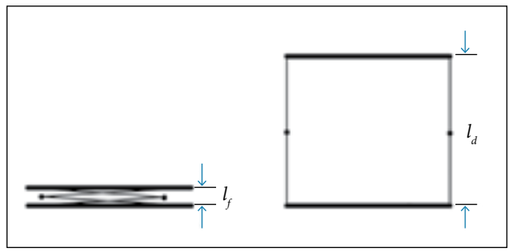

Figure 7. A unit in folded and deployed forms.

The feed support mechanism studied in this paper is limited to the movement in a predetermined cylinder A with radius r. The optimization objective is to find the structure parameters of the unit when it achieves the largest deployment ratio. The schematic diagrams of the two types of parallel mechanisms obtained in the modification and selection of parallel mechanisms are shown in Fig. 8, where θ is the angle between the limb projection and the edge, A is the predetermined cylinder, and α is the angle between the link and the base. When the angle θ changes, the two mechanisms still satisfy their geometric conditions presented in the section about structure synthesis of parallel mechanisms. For the mechanism 3 - R_2R_2S, $0 \le \theta \le \pi/6$; for the mechanism 4 - R_2R_2S, $0 \le \theta \le \pi/4$.

For the mechanism 3 - R_2R_2S, set $r = 300$ mm. When $\alpha = 0$, the mechanism folds. Set $l_f = 30$ mm. When $\alpha = \pi/2$, the mechanism deploys, and the limb turns into a vertical line. Then $l_d = 2l$, where l defines the link length. The links in the limb should not interfere to each other, as shown in Fig. 9.

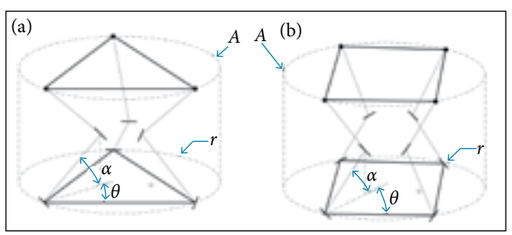

Figure 8. The schematic diagrams of the parallel mechanisms (a) 3 - R_2R_2S and (b) 4 - R_2R_2S.

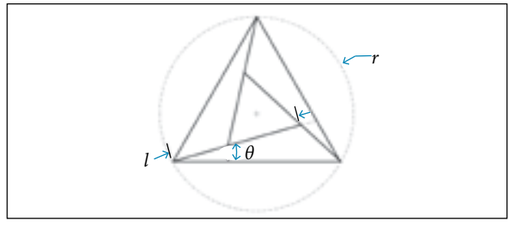

Figure 9. The top view of the mechanism 3 - R_2R_2S.

Then the link length l should follow Eq. 12:

$$l = \frac{\frac{3}{2}(1-\frac{4}{3}\sin^2\theta)}{\sin(\frac{\pi}{3}+\theta)}r \tag{12}$$

The deployment ratio $\lambda_{3\text{ - }R_2R_2S}$ is calculated as:

$$\lambda_{3\text{ - }R_2R_2S} = \frac{2l}{l_f} = \frac{3(1-\frac{4}{3}\sin^2\theta)}{\sin(\frac{\pi}{3}+\theta)l_f}r \tag{13}$$

For the mechanism 4 - R_2R_2S, we set $r = 300$. As in the limbs the two mechanisms are the same, we set $l_f = 30$ mm. Then we take the same process to calculate the deployment ratio as the mechanism 3 - R_2R_2S. The deployment ratio $\lambda_{4\text{ - }R_2R_2S}$ is shown in Eq. 14:

$$\lambda_{4\text{ - }R_2R_2S} = 2\sqrt{2}\cdot\frac{1-\sin^2\theta}{\cos\theta}\frac{r}{l_f} \tag{14}$$

Calculating λ on the value range of θ, we obtain the relation presented in Fig. 10.

According to Fig. 10, we conclude that, if we choose 3 - R_2R_2S as the unit, when $\theta = 0$, the deployment ratio achieves its largest value; if we choose 4 - R_2R_2S as the unit, when $\theta = 0$, the deployment ratio achieves its largest value. If the cylinder A is predetermined, the mechanism 3 - R_2R_2S has the largest deployment ratio.

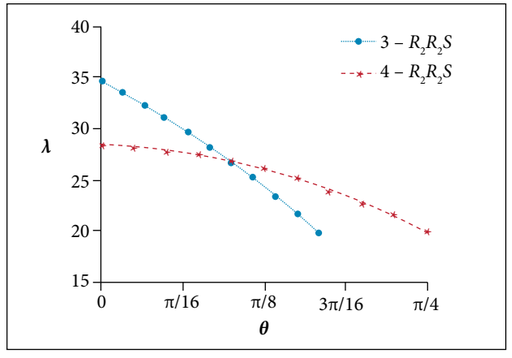

Figure 10. The relation between the deployment ratio λ and θ for mechanisms 3- R_2R_2S and 4 - R_2R_2S.

CONCLUSION

This paper proposes a systematic method to synthesize parallel mechanisms that can be used as feed support mechanisms based on screw theory. To initiate the synthesis, we first study the motion requirement of the feed support mechanisms. Then, three groups of parallel mechanisms are synthesized using the constraint-synthesis method. These mechanisms are then modified according to the practical engineering. Two kinds of parallel mechanisms are selected as the unit for the feed support mechanism. Then the structure parameters of the two kinds of units are optimized, and the mechanism with the largest deployment ratio is obtained. The configurations obtained in this paper can enrich the types of one-dimensional deployable mechanisms in engineering.

ACKNOWLEDGEMENTS

This paper is financially supported by the Natural Science Foundation of China (grant number 51275107) and the "111 Project" (grant number B07018).

REFERENCES

Cherniavsky AG, Gulyayev VI, Gaidaichuk VV, Fedoseev AI (2004). New developments in large deployable space antennae at S.P.A. EGS. Proceedings of the Engineering, Construction, and Operations in Challenging Environments, Earth and Space 2004; Houston, USA.

Fang Y, Tsai L (2002) Structure synthesis of a class of 4-DoF and 5-DoF parallel manipulators with identical limb structures. Int J Robot Res 21(9):799-810. doi: 10.1177/027836490202100931

Gao F, Yang J, Ge Q (2011) Type synthesis of parallel mechanisms having the second class GF sets and two dimensional rotations. J Mech Robot 3(1):011003. doi: 10.1115/1.4002697

Huang Z, Li Q (2002) General methodology for type synthesis of symmetrical lower-mobility parallel manipulators and several novel manipulators. Int J Robot Res 21(2):131-145. doi: 10.1177/027836402760475342

Li Q, Huang Z, Hervé M (2004) Type synthesis of 3R2T 5-DOF parallel mechanisms using the Lie group of displacements. IEEE T Robotic Autom 20(2):173-180. doi: 10.1109/TRA.2004.824650

Merlet JP (2006) Parallel robots. 2nd ed. Dordrecht: Springer.

Pour ZA, Shafai L, Tabachnick B (2014) A practical approach to locate offset reflector focal point and antenna misalignment using vectorial representation of far-field radiation patterns. IEEE T Antenn Propag 62(2):991-996. doi: 10.1109/TAP.2013.2292503

Sauder JF, Thomson MW (2014). The mechanical design of a mesh Ka-band parabolic deployable antenna (KaPDA) for CubeSats. AIAA 2015-1402. Proceedings of the 2nd AIAA Spacecraft Structures Conference; Florida, USA.

Silver S (1949) Microwave antenna theory and design. New York: McGraw-Hill.

Tayebi A, Gomez J, Gonzalez I, Catedra F (2013) Influence of the feed location on the performance of a conformed Fresnel zone reflector. IEEE Antenn Wireless Propag Lett 12:547-550. doi: 10.1109/LAWP.2013.2259460

Tsai LW (1999) Robot analysis: the mechanics of serial and parallel manipulator. New York: John Wiley & Sons.

Xu Y, Yao J, Zhao Y (2012) Type synthesis of spatial mechanisms for forging manipulators. Proc IME C J Mech Eng Sci 226(9):2320-2330. doi: 10.1177/0954406211433246

Yurduseven, O, Smith D, Pearsall N, Forbes I, Bobor-Oyibo F (2012). A solar parabolic reflector antenna design for digital satellite communication systems. Proceedings of the 8th IEEE, IET International Symposium on Communication Systems, Networks and Digital Signal Processing; Poznan, Poland.

doi: 10.5028/jatm.v8i1.509

Unscented Kalman Filter for Determination of Spacecraft Attitude Using Different Attitude Parameterizations and Real Data

Roberta Veloso Garcia[1], Hélio Koiti Kuga[2], Maria Cecília F. P. S. Zanardi[3]

ABSTRACT: The non-linear estimators are certainly the most important algorithms applied to real problems, especially those involving the attitude estimation of spacecraft. The purpose of this paper was to use real data of sensors to analyze the behavior of Unscented Kalman Filter (UKF) in attitude estimation problems when it is represented in different ways and compare it with the standard estimator for non-linear estimation problems. The robustness of the estimation was performed when this was subjected to imprecise initial conditions. The attitude parametrization was described in Euler angles, quaternion and quaternion incremental. The satellite China-Brazil Earth Resources Satellite and measurements provided by the Satellite Control Center of the Instituto Nacional de Pesquisas Espaciais were considered in the study. The results indicate that the behaviors for both estimators were equivalent for such parameterizations under the same conditions. However, comparing the Unscented Kalman Filter with the standard filter for non-linear systems, Extended Kalman Filter (EKF), it was observed that, in the presence of inaccurate initial conditions, the Unscented Kalman Filter presented a fast convergence whereas Extended Kalman Filter had problems and only converged later on.

KEYWORDS: Attitude estimation, Real data, Unscented Kalman Filter, Extended Kalman Filter, Quaternion, Euler angles.

INTRODUCTION

The basic principle of state estimators is to produce a state estimate of the dynamic system at the current time using the knowledge of measurements at the current time and an estimate of the state at the previous time with knowledge of error associated with the system. There are several estimation methods, each one being suitable for a particular type of application. Thus, it is necessary to evaluate the processing time and accuracy to be reached. The method to estimate the attitude used is Unscented Kalman Filter (UKF), since this estimator is capable of performing state estimation in non-linear systems, besides taking into account measurements provided by different attitude sensors. This paper considers real data supplied by gyroscopes, Earth sensors and solar sensors, which are on board of the China-Brazil Earth Resources Satellite (CBERS-2).

REPRESENTATION OF ATTITUDE

The attitude of a spacecraft is defined as its orientation with respect to some reference frame, and, for a successful mission, it is essential that the satellite is stabilized in a determined attitude. The attitude of a rigid body in three-dimension space can be represented in different ways, among which Euler angles and quaternions have been highlighted.

1.Universidade de São Paulo – Escola de Engenharia de Lorena – Departamento de Ciências Básicas e Ambientais – Lorena/SP – Brazil. **2.**Instituto Nacional de Pesquisas Espaciais – Coordenação Geral de Engenharia e Tecnologia Espacial – Divisão de Mecânica Espacial e Controle – São José dos Campos/SP – Brazil. **3.**Universidade Federal do ABC – Centro de Engenharia, Modelagem e Ciências Sociais Aplicadas – Santo André/SP – Brazil.

Author for correspondence: Roberta Veloso Garcia | Universidade de São Paulo – Escola de Engenharia de Lorena – Departamento de Ciências Básicas e Ambientais – Estrada Municipal do Campinho, s/n – Pte. Nova – CEP: 12602-810 - Lorena/SP – Brazil | robertagarcia@usp.br

Received: 06/29/2015 | **Accepted:** 01/29/2016

REPRESENTATION OF ATTITUDE BY EULER ANGLES

The attitude of CBERS-2 satellite is stabilized in three axes called geo-pointed and can be described with respect to the orbital system. In this reference system, the motion around the direction of the orbital velocity is called *roll*; the motion around the direction normal to the orbit is called *pitch*; and the motion around the direction nadir/zenith is called *yaw*. Defining the state vector composed by Euler angles (ϕ, θ and ψ) and the componentes of the gyros *bias* (ε_x, ε_y, ε_z), and assuming that ϕ and θ are small angles, the differential equations of state for attitude and *bias* of the gyros are modeled as follows (Silva *et al.* 2014):

$$\begin{bmatrix} \dot{\hat{\phi}} \\ \dot{\hat{\theta}} \\ \dot{\hat{\psi}} \\ \dot{\hat{\varepsilon}}_x \\ \dot{\hat{\varepsilon}}_y \\ \dot{\hat{\varepsilon}}_z \end{bmatrix} = \begin{bmatrix} \omega_0 \sin\hat{\psi} + \hat{\omega}_x + \hat{\theta}\hat{\omega}_z \\ \omega_0 \cos\hat{\psi} + \hat{\omega}_y + \hat{\phi}\hat{\omega}_z \\ \omega_0(\hat{\theta}\sin\hat{\psi} - \hat{\phi}\cos\hat{\psi}) + \hat{\omega}_z + \hat{\phi}\hat{\omega}_y \\ 0 \\ 0 \\ 0 \end{bmatrix} \quad (1)$$

where: $\hat{\phi}$, $\hat{\theta}$ and $\hat{\psi}$ are the attitude angles obtained by some estimation process; ω_0 is the orbital angular velocity; $\hat{\omega}_x$, $\hat{\omega}_y$ and $\hat{\omega}_z$ are the components of the angular velocity ω on the satellite system. The rotation sequence used in this paper for the Euler angles was the 3-2-1.

REPRESENTATION OF ATTITUDE BY QUATERNIONS

The quaternion is a four-dimensional vector, defined as (Markley *et al.* 2005):

$$\mathbf{q} = \begin{bmatrix} \varrho & q_4 \end{bmatrix}^T \quad (2)$$

with

$$\varrho = \begin{bmatrix} q_1 & q_2 & q_3 \end{bmatrix} = \sin(\tilde{\varphi}/2)\hat{n}$$
$$q_4 = \cos(\tilde{\varphi}/2) \quad (3)$$

where: $\hat{n}$ is the Euler axis and φ is the rotation angle. Because a four-dimensional vector is used in the description of three dimensions, the quaternion elements cannot be independent and should comply with the constraint $\mathbf{q}^T\mathbf{q} = 1$.

The parcel of attitude shown by Eq. 1 is represented by quaternions as:

$$\begin{bmatrix} \dot{q}_1 \\ \dot{q}_2 \\ \dot{q}_3 \\ \dot{q}_4 \\ \dot{\hat{\varepsilon}}_x \\ \dot{\hat{\varepsilon}}_y \\ \dot{\hat{\varepsilon}}_z \end{bmatrix} = \frac{1}{2}\begin{bmatrix} q_4\hat{\omega}_x - q_3\hat{\omega}_y + q_2\hat{\omega}_z \\ q_3\hat{\omega}_x + q_4\hat{\omega}_y - q_1\hat{\omega}_z \\ -q_2\hat{\omega}_x + q_1\hat{\omega}_y + q_4\hat{\omega}_z \\ -q_1\hat{\omega}_x - q_2\hat{\omega}_y - q_3\hat{\omega}_z \\ 0 \\ 0 \\ 0 \end{bmatrix} \quad (4)$$

Given that the gyro dataset is at a fixed rate and the angular velocity of the spacecraft system is constant throughout the sampling interval, a solution to $\dot{\mathbf{q}}$ is presented by (Wertz 1978):

$$\mathbf{q}(t + \Delta t) = \Phi_q(\Delta t, \omega)\mathbf{q}(t) \quad (5)$$

where: Δt is the sampling interval; $\mathbf{q}(t)$ is the quaternion at time t; $\mathbf{q}(t + \Delta t)$ is the quaternion propagated to the next time $t + \Delta t$; and $\mathbf{\Phi}_q$ is the transition matrix that moves the system from time t to $t + \Delta t$.

The transition matrix is given by:

$$\Phi_q(\Delta t, \omega) = \cos\left(\frac{|\omega|\Delta t}{2}\right)\mathbb{I}_4 + \frac{1}{|\omega|}\sin\left(\frac{|\omega|\Delta t}{2}\right)\Omega(\omega) \quad (6)$$

where: Ω is the 4×4 antisymmetric matrix (Lefferts *et al.* 1982).

REPRESENTATION OF ATTITUDE BY QUATERNION INCREMENTAL

A different approach to represent the attitude is by quaternion incremental, where the quaternion is obtained by (Crassidis *et al.* 2007; VanDyke *et al.* 2004):

$$\mathbf{q} = \delta\mathbf{q}(\tilde{\varphi}) \otimes \hat{\mathbf{q}} \quad (7)$$

where: $\hat{\mathbf{q}}$ is the estimated unit quaternion and $\delta\mathbf{q}(\tilde{\varphi})$ is a unit quaternion expressing the rotation from $\hat{\mathbf{q}}$ to the true attitude $\mathbf{q}$, parameterized by a three-component vector in terms of $\tilde{\varphi}$.

The supporting idea is that the three-vector $\delta\varrho$ will be estimated and the correctly normalized four-component $\hat{\mathbf{q}}$ provides a globally non-singular attitude representation. In this way, Eq. 7 shows that $\delta\mathbf{q}(\tilde{\varphi}) \otimes \hat{\mathbf{q}}$ is the estimate of the true attitude quaternion $\mathbf{q}$. The main advantages of this option are that $\hat{\mathbf{q}}$ is a unit quaternion by definition, the covariance matrix has the minimum dimensionality, and the three-vector $\delta\varrho$

never approaches a singularity, since it represents only small attitude errors. For small-angle approximation, the quaternion incremental is represented by (Crassidis *et al.* 2007):

$$\delta\mathbf{q} = \begin{bmatrix} (\bar{\varphi}/2)\hat{n} \\ 1 \end{bmatrix} = \begin{bmatrix} \delta g \\ 1 \end{bmatrix} \tag{8}$$

The quaternion incremental between the quaternion "measured" and the estimated quaternion follows Eq. 7 and is defined by:

$$\delta\mathbf{q} = \begin{bmatrix} \delta g \\ \delta g_4 \end{bmatrix} = \mathbf{q} \otimes \hat{\mathbf{q}}^{-1} \tag{9}$$

THE MEASUREMENTS SYSTEM OF SATELLITE

The attitude of spacecraft can be determined by one or by a combination of several types of sensors. This section presents the mathematical models of the sensors that are on board the CBERS-2 satellite, which are responsible for the measures used in the estimation process.

THE MEASUREMENT MODEL OF GYROSCOPE

The advantage of using gyro measures is that it can provide the angular displacement and/or angular velocity of the satellite directly. However, gyros have an error due to drifting (*bias*), meaning that their measurement error increases with time. The rate-integration gyros (RIGs) are used to measure the angular velocities of the *roll*, *pitch* and *yaw* axes of the satellite. The mathematical model of the RIGs is (Lopes and Kuga 2005):

$$\Delta\boldsymbol{\Theta} = \int_0^{\Delta t} (\omega + \varepsilon)dt \tag{10}$$

where: $\Delta\Theta$ are the angular displacements of the satellite in a time interval Δt. Thus, the measured components of the angular velocity of the satellite are given by:

$$\omega = \left(\frac{\Delta\boldsymbol{\Theta}}{\Delta t}\right) - \varepsilon - \eta = \mathbf{g} - \varepsilon - \eta \tag{11}$$

where: **g** is the output vector of the gyroscope; $\boldsymbol{\eta}$ represents a Gaussian white noise process covering all the remaining unmodelled effects.

THE MEASUREMENT MODEL FOR INFRARED EARTH SENSORS

The Infrared Earth Sensors (IRES) are located on the satellite and aligned with its axes of *roll* and *pitch*, providing direct measurements of these angles. The measurement equations for the Earth sensors are given by (Lopes and Kuga 2005):

$$\begin{aligned} \phi_E &= \phi + v_\phi \\ \theta_E &= \theta + v_\theta \end{aligned} \tag{12}$$

where: v_ϕ and v_θ represent the Gaussian white noise related to small remaining effects of misalignment during installation and/or assembly of sensors.

THE MEASUREMENT MODEL FOR DIGITAL SUN SENSORS

The Digital Sun Sensors (DSS) do not provide direct measurements but coupled angles of *pitch* (α_θ) and *yaw* (α_ψ). The measurement equations for the sun sensor are established as follows (Lopes and Kuga 2005):

$$\begin{aligned} &\alpha_\psi = tg^{-1}\left(\frac{-S_y}{S_z\cos 60^\circ + S_z\cos 150^\circ}\right) + v_{\alpha_\psi}, \\ &\text{when } |S_z\cos 60^\circ + S_z\cos 150^\circ| \geq \cos 60^\circ. \\ &\alpha_\theta = 24^\circ - tg^{-1}\left(\frac{S_x}{S_z}\right) + v_{\alpha_\theta}, \\ &\text{when } \left|24^\circ - tg^{-1}\left(\frac{S_x}{S_z}\right)\right| < \cos 60^\circ. \end{aligned} \tag{13}$$

where: S_x, S_y and S_z are the components of the unit vector associated to the sun vector in the satellite system; the Gaussian white noises are represented by $v\alpha_\psi$ and $v\alpha_\theta$ and represent small effects of misalignment during installation and/or during sensor assembly.

ATTITUDE ESTIMATION BASED ON NON-LINEAR KALMAN FILTER

The state of non-linear estimator covered in this study was UKF. The UKF uses the unscented transformation which calculates a set of samples, or sigma points, defined from the *a priori* mean and covariance of the state (VanDyke *et al.* 2004). The sigma points undergo the non-linear transformation, and the posterior mean and covariance of the state results from the transformed sigma points.

Consider the system model given by:

$$\begin{aligned} \mathbf{x}_k &= \mathbf{f}(\mathbf{x}_{k-1}, k-1) + \boldsymbol{\eta} \\ \mathbf{y}_k &= \mathbf{h}_k(\mathbf{x}_k, k) + \boldsymbol{\nu} \end{aligned} \tag{14}$$

where: **f** represents the non-linear vector function of state **x** with dimension *n*; **y** is the vector of sensor measurement with dimension *m*; **h** is the function associated with the model of sensors shown by Eqs. 12 and 13; $\boldsymbol{\eta}$ and $\boldsymbol{\nu}$ represent the process and measurement noise with Gaussian white noise and covariances given by *Q* and *R* respectively.

In this paper, the state vector is composed by attitude and *bias* of gyro. The two forms used here are shown by Eqs. 1 and 4.

Given the state vector at step $k-1$, we compute a collection of sigma-points, stored in the columns of the $n \times (2n+1)$ sigma point matrix χ_{k-1} in which *n* is the dimension of the state vector. In our case, $n = 6$ for Euler angles parameterization, Eq. 1, or $n = 7$ for quaternion parameterization, Eq. 4. The columns of χ_{k-1} are computed by (Julier and Uhlmann 2004):

$$\begin{aligned} (\chi_{k-1})_0 &= \hat{\mathbf{x}}_{k-1} \\ (\chi_{k-1})_i &= \hat{\mathbf{x}}_{k-1} + \left(\sqrt{(n+\lambda)\mathbf{P}_{k-1}}\right)_i \quad i = 1,\ldots n \\ (\chi_{k-1})_i &= \hat{\mathbf{x}}_{k-1} - \left(\sqrt{(n+\lambda)\mathbf{P}_{k-1}}\right)_{i-n} \quad i = n+1,\ldots 2n \end{aligned} \tag{15}$$

where: $\lambda \in R$; **P** is the covariance of the state estimation error; $\sqrt{(n+\lambda)\mathbf{P}_{k-1}}$ is the *ith* column of the matrix square root of $(n+\lambda)\mathbf{P}_{k-1}$.

TIME UPDATE STEP

Once χ_{k-1} is computed, we perform this first step by predicting each column of χ_{k-1} through time by Δt, using:

$$(\chi_k^-)_i = f((\chi_{k-1})_i) \quad i = 0,\ldots 2n \tag{16}$$

where: *f* is the differential equation defined in Eqs. 1 or 4, depending on the selected parameterization.

In the formulation with Euler angles, Eq. 1, the integration of the state is made via Runge-Kutta. With $(\chi_k^-)_i$ calculated, the *a priori* state estimate and the *a priori* error covariance are:

$$\hat{\mathbf{x}}_k^- = \frac{\lambda}{(n+\lambda)}(\chi_k^-)_0 + \sum_{i=1}^{2n}\frac{1}{2(n+\lambda)}(\chi_k^-)_i \quad i = 1,\ldots 2n \tag{17}$$

$$\begin{aligned} \hat{\mathbf{P}}_k^- = &\frac{\lambda}{(n+\lambda)}[(\chi_k)_0 - \hat{\mathbf{x}}_k^-][(\chi_k)_0 - \hat{\mathbf{x}}_k^-]^T + \\ &+ \sum_{i=1}^{2n}\frac{1}{2(n+\lambda)}[(\chi_k)_i - \hat{\mathbf{x}}_k^-][(\chi_k)_i - \hat{\mathbf{x}}_k^-]^T + \mathbf{Q}_k \end{aligned} \tag{18}$$

MEASUREMENT UPDATE STEP

To compute this step, first we must transform the columns of χ_k^- through the measurement function to $\mathbf{Y}_k$. In this way:

$$\begin{aligned} (\mathbf{Y}_k)_i &= h((\chi_k^-)_i) \quad i = 0,\ldots 2n \\ \hat{\mathbf{y}}_k^- &= \sum_{i=0}^{2n} W_i(\mathbf{Y}_k)_i \end{aligned} \tag{19}$$

With the mean measurement vector $\hat{\mathbf{y}}_k^-$, we compute the *a posteriori* state estimate using:

$$\hat{\mathbf{x}}_k^+ = \hat{\mathbf{x}}_k^- + K_k(\mathbf{y}_k - \hat{\mathbf{y}}_k^-) \tag{20}$$

where: K_k is the Kalman gain. In the UKF formulation, K_k is defined by:

$$K_k = \mathbf{P}_{\hat{\mathbf{y}}_k\hat{\mathbf{y}}_k}\mathbf{P}_{\hat{\mathbf{x}}_k\hat{\mathbf{x}}_k}^{-1} \tag{21}$$

where

$$\mathbf{P}_{\hat{\mathbf{y}}_k\hat{\mathbf{y}}_k} = \sum_{i=0}^{2n} W_i[(\mathbf{Y}_k)_i - \hat{\mathbf{y}}_k^-][(\mathbf{Y}_k)_i - \hat{\mathbf{y}}_k^-]^T + \mathbf{R}_k \tag{22}$$

$$\mathbf{P}_{\hat{\mathbf{x}}_k\hat{\mathbf{y}}_k} = \sum_{i=0}^{2n} W_i[(\chi_k)_i - \hat{\mathbf{x}}_k^-][(\mathbf{Y}_k)_i - \hat{\mathbf{y}}_k^-]^T \tag{23}$$

where: R_k represents the measurement error covariance matrix.

Finally, the last calculation in the step is the *a posteriori* estimate of the error covariance given by:

$$\hat{\mathbf{P}}_k^+ = \hat{\mathbf{P}}_k^- - K_k\mathbf{P}_{\hat{\mathbf{y}}_k\hat{\mathbf{y}}_k}K_k^T \tag{24}$$

RESULTS

The results presented below compares the satellite attitude and the estimated gyro *bias* considering the estimators UKF and Extended Kalman Filter (EKF). For this, it is used

real data of sensors on board the CBERS-2 satellite. Results obtained in previous studies, like Garcia *et al.* (2012, 2014), are used to compare the different parameterizations. The CBERS-2 satellite was launched on October 21st, 2003. The measurements were collected in April 22nd, 2006, available to the ground system at a sampling rate of about 8.56 s. The algorithm was implemented through MATLAB software. The Attitude Control System (ACS) on board the satellite has full access to sensor measurements sampled at a rate of 4 Hz for the three gyros, to axes *x*, *y* and *z* of the satellite; 1 Hz for the two IRES; and 0.25 Hz for both DSS. However, due to limitations, the telemetry system can only acquire telemetries from sensors at 9-s sampling rate when the satellite passes over the tracking station. This means that the ground system does not have the full set of measurements that are available to the ACS on board. In total, we have a set of 54 measurements from 13h46min25s until 13h55min27s, and the measurements are spaced by 10 s on average. The measures of DSS and IRES are presented in Fig. 1, and the measures of gyroscope are presented in Fig. 2. These measures were provided by the Satellite Control Center of the Instituto Nacional de Pesquisas Espaciais (INPE). The set of initial conditions used by the algorithms is presented in Tables 1 to 3.

To analyze the algorithm performance with different parametrizations, the values obtained by UKF and Euler angles (UKFe) were used as reference (Garcia *et al.* 2012). The term "error" in this paper means that the estimated attitude by the different approaches is close to the reference. Figures 3 to 6 show the difference between the state estimated by the UKF when the attitude is represented via Euler angles (UKFe) and the estimated state: (1) via quaternions (q) and quaternion incremental (qi) Figs. 3 and 4; (2) through EKF with Euler angles, q and qi, Figs. 5 and 6. Figures 3a and 3b show that the *roll* and *pitch* estimated by UKF with quaternion incremental (qi) get close to the reference, when compared with results obtained by quaternion (q). The reason for the results with quaternions being more distant from the results of attitude via Euler angles can be justified by the need to reduce the order of the covariance matrix (7 to 6) during the estimation process. For *yaw* angle, Fig. 3c, we can notice an approximate behavior for the two approaches (q and qi) in relation to the reference (Euler angles). However, it is not possible to verify the tendency of error converging to zero in the proposed dataset. A larger measurement dataset is necessary to evaluate such behavior. When the UKF estimator is compared with the EKF estimator it was observed a similar behavior between both for the *roll* and *pitch* angles,

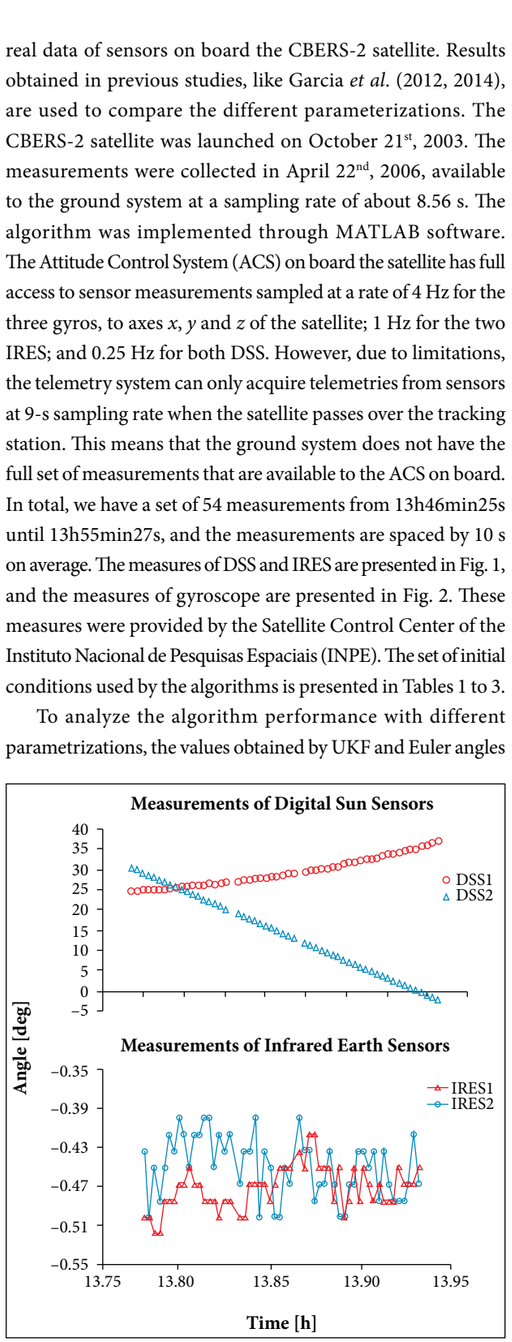

Figure 1. Real measurements supplied by attitude sensors from CBERS-2.

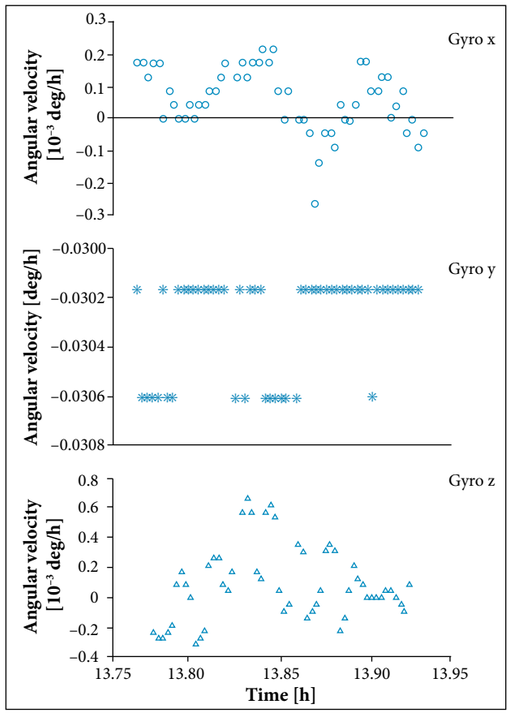

Figure 2. Real measurements supplied by gyroscope from CBERS-2.

Table 1. Initial conditions of attitude and *bias* of gyroscope.

ϕ (deg)	θ (deg)	ψ (deg)	ε_x (deg/h)	ε_y (deg/h)	ε_z (deg/h)
0	0	0	5.76	4.64	2.68

Table 2. Values of the diagonal of the initial covariance matrix P_0.

σ_ϕ (deg)	σ_θ (deg)	σ_ψ (deg)	$\sigma_{\varepsilon x}$ (deg/h)	$\sigma_{\varepsilon y}$ (deg/h)	$\sigma_{\varepsilon z}$ (deg/h)
0.5	0.5	2.0	1.0	1.0	1.0

Table 3. Values of the diagonal of the error observation matrix R.

σ_{DSS1}(deg)	σ_{DSS2}(deg)	σ_{IRES1}(deg)	σ_{IRES2}(deg)
0.6	0.6	0.06	0.06

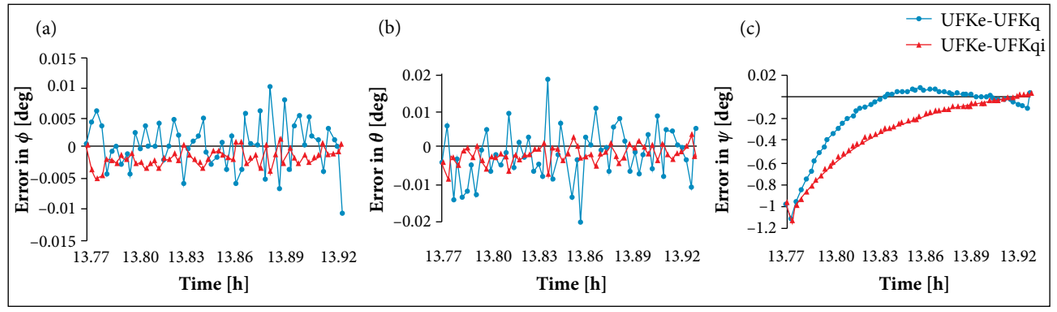

Figure 3. Comparison between attitude estimated by UKFe and different attitude parametrizations.

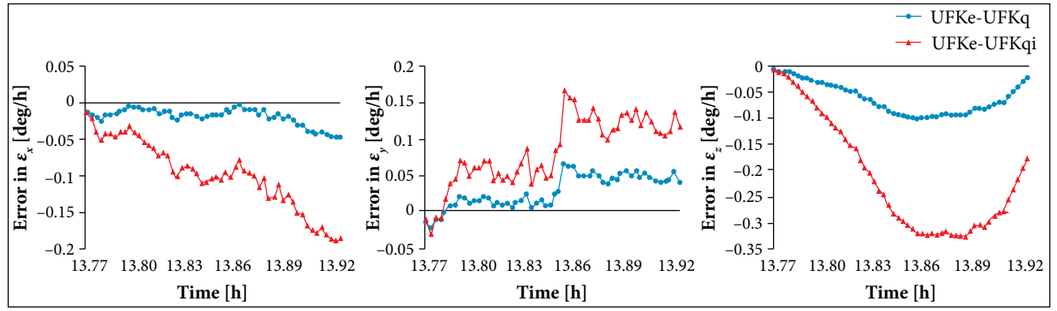

Figure 4. Comparison between *bias* estimated by UKFe and different attitude parametrizations.

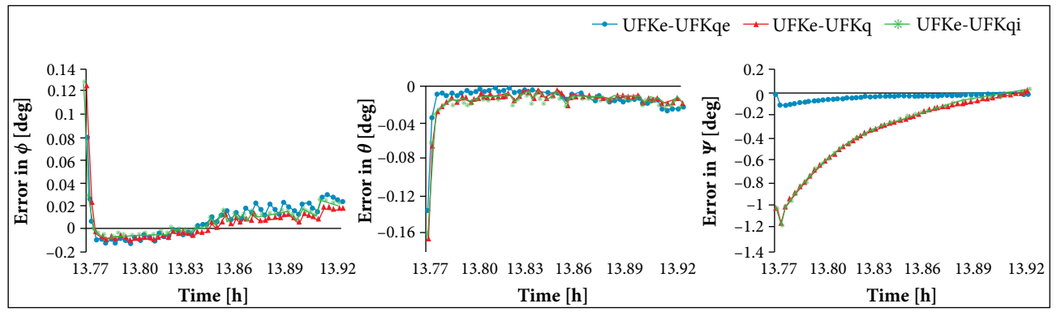

Figure 5. Comparison between attitude estimated by UKFe and EKF and different attitude parametrizations.

Figs. 5a and 5b. For the *yaw* angle, significant differences were not observed between Extended Kalman Filter with quaternion (EKFq) and Extended Kalman Filter with quaternion incremental (EKFqi) compared to UKFe, Fig. 5c. The mean and standard deviation of error for the estimated attitude related to the reference are presented in Table 4. With respect to estimated *bias*, it is not possible to observe the convergence of algorithms for the set of measures used in the study, Fig. 4. However, it is noted that the order of the error associated with the results obtained by EKFq and EKFqi is the same when compared with the Extended Kalman Filter with Euler angles (EKFe), Fig. 6. For the same parameterization attitude, UKFe and EKFe estimators have shown the same behavior. Such considerations can be better evaluated in Table 5.

ROBUSTNESS TEST

The performance of UKF is evaluated by comparing the estimated attitude with Euler angles by EKF and UKF estimators when both are subjected to imprecise initial conditions. In the first column of Fig. 7, we considered the initial values of attitude components very distant from true values, with *roll*, *pitch* and *yaw* equal to 10 deg each. It is known that expected values are close to zero, approximately –0.5, –0.45 and –1.5 deg to the set of measurements on test. The other conditions were kept constant. It is observed that, even taking longer, the EKF still converges to the expected value of the attitude (approximately –0.5 deg for *roll* and *pitch* and –1.5 deg for *yaw*), unlike UKF, which converges instantaneously. We also notice an incompatibility of attitude errors estimated by EKF (covariance)

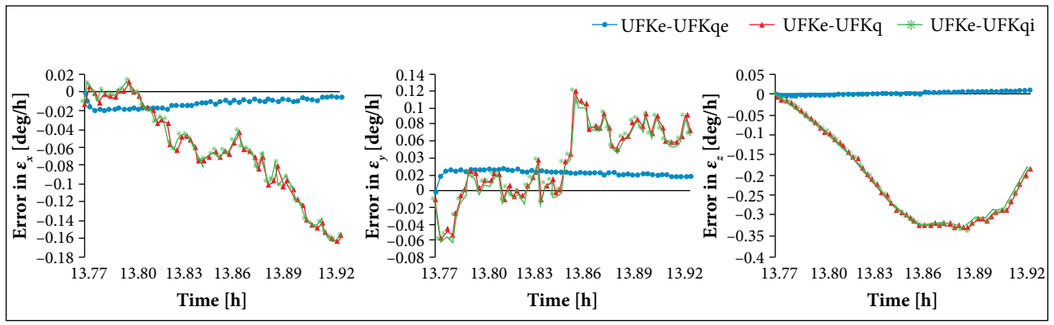

Figure 6. Comparison between *bias* estimated by UKFe and EKF with different attitude parametrizations.

Table 4. Mean and standard deviation of estimated attitude error by different approaches.

	ϕ (deg)	θ (deg)	ψ (deg)
UKFe–UKFq	0.0007 ± 0.0039	–0.0014 ± 0.0072	–0.1470 ± 0.3052
UKFe–UKFqi	-0.0014 ± 0.0014	–0.0011 ± 0.0024	–0.3026 ± 0.3092
UKFe–EKFe	0.0090 ± 0.0164	–0.0123 ± 0.0183	–0.0313 ± 0.0272
UKFe–EKFq	0.0073 ± 0.0189	–0.0145 ± 0.0224	–0.3203 ± 0.3124
UKFe–EKFqi	0.0072 ± 0.0190	–0.0145 ± 0.0224	–0.3247 ± 0.3169

UKFq/EKFq: Quaternions; UKFqi/EKFqi: Quaternion incremental; UKF with Euler angles – UKFe: Reference value.

Table 5. Mean and standard deviation of error from estimated *bias* of gyro by different approaches.

	ε_x (deg/h)	ε_y (deg/h)	ε_z (deg/h)
UKFe–UKFq	–0.0170 ± 0.0117	0.0302 ± 0.0221	–0.0595 ± 0.0304
UKFe–UKFqi	–0.0958 ± 0.0472	0.0858 ± 0.0473	–0.2109 ± 0.1087
UKFe–EKFe	–0.0105 ± 0.0048	0.0226 ± 0.0042	0.0060 ± 0.0038
UKFe–EKFq	–0.0633 ± 0.0499	0.0387 ± 0.0443	–0.2120 ± 0.1095
UKFe–EKFqi	–0.0643 ± 0.0503	0.0391 ± 0.0445	–0.2137 ± 0.1104

UKFq/EKFq: Quaternions; UKFqi/EKFqi: Quaternion incremental; UKF with Euler angles – UKFe: Reference value.

because the estimated attitude is far from the expected value of convergence and the EKF assumes small errors (sigma). This behavior is observed until the EKF reaches convergences and its errors remain around the ones obtained by UKF. In the second column of Fig. 7, it is considered the radically incorrect value of 20 deg for initial angles of *roll*, *pitch* and *yaw*. It clearly appears that the UKF converges in the initial stages, unlike the behavior obtained by the EKF, which is clearly different in *roll*. This case shows that, for degraded initial conditions, the linearizations performed in EKF are not effective, causing the filter to lose its capacity to accurately estimate the state of the system during the considered period. On the other hand, UKF is converged clearly, showing its robustness and superior performance in this situation.

PROCESSING TIME: UNSCENTED KALMAN FILTER VERSUS EXTENDED KALMAN FILTER

A quantitative analysis of the processing time spent by the CPU in the estimation process for different representations of attitude (Euler angles, quaternions and quaternions incremental) is held. We know that the amount of time is not an absolute indicator. However, even if quantitative, this analysis aids in assessing the applicability of UKF in problems in which the estimation is processed in real time, since this algorithm expands the number of vectors from state n to $2n + 1$ of same dimension. Table 6 shows the CPU time spent to process the measurements from the sensors in different approaches used to estimate attitude. The average of 100 runs was calculated for each filter in each parameterization. We remember that the programs were coded in MATLAB language in an Intel Core i3 with 3 GB of dynamical memory, running Windows 7, 64 bits version.

It may be noted that, although the processing time consumed by UKF is greater than that by the EKF, the increase is not proportional to the number of points generated in the UKF (note that UKF works with $2n + 1$ vectors of dimension n (6 or 7), unlike the EKF, which uses only a vector of dimension n). In all cases, the CPU expense via UKF is not 3 times the CPU expense via EKF. This time is still suitable for processing in real time, preserving the UKF advantage of being a more robust algorithm (see Fig. 7) and less prone to divergence

Table 6. Estimated processing time of measures of attitude sensors by UKF and EKF.

Parameterization	State vector dimension n	EKF (s)	UKF (s)
Euler	6	0.0515	0.1430
Quaternions	7	0.0514	0.1389
Quaternion incremental	6	0.0515	0.1266

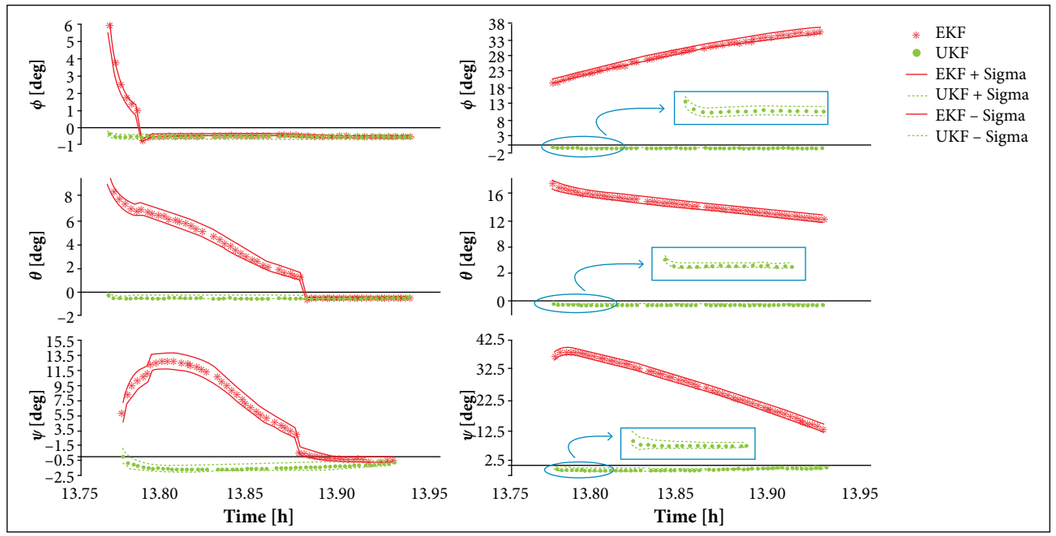

Figure 7. Attitude estimated by EKF and UKF with Euler angles considering initial conditions of ϕ, θ, ψ: 10 deg (first column) and 20 deg (second column).

due to non-linearities. In EKF, we note that the processing time is independent of the formulation adopted. In UKF, it is noticeable that the formulation via the Euler angles has higher computational expense, since this method requires numerical integration of the attitude dynamics. The lower expense occurs in the formulation via quaternion incremental, where the dynamic approach is obtained analytically and the state vector is reduced to dimension $n = 6$.

FINAL COMMENTS

The UKF was tested through diferent parameterizations of attitude, using real data supplied by attitude sensors that are on board the CBERS-2 satellite. Results obtained in previous studies served as a reference for comparisons between parameterizations. The attitude estimated by UKF was adequate when compared to the EKF. This is expected because the best performance of the UKF is based on inaccurate measurements of observations, estimated state errors or even systems involving highly non-linear equations, which is not the purpose of this study. However, the UKF was more consistent in comparison to EKF, since the results indicated that the performance of UKF far exceeds the conventional EKF for large initialization errors. The time spent in the estimation process for the UKF was higher compared to the EKF, but the processing time was adequate for real-time applications. Among the parameterizations considered, the quaternion incremental provided a smaller CPU load, reducing the dimension of the state vector, and its dynamic model equations are linear.

ACKNOWLEDGEMENTS

The authors would like to thank the financial support received by Fundação de Amparo à Pesquisa do Estado de São Paulo (FAPESP; 2012/21023-6) and Conselho Nacional de Desenvolvimento Científico e Tecnológico (CNPq; 303119/2010-1).

REFERENCES

Crassidis JL, Markley FL, Cheng Y (2007) Survey of nonlinear attitude estimation methods. J Guid Contr Dynam 30(1):12-28.

Garcia RV, Kuga HK, Zanardi MC (2012) Unscented Kalman Filter applied to the spacecraft attitude estimation with Euler angles. Math Probl Eng 2012(2012):Article ID 985429. doi: 10.1155/2012/985429

Garcia RV, Kuga HK, Zanardi MC (2014) Attitude estimation process of the sensing remote satellite CBERS-2 with Unscented Kalman Filter and quaternion incremental, using real data. Proceedings of the 24th International Symposium on Space Flight Dynamics; Laurel, USA.

Julier SJ, Uhlmann JK (2004) Unscented filtering and nonlinear estimation. Proc IEEE 92(3): 401-422. doi: 10.1109/JPROC.2003.823141

Lefferts EJ, Markley FL, Shuster MD (1982) Kalman filtering for spacecraft attitude estimation. J Guid Contr Dynam 5(5):417-429. doi: 10.2514/3.56190

Lopes RVF, Kuga HK (2005) CBERS-2: on ground attitude determination from telemetry data. Internal Report C-ITRP. São José dos Campos: INPE.

Markley FL, Crassidis JL, Cheng Y (2005) Nonlinear attitude filtering methods (AIAA 2005-5927). Proceedings of the AIAA Guidance, Navigation, and Control Conference and Exhibit. San Francisco; USA.

Silva WR, Kuga HK, Zanardi MC, Garcia RV (2014) Least square method for attitude determination using the real data of CBERS-2 Satellite. Applied Mechanics and Materials 706:181-190. doi: 10.4028/www.scientific.net/AMM.706.181

VanDyke MC, Schwartz JL, Hall CD (2004) Unscented Kalman Filter for spacecraft attitude state and parameter estimation. AAS-04-115.

Wertz JR (1978) Spacecraft attitude determination and control. Berlin: Springer Science & Business Media.

doi: 10.5028/jatm.v8i1.531

Comparison of the Incident Solar Energy and Battery Storage in a 3U CubeSat Satellite for Different Orientation Scenarios

Sergio Sanchez-Sanjuan[1], Jesus Gonzalez-Llorente[1], Ronald Hurtado-Velasco[1]

ABSTRACT: In CubeSats, because the size is limited, the estimation of the incident solar energy according to the orbital parameters and satellite attitude is more critical for the design process of the electrical power system. This estimation is helpful either for sizing of the power sources and energy storage or for defining the operation modes of the CubeSat with the energy available. This paper describes the kinematic and dynamic equations to derive the CubeSat attitude; similarly, the mathematical models of solar cells and batteries are also derived to calculate the energy harvested and stored. By determining the attitude of a 3U CubeSat over one orbit, we estimated the incident solar energy and thus the energy generated by the solar cells and energy stored in batteries when a direct energy-transfer architecture is used. In addition, these estimations where performed for three orientation scenarios: nadir-pointing, Sun-pointing and free-orientation. The estimated incident average solar energy for the three scenarios indicated that the Sun-pointing and free-orientation scenarios harvest more energy than the nadir-pointing one. This estimation is also helpful to predict the state of charge of the batteries in standby mode, allowing for determination of the time required for charging the batteries and, hence, the operating modes of the CubeSat. We expect to include the consumed energy while considering all of the operating modes of the satellite as well as different orbital parameters.

KEYWORDS: CubeSat, Electrical power system, Low Earth orbit, Satellite attitude.

INTRODUCTION

CubeSat technology has allowed companies and universities to participate in aerospace projects at low costs (Martin *et al.* 2014). This participation was not possible some decades ago, when only developed countries had adequate resources to invest in the aerospace industry. Currently, with the development of science and industry, many emerging and developing countries have developed their own space programs in Asia, Africa and South America (Wood and Wigel 2014; Woellert *et al.* 2010). Examples of these programs are Libertad 2 mission in Colombia by Sergio Arboleda University, which carries out a system of image acquisition (Triana *et al.* 2015), and ALSAT-1 DMC, which performs disaster monitoring in Algeria (Kameche *et al.* 2014).

Similar to traditional satellites, CubeSats consist of several subsystems, such as electrical power, VHF/UHF and S-Band communications, Attitude Determination and Control Systems (ADCS), on-board computer etc.; in the same way, the set of some subsystems for a specific function of the satellite during a period of time is called operation mode and it defines the consumption requirements. The electrical power system (EPS) provides the energy to all of the components of the satellite by means of the following stages: generation, storage and regulation. In a CubeSat, the only viable technology for energy generation is solar cells. Hence, in the design process, it is important to estimate how the incident solar radiation can provide energy for the satellite operation. In this way, it is possible to estimate the amount of energy that will be available per orbit and to design the mission accordingly. CubeSats usually describe a polar orbit, which can be divided

1.Universidad Sergio Arboleda – Escuela de Ciencias Exactas e Ingeniería – Bogotá – Colombia.

Author for correspondence: Jesus Gonzalez-Llorente | Universidad Sergio Arboleda – Escuela de Ciencias Exactas e Ingeniería | Calle 74 No. 14-14 – Bogotá Colombia | Email: jesusd.gonzalez@correo.usa.edu.co

Received: 08/13/2015 | **Accepted:** 02/04/2016

into two periods of energy: Sun stage and eclipse stage. In the Sun stage, which corresponds to the 60% of the orbit period, the satellite receives direct solar radiation; thus, it harvests energy using the solar cells and stores the energy into the lithium-ion batteries in the CubeSat. In the eclipse-stage, the solar radiation is zero; as a result, the only available energy is the one stored in the batteries. The energy harvested by the solar cells is also related to the CubeSat attitude, which is affected by the perturbations that the satellite experiences in its orbit. These perturbations are the gravitational gradient, atmospheric drag or even the action of the ADCS (Wertz 1990). By using mathematical models of the 3U body shape, we describe the attitude of the CubeSat according to the space conditions (Colombo *et al.* 1997; Sidi 2002).

According with literature, EPS mathematical model for simulation is found in Dreisbas (2013), but the author does not consider CubeSat attitude behavior. Conversely, calculations of solar power generation considering attitude and geometry , but without including EPS behavior, can be found in Lee *et al.* (2015). Moreover, the software that simulates attitude and EPS behavior without considering CubeSat geometry is described in Fernandez *et al.* (2014). So, because the amount of energy depends on the orbit characteristics, satellite attitude and geometry, our contribution is modelling the incident radiation of a CubeSat satellite during the Sun stage for three different orientation scenarios and estimating how much energy could be harvested and stored during one orbital period. In addition, we estimate the state of charge and the voltage of the battery by considering a dual EPS in the following way: first, a direct energy transfer with four 3U solar panels and a constant current load (standby); second, direct energy transfer with two 1U solar panels and no load.

MATHEMATICAL MODELS OF THE EPS

The EPS is responsible for harvesting, storing, regulating and distributing energy; in a CubeSat, the unique source of energy is sunlight. For harvesting energy from sunlight, triple-junction solar cells are most commonly used and, for storing energy, lithium-ion batteries are employed (Bouwmeester and Guo 2010). We describe briefly the mathematical models used to establish both of these EPS devices to quantify the power generated by the solar cells and the energy stored in the batteries.

GENERATION STAGE

We used the model that describes the current-voltage characteristic curve of solar cells (Eq. 1). This equation is an analytical model of the electrical behavior of a solar cell (Ortiz-Rivera and Peng 2005), which is given by:

$$I(V) = \frac{I_{sc}}{1 - e^{-\frac{1}{b}}}\left[1 - e^{\frac{V}{bV_{oc}} - \frac{1}{b}}\right] \quad (1)$$

where: I_{sc} and V_{oc} correspond to the short-circuit current and the open-circuit voltage values, respectively; the term b is a characteristic constant of each solar cells.

This model allows us to obtain the I-V representation using the parameters from the solar cell datasheet and adjust it through experimental data. In addition, the voltage and current depend on the environmental conditions, such as radiation and temperature. The temperature value is considered constant (28 °C) in this simulation process. This simplification does not affect significantly the quantification; however, the variation of temperature will be considered in future study.

STORAGE STAGE

As described before, lithium-ion batteries are the storage devices in CubeSats; thus, an electrical model that characterizes the lithium-ion battery voltage is implemented. This model consists of two resistor-capacitor (RC) networks (Fig. 1) to emulate the voltage characteristic curve (Chen and Rincón-Mora 2006).

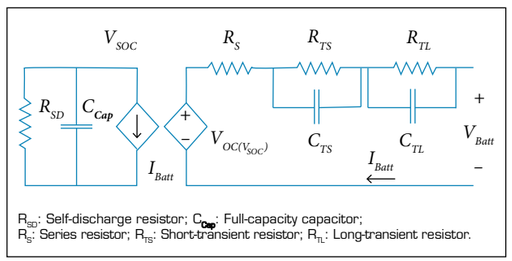

Figure 1. Electrical model of lithium-ion battery.

The left side of the circuit models the state of charge (SOC) of the system with respect to the voltage. The SOC is represented quantitatively as a number between 0 and 1. The right side represents the transient response, with all of the passive elements from the model, which are described in Chen and Rincón-Mora (2006). By applying circuit analysis, the battery voltage (V_{Batt}) is described by:

$$V_{Batt} = V_{oc} - R_S I_{Batt} + \frac{1}{C_{TS}}\int I_{C_{TS}}dt + \frac{1}{C_{TL}}\int I_{C_{TL}}dt \quad (2)$$

where: $I_{C_{TS}}$ and $I_{C_{TL}}$ are the currents in the capacitors C_{TS} and C_{TL}, respectively; these currents are functions of time and SOC.

EPS CONFIGURATION

The analysis of the energy behavior considers direct energy transfer (DET) as the power system architecture, which uses a parallel connection between the solar cells and the batteries. In this case, the operating voltage of the solar cells is fixed by the battery voltage. Furthermore, the loads that define the power consumption of the satellite also determine the battery current. Figure 2 shows a general scheme of the DET configuration for the EPS system.

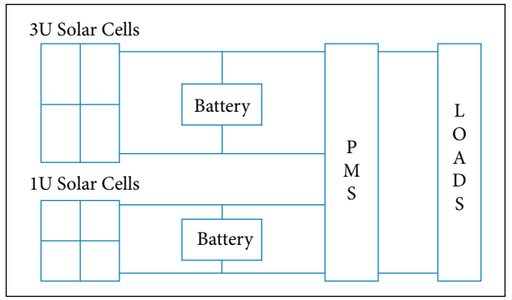

Figure 2. Electrical power supply scheme in DET configuration for 3U and 1U solar cells. Both architectures are connected to a power management system (PMS) to control the current distribution towards the loads.

After describing the system architecture, the operating condition for EPS is defined according to the faces of the CubeSat satellite. We considered two possible cases for evaluating the storage stage: a case with a constant consumption for the 3U faces and a case with no load for the 1U faces. These situations are considered with solar cells on all of the faces of the spacecraft.

DET WITH CONSTANT CONSUMPTION FOR THE 3U FACES

Because the use of solar cells on the 3U faces (30 × 10 cm) provides the highest power for the satellite, the EPS primary system comprises solar cells on that faces. The DET architecture is used to connect the EPS to the load to satisfy the demands of constant power consumption (Fig. 3). A net output power is produced in standby mode, generally, during which a battery can store energy.

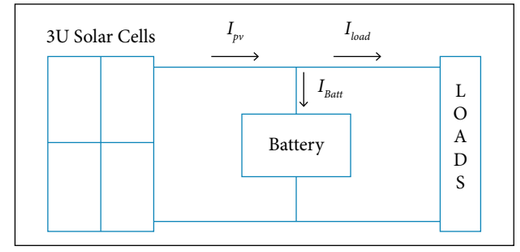

Figure 3. Scheme diagram of EPS in DET-3U topology.

Standby mode corresponds to the lowest consumption state during the satellite flight. In this mode, most subsystems are disconnected. Under these circumstances, the subsystems that are considered to be on for a general CubeSat mission are presented in Table 1.

Table 1. Consumption features for standby mode in CubeSat satellite.

Subsystem	Voltage (V)	Current (A)	Power (W)
On-board computer	3.3	0.303	1.00
ADCS	5.0	0.300	1.50
EPS	3.3	0.045	0.15

In this case, the following are active subsystems: the on-board computer (OBC), EPS and ADCS. These subsystems represent a total consumption of 2.75 W which can change according to the orientation scenario.

For the DET architecture in the primary EPS system, with a topology for 3U faces (DET-3U), a constant consumption of energy in standby mode exists. In this mode, a current relationship is established from an electrical diagram (see Fig. 3) given by:

$$I_{Batt} = I_{pv} - I_{load} \quad (3)$$

where: I_{pv} is the current delivered by the solar cells on the 3U faces; I_{Batt} is the current that flows into lithium-ion battery; and I_{load} is the consumption current for standby mode. The power harvested (W_s) depends directly on the body geometry

and the incident angle of the sunlight at each face. Thus, for any scenario orientation, the inner power corresponds to the sum of the power provided by each face (considering the EPS topology), assuming that all 3U faces have solar cells. In this case, we have:

$$W_s = \sum_{i=1}^{4} V_{pv,i} I_{pv,i} \tag{4}$$

where: V_{pv} is the voltage of the solar cells over 3U face.

The energy harvested per orbit can be determined by integrating over the solar cell power curve in Eq. 4. This energy is evaluated for one orbital period (T) , which is equivalent to 1.65 h. If we know the current stored or consumed from battery, I_{Batt}, then it is possible to obtain the SOC from the device. The SOC corresponds to the integral of the battery current as a function of time with respect to the initial condition of the charge given by Eq. 5.

$$SOC = Q_{ini} - \frac{1}{C}\int I_{Batt}\, dt \tag{5}$$

where: Q_{ini} is the initial charge of the battery and C is the storage capacity of the battery in Amperè-second. For all of the simulations, we considered an initial condition Q_{ini} of 50% to obtain a better analysis over the energy behavior.

DET WITH NO LOAD FOR THE 1U FACE

According to 3U CubeSat satellite geometry, there are two faces with 10 × 10 cm where solar cells can be allocated. To achieve a deep analysis regarding the utility of these faces of the nanosatellites, a second DET configuration is implemented which will be connected in parallel to a 3.7 V lithium-ion battery without load as an output. This configuration comprises a secondary system of energy and it will take all of the energy from the solar cells to the batteries.

For the 1U faces DET topology (DET-1U), the nonexistence of an output load for the consumption energy was determined. This situation is represented by the scheme diagram in Fig. 4, where only the parallel connection between solar cell and battery exists.

In this case, Eq. 3 can be rewritten as:

$$I_{pv} = I_{Batt} \tag{6}$$

In the charge stage, all current provided by the solar cell is delivered to the battery. Similar to DET-3U, the initial condition is taken as a half of the total charge possible (50%) to observe the storage behavior from the EPS system for one orbital period.

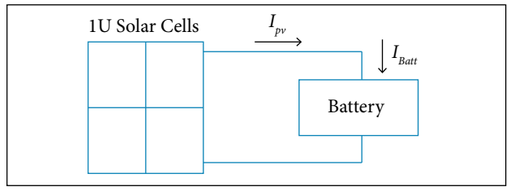

Figure 4. Scheme diagram of EPS in DET-1U topology.

SPACECRAFT MODEL

An object orbiting the Earth is submitted to different disturbances due to various physical factors, such gravity gradient, atmospheric drag, and others, which generate modifications on its attitude (Sidi 2002). To evaluate the satellite performance during power harvesting, the satellite was modeled as a rigid body (10 × 10 × 30 cm^3) with a uniform mass distribution and with its rotation axes parallel to its principal axes.

Two frames of reference were defined: Body Frame centered in the CubeSat (Γ_1) where the axes are orthogonal to the satellite faces, and Inertial Frame centered in the Earth (Γ_2). Both are represented with unitary vectors as follows:

$$\Gamma_1 = \begin{bmatrix} \hat{i} & \hat{j} & \hat{k} \end{bmatrix}^T \qquad \Gamma_2 = \begin{bmatrix} \hat{u} & \hat{v} & \hat{w} \end{bmatrix}^T \tag{7}$$

To relate one frame to the other, a matrix of transformation R must by applied (Wertz 1990), such that

$$\Gamma_2 = R\,\Gamma_1 \Rightarrow \begin{pmatrix} \hat{u} \\ \hat{v} \\ \hat{w} \end{pmatrix} = R \begin{pmatrix} \hat{i} \\ \hat{j} \\ \hat{k} \end{pmatrix} \tag{8}$$

represents how the body frame is seen from the inertial frame. This equation and R matrix will be described in detail later.

DYNAMICS

The rotational motion about a fixed point could be described by a set of equations known as Euler's equations of motion (Goldstein 1964), which describe the angular momentum conservation, $\vec{h} = [h_x \;\; h_y \;\; h_z]^T$, for a rigid body.

$$\dot{\vec{h}} + \vec{\omega} \times \vec{h} = \vec{\tau} \tag{9}$$

Only the torque $\vec{\tau} = [\tau_x \;\; \tau_y \;\; \tau_z]^T$ can change the angular momentum magnitude, which can be external or internal. The term $\vec{\omega} \times \vec{h}$ only generates a change in the angular momentum direction. Equation 9 can be rewritten as:

$$\mathbf{I}\dot{\vec{\omega}} = -\vec{\omega} \times \mathbf{I}\vec{\omega} + \vec{\tau}_{\text{int}} + \vec{\tau}_{\text{ext}} \tag{10}$$

where $\mathbf{I}$ is the satellite moment of inertia tensor (3 × 3):

$$\mathbf{I} = \begin{pmatrix} I_x & 0 & 0 \\ 0 & I_y & 0 \\ 0 & 0 & I_z \end{pmatrix} \tag{11}$$

and $\vec{\omega}$ is the vector of angular velocities (3 × 1). The terms $\vec{\tau}_{\text{int}}$ and $\vec{\tau}_{\text{ext}}$ include the internal and all of the external torque that can modify the body's attitude (3 × 1), respectively (Wertz 1990). The factor $\vec{\omega}\times$ in Eq. 10 is a skew matrix that relates all angular speeds in attitude:

$$\vec{\omega}\times = \begin{pmatrix} 0 & -\omega_z & \omega_y \\ \omega_z & 0 & -\omega_x \\ -\omega_y & \omega_x & 0 \end{pmatrix} \tag{12}$$

When the matrices from Euler's equation are operated upon, we obtain the final Eq. 13 to each axis from the body frame.

$$\begin{aligned} \tau_x &= I_x\dot{\omega}_x + \omega_y\omega_z(I_z - I_y) \\ \tau_y &= I_y\dot{\omega}_y + \omega_x\omega_z(I_x - I_z) \\ \tau_z &= I_z\dot{\omega}_z + \omega_y\omega_x(I_y - I_x) \end{aligned} \tag{13}$$

Figure 5 shows the axial assignment for the body frame that was used.

KINEMATICS

The satellite kinematics is represented using a quaternion $\vec{q}$. The quaternion representation avoids singularities and trigonometric functions (Sidi 2002; Yang 2012), which is an important consideration in an embedded system.

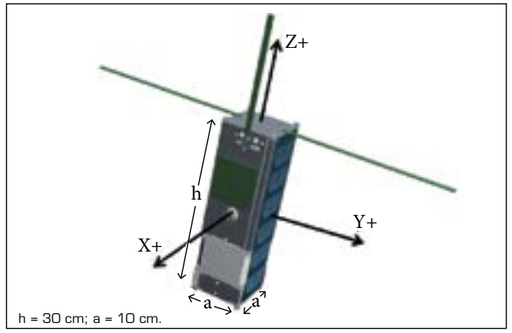

Figure 5. Axial assignment for body frame reference.

$$\dot{\vec{q}} = \frac{1}{2}\Omega(\omega)\vec{q} \tag{14}$$

where: $\Omega(\omega)$ is the angular speed antisymmetric matrix that contains the angular speed of each axis.

$$\Omega(\omega) = \begin{pmatrix} 0 & -\omega_x & -\omega_y & -\omega_z \\ \omega_x & 0 & \omega_z & -\omega_y \\ \omega_y & -\omega_z & 0 & \omega_x \\ \omega_z & \omega_y & -\omega_x & 0 \end{pmatrix} \tag{15}$$

Likewise, $\vec{q}$ is the quaternion vector, which is represented by four elements:

$$\vec{q} = \begin{bmatrix} q_0 & q_1 & q_2 & q_3 \end{bmatrix}^T \tag{16}$$

A review of the quaternion in spacecraft attitude was presented by Yang (2012). To visualize how the incident radiation hits the CubeSat faces, the quaternions are converted to Euler Angles. The transformation equations are:

$$\theta = \arctan\left(\frac{2(q_0q_1 + q_2q_3)}{1 - 2(q_2^2 + q_3^2)}\right) \tag{17}$$

$$\phi = \arcsin\left(2(q_0q_2 - q_3q_1)\right) \tag{18}$$

$$\psi = \arctan\left(\frac{2(q_0q_3 + q_1q_2)}{1 - 2(q_2^2 + q_3^2)}\right) \tag{19}$$

The angles θ, ϕ and ψ are yaw, pitch and roll, respectively. These angles establish the angular location of the body frame axes according to the input torques in the simulation.

METHODOLOGY

This section describes the models used, the perturbations, the orbit features, how the Sun vector is derived and the scenarios chosen for the simulations.

MODEL DIAGRAM

Figure 6 shows the block diagram that describes the system simulated for capturing radiation in each scenario. Using the mathematical models for spacecraft attitude, we calculated the relative radiation for each CubeSat side. This relative radiation value is an input variable for the EPS subsystem, along with the specification of the EPS devices from the manufacturer datasheet. The last stage corresponds to visualization of the main variables for energy analysis.

INITIAL PERTURBATIONS

In the case of the CubeSat geometry, the gravity gradient produces a force over a mass element (*dm*) located at a distance *r* from the center of mass given by:

$$d\vec{F} = -\frac{\mu dm}{|r^3|}\hat{r} \tag{20}$$

where: *r* is the distance from the center of the Earth to the body's center of mass; μ is a gravitational constant for the Earth ($\mu = 3.986 \times 10^5$ km^3/s^2).

The gravitational torque over this *dm* is: $d\vec{G} = \vec{d} \times d\vec{F}$. Thus, the gravitational torque over the body is (Sidi 2002):

$$\vec{G} = \frac{3\mu}{r^5}\int_M [\vec{R}\cdot\vec{d}][\vec{d}\times\vec{R}]dm \tag{21}$$

where: *R* is the distance from the center of Earth to the center of mass of the satellite; $\vec{d}$ is the radius vector from the body center of mass to a mass element *dm*; *M* is the entire body mass.

Furthermore, we applied an initial torque $\tau_0 = [\tau_{0x}\ \tau_{0y}\ \tau_{0z}]$ that corresponds to the first impulse on the satellite when it is ejected from the Poly Picosatellite Orbital Deployer (P-POD); this torque has an order of magnitude of 10^{-6} Nm.

ORBIT FEATURES

The simulated orbit is a Keplerian polar solar-synchronous orbit with a height of 700 km. The satellite trajectory has two stages. One stage is the radiation stage or the sunlight period, during which radiation reaches the object with the possibility of generating and storing energy. The other stage is the eclipse stage, known as the dark period or the eclipse period, during which it hides in Earth's shadow and thus it is not exposed to solar radiation; in this case, we consider a constant eclipse stage. Both periods are shown in Fig. 7.

The duration of either stage depends on the time of the year; however, we will show a simplified and idealized condition, for which every region is marked as shown in Fig. 7. According to Kepler's Third Law, we calculate the orbital period as follows:

$$T^2 = \frac{4\pi^2 R^3}{\mu} \tag{22}$$

According to these calculations, we determine that the orbital period is T = 99.1 min. Because region 1 describes a half orbit, the CubeSat displacement is performed in 49.5 min.

Applying some angular analysis for regions 2 and 4, we determine that the radiation stage has a duration of 62.73 min and the eclipse stage has a duration of 36.27 min, *i.e.* the radiation and eclipse stages correspond to 63.36 and 36.64 %, respectively, of the orbital period in low Earth orbit.

Note that the above discussion ignores albedo radiation. This simplification allows us to perform a better analysis of the energy behavior by using only direct radiation in each scenario; however, albedo will be considered in a future study.

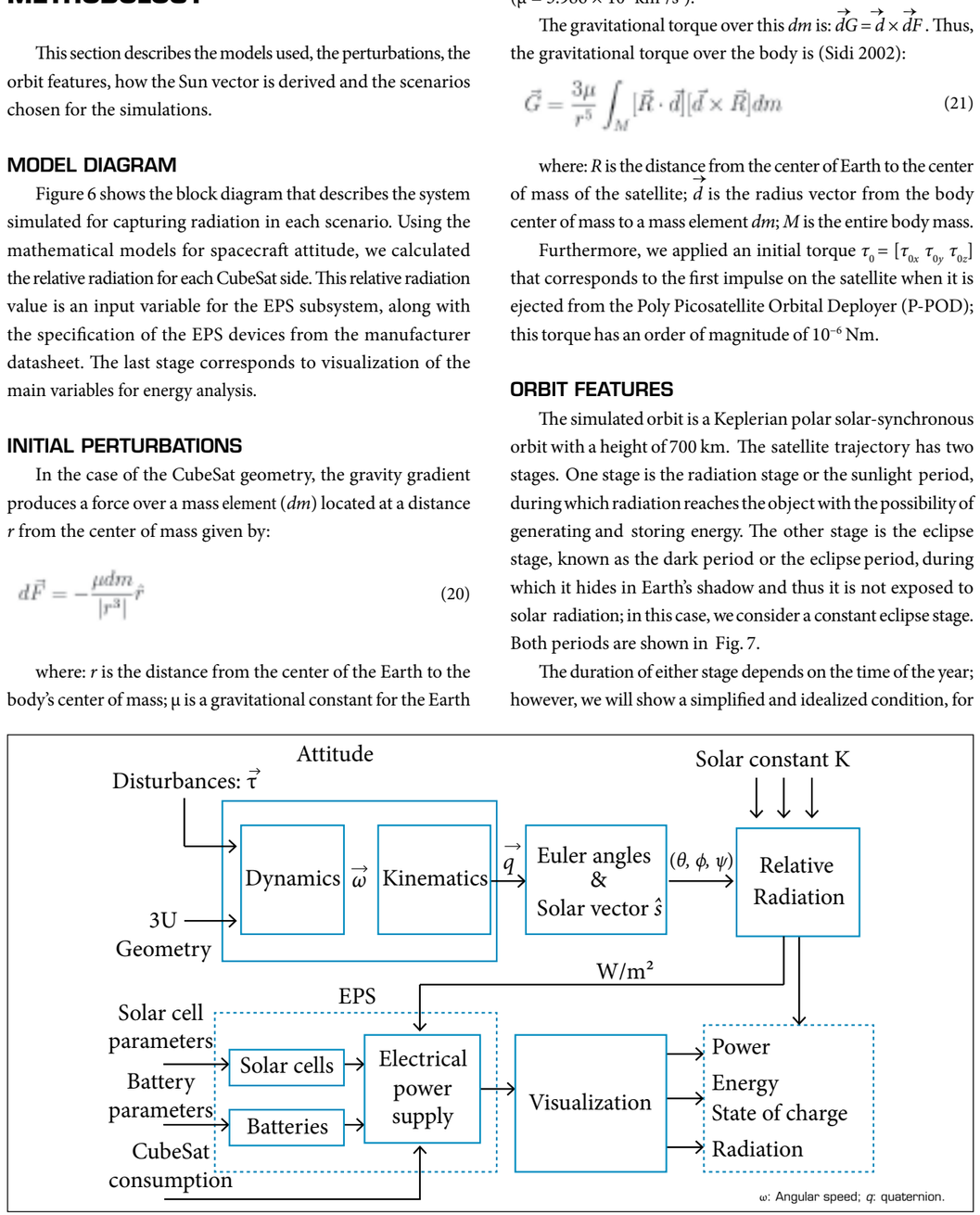

Figure 6. Block diagram of the proposed simulation.

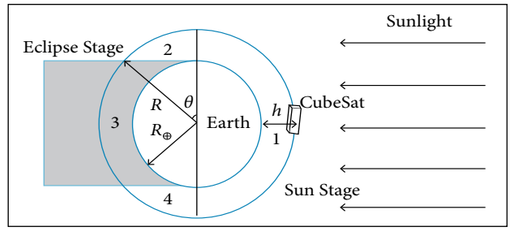

Figure 7. Graphic description for polar solar-synchronous orbit in CubeSat satellite.

DERIVATION OF THE SOLAR VECTOR

We must calculate the incident radiation on each side of the satellite. As a result, all axes on the body frame must be related with one fixed unitary vector that is pointing towards the Sun. As depicted in Fig. 8, this unitary vector is called the solar vector and is denoted by $\hat{s}$.

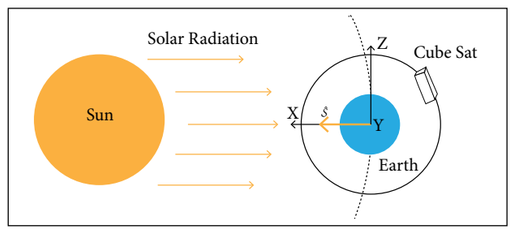

Figure 8. Solar vector representation.

According to the last section, if we assume that the inertial frame is fixed with the *x* axis pointing towards the Sun, then the solar vector is parallel to the $\hat{i}$ vector. Furthermore, assuming that any change of attitude from the satellite is reached with rotation order $X_\theta\ Y_\phi\ Z_\psi$ the rotation matrix used is Eq. 23.

$$R(\theta,\phi,\psi) = \begin{pmatrix} c(\phi)c(\psi) & -s(\phi) \\ -c(\theta)c(\psi)+c(\psi)s(\theta)s(\phi) & c(\phi)s(\theta) \\ s(\theta)s(\psi)+c(\theta)c(\psi)s(\phi) & c(\theta)c(\phi) \end{pmatrix} \tag{23}$$

where: s and c mean sine and cosine, respectively.

To compare each axis from body frame with the solar vector, we define the angle ψ between both vectors as:

$$\cos(\psi) = \frac{\vec{v}\cdot\hat{s}}{||\vec{v}||\ ||\hat{s}||} \tag{24}$$

where: $\vec{v}$ is any new unitary vector from the body frame seen in the inertial frame. Because the solar vector and *x* axis are parallel, $\hat{s}$ has the value:

$$\hat{i} = \hat{s} = [1\ 0\ 0] \tag{25}$$

Because both vectors in Eq. 24 are unitary, we have $||\vec{v}|| = ||\hat{s}|| = 1$. Thus, the angular separation is:

$$\psi = \arccos(\vec{v}\cdot\hat{s}) \tag{26}$$

For three positive axes represented by coordinate transformation, the incident angles between the solar vector and each unitary vector of the body frame are:

$$\alpha_X = \arccos(\hat{u}\cdot\hat{s}) = \arccos(\cos(\phi)\cos(\psi)) \tag{27}$$

$$\alpha_Y = \arccos(\hat{v}\cdot\hat{s}) = \arccos(\cos(\theta)\cos(\psi) + \cos(\psi)\sin(\theta)\sin(\phi)) \tag{28}$$

$$\alpha_Z = \arccos(\hat{w}\cdot\hat{s}) = \arccos(\sin(\theta)\sin(\psi) - \cos(\theta)\cos(\psi)\sin(\phi)) \tag{29}$$

ORIENTATION SCENARIOS

In this section three cases will be described to analyze the energy behavior, with the different faces of the satellite receiving radiation and its incident angle changing in time. The first scenario is called free-orientation; as shown in Fig. 9a,

the satellite makes arbitrary rotations due to the effect of the gravitational gradient and assuming the absence of any attitude control system. This scenario allows all satellite faces to receive radiation. This scenario can be the reference case to perform an energy analysis with respect to the other scenarios.

The second scenario is called Sun-pointing, as shown in Fig. 9b. With an attitude control system assumed, the body reference frame is invariant with respect to the Earth's reference frame. This scenario has as the initial condition the quaternion $q_i = [1\ 0\ 0\ 0]$. Thus, only one 3U face labeled as X+ is receiving sunlight with maximum radiation during the entire simulation, whereas the other faces are not receiving sunlight.

The last scenario is called nadir-pointing, which is described in Fig. 9c. Nadir-pointing represents a case where X– face is always pointing to the center of the Earth. This scenario allows for the four faces exposed to sunlight to exhibit a sinusoidal behavior of radiation. In $t = 0$ with initial condition q_i, the radiation in X+ has a maximum value, which will be reduced in function of the angular separation θ from the $\hat{i}$ vector. A position change increases the relative radiation over Z– toward its maximum in 90°. At this moment, X– face will receive radiation over a short time before and after the eclipse stage. As a result, after the non-radiation region, Z– face will receive sunlight during the rest of the orbit trajectory, and X+ returns to its initial position.

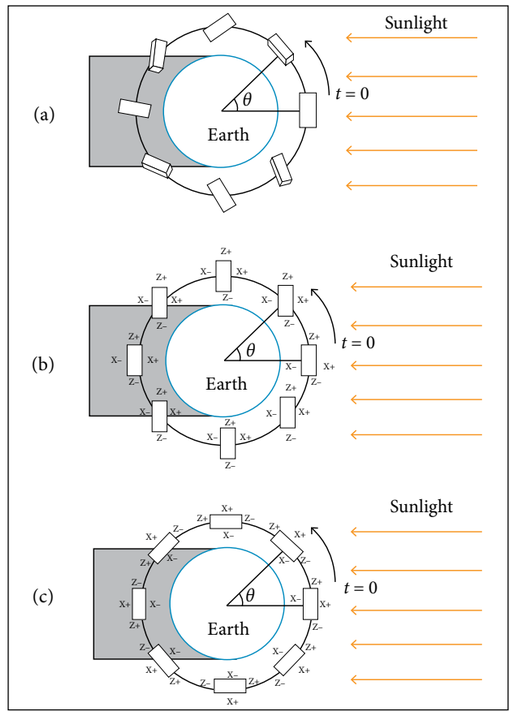

Figure 9. Orientation scenarios. (a) Free-orientation scenario; (b) Sun-pointing scenario; (c) Nadir-pointing scenario.

In all cases, we estimate the quantity of energy harvested during the sunlight period by monitoring the state of charge from the battery model. Additionally, both the body frame and the inertial frame will be aligned for time $t = 0$ with initial condition q_i, *i.e.* just one face of the CubeSat receives the maximum radiation in the first instant, and the other faces do not.

SIMULATION RESULTS

By using the mathematical models and the orbital environments described before, we estimate the incident solar energy according to the CubeSat attitude to quantify the power generated by the solar cells. The parameters of these cells are listed in Table 2, which presents the electrical values of a triple-junction solar cell, manufactured by the Azur Space Company (Azur Space 2009). In addition, we quantify the current that is absorbed or provided by the battery according with the loads. The parameters of a generic lithium-ion battery that were used for the estimation are listed in Table 3. All of the quantifications were performed for the three orientation scenarios previously described: free, solar fix and nadir orientation.

Table 2. High-efficiency triple-junction solar cell parameters from Azur Space.

Parameter	1U value	3U value	Units
Open-circuit voltage	5.334	16.00	V
Short-circuit current	0.506	0.506	A
Efficiency	28	28	%

Table 3. Generic lithium-ion battery.

Parameter	Value	Units
Nominal voltage	3.7	V
Capacity	1,000	mAh

COMPARISON OF THE INCIDENT SOLAR ENERGY FOR THE THREE ORIENTATION SCENARIOS

In the first scenario, the external torque allows the satellite to make aleatory rotations that enable sunlight to reach all faces.

In Fig. 10a, the change in radiation magnitude is shown for the opposite faces (X+, X–). According to the radiation behavior, when one face receives energy, the opposite face does not. The same situation occurs for the remaining faces (Y+, Y– and Z+, Z–), as shown in Figs. 10b and 10c.

Concerning the other scenarios, in the Sun-pointing scenario, only one 3U face receives sunlight, which absorbs the maximum radiation (1,363 W/m^2) during the entire sunlight stage and no radiation during the eclipse stage (Fig. 11). In the last scenario, nadir-pointing, four faces of the CubeSat are illuminated by solar radiation with a sinusoidal behavior, as shown in Fig. 12.

Using the solar radiation on the CubeSat faces, we calculated the orbit average energy for each scenario; likewise, we also calculated the orbit average power. These calculations, presented in Table 4, can be used to compare the solar energy harvested in the three scenarios. These results indicate that both the free-orientation and the Sun-pointing scenarios are the most advantageous solutions with ~ 8.0 Wh of energy per orbit, whereas the nadir-pointing scenario was the worst case, with ~ 5 Wh of energy generated from the solar cells.

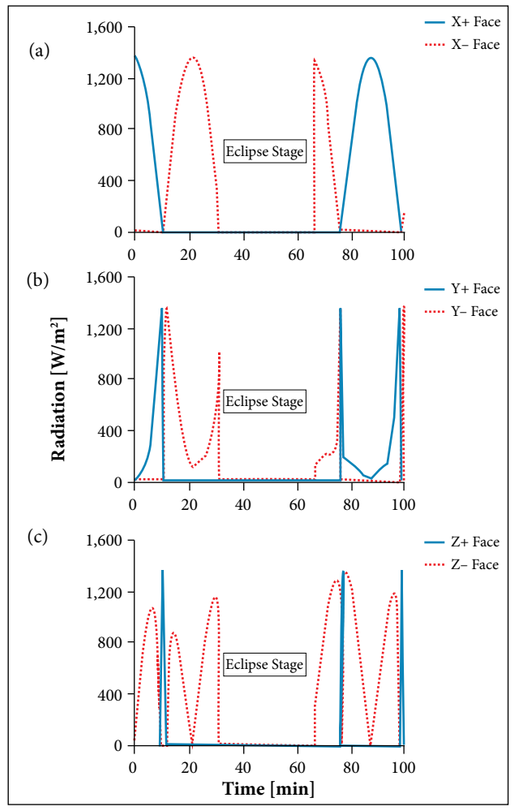

Figure 10. Radiation in free-orientation for: (a) X+ and X– faces; (b) Y+ and Y– faces; (c) Z+ and Z– faces.

Note that the first scenario generates power from all six faces in different orientations. Hence, it is possible to collect the energy from three faces at the same time and increase the energy generated. However, the satellite can harvest enough energy if just one 3U face is illuminated by sunlight during the sunlight stage (Sun-pointing), by which it reaches almost the same energy as the free-orientation scenario. In the last scenario, incident solar radiation is illuminating the four faces in different time intervals. Two of these intervals are on the 1U face, which causes reduced collection of energy with respect to the other

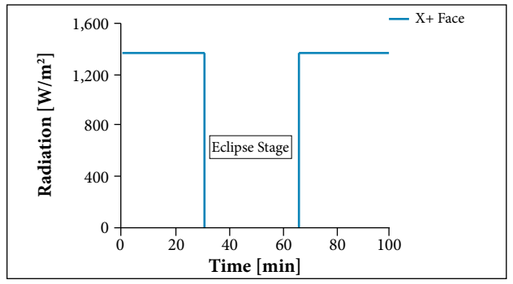

Figure 11. Radiation harvested from Sun-pointing scenario.

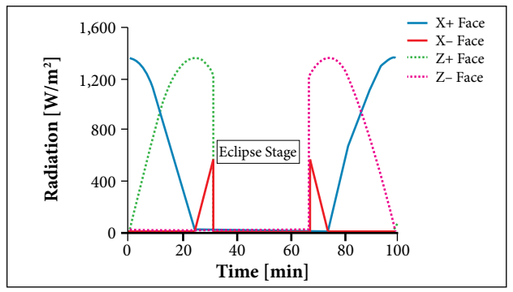

Figure 12. Radiation harvested from nadir-pointing scenario.

Table 4. Energy harvested from each orbital scenario.

Scenario	1U faces	3U faces	Energy (Wh)	Power (W)
Free orientation	Z+, Z–	X+, X–, Y+, Y–	7.91	4.79
Solar fix	—	X+	7.98	4.83
Nadir orientation	Z+, Z–	X+, X–	5.84	3.54

scenarios. Therefore, it is important to have as many 3U faces as possible receiving solar radiation by avoiding the stages where the energy produced depends on the 1U faces.

ESTIMATION OF THE BATTERY STATE OF CHARGE USING THE DET ARCHITECTURE

To examine the energy storage according to the EPS architectures, the SOC behavior is shown for the DET architecture in two cases considered: first, six solar cells on a 3U face in parallel with three batteries (DET-3U) and second, two solar cells on a 1U face in parallel with one battery (DET-1U). In the DET-3U case, a constant current load corresponding to standby mode is studied as this is the best mode for battery charging, whereas, in the DET-1U case, no load is considered because this architecture is designed as a secondary or backup topology, as shown in Fig. 2, that would only deliver energy stored during an emergency mode which is not simulated. In the former case, the load is equivalent to the standby energy consumption; therefore, the number of orbits to complete full charge of battery can be determined when the studied CubeSat operates in low power mode. In the same way, the DET-1U case corresponds to the time required to charge completely one battery, which can be used as the backup system. The battery SOC and voltage are estimated for the three orientation scenarios studied with an initial charge of 50%. This initial condition is considered to observe either its increase or decrease for better visualization at the beginning of the simulation; furthermore, many storage tests indicated that the battery should be kept with depth of discharge of 50% for better capacity performance (McLaren *et al.* 2008).

For the DET-3U case in the free-orientation scenario, the SOC reached 99% after one orbital period (99.1 min) – Fig. 13a, *i.e.* almost the full-charge state is achieved in one orbit around the Earth. Moreover, during the entire orbital period, the battery is always in a charged stage, except during a short period that corresponds to the eclipse stage, where the satellite passes through Earth's shadow. This result indicates that the free-orientation scenario can provide advantage of energy saving after the high consumption periods due to the operation of other subsystems such as VHF/UHF communication, S-Band communication and payload, which have high energy consumption that decreases the energy stored; so the free orientation recovers the SOC in the battery in a few orbits during standby mode. In addition, the battery voltage does not exhibit a significant variation, ranging between 11.6 and 12.4 V, which is near the maximum power point of the solar cell (Fig. 13b).

For scenarios in Sun-pointing and nadir-pointing orientations, unlike free-orientation, there is a higher consumption in the standby mode due to ADCS operation. In Fig. 14a, it is observed that Sun-pointing orientation (red line) can retrieve 14% of the energy after one orbital period requiring around three and a half orbits for total charging. However, nadir-pointing scenario (green line) shows a disadvantage in the process of energy storing; in one orbital period, the SOC decreases 5% with respect to the initial condition because of the low incidence of radiation over the 3U sides; hence the battery will be discharged after around ten orbits. The same behavior can be seen in Fig. 14b; voltage level increases in Sun-pointing while it decreases in nadir-pointing, which is consistent with SOC results.

In the DET-1U case, two 1U faces are available to store the energy harvested into the lithium-ion battery. For each scenario, the SOC behavior and the voltage variation are shown in Fig. 15. According to these results, the nadir-pointing

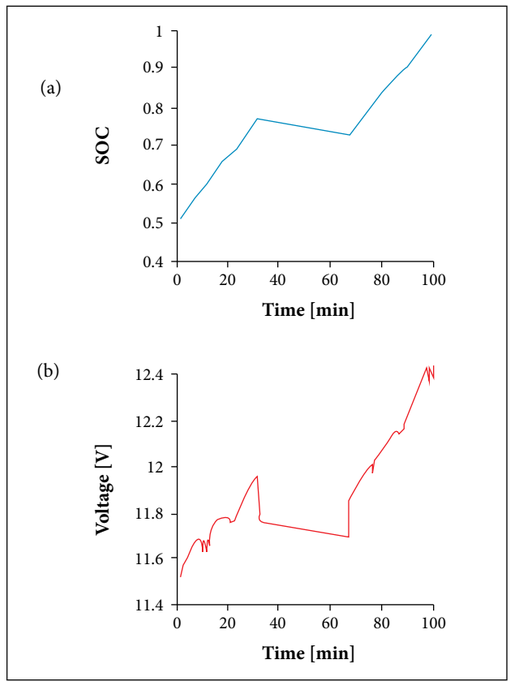

Figure 13. State of charge and voltage behavior for lithium-ion battery in free-orientation scenario.

scenario achieves the best storage condition, with a SOC increase of approximately 30%, followed by free-orientation scenario, with a SOC increase of almost 25%. In these circumstances, the worst scenario is the Sun-pointing because the secondary 1U faces do not receive incident solar energy; the 1U vector normal to the faces is perpendicular to the solar vector.

In general, all results for DET-3U and DET-1U indicate that the satellite orientation has a direct influence in the SOC due to the number of sides exposed to radiation and the ADCS consumption. For example, in the free orientation, several 3U faces are probably receiving solar radiation and the ADCS is not required; thus the CubeSat will operate in a low consumption state. Meanwhile, in scenarios with ADCS, there are only few faces exposed to solar radiation. Sun-pointing can generate enough energy in DET-3U but none in DET-1U, making the backup topology useless. Conversely, nadir-pointing has a bad harvesting in DET-3U, but an excellent performance for DET-1U.

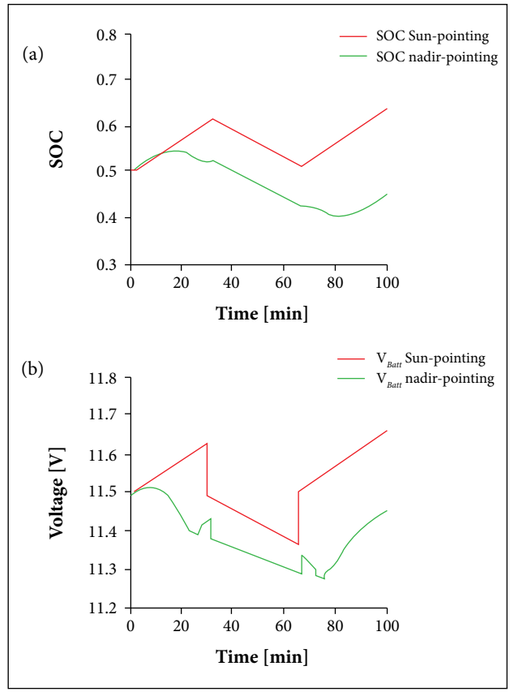

Figure 14. State of charge and voltage behavior for lithium-ion battery in Sun-pointing (red line) and nadir-pointing (green line) orientations.

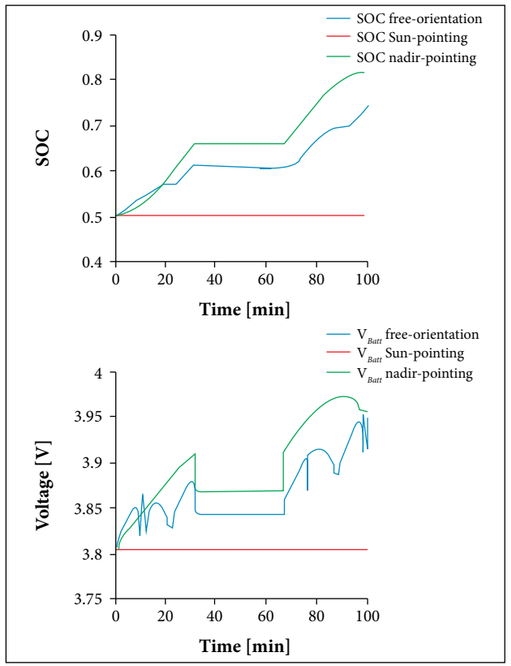

Figure 15. Comparison of state of charge behavior and voltage curves for three scenarios in DET-1U topology.

CONCLUSIONS

This paper described the approach used to estimate the behavior of the incident solar radiation in a 3U CubeSat using dynamic and kinematic equations to determine its attitude with respect to the solar vector. In addition, we calculated the energy harvested by the solar cells and the energy stored in lithium-ion batteries when the CubeSat operates in standby mode. Under these conditions, we considered a low Earth orbit and three orientation scenarios: nadir-pointing, Sun-pointing and free-orientation.

For each orientation scenario, we could estimate the incident solar radiation as a function of time, the orbit average power and the orbit average energy. According to these results, more radiation can be harvested by the solar cells in the free-orientation and Sun-pointing scenarios; however, the free-orientation scenario depends on the initial torque. The nadir-pointing scenario was the worst case because the incident solar radiation reaches only one 1U side during some periods.

In the DET-3U topology with constant consumption, the free-orientation scenario saves 49% more energy after one orbital period than the initial charge in standby mode without attitude control. The other two scenarios with attitude control in low power have a higher consumption and lower storage rate: the Sun-pointing scenario can store 14% more energy, whereas the nadir-pointing has a decrease of 5% in the stored energy, being the worst. For the DET-1U topology, the nadir-pointing has the highest energy storage, with a SOC of more than 30%, followed by the free-orientation scenario, with a SOC of almost 25%. For both scenarios, the storage occurs in one orbital period.

The Sun-pointing scenario cannot store energy because none of the 1U faces receive solar radiation.

In future research, we will expand our study to consider other orbital scenarios and other CubeSat orientations. In addition, the energy consumption over one operation sequence of the satellite will be considered to analyze the battery behavior and to evaluate the EPS design.

REFERENCES

Azur Space (2009) 28% triple junction gas solar cell specifications; [accessed 2014 Dec 18]. http://azurspace.de/index.php?mm=162

Bouwmeester J, Guo J (2010) Survey of worldwide pico- and nanosatellite missions distributions and subsystem technology. Acta Astronaut 67 (7-8): 854-862. doi: 10.1016/j.actaastro.2010.06.004

Chen M, Rincón-Mora G (2006) Accurate electrical battery model capable of predicting runtime and I-V performance. IEEE Trans Energ Convers 21(2): 504-511. doi: 10.1109/TEC.2006.874229

Colombo G, Grasselli A, De Luca A (1997) Satellite power system simulation. Acta Astronaut 40 (1):41-49. doi: 10.1016/S0094-5765(97)00022-2

Dreisbas R (2013) CubeSat electrical power system simulation a generic approach. Saarbrücken: AV Akademikerverlag.

Fernandez A, Accolti GD, Buergler B, Garcia B (2014) PEPS: a tool for power system simulation. Proceedings of the European Space Power Conference (ESPC); Noordwijkerhout, The Netherlands.

Goldstein H (1964) Classical mechanics. Reading: Addison-Wesley.

Kameche M, Benzeniar H, Benbouzid A, Amri R, Bouanani N (2014) Disaster monitoring constellation using nanosatellites. J Aerosp Technol Manag 6(1):93-100. doi: 10.5028/jatm.v6i1.281

Lee DY, Cutler J, Mancewicz J, Ridley AJ (2015) Maximizing photovoltaic power generation of a space-dart configured satellite. Acta Astronaut 111283-299. doi: 10.1016/j.actaastro.2015.01.022

Martin L, Jones W, Shiroma W (2014) Small-satellite projects offer big rewards. IEEE Potentials 33 (4):24-30. doi: 10.1109/MPOT.2014.2315858

McLaren V, Clark C, Simon E, Hendel B (2008) Lithium ion polymer cell for small satellites. Proceedings of the NASA Battery Workshop; Huntsville, USA.

Ortiz-Rivera E, Peng F (2005) Analytical model for a photovoltaic module using the electrical characteristics provided by the manufacturer data sheet. Proceedings of the 36th IEEE Power Electronics Specialists Conference; Recife, Brazil.

Sidi M (2002) Spacecraft dynamics and control: a practical engineering approach. Cambridge: Cambridge University Press.

Triana J, Bautista S, González F (2015) Identification of design considerations for small satellite remote sensing systems in low earth orbit. J Aerosp Technol Manag 7 (1):121-134. doi: 10.5028/jatm.v7i1.405

Wertz J (1990) Spacecraft attitude determination and control. Dordrecht: Kluwer Academic Publishers.

Woellert K, Ehrenfreund P, Ricco A, Hertzfeld H (2010) Cubesats: cost-effective science and technology platforms for emerging and developing nations. Adv Space Res 47(4):663-684. doi: 10.1016/j.asr.2010.10.009

Wood D, Wigel A (2014) Architectures of small satellite programs in developing countries. Acta Astronaut 97:109-121. doi: 10.1016/j.actaastro.2013.12.015

Yang Y (2012) Spacecraft attitude determination and control: quaternion based method. Annu Rev Contr 36 (2):198-219. doi: 10.1016/j.arcontrol.2012.09.003

doi: 10.5028/jatm.v8i1.586

Experimental Magnetometer Calibration for Nanosatellites' Navigation System

Jader de Amorim[1], Luiz S. Martins-Filho[1]

ABSTRACT: This article deals with the problem of Earth's magnetic field sensors calibration in the context of low-cost nanosatellites' navigation systems. The attitude of space vehicles can be determined from the state estimation using information from three-axis inertial and non-inertial sensors. This study considers a three-axis solid-state magnetometer. In the vehicle itself, the presence of ferrous materials and electronic devices creates disturbances, distorting the measured field. The sensor precision can be enhanced through calibration methods which calculate the systematic error. The objective here is to study and implement calibration combining a geometric method and the TWOSTEP algorithm. The methodology is based on numerical simulations, with the development of a database of the Earth's magnetic field along the vehicle orbit, and experimental tests using a nanosatellite mockup, containing an embedded processor Arduino MEGA 2560 platform and the magnetometer HMC5843.

KEYWORDS: Nanosatellites, Attitude, Navigation systems, Magnetometer calibration, TWOSTEP algorithm.

INTRODUCTION

A crucial requisite for an artificial satellite is the control of its spatial orientation, generally called attitude. The attitude must be stabilized and controlled for various reasons, concerning the spacecraft operational functions, like the correct antenna pointing for the communication, the appropriate orientation related to the Sun for the thermal control, and many others. The tasks associated to the satellite mission also demand the accuracy in the orientation of sensors and other devices for a suitable performance. Several phenomena can cause inaccuracies on the space vehicle orbit and attitude. In order to have the spacecraft controlled, the attitude must be known through the various stages of its life cycle. From the launch to final service orbit, the space vehicle attitude should be determined (Pisacane 2005).

Attitude determination implies the measurement of any quantity sensitive to the attitude. One of the most used phenomena in the determination procedures is the Earth's magnetic field. The local geomagnetic field vector is frequently one of the attitude information sources. A magnetometer measures the strength of a magnetic field in one, two or three directions. If $\boldsymbol{B}_k$ is the value of a magnetic field in the spacecraft body coordinate system, as determined from the magnetometer in the time t_k, and $\boldsymbol{T}_k$ is the known value of the magnetic field in the inertial coordinates, then a simple model is (Pisacane 2005):

$$\boldsymbol{B}_k = A_k \boldsymbol{T}_k,\ k = 1, 2, 3, \ldots, N \tag{1}$$

where: A_k is the rotation matrix describing the attitude.

Thus the measurement of the magnetic field provides a measurement of the attitude relative to inertial coordinates. The vector is generally given by a geomagnetic reference field

1.Universidade Federal do ABC – Centro de Engenharia, Modelagem e Ciências Sociais Aplicadas – Santo André/SP – Brazil.

Author for correspondence: Luiz S. Martins-Filho | Universidade Federal do ABC – Centro de Engenharia, Modelagem e Ciências Sociais Aplicadas | Avenida dos Estados, 5.001 – Bangu | CEP: 09.210-971 – Santo André/SP – Brazil | Email: luizsmf@gmail.com

Received: 12/16/2015 | **Accepted:** 01/29/2016

model, which requires knowledge of the spacecraft position. The magnetometer does not measure the magnetic field in the body frame but in a frame fixed in the magnetometer. The measured magnetic field in the body frame is obtained from the measured field in the sensor frame according to:

$$\boldsymbol{B}_k = S_{mag\,k}\boldsymbol{B}_k, \quad k = 1,2,3,\ldots,N \tag{2}$$

where: $S_{mag\,k}$ is the magnetometer alignment matrix, a proper orthogonal matrix that transforms representations from the magnetometer frame to the body frame.

Moreover, measurement of the magnetic field alone is not sufficient to determine the attitude. Therefore the magnetic field measurement, although a vector, has only two degrees of freedom that are sensitive to the attitude (namely, the direction). Since we need three parameters to specify the attitude, one vector measurement is not enough. Other sensors, *e.g.* the Sun sensor, are used to complete the necessary information to determine the attitude.

In the literature, there are a number of studies around the subject of magnetometer calibration. For instance, Juang *et al.* (2012) deals with the problem of magnetometer data based on orbit determination and the sensor calibration. The proposed solution applies an unscented Kalman filter for estimation of satellite position and velocity. The results show the adequacy of the extension strategy of orbit determination algorithm to the problem of magnetometer calibration. In Inamori and Nakasuka (2012), in the context of a scientific nanosatellite mission, the magnetometer calibration algorithm is also based on the unscented Kalman filter.

Three different algorithms are tested in terms of performance and computational costs in Crassidis *et al.* (2005): the TWOSTEP (Alonso and Shuster 2002), the extended Kalman filter, and the unscented Kalman filter. The study presented in Vasconcelos *et al.* (2011) formulates a maximum likelihood estimator to an optimal parameter calibration without using external attitude references. The proposed calibration procedure corresponds to an estimation of rotation, scaling and translation transformation and represents an interesting tridimensional refinement of the geometric method proposed in Caruso (2000).

The purpose of our study is to implement and evaluate two procedures in a quite simple and low-cost experimental setup. One dedicated to ground calibration and the other, to in-flight calibration. The adopted strategies, based on the precedent studies discussed above, are the geometric method (Caruso 2000) and TWOSTEP (Alonso and Shuster 2002), respectively for ground and in-flight procedures.

THE MAGNETOMETER CALIBRATION ALGORITHMS

The magnetometer determines the direction and the magnitude of the magnetic field with several operational advantages such as low weight, small power consumption, and no moving parts; therefore, it does not interfere with vehicle dynamics. The main problem of this instrument is the low accuracy of its measurements as a function of considerable errors from Earth's magnetic field model.

Besides, the accuracy of the magnetometer can be disrupted by a series of magnetic disturbances generated in the spacecraft. The TWOSTEP algorithm was developed to determine the bias, i.e. the measurement systematic error. Besides, the accuracy of the magnetometer can be disrupted by a series of magnetic disturbances generated in the spacecraft. The TWOSTEP algorithm was developed to determine the bias, i.e. the measurement systematic error. Some algorithms have been proposed to avoid this type of calculation.

GEOMETRICAL CALIBRATION APPROACH

The first approach for the magnetometer calibration is an extension of the method proposed in Caruso (2000) and is developed as an application note for the LSM303DLH sensor module (ST Microelectronics 2012). Considering a tridimensional space, the relation between the geomagnetic field ($\hat{H}_x$, $\hat{H}_y$, $\hat{H}_z$) and the measurements vector (B_x, B_y, B_z) can be expressed as:

$$\begin{bmatrix}\hat{H}_x\\ \hat{H}_y\\ \hat{H}_z\end{bmatrix} = M_m \begin{bmatrix}1/x_{sf} & 0 & 0\\ 0 & 1/y_{sf} & 0\\ 0 & 0 & 1/z_{sf}\end{bmatrix} M_{si} \begin{bmatrix}B_x - b_x\\ B_y - b_y\\ B_z - b_z\end{bmatrix} \tag{3}$$

where: M_m is the misalignment matrix (between magnetic field and sensor frame axes); x_{sf}, y_{sf} and z_{sf} are the scale factors; b_x, b_y and b_z are the systematic errors due to strong magnetic disturbances (bias); and M_{si} is a matrix that represents the weak magnetic distortion.

The calibration procedure can be done by data acquisition during rotations around the three axes (X, Y, Z) or randomly combined rotations (ST Microelectronics 2012). In the case of presence of strong or weak magnetic distortions, the measurement will reproduce these disturbs by a bent and displaced ellipsoid. This calibration procedure is able to compensate these disturbs that are solidary with the satellite body and to allow the magnetometer to measure the external field. An example of graphical representation of measurements taken during tridimensional and planar rotations is shown in Fig. 1. In this case, the sensor measurement is clearly affected by internal disturbances. The ellipsoid can be described by:

$$\begin{aligned}&\frac{(x-x_0)^2}{{a_1}^2} + \frac{(y-y_0)^2}{{a_2}^2} + \frac{(z-z_0)^2}{{a_3}^2} +\\ &+\frac{(x-x_0)(y-y_0)}{{a_4}^2} + \frac{(x-x_0)(z-z_0)}{{a_5}^2} +\\ &+\frac{(y-y_0)(z-z_0)}{{a_6}^2} = R^2\end{aligned} \tag{4}$$

where x_0, y_0 and z_0 are offsets of b_x, b_y and b_z caused by the strong magnetic distortion; x, y and z are the measurements (B_x, B_y, B_z); a_1, a_2 and a_3 are the lengths of ellipsoid semi axes; a_4, a_5 and a_6 represent the effects of cruised axes measurements, responsible for the ellipsoid inclination; and R is a geomagnetic field constant.

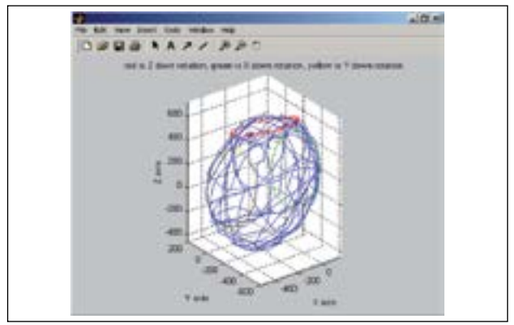

Figure 1. The geomagnetic field measure before sensor calibration (*mG*) (Alonso and Shuster 2003).

When the weak magnetic distortion is negligible, the ellipsoid is not bent and M_{si} is an identity matrix. Consequently, Eq. 4 can be simplified as follows:

$$\frac{(x-x_0)^2}{{a_1}^2} + \frac{(y-y_0)^2}{{a_2}^2} + \frac{(z-z_0)^2}{{a_3}^2} = R^2 \tag{5}$$

And the least square method provides the adjustment of the magnetometer data to the equation of an ellipsoid by determining the parameters x_{sf}, y_{sf}, z_{sf}, b_x, b_y and b_z. After these adjustments, the graphic representation of calibrated magnetometer data becomes a unitary sphere (Fig. 2).

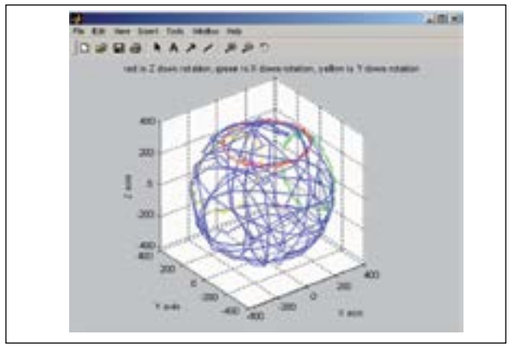

Figure 2. The geomagnetic field measure after sensor calibration (*mG*) (Alonso and Shuster 2003).

Equation 5 can be rewritten as:

$$x^2 = \begin{bmatrix}x & y & z & -y^2 & -z^2 & 1\end{bmatrix} \begin{bmatrix}2x_0\\ \frac{{a_1}^2}{{a_2}^2}2y_0\\ \frac{{a_1}^2}{{a_3}^2}2z_0\\ \frac{{a_1}^2}{{a_2}^2}\\ \frac{{a_1}^2}{{a_3}^2}\\ {a_1}^2R^2 - x_0^2 - \frac{{a_1}^2}{{a_2}^2}y_0^2 - \frac{{a_1}^2}{{a_3}^2}z_0^2\end{bmatrix} \tag{6}$$

Consequently, the non-calibrated magnetometer data (B_x, B_y, B_z) can be combined into a matrix $N \times 6$ dimentional, T, where N is the number of measurements ($N \neq 0$ and $N \in$ N). Then, Eq. 6 becomes:

$$w = TU \tag{7}$$

The parameter vector $\boldsymbol{U}$ can be determined using least squares method (ST Microelectronics 2012):

$$\boldsymbol{U} = [T^T T]^{-1} T^T w \tag{8}$$

Then,

$$b_x = x_0 = \boldsymbol{U}(1)/2 \tag{9}$$

$$b_y = y_0 = U(2)/(2 - U(4)) \tag{10}$$

$$b_z = z_0 = U(3)/(2 - U(5)) \tag{11}$$

$$A_1 = a^2R^2 = U(6) + x_0^2 + U(4).y_0^2 + \\ + U(5).z_0^2 \tag{12}$$

$$A_2 = \frac{A}{U(4)} \tag{13}$$

$$A_3 = \frac{A}{U(5)} \tag{14}$$

where: $U(i)$, i= 1, ..., 6, are the components of U. Taking the differences,

$$\begin{aligned} x_b &= B_x - b_x \\ y_b &= B_y - b_y \\ z_b &= B_z - b_z \end{aligned} \tag{15}$$

Equation 5 becomes:

$$\frac{x_b^2}{A_1} + \frac{y_b^2}{A_2} + \frac{z_b^2}{A_3} = 1 \tag{16}$$

Finally, the scale factors for calibration can be computed:

$$\begin{aligned} x_{sf} &= \sqrt{A_1} \\ y_{sf} &= \sqrt{A_2} \\ z_{sf} &= \sqrt{A_3} \end{aligned} \tag{17}$$

THE TWOSTEP ALGORITHM

A method to estimate the magnetometer systematic error without the knowledge of the ship attitude is the verification scale, which minimizes the differences of the squares of the magnitudes from measured and modeled magnetic fields. The scalar verification is based on the principle that parameters, such as the magnitude of a vector, do not depend on the coordinate system. However, the disadvantage of this approach is that the resulting cost function to be minimized is an equation of the fourth degree with respect to the bias vector.

Some algorithms have been proposed to avoid this type of calculation. The TWOSTEP algorithm is an improvement of these methods, by discarding less data during the centering process. Through this mathematical operation, the highest order term of the cost function can be eliminated, finding a simplified mathematical model (Alonso and Shuster 2002). A more complete mathematical model of the magnetic field vector measurement is given by (Kim and Bang 2007):

$$\begin{aligned} &\boldsymbol{B}_k = A_k \boldsymbol{T}_k + \boldsymbol{b} + \boldsymbol{\varepsilon}_k, \\ &k = 1,2,3,\ldots,N \end{aligned} \tag{18}$$

where: $\boldsymbol{b}$ is the magnetometer measurement systematic error (bias); $\boldsymbol{\varepsilon}_k$ is the measurement noise considered, for simplicity, white and Gaussian, whose covariance matrix is $\boldsymbol{\Sigma}_k$.

Minimization of Measurement Systematic Error

For the scalar verification, the equations are defined as follows (Kim and Bang 2007):

$$\mathbb{z}_k = \|\boldsymbol{B}_k\|^2 - \|\boldsymbol{T}_k\|^2 \tag{19}$$

$$\mathbb{z}_k = 2\boldsymbol{B}_k\boldsymbol{b} - \|\boldsymbol{b}\|^2 + \mathbb{v}_k, \quad k = 1,\ldots,N \tag{20}$$

$$\mathbb{v}_k \equiv 2(\boldsymbol{B}_k - \boldsymbol{b})\boldsymbol{\varepsilon}_k - \|\boldsymbol{\varepsilon}_k\|^2 \tag{21}$$

where: $\boldsymbol{z}_k$ is defined as actual measurement and $\boldsymbol{v}_k$ is defined as the effective noise measurement.

The negative log-likelihood function of magnetometer bias vector is given by Alonso and Shuster (2003):

$$J(\boldsymbol{b}) = \frac{1}{2}\sum_{k=1}^{N}\left[\frac{1}{\sigma_{vk2}}(\mathbb{z}_k' + 2\boldsymbol{B}_k\times\boldsymbol{b} + \|\boldsymbol{b}\|^2 - \right. \\ \left. - \mu_{vk})^2 + \log\sigma_{vk}^2 + \log 2\pi\right] \tag{22}$$

where: μ_{vk} is the mean and σ_{vk}^2 is the variance of the effective measurement noise, considered as Gaussian for simplicity; $\boldsymbol{z}_k'$ is the real value of $\boldsymbol{z}_k$.

$$\mu_{vk} = -tr(\boldsymbol{\Sigma}_k) \tag{23}$$

$$\sigma_{vk}^2 = 2(\boldsymbol{B}_k - \boldsymbol{b})^T\boldsymbol{\Sigma}_k(\boldsymbol{B}_k - \boldsymbol{b}) + 2\sum_{i=1}^{3}(\boldsymbol{\Sigma}_k)_{ii}^2 \tag{24}$$

where: $tr(\boldsymbol{\Sigma}_k)$ is the trace of matrices function.

The Centering Operation

By means of a mathematical operation called centering, the term of highest order can be removed. Therefore, the following weighted averages are defined (Alonso and Shuster 2002):

$$\begin{aligned} \bar{\mathbb{z}} &\equiv \bar{\sigma_v}^2\sum_{k=1}^{N}\frac{1}{\sigma_{vk}^2}\mathbb{z}_k \\ \bar{\boldsymbol{B}} &\equiv \bar{\sigma_v}^2\sum_{k=1}^{N}\frac{1}{\sigma_{vk}^2}\boldsymbol{B}_k \\ \bar{\mathbb{v}} &\equiv \bar{\sigma_v}^2\sum_{k=1}^{N}\frac{1}{\sigma_{vk}^2}\mathbb{v}_k \\ \bar{\mu_v} &\equiv \bar{\sigma_v}^2\sum_{k=1}^{N}\frac{1}{\sigma_{vk}^2}\mu_{vk} \\ \frac{1}{\bar{\sigma_v}^2} &\equiv \sum_{k=1}^{N}\frac{1}{\sigma_{vk}^2} \end{aligned} \tag{25}$$

Therefore:

$$\mathbb{z} = 2\bar{\boldsymbol{B}}.\boldsymbol{b} - \|\boldsymbol{b}\|^2 + \bar{\mathbb{v}} \tag{26}$$

The following centered quantities are defined:

$$\begin{aligned} \widetilde{\mathbb{z}}_k &\equiv \mathbb{z}_k - \bar{\mathbb{z}} \\ \widetilde{\boldsymbol{B}}_k &\equiv \boldsymbol{B}_k - \bar{\boldsymbol{B}} \\ \widetilde{\mathbb{v}}_k &\equiv \mathbb{v}_k - \bar{\mathbb{v}} \\ \widetilde{\mu}_{vk} &\equiv \mu_k - \overline{\mu_v} \end{aligned} \tag{27}$$

That implies in (Alonso and Shuster 2002):

$$\widetilde{\mathbb{z}}_k = 2\widetilde{\boldsymbol{B}}_k.\boldsymbol{b} + \widetilde{\mathbb{v}}_k, \quad k = 1,\ldots,N \tag{28}$$

The Procedure of the TWOSTEP Algorithm

The TWOSTEP algorithm, as the name implies, consists of two steps. In the first step, the centered magnetometer systematic error estimate is calculated, as well as its covariance matrix. The need of an additional correction step due to the discarded central term is measured by a direct comparison of the centered and central Fisher information matrices. In the step two, the obtained centered bias vector value is used as an initial estimate. The TWOSTEP algorithm can be described by Alonso and Shuster (2003):

Step one

1. Calculate the centered estimate of the magnetometer systematic error, $\widetilde{\boldsymbol{b}}^*$, and the covariance matrix, $\widetilde{\boldsymbol{P}}_{bb}$, using data from the centered quantities and the equations:

$$\widetilde{\boldsymbol{b}}^* = \widetilde{\boldsymbol{P}}_{bb}\sum_{k=1}^{N}\frac{1}{\sigma_{vk}^2}(\widetilde{\mathbb{z}}_k - \widetilde{\mu}_{vk})\,2\,\widetilde{\boldsymbol{B}}_k \tag{29}$$

$$\widetilde{\boldsymbol{P}}_{bb}^{-1} = \widetilde{\boldsymbol{F}}_{bb} = \left(\sum_{k=1}^{N}\frac{1}{\sigma_{vk}^2}4\,\widetilde{\boldsymbol{B}}_k\,\widetilde{\boldsymbol{B}}_k^T\right)^{-1} \tag{30}$$

2. From the centered estimate, $\widetilde{\boldsymbol{b}}^*$, calculate $\widetilde{\boldsymbol{F}}_{bb}$ and $\overline{\boldsymbol{F}}_{bb}$ through the above equations and the following equation:

$$\boldsymbol{F}_{bb} = \widehat{\boldsymbol{P}}_{bb}^{-1} + \frac{4}{\sigma_v^2}(\boldsymbol{B} - \boldsymbol{b})(\boldsymbol{B} - \boldsymbol{b})^T = \widehat{\boldsymbol{F}}_{bb} + \overline{\boldsymbol{F}}_{bb} \tag{31}$$

where: $\widetilde{\boldsymbol{F}}_{bb}$ and $\overline{\boldsymbol{F}}_{bb}$ are the Fisher information matrices.

If the diagonal elements of $\overline{\boldsymbol{F}}_{bb}$ are sufficiently smaller than the diagonal elements of $\widetilde{\boldsymbol{F}}_{bb}$ ($[\overline{\boldsymbol{F}}_{bb}]mm < C\,[\widetilde{\boldsymbol{F}}_{bb}]mm$, m = 1,2,3), the calculation of the magnetic field systematic error vector can be terminated at that point, and $\widetilde{\boldsymbol{b}}^*$ can be accepted as the best estimated value. The covariance matrix of the estimated error will be the inverse of $\widetilde{\boldsymbol{F}}_{bb}$.

Step two

1. If the inequality from the previous step is not true, use the centered value $\widetilde{\boldsymbol{b}}^*$ as an initial estimate. The correction due to the central term is computed using the Gauss-Newton method:

$$\boldsymbol{b}_{i+1} = \boldsymbol{b}_i - \boldsymbol{F}_{bb}^{-1}(\boldsymbol{b}_i)\boldsymbol{g}(\boldsymbol{b}_i) \tag{32}$$

The Fisher information matrix ($\boldsymbol{F}_{bb}$) is given by the equation:

$$\boldsymbol{F}_{bb} = \widehat{\boldsymbol{P}}_{bb}^{-1} + \frac{4}{\bar{\sigma_v}^2}(\bar{\boldsymbol{B}} - \boldsymbol{b})(\bar{\boldsymbol{B}} - \boldsymbol{b})^T = \boldsymbol{P}_{bb}^{-1} \tag{33}$$

where the gradient vector $\boldsymbol{g}(\boldsymbol{b})$ is given by:

$$\boldsymbol{g}(\boldsymbol{b}) = \widehat{\boldsymbol{P}}_{bb}^{-1}\left(\boldsymbol{b} - \widetilde{\boldsymbol{b}}^*\right) - \frac{1}{\bar{\sigma_v}^2}(\bar{\mathbb{z}}' - 2\bar{\boldsymbol{B}}\boldsymbol{b} + \\ + \|\boldsymbol{b}\|^2 - \overline{\mu_v})2(\bar{\boldsymbol{B}} - \boldsymbol{b})\boldsymbol{F}_{bb} \tag{34}$$

2. The previous step is repeated until η_{ii} is less than a predetermined value, where:

$$\eta_i = [\boldsymbol{b}_i - \boldsymbol{b}_{i-1}]^T\boldsymbol{F}_{bb}(\boldsymbol{b}_i)[\boldsymbol{b}_i - \boldsymbol{b}_{i-1}] \tag{35}$$

In this study, the adopted stopping criterion is $\eta_i \leq 10^{-5}$.

THE EXPERIMENTAL SETUP

The experimental implementation and tests were based on a CubeSat mockup equipped with a processor device Arduino MEGA 2560 (Arduino 2005) and a solid state magnetometer HMC5843 (Honeywell 2009). This mockup was built to perform

J. Aerosp. Technol. Manag., São José dos Campos, Vol.8, Nº 1, pp.103-112, Jan.-Mar., 2016

experimental simulations of attitude movements and embedded calibration procedures.

The Arduino platform is a development device based on a single microcontroller conceived to make accessible the use of electronic embedded system. The platform consists of an open hardware equipped with an AVR Atmel ATmega2560 processor, memories, clock and with a number of convenient digital and analog I/O gates. The software comprises a standard programming language compiler (Wiring, a simplified C++), a bootloader executed by the processor itself, and an IDE environment.

THE SATELLITE MOCKUP

The experimental tests used a CubeSat mockup built to provide three-axis movements (*X*, *Y* and *Z* axis of the body coordinates frame). The CubeSat body is composed of transparent acrylic polyethylene plates, a system of bearings, and supports for the Arduino platform and for the magnetometer HMC5843. Figure 3 shows the CubeSat mockup.

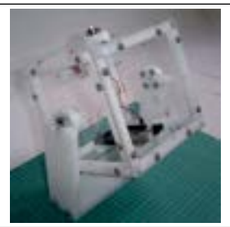

Figure 3. The CubeSat mockup for experimental tests of magnetometer calibration.

SATELLITE MANEUVERS FOR MAGNETIC DATA ACQUISITION

The tests of magnetometer calibration use single mockup rotations around the three axes of the body coordinates frame (*X*, *Y*, *Z*), as can be seen in Fig. 4. The rotations are manually performed, without strict control of rapidity or duration of the motion, because these parameters are not important in the calibration tests. The calibration can also be done using aleatory motion combining rotations around all axes (Fig. 4).

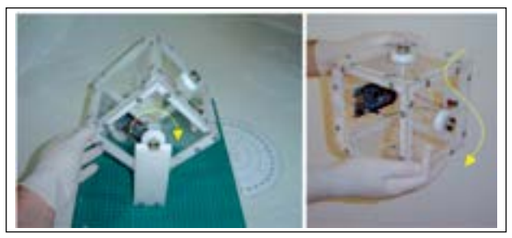

Figure 4. Two maneuvers of the CubeSat mockup for magnetometer data acquisition: rotation around one axis and aleatory motion.

TESTS RESULTS

TESTS OF THE GEOMETRIC CALIBRATION APPROACH

The geometric method is applied for experimental tridimensional calibration of the magnetometer HMC5843. The experimental procedure consists of rotation of the satellite mockup around the three axes of magnetometer frame. The first rotation is around the *Z* axis, the second one, around *Y* axis, and the last rotation, around *X* axis. The resulting magnetic field measurements are shown in Fig. 5.

The results of parameters calculation for the calibration are shown in Table 1.

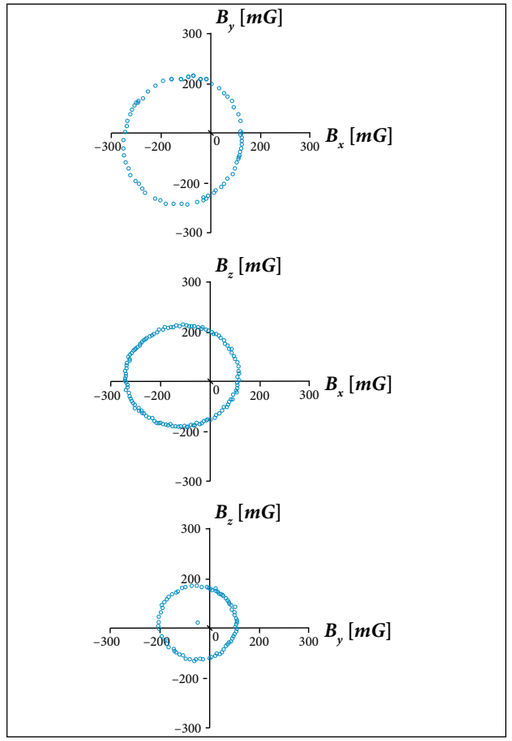

Figure 5. The measurements of B_x, B_y and B_z during the rotation maneuvers by using the sensor HMC5843.

Figure 6 shows the graphics of $\hat{H}_x$, $\hat{H}_y$ and $\hat{H}_z$ measurements, obtained by the magnetometer HMC5843, calibrated by the geometric method applied to three-dimensions problem.

Table 1. Results of calibration process by geometric method.

$b_x = -115.876\ mG$	$x_{sf} = 0.935$
$b_y = -27.701\ mG$	$y_{sf} = 0.998$
$b_x = -2.178\ mG$	$z_{sf} = 1.081$

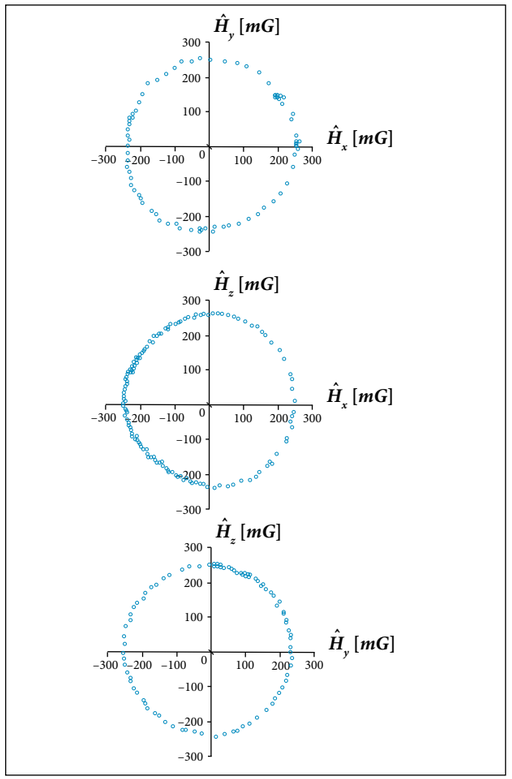

Figure 6. The graphics of $\hat{H}_x$, $\hat{H}_y$ and $\hat{H}_z$ measurements of the sensor HMC5843 after calibration using 3-D geometric method.

TESTS OF THE TWOSTEP ALGORITHM

The first tests using TWOSTEP calibration algorithm comprehended numerical simulations using a CubeSat flying in typical orbit, with stabilized attitude keeping the *X* axis pointed to the Sun, and considering a simulated noise disturbing the magnetometer HMC5843 of magnitude $\sigma_0 = 2.8\ mG$ per axis. The resulting simulated geomagnetic field is shown in Fig. 7.

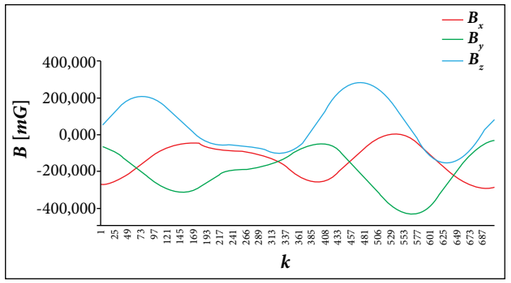

Figure 7. Simulated measurements of the geomagnetic field for the magnetometer calibration procedure, with *X* axis of satellite pointed to the Sun.

In the first step of TWOSTEP algorithm, the results are:

$$\begin{aligned}
&\overline{\sigma_{v0}}^2 = 3672.827\\
&\widehat{\boldsymbol{b}_0}^* = [-18.203\ \ -38.215\ \ 11.686] \pm\\
&\quad \pm [0.709\ \ 0.591\ \ 0.248]mG
\end{aligned} \tag{36}$$

$$\begin{aligned}
&\overline{\sigma_v}^2 = 2864.446\\
&\widehat{\boldsymbol{b}}^* = [-16.966\ \ -36.478\ \ 12.007] \pm\\
&\quad \pm [0.632\ \ 0.532\ \ 0.222]mG
\end{aligned}$$

The centralized Fisher information matrix is then obtained:

$$\widehat{F}_{bb} = \begin{bmatrix} 9.119 & -9.229 & 0.035 \\ -9.229 & 12.897 & -0.672 \\ 0.035 & -0.672 & 20.417 \end{bmatrix} (mG)^{-2} \tag{37}$$

And the Fisher information matrix for the central value correction is given by:

$$\bar{F}_{bb} = \begin{bmatrix} 23.750 & 27.045 & -0.873 \\ 27.045 & 30.797 & -0.995 \\ -0.873 & -0.995 & 0.032 \end{bmatrix} (mG)^{-2} \tag{38}$$

The resulting factor is $c = 2.604$. In this case, where the satellite is stabilized, the error vector components are less observable. Consequently, the estimation of the systematic error obtained in the second step of the algorithm (see details of the iterations in Table 2) is:

$$\begin{aligned}
&\boldsymbol{b}_2 = [-17.361\ \ -36.809\ \ 11.997] \pm\\
&\quad \pm [0.198\ \ 0.172\ \ 0.221]mG
\end{aligned} \tag{39}$$

A second case for numerical simulation of the calibration

procedure considers the same noise disturbing the magnetometer HMC5843, *i.e.* the magnitude per axis. But now the satellite keeps the *Z* axis pointed to the center of the Earth. The resulting simulated geomagnetic field is shown in Fig. 8.

Table 2. Results of iterations of the second step of the algorithm (σ_0 = 2.8 *mG*, satellite stabilized, axis *X* pointing to the Sun).

Iteration	b_{ix}	b_{iy}	b_{iz}
0	−16.966	−36.478	12.007
1	−17.361	−36.809	11.997
2	−17.361	−36.809	11.997

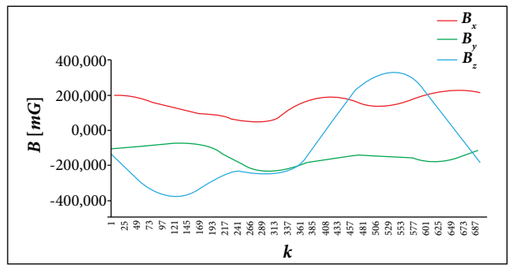

Figure 8. Simulated measurements of the geomagnetic field for the magnetometer calibration procedure, with *Z* axis of satellite pointed to the center of the Earth.

In the first step of TWOSTEP algorithm, the results are:

$$\begin{aligned}\overline{\sigma_{v0}}^2 &= 2593.442\\ \widehat{\boldsymbol{b}_0}^* &= [-14.638 \quad -38.229 \quad 11.733] \pm\\ &\pm [0.779 \quad 0.785 \quad 0.233]mG\\ \overline{\sigma_v}^2 &= 2850.384\\ \widehat{\boldsymbol{b}}^* &= [-15.763 \quad -37.764 \quad 11.679] \pm\\ &\pm [0.822 \quad 0.824 \quad 0.236]mG\end{aligned} \tag{40}$$

One can remark that $\overline{\sigma}_{v0}^2$ is bigger than the precedent case. The vector $\boldsymbol{b}$ tends to be more distant from the magnitude of the geomagnetic field vector.

The centralized Fisher information matrix is then obtained:

$$\widehat{F}_{bb} = \begin{bmatrix} 3.081 & 1.030 & 5.441 \\ 1.030 & 2.165 & -0.965 \\ 5.441 & -0.965 & 31.751 \end{bmatrix} (mG)^{-2} \tag{41}$$

And the Fisher information matrix for the central value correction is given by:

$$\bar{F}_{bb} = \begin{bmatrix} 57.080 & 0.268 & -11.704 \\ 0.268 & 0.001 & -0.055 \\ -11.704 & -0.055 & 2.400 \end{bmatrix} (mG)^{-2} \tag{42}$$

In this case, the resulting factor is c = 18.527. Again, with the satellite body stabilized, the error vector components are weakly observable. The estimation of the systematic error obtained in the second step of the algorithm (see details of the iterations in Table 3) is:

$$\begin{aligned}\boldsymbol{b}_2 &= [-16.787 \quad -37.189 \quad 11.881] \pm\\ &\pm [0.130 \quad 0.687 \quad 0.174]mG\end{aligned} \tag{43}$$

Table 3. Results of the second step of the algorithm (σ_0 = 2.8 *mG*, satellite stabilized, axis *Y* pointing to the center of the Earth).

Iteration	b_{ix}	b_{iy}	b_{iz}
0	−15.763	−37.764	11.679
1	−16.790	−37.189	11.882
2	−16.787	−37.189	11.881

The experimental magnetometer calibration was performed using the algorithm TWOSTEP embedded in the satellite mockup. The main supposition for the tests is that the geomagnetic field is constant for a fixed point and for a short time period. This is not the case for a satellite orbiting the Earth at a high displacement speed. Meanwhile, the main purpose of these tests is to verify the performance of the calibration algorithm to filter noises in the magnetic field measurement. The results shown in Fig. 9 are related to data acquisition during aleatory maneuvers as illustrated in Fig. 4.

Considering the calculations of the first step of TWOSTEP algorithm, the results are:

$$\begin{aligned}\overline{\sigma_{v0}}^2 &= 1492.421\\ \widehat{\boldsymbol{b}_0}^* &= [-112.605 \quad -42.239 \quad 22.172] \pm\\ &\pm [0.172 \quad 0.179 \quad 0.187]mG\\ \overline{\sigma_v}^2 &= 2029.324\\ \widehat{\boldsymbol{b}}^* &= [-115.998 \quad -35.452 \quad 15.330] \pm\\ &\pm [0.175 \quad 0.180 \quad 0.244]mG\end{aligned} \tag{44}$$

The Fisher information matrix is then obtained:

$$\widehat{F}_{bb} = \begin{bmatrix} 32.913 & 1.334 & 0.637 \\ 1.334 & 32.538 & -5.193 \\ 0.637 & -5.193 & 17.681 \end{bmatrix} (mG)^{-2} \tag{45}$$

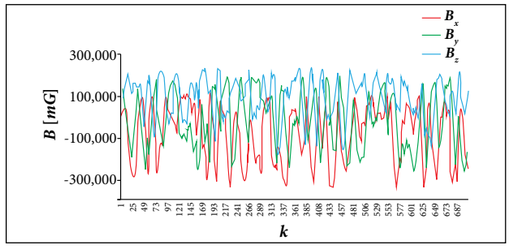

Figure 9. Earth magnetic field measurements by the magnetometer embedded in the CubeSat mockup.

For the centralized value correction, the Fisher matrix is calculated:

$$\bar{F}_{bb} = \begin{bmatrix} 2.308 & 0.691 & 5.330 \\ 0.691 & 0.207 & 1.595 \\ 5.330 & 1.595 & 12.307 \end{bmatrix} (mG)^{-2} \tag{46}$$

In this case, the proportion factor is c = 0.696. It means that the second step of the calibration algorithm must continue. The estimation of systematic error with the centralized correction calculated after four iterations (the details of the iterations results are shown in Table 4) of the second step is:

$$\begin{aligned}\boldsymbol{b}_4 &= [-117.452 \quad -37.268 \quad 7.184] \pm\\ &\pm [0.172 \quad 0.176 \quad 0.180]mG\end{aligned} \tag{47}$$

Table 4. Results of the second step of the algorithm.

Iteration	b_{ix}	b_{iy}	b_{iz}
0	−115.998	−35.452	15.330
1	−117.506	−37.172	7.442
2	−117.458	−37.262	7.198
3	−117.453	−37.268	7.185
4	−117.452	−37.268	7.184

In general, it appears that the use of a noisy magnetometer makes the results show less precisely in relation to those obtained by Alonso and Shuster (2002). In the case where the satellite is stabilized, with *Z* axis pointing to the Earth, it can be noted that the measurements of the *Y* axis of the magnetic field vector are hardly observable, even after the application of step two. This can be seen in Fig. 8, where there is little variation in the measured values.

In cases where the satellite is spinning at 15.1 rpm (*X* axis pointing to the Sun) or it is inertially stabilized (*X* axis pointing to the Sun) or it is stabilized (*Z* axis pointing to the Earth), the use of noisy data measured by magnetometer HMC5843 made the central values obtained in step two stay slightly outside the expected range. This leads to the need for investing in better magnetometers in order to improve the accuracy of the results.

As shown by simulations, the TWOSTEP algorithm works well in all phases of spaceship operation, especially in the case of artificial satellites, from the orbit injection phase, with the spacecraft spinning, to the moment when the ship has its attitude completely stabilized (with the *Z* axis, simulating the load direction, pointing to the Earth). The systematic error vector (bias) components are more observable when the Earth's magnetic field vector is changing regularly. Therefore, the best time to measure the systematic error is immediately after the orbit injection when the satellite is still spinning. In the tests, the worst time is when the satellite is fully stabilized, with its *Z* axis pointing to the Earth, when the components vary slightly.

The simulations also show that, for a spaceship in a geostationary orbit, with the attitude stabilized, the TWOSTEP algorithm will not converge. The estimate of the systematic error of the measured value tends to the magnetic field vector in this particular case.

CONCLUSION

This project presented a review and an experimental implementation of methods for magnetic field sensor calibration in the context of an embedded device for applications in vehicle navigation systems like artificial satellites. The Arduino MEGA 2560 was perfectly capable of performing the most complex mathematical calculations required by the geometric method. This method requires absolute attitude control during calibration. It also applies most commonly to small devices and vehicles. It is not ruled out, however, the need to recalibrate the magnetometer during the mission, using other methods. The test results showed that TWOSTEP algorithm is fast and robust in the calculation of the bias magnetic field vector. This method, despite the simplicity of the equations, requires accumulation of data to calculate some parameters preliminarily. Therefore, the primary bias was estimated from the first batch of magnetometer measurements.

Comparing these two implemented methods of calibration, it can be seen that all are fast and reach the desired results, with comparable estimates. However, the navigation system,

the mission, and especially the device or vehicle will determine which magnetometer calibration method is the most applicable in each case, including the possibility of using a combination of methods.

ACKNOWLEDGEMENTS

The authors acknowledge the institutional support of the Universidade Federal do ABC (Brazil).

REFERENCES

Alonso R, Shuster MD (2002) TWOSTEP: a fast robust algorithm for attitude-independent magnetometer-bias determination. J Astronaut Sci 50(4):433-451.

Alonso R, Shuster MD (2003) Centering and observability in attitude-independent magnetometer-bias determination. J Astronaut Sci 51(2):133-141.

Arduino (2005) Smart Projects, Ivrea, Italy; [accessed 2012 Feb 14]. www.arduino.cc

Caruso MJ (2000) "Applications of magnetic sensors for low cost compass systems. Proceedings of the IEEE on Position Location and Navigation Symposium, San Diego, USA.

Crassidis JL, Lai KL, Harman RR (2005) Real-time attitude-independent three-axis magnetometer calibration. J Guid Contr Dynam 28(1):115-120.

Honeywell (2009) HMC5843 3-axis digital compass IC. Honeywell Inc., Morristown, NJ, 1-19; [accessed 2012 Feb 14]. www.honeywell.com

Inamori T, Nakasuka S (2012) Application of magnetic sensors to nano- and micro-satellite attitude control systems. In: Kuang K, editor. Magnetic sensors: principles and applications. Rijeka, Croatia: InTech. p. 85-102.

Juang JC, Tsai YF, Tsai CT (2012) Design and verification of a magnetometer-based orbit determination and sensor calibration algorithm. Aero Sci Tech 21(1):47-54. doi: 10.1016/j.ast.2011.05.003

Kim E, Bang HC (2007) Bias estimation of magnetometer using genetic algorithm. Proceedings of the International Conference on Control, Automation and Systems; Seul, Korea.

Pisacane VL (2005) Fundamentals of space systems. New York: Oxford University Press.

ST Microelectronics (2012) AN3192 application note: using LSM303DLH for a tilt compensated electronic compass; [accessed 2012 Apr 17]. www.st.com

Vasconcelos JF, Elkaim G, Silvestre C, Oliveira P, Cardeira B (2011) Geometric approach to strapdown magnetometer calibration in sensor frame. IEEE Trans Aero Electron Syst 47(2):1293-1306. doi: 10.1109/TAES.2011.5751259

INSTRUCTIONS TO AUTHORS (Revised in December 2015)

SCOPE AND EDITORIAL POLICY: The JATM is an open access journal, quarterly published and devoted to research and management on different aspects of aerospace technologies. The authors are solely responsible for the contents of their contribution and it is assumed that they have the necessary authority for publication. The JATM is under a Creative Commons 4.0 International License (CC-BY). All the published material are free of any Article Processing Charges (APC).

PAPER SUBMISSION: The manuscript should be digitalized using a Microsoft® Office document (.doc), 12-pt. Times New Roman, double-spaced throughout, justified paragraphs and leaving one space after a period. Do not try to fit the manuscript in the final template. For those authors that prefer to edit in LaTex, submit a PDF file instead. Do not include a list of symbols, nomenclature and/or abbreviations. Instead, define them at the first time they appear in text. Accepted manuscripts can be edited by the editorial office to comply with the format of the journal, remove redundancies, and improve clarity and understanding without altering meaning. The edited text will be presented to authors for approval. To ensure the integrity of the blind peer-review process, it is mandatory to prevent the identities of the authors. So, check if the following steps have been taken with regard to the text and the file properties: (1) delete the authors' name from the text, with "Author" and year used in citation and in the references, instead of the authors' name, article title etc.; (2) do not include the section "Acknowledgements". You should do it in the copyediting step, after approval of the manuscript; and (3) author identification should also be removed from the properties of the file (see: ensuring peer review for detailed instructions). The manuscript should be submitted electronically only in English, at http://www.jatm.com.br/ojs/index.php/jatm/about/submissions#onlineSubmissions. If there is any conflict of interest regarding the evaluation of the manuscript, the author must send a declaration indicating the reasons, so that the review process occurs fairly. It is extremely important that all data about the authors are entered correctly at the time of submission. The data refer to the full name; affiliation with three instances (e.g. university/college/department); city, state and country. It is highly recommended to adopt and inform the ORCID number of each author and to indicate the corresponding author with full postal address. At the time of submission, the corresponding author assumes that all other authors actively participated in the research and/or performed the final review and approval of the article. Papers already presented at conferences will be accepted if they were not published in complete form in the Annals of the conference or if they are extended with additional results or new findings. Articles from guest authors will be published after approval of one specialist Associated Editor. The JATM does not publish translated articles from other journals. You must submit also highlights, about 3 short sentences (maximum of 100 characters) with core results of the paper for promotion purposes.

PEER REVIEW: The manuscripts will be received by the assistant editors who initially will verify the similarity of the content (plagiarism) using the iThenticate system. For manuscripts with no or low content of similarity, a Section Editor (SE) will be assigned. The SE will appoint 2 to 4 external evaluators (ad hoc referees) in double-blind peer review mode, ensuring complete anonymity. After receiving the evaluations, the SE must give a decision about the manuscript addressing the evaluator's recommendations. The SE can accept the manuscript in the form it was submitted; can reject it or request revisions. The manuscript that requires revision will be sent to the author, who is supposed to submit a new version and a letter to the Editor, where each recommendation of the evaluators should be commented. In the case the author does not agree with the evaluator's suggestions, it is necessary to explain the reasons. After verifying the adherence to the recommendations in the new version, the SE should give the final decision or, exceptionally, send to another evaluation round if the changes have not been sufficiently addressed. The entire process is available to the authors at any moment. In the cases the authors do not agree with the final decision, it is allowed to appeal on the decision by sending an email to the Executive Editor, who will review the process and ask for reconsideration to the Editors in Chief, if justified.

MANUSCRIPT CATEGORIES: **Editorial** - Any researcher may write the editorial on the invitation of the Editors in Chief. Editorials should cover broad aspects of Aerospace Technology, with scientific content. Such manuscripts are not submitted to peer review; **Review articles** - These should cover subjects that are relevant to the scope of the journal. Authors should bear in mind that they are expected to have expertise in the reviewed field. The article may be of any length required for the concise presentation of the subject; **Original papers** - These articles should report results of the scientific research. The article should not present more than 60,000 characters with space, as succinct papers are favored in terms of impact as well as in readability; **Communications** - They should report previous results of ongoing research and should not content more than 40,000 characters with space.

MANUSCRIPT STRUCTURE: Whenever possible, manuscripts should include the following subsections; however, articles from some areas should follow their usual format. Please, do not number the sections. Use different styles for differentiate subsections. **Title and names of authors:** The title should not contain abbreviations. All authors should be identified with full name, email, institution to which they are related, city, state, and country. One of them should be indicated as the author for correspondence and his/her full postal address is required; **Abstract:** They are limited to 250 words and structured into objectives, methods, results, and conclusions. Citations or abbreviations (except internationally recognized abbreviations, such as weights, measures, and physical or chemical ones) are not permitted; **Keywords:** It is highly recommended to choose the keywords accurately, selecting three to six items based on NASA Thesaurus volume 2 – Access Vocabulary, which can be accessed at http://www.sti.nasa.gov/thesvol2.pdf; Introduction: It should set the purpose of the study, providing a brief summary (not a review) of previous relevant studies, and stating the new advances in the current investigation. The introduction should not include data or conclusions from the work being reported. A final sentence summarizing the novel finding to be presented is permissible; **Methodology:** The authors are free to use any structure in this section to fit the objectives of the study. They could also rename it (e.g. Numerical analysis, Case study, and so on), and in some cases it may be advisable to omit it. Clear and sufficient information to permit the study to be repeated by others should be briefly given. Standard techniques need only to be referenced. Previously published methods may be briefly described following the reference; **Results:** This section should be a concise account of the new information that was discovered, with the least personal judgment. Do not repeat in text all the data in the tables and illustrations, but briefly describe what these data comprise; **Discussion:** The discussion should include the significance of the new information and relevance of the new findings in light of existing knowledge. Only unavoidable citations should be included. Citations to review articles are not encouraged in this section. In some cases, this section may be advisable to merge with the previous section ("Results and Discussion"); **Acknowledgements:** This section should be short, concise, and restricted to acknowledgements that are necessary. The financial support received for the elaboration of the manuscript must be declared in this item. Also, references to personal or private communication placed in running text should be acknowledged in this section; **References:** Acceptable references include journal articles, numbered papers, books, and submitted articles, if the journal is identified. Self-citation should be limited to a minimum.

REFERENCES STYLE AND FORMAT CITATION: The JATM uses the name-year system. The references should be mentioned in the text by giving the last name of the author and the year of publication, eg.: Smith 1997. For articles with 2 authors, use the form: Smith and Farias 1997. With 3 or more names, use the form: Smith et al. 1997. If two or more references have the same identification, distinguish them by appending "a", "b" etc. to the year of publication. Where citing more than one reference, they should be separated by semicolon. Standards should be cited in text by the acronym of the entity followed by the number, and they do not appear in the references list. Organization as author should be cited by the acronym. For the in-text reference of websites or other online formats, include only the first word or two words of the title (enough to distinguish it from other titles in the references list), followed by an ellipsis (APSnet . . . c1994–2005). The references list is unnumbered and appears in alphabetical order by author and year of publication, with multiple studies by the same author listed in chronological order. It is highly recommended that each reference contains the digital object identifier number (doi). References retrieved from the Internet should be cited by the last name of the author(s) and the year of publication, or n.d., if not available, followed by the date of access. A complete list of examples can be found at http://www.jatm.com.br/ojs/index.php/jatm/about/submissions#authorGuidelines. The most usual are listed below:

Journals: List authors in the order in which they appear in the original text, separated by colon. The year of publication follows the authors list in parentheses, followed by article and journal title, as well as volume or issue information. The page range for the article is preceded by colon. Journal titles are generally abbreviated according to the list of title word abbreviations maintained by the ISSN International Centre:

Costa S (1996) Dassault adaptative cells. Ind Robot Int J 23(1):34-40. doi: 10.1108/01439919610108837

Alves MB, Morais AMF (2009) The management of knowledge and technologies in a space program. J Aerosp Technol Manag 1(2):265-272. doi: 10.5028/ jatm.2009.0102265272;

Sparrow EM (1980a) Forced convection heat transfer in a duct having spanwise-periodic rectangular protuberances. Num Heat Transfer 3:149-167

Sparrow EM (1980b) Fluid-to-fluid conjugate heat transfer for a vertical pipe-internal and external natural convection. ASME J Heat Transfer 102:402-407.

Books: The basic format is: Author(s) (Date) Title. Edition. Place of publication: Publisher. Extent. Notes. Extent can include information about pagination or number of volumes and is considered optional. Notes can include information of interest to the reader, such as language of publication other than English; such notes are optional. These notes also provide information about location, such as a URL for online works:

Rohsenow W, Hartnett JP, Cho YI (1998) Handbook of heat transfer. New York: McGraw-Hill.

Patents: Blanco EE, Meade JC, Richards WD, inventors; Ophthalmic Ventures, assignee. 1990 Nov 13. Surgical stapling system. United States patent US 4,969,591.

Websites and other online formats: References to websites and other online formats follow the same general principles as for printed references, with the addition of a date of update/revision (if available) along with an access date and a URL: Title of the homepage. Date of publication. Edition. Place of publication: publisher; [date updated; date accessed]. Notes. If no date of publication can be determined, use a copyright date (if available), preceded by "c". Include the URL in the notes:

APSnet: plant pathology online. c1994-2005. St Paul (MN): American Phytopathological Association; [accessed 2005 Jun 20]. http://www.apsnet.org/

TABLES FIGURES AND EQUATIONS: **Tables** - should be numbered in order of appearance in the text, using Arabic numerals. Each table should have a title and an explanatory legend, if necessary. All tables must be referenced and mentioned in the text as "Table" and succinctly described in the text. Under no circumstances should a table repeat data that are presented in an illustration. Statistical measures of variation (i.e. standard deviation or standard error) should be identified, and decimal places in tabular data should be restricted to those with mathematical and statistical significance. **Figures** - All illustrations, line graphs, charts, schemes, photographs, and graphs should be referred as "Figure" and submitted with good definition (JPEG files of at least 300 dpi resolution and 12 cm wide); otherwise, authors will be requested to withdrawn from the text. Number the figures consecutively using Arabic numerals in order of appearance. References should be made in the text to each figure using the abbreviated form "Fig.", except if they are mentioned in the beginning of the sentences. Captions should be descriptive and allow the examination of the figures, without reference to text. You are welcome to paste images into Microsoft® Word documents, but you must send the images as separate JPEG files as well, when required. **Equations:** Type them on individual lines, in 12-pt. Times New Roman, with symbols in italic, and identifying them by Arabic numerals enclosed in parenthesis. References should be made in the text to each equation using the abbreviated form "Eq.", except in the beginning of the sentences, where the form "Equation" should be used.

J. Aerosp. Technol. Manag., São José dos Campos, Vol.8, Nº 1, pp.113-116, Jan.-Mar., 2016

www.linceu.com.br